

TALLINN UNIVERSITY OF TECHNOLOGY
DOCTORAL THESIS
28/2019

Radar Remote Sensing of Meteo-Marine Parameters in the Baltic Sea

SANDER RIKKA



TALLINN UNIVERSITY OF TECHNOLOGY

School of Science

Department of Marine Systems

This dissertation was accepted for the defence of the degree 18/04/2019

Supervisor: Dr Rivo Uiboupin
Department of Marine Systems
Tallinn University of Technology
Tallinn, Estonia

Co-supervisor: Dr Andrey Pleskachevsky
German Aerospace Center (DLR)
Remote Sensing Technology Institute, SAR Signal Processing
Bremen, Germany

Opponents: Dr Johannes Schulz-Stellenfleth
Helmholtz-Zentrum Geesthacht (HZG)
Institute of Coastal Research (IfK)
Geesthacht, Germany

Dr Kaupo Voormansik
Department of Remote Sensing, Tartu Observatory
University of Tartu
Tartu, Estonia

Defence of the thesis: 12/06/2019, Tallinn

Declaration:

Hereby I declare that this doctoral thesis, my original investigation and achievement, submitted for the doctoral degree at Tallinn University of Technology has not been submitted for doctoral or equivalent academic degree.

Sander Rikka

signature



European Union
European Regional
Development Fund



Investing
in your future

Copyright: Sander Rikka, 2019

ISSN 2585-6898 (publication)

ISBN 978-9949-83-429-7 (publication)

ISSN 2585-6901 (PDF)

ISBN 978-9949-83-430-3 (PDF)

TALLINNA TEHNIKAÜLIKOO
DOKTORITÖÖ
28/2019

Laine- ja tuuleväljade määramine Läänemeres radarkaugseire andmetest

SANDER RIKKA



Contents

List of Publications	6
Author's Contribution to the Publications	7
Introduction	8
1 BACKGROUND	9
1.1 Wind and wave field conditions in the Baltic Sea.....	9
1.2 Ocean wave basics.....	9
1.3 Radar signal interactions with the ocean surface	11
1.4 Overview of wind-wave field estimation methods from radar	14
2 MOTIVATION AND OBJECTIVES.....	16
3 MATERIALS AND METHODS	18
3.1 <i>In situ</i> measurements and radar data	18
3.2 Wave model	20
3.3 Image processing methods.....	21
3.4 Surface wind estimation from TS-X/TD-X and Sentinel-1.....	22
3.5 Methods to estimate sea state from radar data	23
3.6 Comparison methods	24
4 RESULTS AND DISCUSSION	25
4.1 Improvements on XWAVE_C function.....	25
4.2 Wave height estimation function for marine radar data	26
4.3 Validation of wave and wind field retrieval algorithms.....	26
4.4 Local variability of sea state conditions in the Baltic Sea	28
4.4.1 Wave field parameters from high resolution SAR imagery	29
4.4.2 Wave field studies from medium resolution SAR imagery	31
4.5 SAR and marine radar data for operational use in the Baltic Sea	33
4.5.1 Sentinel-1 imagery for practical applications	33
4.5.2 Temporal variability of sea state parameters from marine radar	34
4.5.3 Climatological aspect of Sentinel-1 data.....	36
CONCLUSION.....	37
REFERENCES	39
Acknowledgements.....	46
Abstract.....	47
Lühikokkuvõte.....	48
Appendix	49
Curriculum vitae.....	142
Elulookirjeldus.....	144

List of Publications

The list of author's publications, on the basis of which the thesis has been prepared:

- I Rikka, S., Pleskachevsky, A., Uiboupin, R. and Jacobsen, S. (2018). Sea state in the Baltic Sea from space-borne high-resolution synthetic aperture radar imagery. *International Journal of Remote Sensing*, 39(4), pp. 1256–1284.
- II Rikka, S., Pleskachevsky, A., Jacobsen, S., Alari, V. and Uiboupin, R. (2018). Meteo-marine parameters from Sentinel-1 SAR imagery: towards near real-time services for the Baltic Sea. *Remote Sensing*, 10(5), pp. 757.
- III Rikka, S., Uiboupin, R., Kõuts, T., Vahter, K. and Pärt, S. (2019). A Method for Significant Wave Height from Circularly Polarized X-band Marine Radar Images. *IEEE Geoscience and Remote Sensing Letters*, pp. 1–5.
- IV Rikka, S., Uiboupin, R. and Alari, V. (2017). Applicability of SAR-based wave retrieval for wind-wave interaction analysis in the fetch-limited Baltic. *International journal of remote sensing*, 38(3), 906–922.
- V Viitak, M., Maljutenko, I., Alari, V., Suursaar, Ü., Rikka, S. and Lagemaa, P. (2016). The impact of surface currents and sea level on the wave field evolution during St. Jude storm in the eastern Baltic Sea. *Oceanologia*, 58(3), 176–186.

Author's Contribution to the Publications

Contribution to the publications in this thesis are:

*** – complete contribution (100%)

** – leading contribution (> 50%)

* – supporting contribution (<50%)

- – no contribution

Publication	I	II	III	IV	V
Concept	**	**	**	**	*
Method development	*	-	***	**	*
Data processing	**	***	***	***	*
Data analysis	**	**	***	**	*
Manuscript preparation	**	**	**	**	*

Introduction

The Earth's oceans and regional water bodies, such as the Baltic Sea, have an important role in forming the weather systems and coastal environments. Surface gravity waves are an obvious feature of the ocean which upon surface winds impact many oceanographic processes. Due to the sparse amount of *in situ* measurements of wave parameters in the open ocean, as well as in the Baltic Sea, remote sensing techniques could be utilised to obtain additional information about wind and wave field parameters.

Synthetic Aperture Radar (SAR) is a space-borne remote sensing instrument providing two-dimensional (2D) sea surface wave information on a global and continuous scale. Because of the independence of daylight and weather conditions SAR data with global coverage are a unique source of information for the open sea and coastal applications (Lehner et al. 2008; Li, Lehner, and Rosenthal 2010; Pleskachevsky, Rosenthal, and Lehner 2016; Ressel et al. 2016; Singha, Velotto, and Lehner 2015; Velotto et al. 2016). The current thesis contributes to the exploitation of remote sensing data from different radar sensors (TerraSAR-X/TanDEM-X, Sentinel-1A/B and marine radar) over the Baltic Sea by further improving the methods for estimating significant wave height of the windsea conditions.

The main characteristic of the Baltic Sea wave field is the general lack of swell contribution in total wave height. The significant wave height of short-crested and steep windsea waves remains mostly in the range of 0–2 m (rarely exceeding 5 m) (Leppäranta and Myrberg 2009; Raudsepp et al. 2011; Tuomi, Kahma, and Pettersson 2011; Björkqvist et al. 2018). The wave field is also characterized by short wave “memory” (Soomere and Räämet 2011), which is also disturbed by shallow areas with thousands of islands. All these aspects contribute to complications in SAR imaging, data processing and interpretation.

Previous studies have shown that swell waves with wavelengths over about 100 m and with long wave crests are well imaged by SAR (Lehner et al. 2013; Bruck 2015; Pleskachevsky, Rosenthal, and Lehner 2016). They result in well pronounced peak in the image spectrum and their contribution to total wave height amplitude can be accurately estimated. Windsea wave crests on the other hand are short and presented as small, nonstable, fast and erratically moving targets for a SAR sensor. Those waves (dominant in the Baltic Sea) have a hardly recognizable wave pattern for SAR and typically produce image clutter (Pleskachevsky, Rosenthal, and Lehner 2016). A strong windsea contribution to the total wave height results in more substantial uncertainties in the SAR image, which requires additional effort in method development to achieve sufficient reliability in meteo-marine parameter (wind and wave) retrieval.

The main outcome of the Ph.D. work were the improvements and developments of radar data (SAR and marine radar) processing algorithms for monitoring windsea waves. The results show that the developed empirical data processing methods provide accurate significant wave height estimations in the Baltic Sea. The SAR data also show spatially more variable significant wave height fields which provide more detailed information compared to the wave model or other EO sensors (e.g. altimetry). The state-of-the-art near-real time (NRT) SAR processing methods used in the study demonstrate their value for operational and statistical monitoring of the coastal regions of the Baltic Sea.

1 BACKGROUND

1.1 Wind and wave field conditions in the Baltic Sea

The Baltic Sea lies in temperate latitudes between 53 °N to 66 °N and from 9 °E to 30 °E and is therefore primarily affected by westerly airflow. Consequently, about half of the time the wind blows from West, South-West or South at the coastal stations of Western Estonia (Jaagus and Kull 2011). The dominant wind direction in different sub-basins of the Baltic Sea has a quite uniform distribution since the scale of the weather patterns are much larger than the dimensions of the sub-basin (Launiainen and Laurila 1984; Tuomi, Kahma, and Pettersson 2011; Karagali et al. 2012).

The annual average wind speeds in the Baltic Sea and its' various sub-basins are 6–8 m s⁻¹ (Niros, Vihma, and Launiainen 2002; Suursaar, Jaagus, and Kullas 2006; Publication II). The wind speed has a clear annual cycle with monthly average wind speeds above the yearly average in the autumn-winter and vice-a-versa during the spring-summer period (Niros, Vihma, and Launiainen 2002; Björkqvist et al. 2018). The overall maximum sustained wind speed in the Baltic Sea region has been reported to be around 30 m s⁻¹ (Suursaar et al. 2006; Lehmann, Getzlaff, and Harlaß 2011; BACC 2015).

The Baltic Sea is disconnected from the open ocean waves; therefore, the wave field is mainly influenced by local winds. As a result, the wave field has a short wave “memory” (Soomere and Räämet 2011) without prominent long swell waves. Typical wave field parameters can differ significantly, depending on the sub-basin of the Baltic Sea. Wave periods remain relatively short, usually not exceeding 7–8 s (Leppäranta and Myrberg 2009; Raudsepp et al. 2011). The dominant wavelengths are between 20 and 70 m. However, wavelengths can grow up to 130 m in case of favourable conditions: wind speed, duration, direction stability, and fetch (*Hydrometeorological State of the Marine Shelf Zone in the USSR* 1983; Kriaučiūnienė, Gailiūšis, and Kovalenkoviėnė 2006; Publication IV). The dominant significant wave height in the Baltic Sea remains in the domain of 0–2 m and prominent swell waves with distinct amplitude (wave height over 5 m) are rarely registered in the Baltic Sea (Leppäranta and Myrberg 2009; Raudsepp et al. 2011; Tuomi, Kahma, and Pettersson 2011; Björkqvist et al. 2018).

The wave field in the Baltic Sea is influenced by the complex coastline and the Archipelago Sea with thousands of islands as well as by shallow areas (mean depth of the Baltic Sea is 50 m (Leppäranta and Myrberg 2009)). Moreover, the presence of numerous rocks and underwater banks is influencing the local sea state¹ via wave breaking, shadowing effects and the generation of cross-sea. In addition, the Baltic Sea is seasonally ice-covered which furthermore complicates instrumental (and visual) measurements, mathematical modelling and interpretation of satellite imagery.

1.2 Ocean wave basics

The moving sea surface elevation $\eta(t)$ at a location as a function of time, with duration D , appears to be a composition of random waves propagating with various frequencies (or wavelengths in spatial domain) and wave directions. The model to describe such situation is the random-phase/amplitude model (Holthuijsen 2010), in which the sea

¹ The general condition of the free surface on a body of water at a certain location and moment; expressed for example in significant wave height (“WMO-No. 8” 2008).

surface elevation is a sum of many harmonic waves, each with a different amplitude and phase:

$$\eta(t) = \sum_{i=1}^N a_i \cos(2\pi f_i t + \psi_i), \quad (1.1)$$

where N is a large number, a_i and ψ_i are the amplitude and phase, respectively, of each frequency $f_i = i/D$ ($i = 1, 2, 3, \dots$; therefore frequency interval is $\Delta f = 1/D$).

The harmonic wave is described as a one-dimensional process without considering the directions. For the real sea surface though, the horizontal dimension, i.e. wave propagation direction, must be added:

$$\eta(x, y, t) = a \sin(2\pi f t - k_x x - k_y y + \psi), \quad (1.2)$$

where wavenumber components are $k_x = k \cos \varphi$ and $k_y = k \sin \varphi$, where $k = \sqrt{k_x^2 + k_y^2}$ and wave propagation angle $\varphi = \arctan(k_y/k_x)$. The corresponding three-dimensional random sea surface elevation can then be characterised by linearly adding many propagating harmonic waves having different amplitudes, frequencies, and phases:

$$\eta(x, y, t) = \sum_{i=1}^n \sum_{j=1}^m a_{i,j} \sin(2\pi f_i t - k_i x \cos \varphi_j - k_i y \sin \varphi_j + \psi_{i,j}), \quad (1.3)$$

where each wave component is indicated with two indices: i for the frequency (or wave number) and j for the direction (Holthuijsen 2010).

To describe ocean waves as a stochastic process, i.e. to characterise all possible realisations that could appear under the conditions of the actual observation, a wave spectrum can be used. Since sea surface can be expressed as substantial number of component sine waves at fixed point, using a discrete Fourier analysis, amplitude and phase spectrum can be retrieved. However, both spectrums are based on discrete values, whereas in nature all frequencies are present at sea. The random-phase/amplitude model is therefore modified by distributing the variance $\frac{1}{2} a_i^2$ over the frequency interval Δf_i which width approaches zero. The continuous two-dimensional variance density spectrum for three-dimensional sea surface elevation in time domain is then given by:

$$E(f, \varphi) = \lim_{\Delta f \rightarrow 0} \lim_{\Delta \varphi \rightarrow 0} \frac{1}{\Delta f \Delta \varphi} E \left\{ \frac{1}{2} a_i^2 \right\}, \quad (1.4)$$

or in spatial domain as:

$$E(k, \varphi) = \lim_{\Delta k \rightarrow 0} \lim_{\Delta \varphi \rightarrow 0} \frac{1}{\Delta k \Delta \varphi} E \left\{ \frac{1}{2} a_i^2 \right\}, \quad (1.5)$$

where $E(\cdot)$ means variance density while $E\{\cdot\}$ stands for expected value.

The variance density spectrum gives a complete overview of the surface elevation of ocean waves, given that it can be seen as a stationary (Gaussian) process. The two-dimensional spectrum $E(f, \varphi)$ shows how the variance of sea surface elevation is distributed over the frequencies and directions. By integrating the variances in all directions, one-dimensional frequency spectrum is retrieved:

$$E(f) = \int_0^{2\pi} E(f, \varphi) d\varphi \quad (1.6)$$

and similarly for wavenumber:

$$E(k) = \int_0^{2\pi} E(k, \varphi) d\varphi. \quad (1.7)$$

Usually the information contained in the directional spectra $E(f, \varphi)$ or frequency spectra $E(f)$ is summarized into parameters describing the sea state. One of the most used parameters, significant wave height H_s , defined as the average of the third of the highest waves during the observation period, can be expressed as:

$$H_s = 4 \sqrt{\int E(f, \varphi) df d\varphi}. \quad (1.8)$$

The propagating ocean surface waves are generated by the wind field which is a complex mechanism. The shape of windsea spectrum depends on the fetch F (effective distance over which the wind blows with constant velocity) as well as duration and stability of the wind impact. An empirical model for the windsea spectrum was developed with the data acquired during the JONSWAP (JOint North Sea WAVE observation Project) experiment (Hasselmann et al. 1973; Hasselmann, Dunckel, and Ewing 1980). In the frequency domain, the distribution of wave energy among different wave frequencies $E_{\text{JONSWAP}}(f)$ can be expressed as:

$$E_{\text{JONSWAP}}(f) = \alpha g^2 (2\pi)^{-4} f^{-5} \exp\left(-\frac{5}{4}\left(\frac{f}{f_m}\right)^{-4}\right) \gamma^{\exp\left(-\frac{(f-f_m)^2}{2\sigma^2 f_m^2}\right)},$$

$$\sigma = \begin{cases} 0.07 & \text{for } f \leq f_m \\ 0.09 & \text{for } f > f_m \end{cases}. \quad (1.9)$$

Here g is gravitational constant, f_m represents the frequency at the maximum of the spectrum and the parameter α is Phillips curve:

$$\alpha = 0.076 \left(\frac{U_{10}^2}{Fg}\right)^{0.22}, \quad (1.10)$$

where U_{10} is wind speed at the height of 10 m.

For the random cases the averaged parameters can be applied with peak enhancement factor $\gamma = 3.3$ and the frequency at the maximum of the spectrum f_m :

$$f_m = 22 \left(\frac{g^2}{U_{10}F}\right)^{\frac{1}{3}}. \quad (1.11)$$

For calculation of the integrated wave energy $E_{\text{JONSWAP}} = \int E_{\text{JONSWAP}}(f) df$ the input of wind speed U_{10} and fetch F are required.

1.3 Radar signal interactions with the ocean surface

Over the ocean, a SAR image consists of information of the roughness of the surface, which depends on radar signal wavelength, polarization, viewing geometry, and the roughness of the ocean surface itself. The returned energy, i.e. backscatter, over the sea surface is primarily scattered by the wind induced surface waves. For moderate radar beam incidence angles between 20° and 60° , the Bragg scattering is the dominant mechanism for SAR ocean surface imaging (Hasselmann et al. 1985; Plant 1990). Constructive interference in the direction of the sensor occurs when short capillary wave components on the ocean surface with wavelength λ_B are related to radar wave frequency or wavelength λ_R at an incidence angle θ by

$$\lambda_B = \lambda_R / 2 \sin \theta. \quad (1.12)$$

For X-band SAR, e.g. TerraSAR-X and TanDEM-X (TS-X and TD-X), with the wavelength λ_R of 3.1 cm, the resonant Bragg wavelength is 3.9 cm (at $\theta = 23^\circ$), whereas for C-band SAR, e.g. Sentinel-1, the λ_R is 5.6 cm and therefore λ_B equals 7.1 cm.

The two-scale approximation is used to describe the imaging process of long ocean waves by SAR as short Bragg waves are modulated by the long ocean gravity waves. There are three possible mechanisms in which long waves modify Bragg waves, hence affecting SAR imaging: tilt and hydrodynamic modulations, and wave orbital motion effects also known as velocity bunching (Hasselmann et al. 1985; Jackson and Apel 2004).

Since individual water particles have a periodic orbital motion, an apparent increase (bunching) and decrease in the density of scatters occur. The velocity bunching effect is a governing factor for SAR imaging of azimuth travelling waves and is in general strongly non-linear (Alpers and Bruening 1986). A target moving with a radial velocity corresponding to a projected line-of-sight velocity of u_r towards the sensor results in a Doppler shift (i.e. the shift from the real position) of the corresponding SAR image point by a distance D_y (Lyzena et al. 1985):

$$D_y = \frac{R_0}{V_{SAR}} u_r, \quad (1.13)$$

where the V_{SAR} is platform velocity and the location of a point scatterer on the surface is given by its distance to the radar R_0 at the time t_0 of the closest approach (Doppler zero).

Assuming the wave height consisting of different components, e.g. swell being $H_{s,1}$ and windsea $H_{s,2}$, the total significant wave height can be defined as:

$$H_S = \sqrt{\sum_i H_{s,i}^2}. \quad (1.14)$$

For large swell waves, a linear wave theory can be applied to estimate surface motion (Alpers and Rufenach 1979) whereas even 10 Fourier components hardly describe non-linear wind waves. This means that for different sea state components with the same total significant wave height, the Doppler shift can differ strongly. In Figure 1 the Doppler shift for TS-X and Sentinel-1 satellites in different sea state conditions is presented (Publication I). Large contrasts in maximal velocity bunching can be observed in case of varying swell and windsea components and corresponding maximal possible orbital speeds (Figure 1) (Holthuijsen 2010; Publication I).

The orbital motion of waves during SAR acquisition leads to distortions in the image spectrum, as well as to the cut-off effect in the azimuth (flight) direction (Alpers and Bruening 1986). SAR does not image waves shorter than a certain threshold value due to the cut-off effect. A relatively simple relationship for cut-off wavelength λ_{\min} is proposed by Beal, Tilley, and Monaldo (1983):

$$\lambda_{\min} = K \frac{R_0}{V_{SAR}} \sqrt{H_S}, \quad (1.15)$$

where $K = 1 \text{ m}^{1/2} \text{ s}^{-1}$.

However, it is reported by other authors that cut-off wavelength is dependent on more geophysical parameters, such as mean wave period or wind speed (Milman, Scheffler, and Bennett 1993; Vachon, Krogstad, and Paterson 1994) as well as incidence angle and scene coherence time (Milman, Scheffler, and Bennett 1993). An example of a cut-off effect can be observed in Figure 2 where different sea state conditions with different total significant wave height produce diverse image spectrum signatures (Publication I; Publication II). Figure 2 (f) and (g) show that from a certain point forward, little information is present on the azimuth (flight) direction illustrating the cut-off effect.

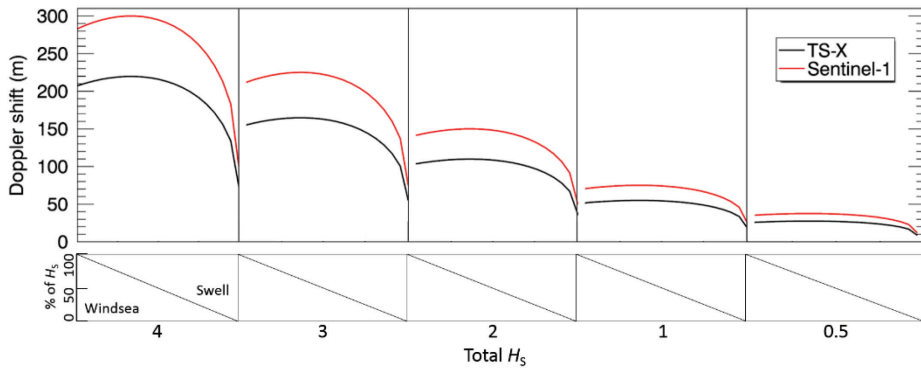


Figure 1. Doppler shift for TS-X and Sentinel-1 satellites for varying sea states using equation 1.13 with the incidence angle of 35° .

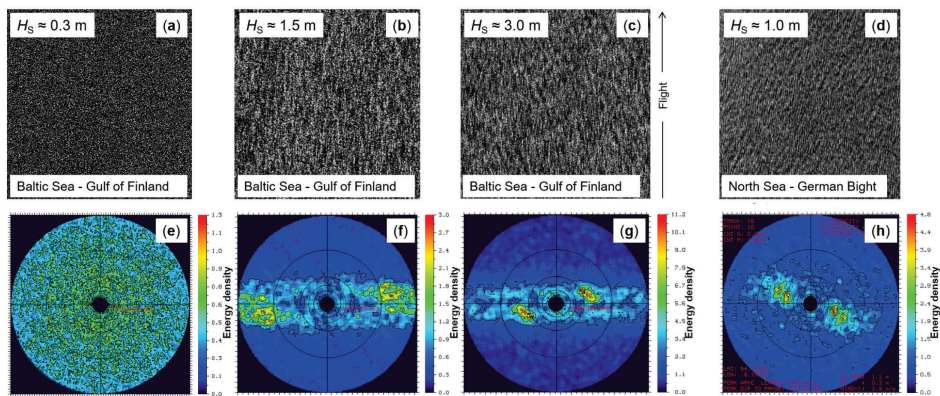


Figure 2. An example of the synthetic aperture radar (SAR) subscenes (a–c) and corresponding image spectrums (e–g) for different sea state conditions in the Gulf of Finland (three typical situations for an approximate wave height of 0.5 m (a), 1.5 m (b) and 3 m (c)). Short wave crests, which are fast and chaotically moving targets, are not imaged individually by SAR in original shape, but jointly produce a clutter in the SAR image and smoothed structures in sensor flight direction. For comparison, a typical acquisition in German Bight of the North Sea is given in (d). A stronger swell component is clearly visible in (h) as well as a reduced cut-off wavelength compared to Baltic Sea cases.

In addition to already mentioned space-borne SAR modulations of sea surface – hydrodynamic and tilt modulation – marine X-band radars imaging mechanisms introduce additional effects. The sea surface signatures are visible to X-band marine radar in HH or VV polarizations known as sea clutter (Wetzel 1990). Since marine radars “look” at high incidence angles above 85° , additional scattering mechanisms, e.g. shadowing (Plant and Keller 1990; Wetzel 1990; Lee et al. 1995), wedge scattering (Lyzenga, Maffett, and Shuchman 1983) and scattering from micro breakers (Wetzel 1990) must be considered. Other effects such as range dependence (Croney 1970), azimuthal dependence on the wind direction and speed (Hatten et al. 1998) as well as wave propagation direction (Reichert 1994) are reported to affect marine radar images. However, at grazing incidence, shadowing modulation which is caused by the very low radar backscatter coming from diffraction in the geometrically shadowed areas of the waves has major importance (Barrick 1995; Plant and Farquharson 2012).

1.4 Overview of wind-wave field estimation methods from radar

The investigation of SAR ocean surface imaging mechanisms and the extraction of wave and wind field parameters started with the data from L-band SAR on-board SEASAT satellite launched in 1978 (Beal, Tilley, and Monaldo 1983; Masuko et al. 1986). Since then, different algorithms have been developed to estimate geophysical parameters, such as ocean wave spectra from SAR imagery (Hasselmann and Hasselmann 1991; Hasselmann et al. 1996; Schulz-Stellenfleth, Lehner, and Hoja 2005).

Wind field retrieval approaches from SAR data have also been an important issue. The first algorithm was developed for C-band SAR provided by, for example, ERS-2 (European Remote Sensing Satellite) and Envisat ASAR (Advanced Synthetic Aperture Radar). The empirically derived geophysical model functions (GMF) relate the local wind conditions and sensors viewing geometry to radar cross section values (e.g. CMOD4 or CMOD5) (Stoffelen and Anderson 1997; Hersbach, Stoffelen, and de Haan 2007). The non-linear wind speed estimation algorithm XMOD-2 has also been adopted for X-band SAR data (Ren et al. 2012; Li and Lehner 2014). In the common procedure, GMFs in general are inversion methods and require the local wind direction to reduce the number of free parameters in the forward calculation. *A priori* wind direction is usually derived from other sources, e.g. atmospheric models or scatterometers.

The methods for sea state estimation are largely divided into two main groups; the first one being the function where image spectrum is transferred into wave spectrum using transfer functions (e.g. Alpers, Ross, and Rufenach 1981; Hasselmann and Hasselmann 1991; Hasselmann et al. 1996; Lyzenga 2002). These methods are suitable for estimation of swell's spectrum, and its output could be assimilated into spectral wave models. The key to success is to understand the non-linear SAR imaging of the moving sea surface waves that can be incorporated in transfer functions (Alpers, Ross, and Rufenach 1981). This approach requires SAR acquisitions with clearly visible wave-looking patterns (e.g. data from Sentinel-1 Wave Mode (WM) data, high resolution Stripmap Mode TerraSAR-X data). Otherwise, the waves are substantially distorted and are not visible/detectable in the SAR images and thus are not represented in the image spectra.

The second group of sea state estimation algorithms use the direct estimation of the wave parameters from the image spectrum with empirical functions (e.g. Schulz-Stellenfleth, König, and Lehner 2007; Li, Lehner, and Bruns 2011; Bruck 2015; Pleskachevsky, Rosenthal, and Lehner 2016; Publication III). Windsea wave crests are short and present a considerable number of small, nonstable, fast and erratically moving targets for a SAR sensor. Such a sea state is typically imaged as noise and has hardly recognizable wave pattern. A strong windsea contribution to the total wave height is therefore equivalent to more substantial uncertainties in SAR imaging which is rarely transferrable to the wave spectrum. Empirical functions, deduced from large sets of representative data, are shown to provide sufficiently accurate results in these conditions (Li, Lehner, and Rosenthal 2010; Lehner et al. 2013; Bruck 2015; Pleskachevsky, Rosenthal, and Lehner 2016). Moreover, direct estimation of wave parameters from subscene spectra allows fast, straightforward and trustworthy NRT processing of satellite scenes while excluding only a fragment of the data (Schwarz et al. 2015; Pleskachevsky, Rosenthal, and Lehner 2016).

Sequential marine radar images with high spatio-temporal resolution have also been used in a variety of applications, such as measuring spectral wave parameters (Nieto Borge, Reichert, and Dittmer 1999), wave groups (Dankert et al. 2003) or individual waves (Dankert and Rosenthal 2004; Nieto Borge et al. 2004). Other related measurements

include near-surface currents (Senet, Seemann, and Ziemer 2001; Huang et al. 2016) and bathymetry (Senet et al. 2008; Bell and Osler 2011) as well as surface winds (Dankert, Horstmann, and Rosenthal 2004; Dankert and Horstmann 2007; Vicen-Bueno et al. 2013).

Various methods to estimate significant wave height have also been developed for marine radar data. Similarly to SAR data processing, one could transfer radar image spectrum to a wave amplitude spectrum using a modulation transfer function (Nieto Borge, Reichert, and Dittmer 1999; Nieto Borge et al. 2004; “WaMoS II: Version 4.0” 2012). A major disadvantage of this method is the need for calibration of each single radar installation site using *in situ* wave-measuring sensors (Vicen-Bueno, Lido-Muela, and Nieto-Borge 2012; Carrasco, Streßer, and Horstmann 2017). Alternative methods evaluate shadowing in the X-band marine radar to estimate H_s without external reference for calibration (Gangeskar 2014; Liu, Huang, and Gill 2016; Wei et al. 2017). As the sea surface is seen as clutter in marine radar images (similar to low sea state cases for SAR sensor), the empirical method has also been used to retrieve the significant wave height from marine radar data (Publication III).

2 MOTIVATION AND OBJECTIVES

The main motivation behind the thesis is to contribute to the uptake of radar data over the Baltic Sea to advance maritime situational awareness. The research on method development for retrieving significant wave height from SAR and marine radar data over the Baltic Sea has been limited so far. However, applications based on the radar data could be beneficial for many potential remote sensing data users such as meteorological service organizations. The present study investigates one of the applications for using satellite-based and land-based radar-techniques to estimate wave and wind field parameters in the Baltic Sea.

Short and steep wind waves dominating in the Baltic Sea generally produce radar image clutter with a hardly recognizable wave pattern (Pleskachevsky, Rosenthal, and Lehner 2016; Publication I; Publication II). This will often lead to inaccuracies in wave height estimation with traditional methods that are suitable for estimating long swell wave spectra. On the other hand, empirical methods deduced from a large amount of representative data could be used to overcome the complications of radar imaging of windsea waves (e.g. Schulz-Stellenfleth, König, and Lehner 2007; Li, Lehner, and Bruns 2011; Bruck 2015; Pleskachevsky, Rosenthal, and Lehner 2016). Therefore, the objective of the thesis is to determine the precision of fully empirical algorithms for deriving total significant wave height in the Baltic Sea.

The sea state parameters retrieved from radar data using the empirical methods have not been extensively validated over the Baltic Sea using *in situ* measurements. Moreover, the spatial representation of H_s fields derived from SAR data have not been thoroughly compared with corresponding wave model results in the Baltic Sea. The current thesis attempts to resolve the mentioned issues.

Empirical algorithms enable to use the radar data for process studies related to wind-wave interactions over the Baltic Sea. Moreover, validated wave and wind products would be a basis for NRT services, which allow retrieval of maritime information in about 20 minutes after satellite data downlink (Schwarz et al. 2015; Pleskachevsky, Rosenthal, and Lehner 2016). Operational services complemented with other maritime situational awareness elements such as ice coverage classification (e.g. Ressel et al. 2016), oil pollution detection (e.g. Singha, Velotto, and Lehner 2015), ship detection and classification (e.g. Velotto et al. 2016) have large potential over the Baltic Sea region for a comprehensive interdisciplinary maritime analysis. The SAR data processing for the thesis were done using the same methods that are implemented in DLR's (German Aerospace Center) ground station Neustrelitz which allow to evaluate the benefits of NRT services over the Baltic Sea (Publication II).

The specific objectives of the study are:

- to improve the empirical XWAVE_C algorithm by introducing JONSWAP parametrization function and to validate the corresponding wave height retrievals for TS-X/TD-X imagery over the Eastern Baltic Sea (Publication I);
- to validate CWAVE_S1-IW algorithm wave retrievals from medium resolution Sentinel-1A/B space-borne SAR data over the Baltic Sea (Publication II);
- to validate XMOD-2 and CMOD wind speed retrievals in the coastal zone of the Baltic Sea from TS-X/TD-X and Sentinel-1A/B data correspondingly (Publication I; Publication II);

- to compare SAR (TS-X/TD-X and Sentinel-1A/B) wave retrievals with other data sources such as (operational) wave model results and altimetry wave products (Publication I; Publication II; Publication IV; Publication V);
- to develop and validate an empirical method for estimating the total significant wave height from marine radar images (Publication III);
- to determine the benefits of texture analysis of marine radar data by using Grey Level Co-occurrence Matrix (GLCM) image statistics for empirical wave retrieval algorithms (Publication III).
- to characterize the spatial variability of wave field derived from Sentinel-1 A/B SAR data with CWAVE_S1-IW algorithm and therefore demonstrate the potential for monitoring services in the coastal area (Publication II);
- to study the benefits of radar data to maritime situation awareness, spatial planning and for environmental monitoring in the Baltic Sea.

3 MATERIALS AND METHODS

3.1 *In situ* measurements and radar data

In situ wave measurements were either retrieved from open databases or from specific experiments carried out for the published papers (Publication I; Publication II; Publication III; Publication IV; Publication V). Three different types of equipment for wave measurements were available: Acoustic Doppler Current Profiler (ADCP), Waverider and pressure sensors. In total, wave height measurements from 18 stations (Table I) were compared with radar-derived wave height values. In addition, two virtual buoys are used for comparison of remote sensing and model data. Wind measurements from 47 stations around the Baltic Sea were used for statistical validation of SAR wind retrievals. The Finnish Meteorological Institute (FMI), Swedish Meteorological and Hydrological Institute (SMHI), Estonian Environmental Agency (KAUR) and Latvian Environment, Geology and Meteorology Centre provided the wind measurement data. The overview of all wave and wind speed measurement locations used for the thesis can be seen in Figure 3 and the corresponding SAR collocations are given in Table II.

Three sources of radar data have been used: X-band SAR data from TS-X and TD-X, C-band SAR data from Sentinel-1A/B, and circularly polarized X-band coastal marine radar data.

The TS-X and TD-X are twin satellites operating in a sun-synchronous orbit from a height of 514 km with a wavelength of 31 mm and a frequency of 9.6 GHz (Breit et al. 2010). The revisit cycle of the satellites is 11 days. However, the same region can be imaged more frequently at different incidence angles θ , which vary between 20° and 55°. The TS-X sensor has several imaging modes with different swath widths, scene lengths, and resolutions (Eineder et al. 2008). For sea state analysis in the Baltic Sea, the StripMap mode with 3 m resolution is most suitable as it provides a reasonable balance between spatial resolution and coverage. An individual StripMap image with the pixel spacing of 1.25 m covers approximately 30 km × 50 km, yet the length of the covered area can be extended by acquiring sequential images. The TS-X/TD-X data for the current study were acquired between 2012 and 2017 and the data was used for method development and validation as well as for sea state analysis (Table II). On five occasions the data were used for spatial studies with wave model results.

C-band SAR satellite Sentinel-1A/B, operating also in a sun-synchronous orbit at the height of 693 km, allows combining a large swath width of 250 km in range direction (200 km in azimuth direction) with moderate geometric (5 × 20 m) and pixel (10 × 10 m) resolution in Interferometric Wide (IW) swath mode. Sentinel-1A/B products are available in different modes and polarizations: single (HH or VV) or dual polarizations (HH/HV, VV/VH) (Torres et al. 2012). For the meteo-marine parameter estimation, either one of the single polarisation data is used. Almost all the Sentinel-1 A/B single polarization data from 2015-2016 (460 overpasses in total) were used for the thesis (Table II). The data were used for method validation, comparison with *in situ* measurements and wave model (three spatial studies). Sentinel-1 IW data were also used to analyse regional wave statistics over the study period (Publication II).

Finally, incoherent non-Dopplerized circularly polarized X-band (9374 ± 30 MHz) marine radar data over the Tallinn Bay area were acquired and analysed. The radar is located on the Paljassaare peninsula (24.70753 °E, 59.48558 °N) with the tower high of 26 meters (27 m from sea level). The radar images are rasterized to 5 by 5 m pixel

resolution with the dimensions of 4096 by 4096 pixels with the range of about 10 km from radar tower. Radar data from 18.10.2016 to 14.11.2016 were used for the method development (1678 match-up with *in situ* data) and data from January and June 2017 were selected for the method validation (1464 match-ups) (Table II) (Publication III).

Table I. Overview of wave measurement stations used in the study.

No. (Origin)	Station	Lat (°N)	Lon (°E)	Sensor type
1 (FIN)	Selkämeri	61.8001	20.2327	Waverider
2 (SWE)	Finngrundet	61.0000	18.6667	Waverider
3 (FIN)	Norther Baltic Proper (NBP)	59.2500	20.9968	Waverider
4 (EST)	Vilsandi	58.4889	21.6333	Waverider
5 (SWE)	Knolls grund	57.5167	17.6167	Waverider
6	NBP Extra	58.7500	20.8271	Virtual buoy
7	Södra Östersjön	55.9167	18.7833	Virtual buoy
8 (EST)	Liivi LM-2	58.0860	24.1255	Pressure
9 (EST)	Liivi Anderaa	58.1065	24.1844	Pressure
10 (FIN)	Hanko	59.9650	23.1010	ADCP
11 (EST)	Neugrundi	59.3451	23.5191	Pressure
12 (FIN)	Hästgrund	59.9128	24.2085	Pressure
13 (FIN)	Länsi-tonnttu	60.0817	25.1288	Pressure
14 (FIN)	GoF	59.9650	25.2350	Waverider
15 (EST)	Tallinna madal-1	59.7120	24.7320	Pressure
15 (EST)	Tallinna madal-2	59.7028	24.7250	Waverider
16 (EST)	Hülkari	59.5394	24.6116	Pressure
17 (EST)	Vahemadal	59.5102	24.6662	Pressure
18 (EST)	Paljassaare	59.4982	24.7033	Pressure

Table II. Overview of the number of SAR and marine radar (TerraSAR-X/TanDEM-X (TS-X/TD-X), Sentinel-1, marine radar) images and observation periods as well as a number of collocations with *in situ* measurements or wave model. H_s corresponds to total significant wave height and U_{10} to wind speed; L_p and γ_p are peak wavelength and peak wave propagation direction respectively where P denotes to peak.

Sensor	Period	No. of images	Purpose	<i>In situ</i> collocations	Wave model collocations
TS-X TD-X	2012–2017	92	Development	117 H_s	55 L_p, γ_p
			Validation	102 U_{10}	
			Comparison	44 L_p, γ_p	
Sentinel-1	2015–2016	15	Validation	52 H_s 357 U_{10}	49314 H_s
		460	Comparison Statistics	101 H_s	201 H_s
Marine radar	18.10.– 14.11.2016	559	Development	1678 H_s	-
	Jan. & Jun. 2017	1464	Validation	1464 H_s	-

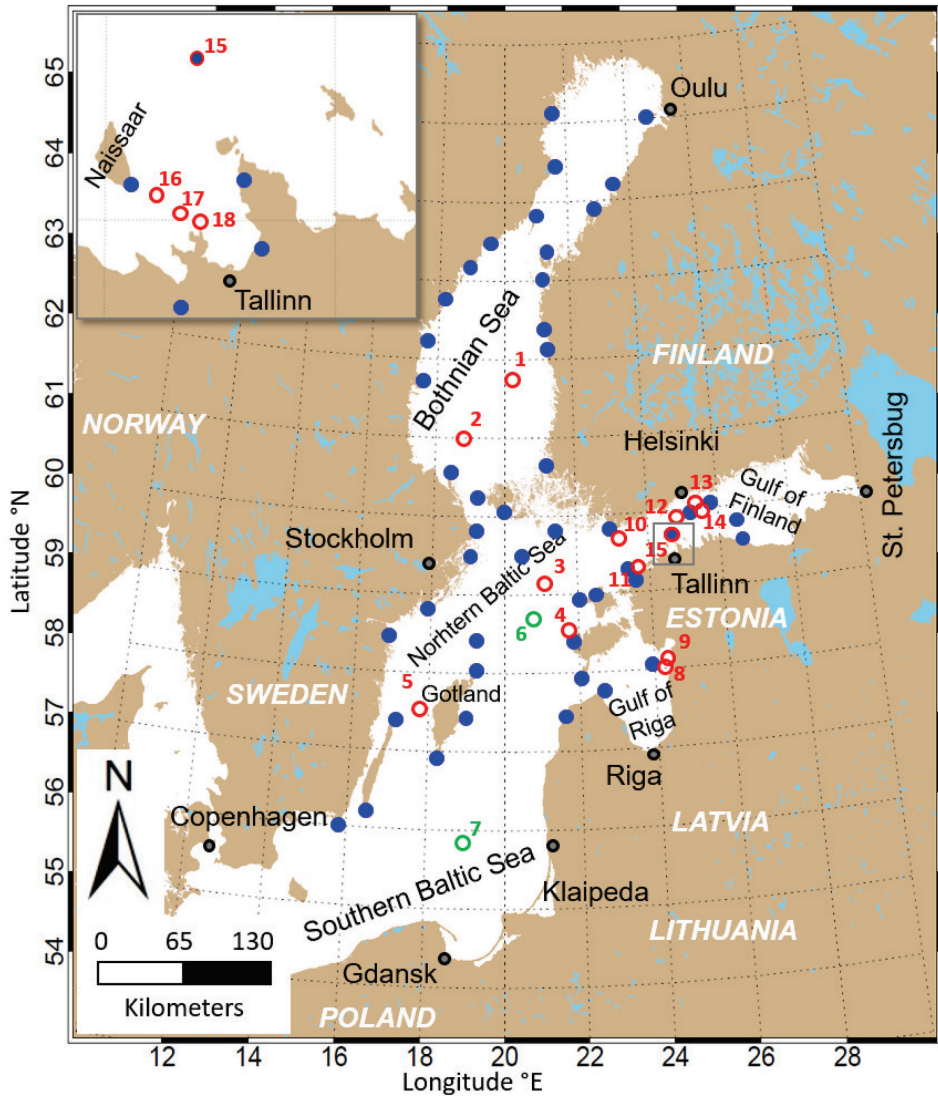


Figure 3. The map of the Baltic Sea and locations of measurement stations used in the thesis. Specific information can be found in Publication I–IV. The location of wave measurements – significant wave height, wave propagation direction, wave period (red) – and coastal wind measurements – speed, gusts, and direction (blue) – are indicated on the map. Virtual buoys mark additional stations used for comparison of remote sensing and model data (green). The zoom over Tallinn Bay shows the location of stations used for marine radar method development and validation.

3.2 Wave model

To evaluate the spatial characteristics of a SAR-derived wave field and its added benefit, wave height results from third-generation wave models SWAN (Simulating WAVes Nearshore) (Booij, Ris, and Holthuijsen 1999) and WAM (The WAMDI Group 1988) were used. Both models solve the action balance equation without any *a priori* restriction to

the evolution of spectrum. Significant wave height, peak wavelength and peak propagation direction were used for the comparison in the thesis.

The results of the SWAN wave model which was running in operational mode during 2012–2014 over the Baltic Sea were used (Publication I; Publication IV; Publication V). The model covered the Baltic Sea with one nautical mile grid and with the data output of 1 hour. European Centre for Medium Range Weather Forecast (ECMWF) wind fields with a spatial resolution of 9 km and temporal resolution of 3 hours were used for wave model forcing.

Secondly, data from pre-operational version of the WAM model (2015–2016) which is used for the production of Copernicus Marine Environment Monitoring Service (CMEMS) wave forecast since April 2017 over the Baltic Sea was also used (Tuomi, Vähä-Piikkiö, and Alari 2017; Publication II). The model domain covers the Baltic Sea with a grid resolution of one nautical mile. The model was forced with High Resolution Limited Area Model (HIRLAM) winds with a spatial resolution of 11 km and temporal resolution of one hour.

3.3 Image processing methods

As an active remote sensing device, radar provides two-dimensional information of the normalized radar cross section σ_0 (NRCS). The NRCS represents the surface reflectance of the radar signal and is defined as the normalized energy flux scattered by a unit area of the surface into a given direction. The backscatter is governed by the surface roughness on the scale of the radar wavelength. If the roughness of the imaged surface approximately satisfies the Bragg condition, constructive interference of the reflected radar signal in the direction of the sensor occurs.

The σ_0 used is obtained from pixel digital number DN :

$$\sigma_0(x, y) = (DN)^2 k_s \sin(\theta), \quad (3.1)$$

$$\sigma_0(x, y) = \frac{DN^2}{k_s^2}, \quad (3.2)$$

where k_s is the calibration factor given in SAR product file, θ is the local incidence angle of the radar signal, x and y are image coordinates in range and azimuth correspondingly. Equation 3.1 is given for TS-X and TD-X data while 3.2 is used for Sentinel-1A/B data. For coastal radar data, similar incidence angle dependent scheme as for TS-X data is used without using calibration factor.

Radar image analysis for sea state estimation is based on two-dimensional Fast Fourier Transform (FFT) of subscene which results in image spectra. A FFT window of $2^n \times 2^n$ where n is a positive integer (e.g. 1024×1024 pixels) is used. The value of each pixel $\sigma_0(x, y)$ in the subscene is normalized according to:

$$\sigma_n(x, y) = \frac{\sigma_0(x, y) - \langle \sigma_0 \rangle}{\langle \sigma_0 \rangle}, \quad (3.3)$$

where $\langle \sigma_0 \rangle$ is the mean value of the σ_0 for the subscene and the $\sigma_n(x, y)$ are the normalized values of the subscene. The idea behind normalization is to separate sea state (modulation) signal from the mean NRCS value (due to local wind speed) in the SAR image (Schulz-Stellenfleth 2004).

An important part of sea state estimation is pre-filtering of any natural or man-made objects from a subscene which yields to inaccuracies in wave height estimation. Such spectral perturbations result in an integrated value which leads to the total image energy

not related to the sea state. The radar signal disturbances can be divided into two main groups:

- radar signal much stronger than background backscatter from the sea state produced mainly by ships or offshore constructions. In these cases, the subscene is additionally analysed with a sliding window. The statistics of each window $\langle \sigma_0^{win} \rangle$ is compared with $\langle \sigma_0 \rangle$ of the subscene. In a case of $\langle \sigma_0^{win} \rangle$ is larger than a threshold $q_{ship} \langle \sigma_0 \rangle$, the outliers in the current window are replaced with the mean value of the subscene $\langle \sigma_0 \rangle$;
- radar signal much weaker than background backscatter from the sea state produced, for example, by oil spills, or commonly occurring algae blooms in the Baltic Sea. The filtering applies in cases, when $\langle \sigma_0^{win} \rangle$ is larger than tuned threshold $q_{spills} \langle \sigma_0 \rangle$.

The FFT operation is applied to the calibrated and normalised subscenes to obtain integrated wave parameters. The integrated image energy spectrum $IS(k_x, k_y)$ is the basis for sea state parameters estimation. It is defined by the following formula describing a 2D integration in the wavenumber domain:

$$E_{IS} = \int_{k_x^{min}}^{k_x^{max}} \int_{k_y^{min}}^{k_y^{max}} IS(k_x, k_y) dk_x dk_y. \quad (3.4)$$

The integration over the wavenumber domain is limited depending on the sensor by k_{max} and k_{min} (Publication I; Publication II; Publication III), where wavenumber $k = \sqrt{k_x^2 + k_y^2}$.

In addition to traditional image spectrum parameters (e.g. image spectrum energy in different wavelength domains, image spectrum noise statistics, etc.) the Grey Level Co-occurrence Matrix (GLCM) (Haralick and Shanmugam 1973) statistics of the input subscene were also calculated. GLCM is a tabulation of the frequency of different combinations of pixel brightness values occurring with certain distances in certain directions to each other on an image. In other words, GLCM describes image texture. The idea of using GLCM image analysis for oceanography applications is not new and is widely used for ice coverage classification (e.g. Ressel, Frost, and Lehner 2015) and oil detection (e.g. Singha, Vespe, and Trieschmann 2013). However, it is not widely used for wave field analysis from radar data.

The sensitivity of well-known GLCM parameters (such as entropy, energy, dissimilarity, homogeneity, contrast, correlation, variance and mean) to wave signal on radar image was analysed within the study. The GLCM matrix is computed for the original radar subscene with a corresponding number of grey levels, directions and distances (Pleskachevsky et al. 2019; Publication II; Publication III).

3.4 Surface wind estimation from TS-X/TD-X and Sentinel-1

Sea state is strongly dependent on local wind characteristics which SAR data can provide. Therefore, wind speed is also an additional parameter for sea state estimation (Schwarz et al. 2015; Pleskachevsky, Rosenthal, and Lehner 2016; Pleskachevsky et al. 2019).

The conversion between the roughness of the sea surface reflected in the NRCS and local wind conditions is described by Geophysical Model Function (GMF) and is given for CMOD and XMOD algorithms as:

$$\sigma_0(U, \theta, \phi) = B_0^p(U_{10}, \theta) (1 + B_1(U_{10}, \theta) \cos(\phi) + B_2(U_{10}, \theta) \cos(2\phi)), \quad (3.5)$$

where σ_0 is NRCS, and ϕ is the relative angle between wind direction and radar look direction. B_0 , B_1 , and B_2 are functions of incidence angle θ and sea surface wind speed U_{10} at 10 m height. The parameter ρ has a constant value of 0.625. In CMOD5, the isotropic term B_0 , the upwind/downwind amplitude B_1 , and the upwind/crosswind amplitude B_2 are all functions of wind speed and incidence angle. In the XMOD-2 on the other hand, a second-order polynomial function is used to describe the dependence of B_1 on the sea surface wind speed and incidence angle. The transfer functions inside B_0 , B_1 and B_2 include several conditions and coefficients which differ for various GMFs (e.g. Stoffelen and Anderson 1997; Hersbach, Stoffelen, and de Haan 2007; Ren et al. 2012; Li and Lehner 2014).

Separate GMFs are used for Sentinel-1 IW HH and VV polarizations data. For HH polarization, the CMOD4 function was used while for VV polarization the CMOD5.N algorithms have shown the best performance (Monaldo et al. 2016). The selection of the respective GMF is based on extensive comparison of GMF performance in comparison with ASCAT, scatterometer, METOP-A and METOP-B satellite data performed by (Monaldo et al. 2016).

3.5 Methods to estimate sea state from radar data

An empirical function XWAVE_C uses the approach of direct estimation of significant wave height from TS-X and TD-X image spectra without transformation into wave spectra. This method was chosen because of the need for robust and rapid data processing which does not involve long and resource demanding mathematical iterations for the spectral transformation. Empirical algorithm XWAVE_C, developed for coastal areas, is based on analysis of image spectra and was tuned according to collocated buoy data and coastal wave model results (Pleskachevsky, Rosenthal, and Lehner 2016).

In comparison to TS-X/TD-X StripMap scenes with about 3 m resolution, the Sentinel-1A/B IW mode resolution is roughly an order of magnitude larger. In case of such Sentinel-1 SAR imaging setting, the wave structures, if visible, are disturbed by a large amount of noise. In addition, complex wave fields of the Baltic Sea pose an additional challenge. In the case of Sentinel-1A/B IW data, an empirical algorithm CWAVE_S1-IW, developed by Pleskachevsky et al. (2019), is used to estimate integrated sea state parameters straight from SAR image spectra. Furthermore, GLCM image statistics are used for sea state analysis.

In general, empirical algorithms for different radar sensors covering the low sea state conditions of the Baltic Sea can be expressed as:

$$H_S = a_0 \sqrt{B_0 E_{IS} \tan(\theta)} + \sum_{i=1}^n a_i B_i, \quad (3.6)$$

where θ is local incidence angle, a_i are calibration coefficients, and B_i are correction functions of spectral parameters. The coefficients and functions account for local surface wind estimated by respective GMFs and GLCM results. Different function parameters are designed to remove the influence of non-sea state produced signals, such as dry sandbars as well as non-linear SAR image distortions produced by e.g. short wind waves and breaking waves. For example, B_0 represents noise scaling of the total energy E_{IS} (short wind waves and their breakings produce an additional noise that influences resulting energy) where $B_0 = x_0 R^{\text{in/out}}$ with x_0 tuned using collocated buoy data for TS-X/TD-X and Sentinel-1 data. $R^{\text{in/out}}$ represents the character of non-linearity of the imaging mechanism with spectrum noise in the domain of inside the azimuthal cut-off wave number

and spectrum noise outside of the azimuthal cut-off (Pleskachevsky, Rosenthal, and Lehner 2016; Pleskachevsky et al. 2019).

3.6 Comparison methods

The total significant wave height H_s and wind speed U_{10} derived from radar data are used for comparisons with *in situ* measurements. The collocations were done with a minimum possible time window (usually less than 20 minutes) for comparison with measurements and wave model data (Publication I; Publication II; Publication III; Publication IV; Publication V). The same applies to spatial collocation where the closest subscene to measurement station or wave model grid point is used. However, data up to 10 km are incorporated in case the measurement station is outside of the image.

The Pearson correlation coefficient r , root mean square error (RMSE) and Scatter Index (SI, where $SI = RMSE/\text{average of the sample}$) are calculated for each dataset for the comparisons and algorithm tuning. Standard deviation (STD) is used to measure the spatial variability of datasets.

4 RESULTS AND DISCUSSION

4.1 Improvements on XWAVE_C function

During the thesis, the XWAVE_C algorithm for retrieving meteo-marine parameters from X-band high-resolution SAR data was improved by considering the wave conditions over the Baltic Sea. Due to complications of windsea wave (typical in the Baltic Sea) SAR imaging, the wave height is mostly estimated from noisy subscenes. To overcome the complications in cases when waves are not visible on the image, a minimum wave height estimated from JONSWAP (Hasselmann, Dunckel, and Ewing 1980; Hasselmann et al. 1973) spectrum based on local wind speed was introduced. The local wind speed required for JONSWAP calculations is available from the analysed SAR subscene and the corresponding input fetch was set to 10 km. The areas where XWAVE_C underestimates wave height and JONSWAP parametrization is needed are typically located in wind shadow areas ($0 \text{ m s}^{-1} < U_{10} < \approx 8 \text{ m s}^{-1}$). For the areas with longer fetch, the sea state is more developed which allows correct estimates for the wave height. The second term to compensate spectral distortions triggered by windsea waves moving in SAR flight direction has also been introduced (Publication I). The JONSWAP parametrization was also included into DLR's near-real time operational service running in ground station Neustrelitz.

Compared to the original XWAVE_C, the improvements increased the accuracy of the algorithm: r increased by 5% and RMSE was reduced by 20% between SAR-derived H_s and measured H_s . The modified method had the following statistical characteristics: $r = 0.88$, RMSE = 0.32 m (SI = 0.33, $n = 117$). The differences are mostly visible in coastal areas for the low wind conditions and over the open sea for the strong winds under storm conditions (Figure 4).

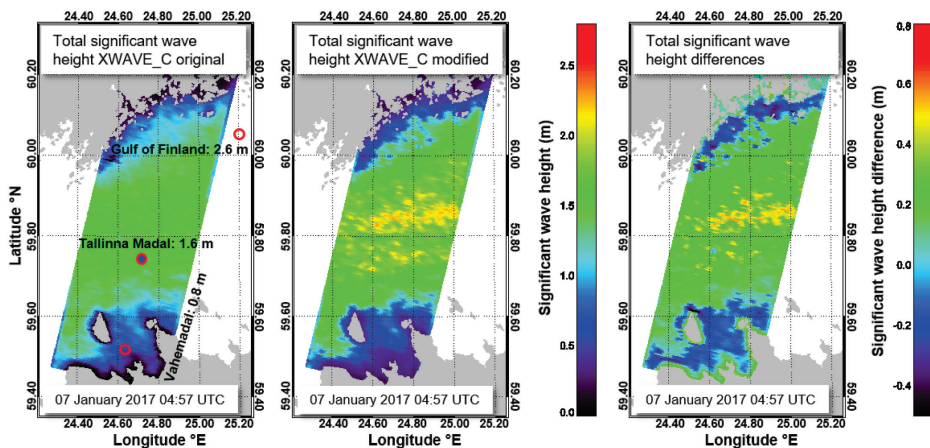


Figure 4. Example for spatial estimation of significant wave height from TS-X StripMap scene acquired over the Gulf of Finland on 7 January 2017 at 04:55 UTC under storm conditions. The significant wave height estimated by original algorithm (left panel), using corrections (middle panel) and difference (right panel). Left panel also show measured H_s values in Vahemadal, Tallinna madal and at Gulf of Finland stations.

4.2 Wave height estimation function for marine radar data

An empirical method was also developed and implemented on marine radar data in order to estimate sea state conditions in the Tallinn Bay. Sea state in the Tallinn Bay is mainly low; therefore, traditional methods where backscatter intensity variance spectrum is transferred to wave spectrum do not resolve wave height retrievals sufficiently accurately. An algorithm was developed for the windsea with short and steep waves dominating in the Tallinn Bay using image spectrum parameters as well as GLCM statistics of the radar signal intensity.

The H_s retrieval method was tuned using the collocated *in situ* data from three pressure sensors deployed in the Tallinn Bay. The calculated parameters were tested against measured *in situ* values and best-fit trendline techniques together with the Pearson correlation coefficient was used to choose image parameters that contain valuable information for H_s estimation.

The algorithm is based on image spectra analysis where integrated sea state parameters are derived from radar image spectra without transformation into wave spectra.

The specific parameters for estimating total significant wave height from marine radar images using equation 3.6 are defined as follows:

$$B_0 = f(d, \theta) = \frac{\theta}{d^4}, \quad (4.1)$$

$$B_1 = f(d, \theta, \mu) = \mu((1 - \tan(\theta)) + \tan(d)), \quad (4.2)$$

$$B_2 = f(d, \theta, \sigma^2) = \sigma^2(\tan(\theta) + \tan(d)), \quad (4.3)$$

where the d is distance, $\mu = (\mu_x + \mu_y)/2$ and $\sigma^2 = (\sigma_x^2 + \sigma_y^2)/2$ are mean and variance values respectively:

$$\mu_x = \sum_{i=0}^{G-1} i P_x(i); \mu_y = \sum_{j=0}^{G-1} j P_y(j), \quad (4.4)$$

$$\sigma_x^2 = \sum_{i=0}^{G-1} (P_x(i) - \mu_x(i))^2; \sigma_y^2 = \sum_{j=0}^{G-1} (P_y(j) - \mu_y(j))^2, \quad (4.5)$$

where μ_x, μ_y, σ_x and σ_y are the means and variances of P_x and P_y . $P_x(i)$ is the i th entry in the marginal-probability matrix obtained by summing the rows of $P(i, j)$ (analogous for $P_y(j)$ for columns of $P(i, j)$). G denotes to number of GLCM levels used.

4.3 Validation of wave and wind field retrieval algorithms

The comparison statistics between three radar sensors and corresponding buoy measurements or wave model data is given in Table III.

Figure 5 (a) shows the comparison between *in situ* buoy measurements and estimated significant wave height from TS-X sensor using the XWAVE_C method with the correction procedures discussed in Section 4.1. Figure 5 (a) also shows the scatterplot for sea state derived with CWAVE_S1-IW algorithm for available collocated data acquired over the Baltic Sea including 15 Sentinel-1A/B scenes with 52 buoy collocations. From Table III it is seen that both methods provide accurate wave height estimates in the Baltic Sea with a Pearson correlation coefficient of 0.88. However, RMSE and consequently scatter index are slightly higher for the results derived from Sentinel-1 data (RMSE = 0.32 m and SI = 0.33 for TS-X/TD-X; RMSE = 0.40 m and SI = 0.37 for Sentinel-1).

For the wind speed derived from high-resolution X-band radar using XMOD-2 algorithm (Figure 5 (b), Table III), the r shows values of 0.90 with low RMSE of 2.02 m s^{-1} and SI of 0.23. Even better results are seen when comparing CMOD algorithm wind speed estimations (Section 3.4) from Sentinel-1 data with the corresponding measurements ($r = 0.91$; SI = 0.19). Low RMSE value of 1.43 m s^{-1} indicates the suitability of Sentinel-1 wind speed estimates for operational use over the Baltic Sea.

Figure 5 (c) shows a histogram plot (bin size 0.2 m) for the collocated SAR and WAM results. The dominant significant wave height of the Baltic Sea is clearly seen from the figure as most of the measurements are in a range of up to 3 m. The statistics between the datasets are as follows: $r = 0.86$, RMSE = 0.47 m, and SI = 0.33.

Figure 5 (d) represents the scatterplot between the measured significant wave height and H_s derived from marine radar from January and June 2017. Using the empirical method for marine radar data processing introduced in Section 4.2, the accuracy of sea state estimates is comparable with the results of SAR data with r of 0.86, RMSE of 0.25 m and SI of 0.46.

Table III. Overview of inter-comparison of significant wave height and wind speed between different datasets: correlation coefficient (r), root mean square error (RMSE), scatter index (SI), and number of collocations (n).

Collocation pair	TS-X TD-X vs. <i>in situ</i>	TS-X TD-X vs. <i>in situ</i>	Sentinel-1 vs. <i>in situ</i>	Sentinel-1 vs. <i>in situ</i>	Sentinel-1 vs. WAM	Marine radar vs. <i>in situ</i>
Method	XWAVE_C	XMOD-2	CWAVE_S1-IW	CMOD4 CMOD5.N	CWAVE_S1-IW	Empirical method
Figure 5	(a)	(b)	(a)	(b)	(c)	(d)
Parameter	H_s	U_{10}	H_s	U_{10}	H_s	H_s
r	0.88	0.90	0.88	0.91	0.86	0.86
RMSE (m; m s^{-1})	0.32	2.02	0.40	1.43	0.47	0.25
SI	0.33	0.24	0.37	0.19	0.33	0.46
n	117	102	52	357	49314	1464

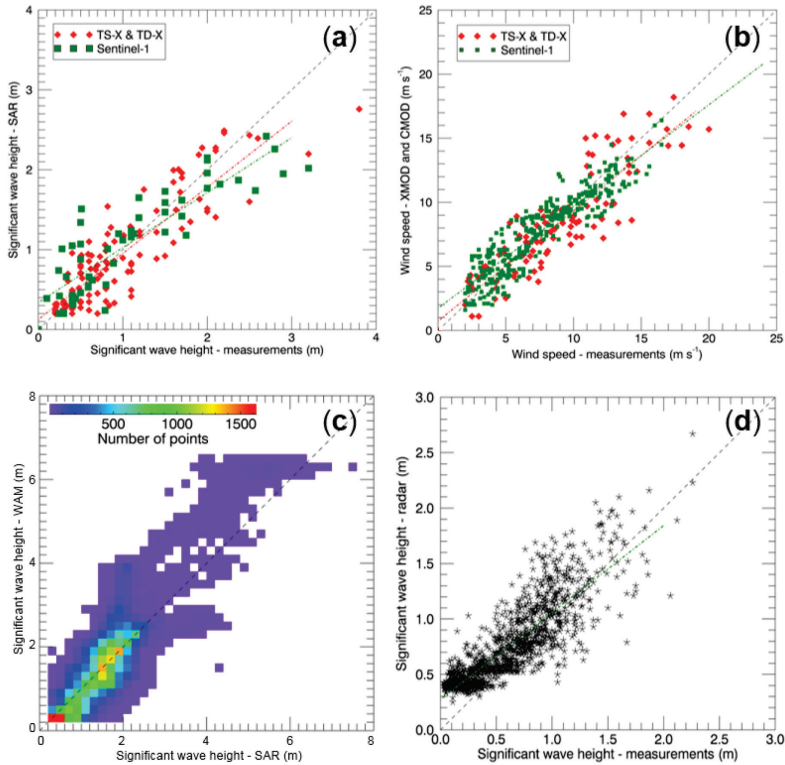


Figure 5. (a) Scatterplots for the sea state from 95 individual TS-X/TD-X StripMap images and 117 buoy collocations. The plot also shows the sea state for available collocated data acquired over the Baltic Sea including 15 Sentinel-1A/B scenes (overflights/events/days) with 116 individual Sentinel-1 IW mode images and 52 buoy collocations. (b) Scatterplot of surface wind speed for all available collocated TS-X/TD-X data acquired over the Eastern Baltic Sea (102 collocations). The plot also includes the wind speed retrieved from the Sentinel-1A/B dataset over the Baltic Sea. (c) Histogram plot for the validation dataset between Sentinel-1 and WAM results. The bin size for histogram calculations is 0.2 m. (d) Scatterplot for measured significant wave height against H_S derived from marine radar data using the developed empirical method. 1:1 lines are marked as black dotted lines; coloured and dotted lines show regression lines for corresponding datasets.

4.4 Local variability of sea state conditions in the Baltic Sea

The Baltic Sea is a very complex region for retrieving wave height from SAR data. It is seen from previous studies, that SAR methods work accurately in open ocean regions where swell waves are the major contributor to the total wave field (Li, Lehner, and He 2008; Lehner et al. 2013; Bruck 2015; Pleskachevsky, Rosenthal, and Lehner 2016).

In the Baltic Sea, the wave field is mostly influenced by local wind fields and it is disturbed by numerous shallow areas, islands and rugged coastline, which oblige to estimate wave height from noisy SAR information. However, similarly to the ocean, swell-like waves can be observed in coastal areas sheltered from the wind. For example, a unique situation was observed by TS-X/TS-X in the Baltic Sea on 20th February 2017 (Figure 6) when refracted waves produce cross seas behind the island of Naissaar. This demonstrates that SAR data/methods can be valuable for case studies in complex sea areas.

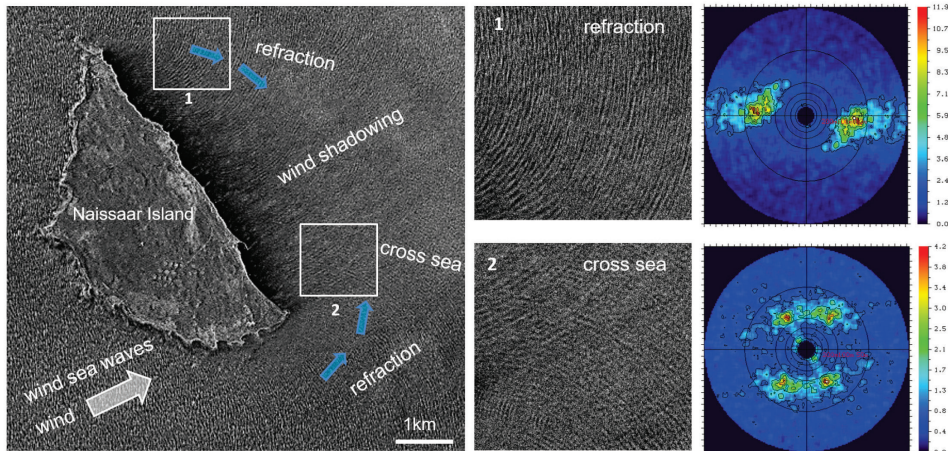


Figure 6. An example of wave refraction and cross sea near Naissaar Island in the Tallinn Bay acquired by TS-X on 20 February 2017 at 04:58 UTC. The average wavelengths of the swell-like waves are about 80 m.

4.4.1 Wave field parameters from high resolution SAR imagery

To evaluate the spatial distribution of wave characteristics retrieved from SAR, wave model results (e.g. SWAN or WAM) were used. It was observed that the TS-X wave retrievals follow the spatial pattern that is caused by wind dependent growth of the sea state (fetch dependence), shadowing effects by islands, etc. as in the wave model. However, wind gusts and local variations of H_5 that are connected to local wind effects are not present in the model results (Publication I; Publication II; Publication IV). In numerical wave modelling, the wind gustiness is hidden in the parameterisations of the wind input function, which is usually tuned to the mean value of U_{10} . Thus, the standard input for the wave modelling is a smoothed wind field where the spatial and temporal variability on local scale wind variability is routinely not included.

The storm on 29 October 2013 developed wind speeds reaching up to 21.6 m s^{-1} with a south-western direction. SWAN wave field from 29 October 2013 at 16:00 UTC was selected for the comparison with TS-X scene acquired at 15:45 UTC (Figure 7 (a–b)). The difference between the two fields can be observed in the middle of the Gulf of Finland, where SAR-derived wave height reflects the local wind effects and is more variable due to wind gusts. In general, wind gusts and local variations of H_5 are not present in the model results. This is also expressed in numbers where SAR derived values present about a 40% higher maximal wave height (3.86 m from SAR vs. 2.80 m from SWAN) and double the standard deviation (1.19 m vs. 0.61 m for SAR and SWAN correspondingly).

Higher variability can also be observed in wave propagation direction and wavelength retrievals from SAR for the same example (Figure 7 (c–d)). The standard deviation of wave propagation direction is 21.90° for SWAN and 26.80° for SAR while the corresponding standard deviation of wavelengths are 8.40 m and 9.60 m. In general wave propagation directions are similar. However, the wave propagation direction and wavelength values from SWAN data (Figure 7 (d)) are more homogeneous with deterministic changes whereas from SAR image (Figure 7 (c)) the values change on a much smaller scale. The greatest difference is seen in the central part of the Gulf of Finland where wavelength values from SAR imagery vary from 60 m to 90 m whereas from SWAN results the values remain all over 80 m.

The sea state fields derived from TS-X/TD-X imagery show the strongest inhomogeneities in areas which are related to local wind speed variations. The local impact of wind gusts on waves can increase significantly if the gust speed is similar to the speed of the wave groups. Wind energy feeding the same wave group for a longer period causes the growth of individual waves and results in resonance. Earlier studies using SAR data have shown that wave groups with an abnormal height in the North Sea are connected to atmospheric effects (Pleskachevsky, Lehner, and Rosenthal 2012). This effect is caused by mesoscale wind gusts that are moving as an organized system across the sea and “drag” the continuously growing waves.

Similarly, this effect was observed in the Gulf of Finland on a smaller scale using techniques based on satellite-borne high-resolution SAR. Accompanied by wind gusts, the wave height was increased in kilometre-size clusters (Publication I).

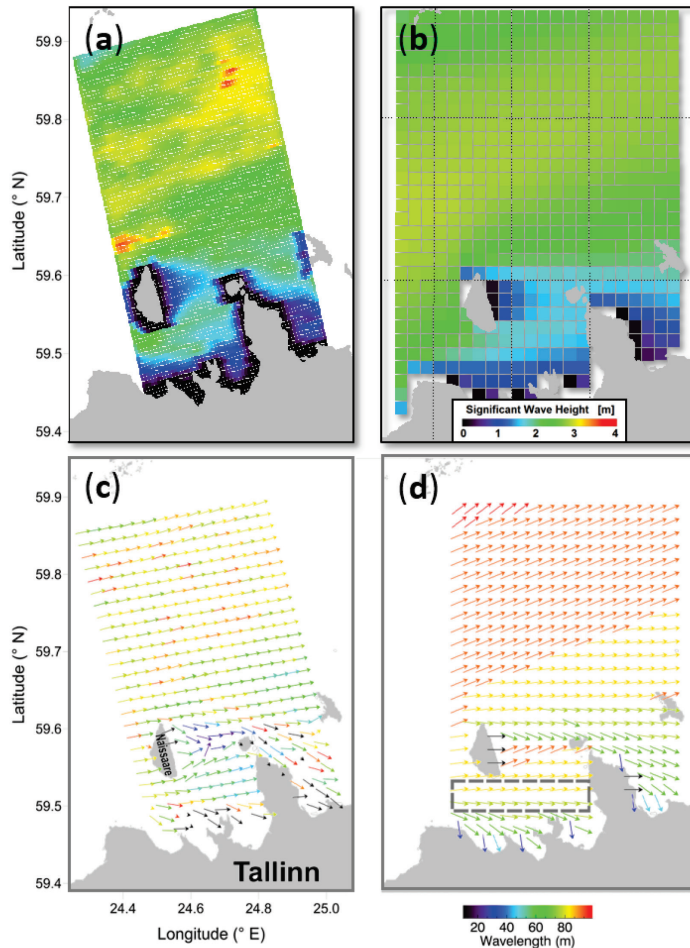


Figure 7. A comparison of spatial variability of significant wave height (a–b) and wave propagation direction (c–d) between TS-X and SWAN wave model results for storm conditions. The SAR scene acquired on 29 October 2013 at 15:45 depicts a more inhomogeneous sea state than the model. In both cases, SAR-derived values show a higher standard deviation compared to SWAN model results: 1.19 m vs. 0.61 m for H_s , 26.80° vs. 21.90° for wave propagation direction and 9.60 m vs 8.40 m for wavelength, correspondingly.

4.4.2 Wave field studies from medium resolution SAR imagery

For the second example, the variability of meteo-marine conditions is explored using medium resolution Sentinel-1A/B IW data and WAM wave model results.

Comparing the SAR wave field (Figure 8 (b)) with WAM wave field (Figure 8 (c)), one can observe a good general agreement in the wave height values and location of maximum ($r = 0.91$). However, the area of the storm on the SAR image is smaller and does not spread as much to the north as in the WAM results. The maximum significant wave height from SAR is about 0.5 m higher. Another region with some differences between the wave fields retrieved with the two different methods is seen in the Bothnia Sea area, where SAR-derived wave height along the Swedish coast is about two meters lower compared to the model data. The standard deviation in this case is very similar for both dataset, 1.51 m for SAR and 1.48 m for WAM, since both the high significant wave height values (up to 7.5 m) in the Southern Baltic, as well as the low wave height values in the Bothnia Sea are present.

In contrast, large differences in standard deviation values are observed in the low sea state example on 5 July 2015 (Figure 8 (g–i)). Although WAM wave model results are smoother and lower than SAR-derived values, they represent a very similar large-scale general pattern. One can notice the increased wave height values to the north and to the south of Gotland Island. A similar pattern from both datasets is also observed in the Bothnia Sea region. Operational monitoring of low sea state conditions is relevant for routine environmental observations and it is noteworthy that most of the wave field variability is lost in the model outcome (STD = 0.17 m) compared to SAR-derived values (STD = 1.14 m).

The examples in Figure 8 showed a good general agreement between the SAR-derived and WAM model wave fields. However, there are some differences between the results obtained with the two methods: (i) the area and the location of the storm might be different; (ii) the wave height variability of WAM model fields is lower compared to the SAR-derived fields. Both cases are again connected to how the wave model resolves wind forcing information. In most practical cases, wave model forcing fields have much coarser spatial resolution and do not include as much local variability as SAR data are able to provide.

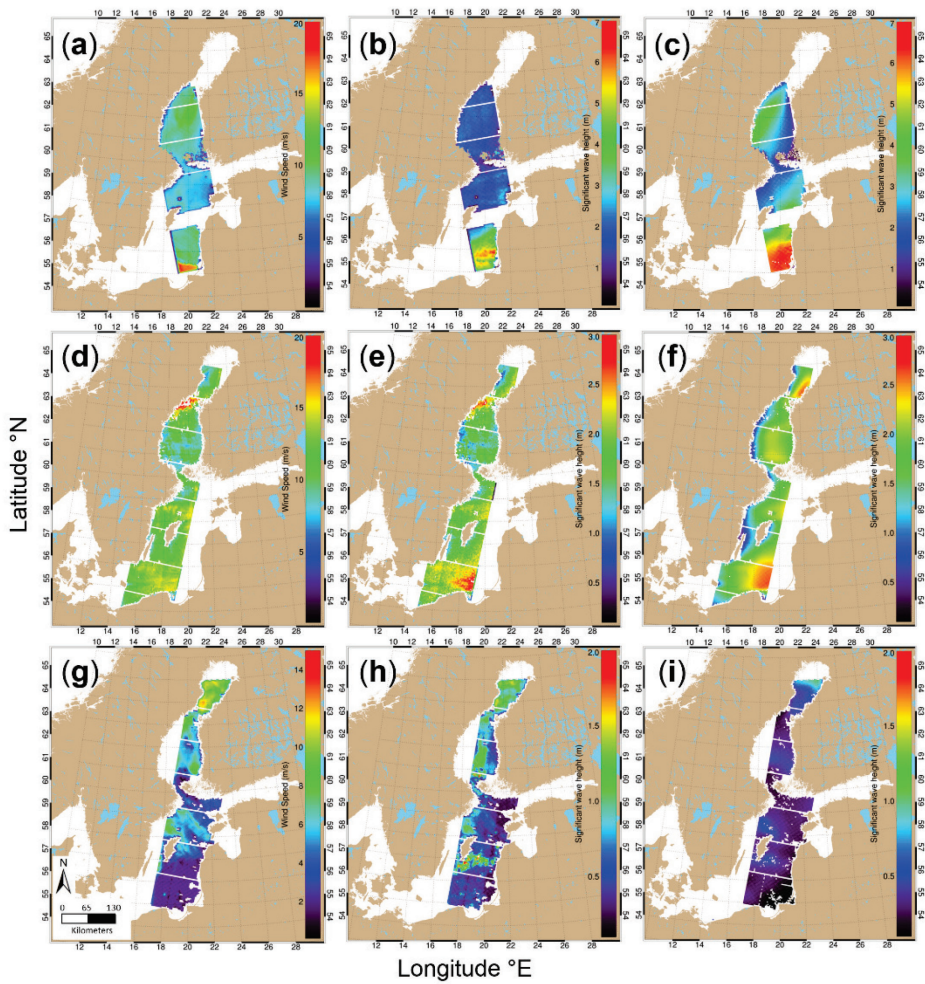


Figure 8. Examples of spatially collocated SAR wind (a, d, g) fields, SAR wave fields (b, e, h) and WAM wave model fields (c, f, i) during three characteristic situations over the Baltic Sea: high sea state on 11 January 2015 at 16:19 (a–c), medium sea state on 2 October 2015 at 04:56 (d–f) and low sea state on 5 July 2015 at 04:56 (g–i).

4.5 SAR and marine radar data for operational use in the Baltic Sea

4.5.1 Sentinel-1 imagery for practical applications

The Baltic Sea is one of the most frequently imaged locations by the Sentinel-1A/B satellites because of the location in the temperate latitudes. Various parts of the Baltic Sea are imaged by Sentinel-1A/B daily and often even twice a day by ascending and descending orbits in the morning and in the evening correspondingly

To demonstrate the advantages of Sentinel-1 A/B IW data for the operational sea state monitoring purposes, an independent time series from 1 August 2016 until the end of 2016 was analysed (Figure 9). Almost 800 single acquisitions from the selected period covering various parts of the Baltic Sea were processed. Time series of SAR-derived significant wave height was retrieved from four locations and compared with corresponding *in situ* measurements or wave model results.

In Figure 9 (b, c) three cases highlighted in green are brought out to explain the benefits of using SAR-derived wave fields. In “case 1” of Figure 9 (b), one can observe that both WAM wave model results and SAR-derived results match closely with the *in situ* measurements of the Northern Baltic Proper (NBP) station. However, in Figure 9 (c) which represents a location 60 km away from NBP, a mismatch between SAR and WAM results can be seen in the “case 1” region. The reason could be that since SAR represents better detailed spatial variability/pattern, the actual significant wave height was lower than WAM had predicted at the specific time and location.

In contrast, the “Case 3” in Figure 9 (b, c) shows good general match between *in situ* measurements, SAR-derived wave height, and WAM output in the two different locations, suggesting that the wave field was spatially more uniform. In general, SAR-derived results would be beneficial for wave model validation.

Since the Baltic Sea is seasonally ice-covered, *in situ* measurement devices are removed for the winter period. Similarly, when the buoys have technical problems (e.g., no data connection) or during their maintenance, valuable wave information is lost. Moreover, wave models may also have short periods with technical problems when no wave forecast is provided. These situations can be observed in “case 2” in Figure 9 (c), where SAR-derived results become the only source of wave information.

This is further amplified in Figure 9 (d) which demonstrates the added benefit of using SAR data to retrieve wave information over the poorly sampled area. Although Södra Östersjön station (55.9167 °N, 18.7833 °E) is included into Baltic Operational Oceanography System (BOOS) measurement stations, the last unrestricted access measurement data was received in 2011. The Southern Baltic Sea is a region where the highest waves frequently occur (Tuomi, Kahma, and Pettersson 2011; Björkqvist et al. 2018). As no *in situ* measurements are carried out in the region, the SAR-derived results would be highly valuable for model validation and/or assimilation into the wave model.

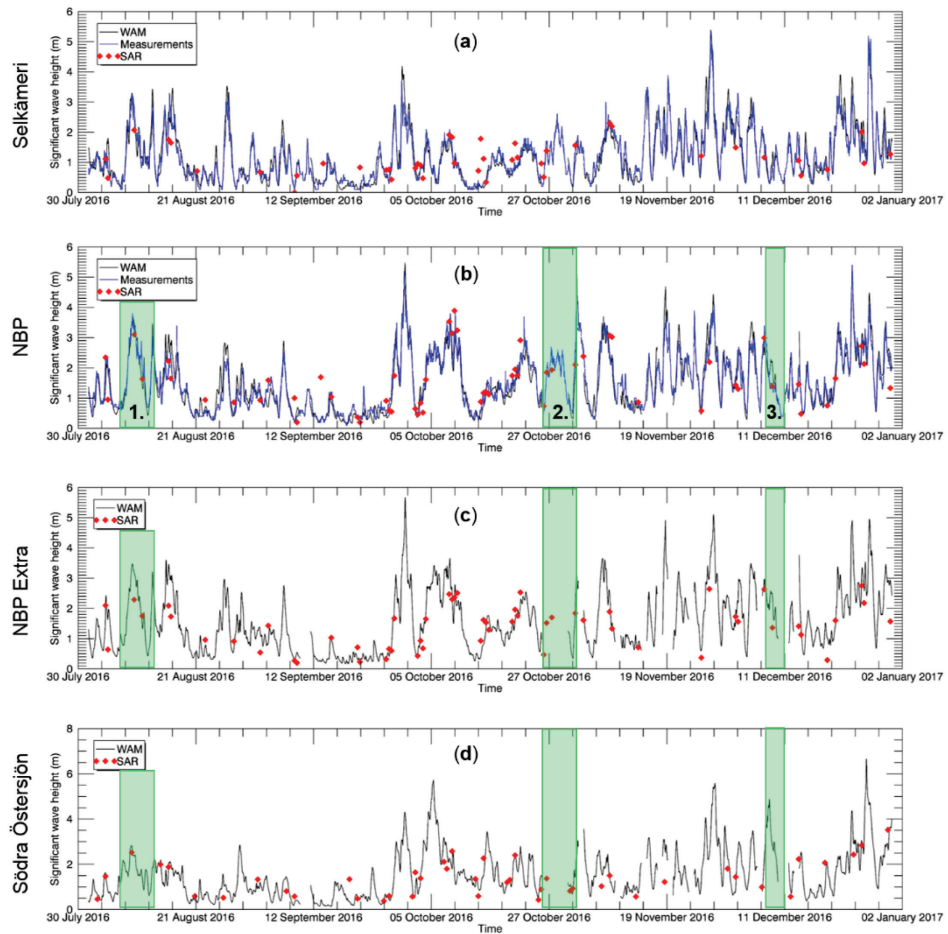


Figure 9. A time series from 1 August 2016 until the end of 2016 from four stations. Two stations—Selkämeri and Northern Baltic Proper (NBP) (Figure 3, Table 1)—include all the data: measurement, WAM, and SAR-derived results; other two stations—NBP Extra (58.7500 °N, 20.8271 °E; no. 6 in Figure 3) and Södra Östersjön (55.9167 °N, 18.7833 °E; no. 7 in Figure 3) include WAM result and SAR-derived significant wave height. Highlighted areas indicate the benefits of using SAR data over the Baltic Sea: “case 1” and “case 3” bring out the variability aspect of SAR-derived values whereas “case 2” shows missing measurements that can be replaced with SAR data.

4.5.2 Temporal variability of sea state parameters from marine radar

In comparison to *in situ* buoy measurements at a specific location, the marine radar data allows to cover larger areas and estimate the spatial and temporal distribution of investigated characteristics. Figure 10 (a) shows an example of spatial estimation of average H_5 from marine radar images acquired between 26.03.–28.03.2017 when north-western winds were blowing with the average wind speed of about 6.3 m s^{-1} (gusts up to 21.9 m s^{-1}).

The results in Figure 10 (a) are retrieved by using the developed empirical algorithm introduced in Section 4.2 and by interpolation using the Kriging method (Isaaks and Srivastava 1989). Although the interpolation has some negative effects on the edges of the visualized data, the general H_5 results show the similar outcome as previous studies

(Soomere 2005; Alari and Raudsepp 2010) where a similar north-western storm in the Tallinn Bay was analysed.

It is well seen from the Figure 10 (a), how higher waves propagate into the Tallinn Bay between the mainland and Naissaar island having the local maximum around the tip of Paljassaare peninsula where the depth of the sea is up to 40 m. As the depth decreases, the wave height also decreases while propagating towards the coast.

The time series of *in situ* measurements and radar estimates of H_s also show good agreement during the storm event (Figure 10 (b)) with the correlation of 0.93 (RMSE = 0.15). Also, the effect of wind speed variations (retrieved from Rohuneeme station) on local wave conditions can be observed.

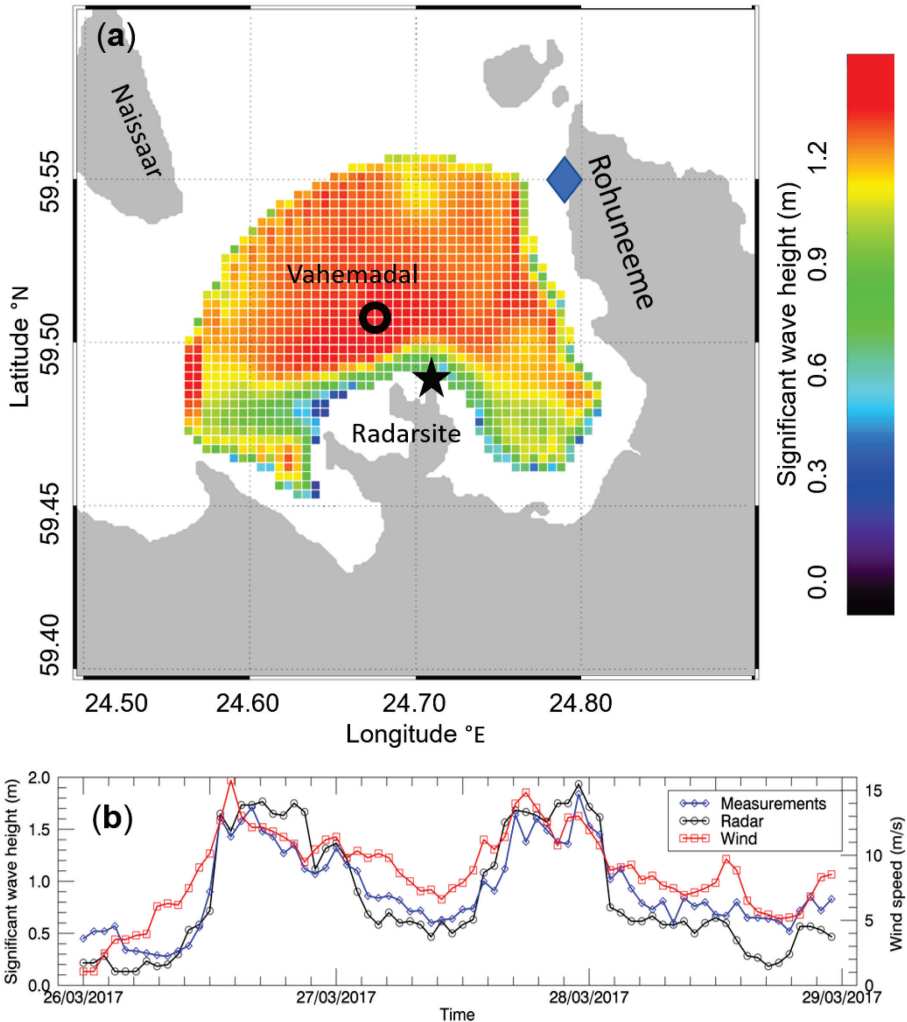


Figure 10. (a) average significant wave height for the North-West storm over the Tallinn Bay area; (b) measured H_s (blue), radar-derived H_s (black) and wind speed at the Rohuneeme station (red) for the storm period.

4.5.3 Climatological aspect of Sentinel-1 data

Routine monitoring of meteo-marine parameters forms a basis for long-term studies, e.g. regional changes in wave climate. Figure 11 (b, c) represents the average wind speed and significant wave height values from Sentinel-1A/B IW data during 2015 and 2016. The average significant wave height values over the two-year period (Figure 11 (c)) generally represent similar values to previous studies that used either model data reanalysis or altimetry products over a longer period (up to 23 years) (e.g. Figure 6 in Tuomi, Kahma, and Pettersson 2011; Figure 2 in Kudryavtseva and Soomere 2017). There are clearly higher average wave height values in the open parts of the Baltic Sea (around 1.8 m) and lower values in the Gulf of Riga (up to 1.0 m in the open part; below 0.8 m in the coastal areas) or the Bothnian Sea (from 0.7 m to 1.2 m).

Altimetry products validations have shown reliable performance (RMSE less than 0.5 m) in the open ocean (Ducet, Le Traon, and Reverdin 2000; Ray and Beckley 2003; Pascual et al. 2006; Pujol et al. 2016) and in the coastal sea (RMSE up to 0.37 m) (Cazenave et al. 2002; Vignudelli et al. 2005; Madsen, Høyer, and Tscherning 2007; Bouffard et al. 2008; Kudryavtseva and Soomere 2016). However, the spatial coverage of standard altimetry wave products is limited and restricted to offshore areas (30–70 km from coast) (Monaldo 1988; Høyer and Nielsen 2006; Passaro, Fenoglio-Marc, and Cipollini 2015; Sepulveda, Queffeuou, and Arduin 2015). The low-resolution altimetry wave products/algorithms and open ocean SAR wave mode products (not available for the coastal areas, including the Baltic Sea) are not sufficient for local and regional applications in the complex coastal environment, such as the Baltic Sea. The sea state products derived from Sentinel-1 SAR IW data provide information over a large area, including the coastal zone with similar product accuracy ($r = 0.88$, RMSE = 0.40 m) to the altimetry products. Thus, the high-resolution SAR wave data would provide added value for user communities dealing with coastal processes. Moreover, SAR wave products enable to resolve detailed spatial variability while *in situ* data describes detailed temporal variability in a limited number of locations. Considering the long-term objectives of the Copernicus program and the revisit cycle of the Sentinel-1 mission, the statistical bases for wave field mapping will improve over time.

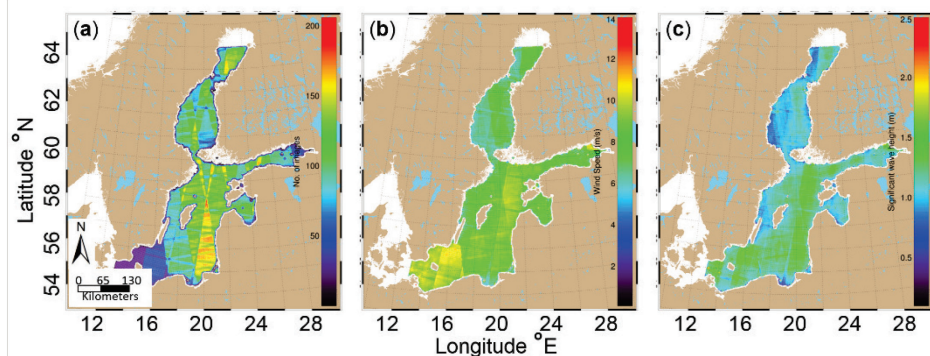


Figure 11. (a) Number of SAR points; (b) average wind speed; and (c) average significant wave height over 2015–2016 interpolated to WAM model grid.

CONCLUSION

The dissertation demonstrates that radar (SAR and marine radar) remote sensing data processing methods can be effectively used to retrieve accurate significant wave height estimates in the Baltic Sea where short and steep wind waves dominate. The focus was on developing/improving and validating empirical methods to estimate significant wave height in the coastal regions of the Baltic Sea. The obtained results showed that significant wave height fields derived from radar sources are spatially more variable and would provide more detailed information compared to the wave model or other EO sensors (e.g. altimetry).

The main results of the present dissertation can be summarized as follows:

- The empirical algorithm XWAVE_C to estimate total significant wave height from TS-X/TD-X SAR data was improved by implementing JONSWAP parametrization. The proposed algorithm adjustment increased the accuracy of wave retrievals by 5–20% (based on r and RMSE respectively). The method validation resulted in the following statistics: $r = 0.88$, RMSE = 0.32m and SI = 0.33. The JONSWAP correction function was also implemented in DLRs near-real time SAR data processing chain.
- The empirical method CWAVE_S1-IW to estimate meteo-marine parameters from Sentinel-1 IW images was validated with *in situ* measurements over the Baltic Sea region. The validation showed good agreement between the datasets: r of 0.88, RMSE of 0.40 m and SI of 0.37. The comparison between significant wave height derived from Sentinel-1 data and from corresponding WAM wave model fields showed good agreement: $r = 0.86$, RMSE = 0.47 and SI = 0.33.
- Wind speed estimation functions, XMOD-2 and CMOD4/CMOD5.N applied on TS-X/TD-X and Sentinel-1 IW data respectively were validated with *in situ* wind measurements. Both wind speed retrieval algorithms showed high accuracy with correlation coefficient r for XMOD-2 being 0.90 and for CMOD $r = 0.91$. The RMSE shows low deviation from measurements, especially for Sentinel-1 data with the value being 1.43 m s^{-1} . Slightly higher RMSE values were observed for high-resolution TS-X/TD-X data (RMSE = 2.02 m s^{-1}).
- An empirical algorithm was developed to estimate significant wave height from X-band marine radar data. The method is based on image spectrum analysis complemented with GLCM image texture statistics to bypass the transformation to wave spectra. The validation results show that wave height retrievals of the proposed algorithm are with similar accuracy in space and time ($r = 0.86$; RMSE = 0.25 m) as SAR counterparts. In addition to marine radar, the GLCM image statistics proved to be useful for the empirical sea state retrievals from Sentinel-1 IW SAR data.
- Wind speed and significant wave height results derived from SAR were compared to other data sources such as wave model and altimetry wave products.
 - The results show that wave field data derived from SAR have a higher standard deviation meaning that parameters are spatially more variable and would provide more detailed wave field information compared to model results.

- In case of wind speed, SAR data include local fine-scale wind field variations (fast moving cyclones, fronts and gusts) that influence radar backscatter and the related wave height retrievals. This allows obtaining storm peak areas and location more accurately from radar data.
- SAR data enable to observe coastal wave field variations in the Baltic Sea in more detail compared to, e.g. altimetry. Based on Sentinel-1A/B data from 2015 and 2016, the average significant wave height closely resembles values found by previous studies in open parts of the Baltic Sea and all its sub-basins. However, SAR data enable to provide precise results as close as about 500 m from the coastline whereas altimetry products results are accurate an order of magnitude farther from the coast.

Using wave fields from radar data over the Baltic Sea has the following general benefits: (i) retrieving additional wave information over the poorly sampled area or in cases when data is missing (e.g. during ice season); (ii) SAR wave field values could be used for wave model validation and to improve model forcing. Additionally, the average significant wave height fields from SAR prove that the data enable to perform wave climate studies. Wave height and wind speed information could be derived in a seasonal and regional scale for a number of applications, e.g. routine environmental monitoring (downstream) services, operational sea state monitoring, situational awareness services, wave energy assessment, climate studies, wind farming, etc.

Future outlook: The longevity of Sentinel-1 mission (at least a few decades) makes it reasonable to improve/adjust the proposed wave retrieval algorithms so that the methods could be implemented on Sentinel-1A/B Extra Wide swath (EW) products. This would increase the availability of spatial wave field data and consequently improve the knowledge of the Baltic Sea wave conditions.

Also, a more detailed comparison should be carried out between wave model results and SAR-derived wave height during extreme wave events to analyse the unexpectedly high local wave maxima in deep waters (reported in previous studies). Future studies on image spectra analysis, wave steepness and sampling variability would allow understanding the fine scale wave height variability in the Baltic Sea.

Future studies are also related to wind speed estimation algorithm development and implementation for marine radar data over the Tallinn Bay.

REFERENCES

- Alari, Victor, and Urmas Raudsepp. 2010. "Depth Induced Breaking of Wind Generated Surface Gravity Waves in Estonian Coastal Waters." *Boreal Environment Research* 15 (3).
- Alpers, W R, D B Ross, and C L Rufenach. 1981. "On the Detectability of Ocean Surface Waves by Real and Synthetic Aperture Radar." *Journal of Geophysical Research: Oceans* 86 (C7): 6481–6498.
- Alpers, W R, and C L Rufenach. 1979. "The Effect of Orbital Motions on Synthetic Aperture Radar Imagery of Ocean Waves." *IEEE Transactions on Antennas and Propagation* 27 (5): 685–690.
- Alpers, W R, and Claus Bruening. 1986. "On the Relative Importance of Motion-Related Contributions to the SAR Imaging Mechanism of Ocean Surface Waves." *IEEE Transactions on Geoscience and Remote Sensing*, no. 6: 873–885.
- BACC II. 2015. *Second Assessment of Climate Change for the Baltic Sea Basin*. SpringerOpen.
- Barrick, Donald E. 1995. "Near-grazing Illumination and Shadowing of Rough Surfaces." *Radio Science* 30 (3): 563–580.
- Beal, R C, D G Tilley, and F M Monaldo. 1983. "Large-And Small-Scale Spatial Evolution of Digitally Processed Ocean Wave Spectra from SEASAT Synthetic Aperture Radar." *Journal of Geophysical Research: Oceans* 88 (C3): 1761–1778.
- Bell, Paul S, and John C Osler. 2011. "Mapping Bathymetry Using X-Band Marine Radar Data Recorded from a Moving Vessel." *Ocean Dynamics* 61 (12): 2141–2156.
- Björkqvist, Jan-Victor, Ingvar Lukas, Victor Alari, Gerbrant Ph van Vledder, Sander Hulst, Heidi Petterson, Arno Behrens, and Aarne Männik. 2018. "Comparing a 41-Year Model Hindcast with Decades of Wave Measurements from the Baltic Sea." *Ocean Engineering* 152: 57–71. <https://doi.org/10.1016/j.oceaneng.2018.01.048>.
- Booij, N, R C Ris, and L H Holthuijsen. 1999. "A Third-Generation Wave Model for Coastal Regions: 1. Model Description and Validation." *Journal of Geophysical Research: Oceans* 104 (C4): 7649–7666.
- Bouffard, Jerome, S Vignudelli, P Cipollini, and Yves Menard. 2008. "Exploiting the Potential of an Improved Multimission Altimetric Data Set over the Coastal Ocean." *Geophysical Research Letters* 35 (10).
- Breit, H, T Fritz, U Bals, M Lachaise, A Niedermeier, and M Vonavka. 2010. "TerraSAR-X SAR Processing and Products." *IEEE Transactions on Geoscience and Remote Sensing* 48 (2): 727–740.
- Bruck, Miguel. 2015. "Sea State Measurements Using TerraSAR-X/TanDEM-X Data." Christian-Albrechts-Universität zu Kiel.
- Carrasco, Ruben, Michael Streßer, and Jochen Horstmann. 2017. "A Simple Method for Retrieving Significant Wave Height from Dopplerized X-Band Radar." *Ocean Science* 13 (1): 95.
- Cazenave, A, P Bonnefond, F Mercier, K Dominh, and V Toumazou. 2002. "Sea Level Variations in the Mediterranean Sea and Black Sea from Satellite Altimetry and Tide Gauges." *Global and Planetary Change* 34 (1–2): 59–86.
- Crony, J. 1970. "Civil Marine Radar." In *Radar Handbook*, edited by I. Skolnik Merrill.
- Dankert, Heiko, and W Rosenthal. 2004. "Ocean Surface Determination from X-band Radar-image Sequences." *Journal of Geophysical Research: Oceans* 109 (C4).

- Dankert, Heiko, and Jochen Horstmann. 2007. "A Marine Radar Wind Sensor." *Journal of Atmospheric and Oceanic Technology* 24 (9): 1629–1642.
- Dankert, Heiko, Jochen Horstmann, Susanne Lehner, and Wolfgang Rosenthal. 2003. "Detection of Wave Groups in SAR Images and Radar Image Sequences." *IEEE Transactions on Geoscience and Remote Sensing* 41 (6): 1437–1446.
- Dankert, Heiko, Jochen Horstmann, and Wolfgang Rosenthal. 2004. "Ocean Surface Winds Retrieved from Marine Radar-Image Sequences." In *Geoscience and Remote Sensing Symposium, 2004. IGARSS'04. Proceedings. 2004 IEEE International*, 3:1903–1906. IEEE.
- Ducet, N, Pierre-Yves Le Traon, and Gilles Reverdin. 2000. "Global High-resolution Mapping of Ocean Circulation from TOPEX/Poseidon and ERS-1 And-2." *Journal of Geophysical Research: Oceans* 105 (C8): 19477–19498.
- Eineder, M, T Fritz, J Mittermayer, A Roth, E Boerner, and H Breit. 2008. "TerraSAR-X Ground Segment, Basic Product Specification Document." CLUSTER APPLIED REMOTE SENSING (CAF) OBERPFAFFENHOFEN (GERMANY).
- Gangeskar, Rune. 2014. "An Algorithm for Estimation of Wave Height From Shadowing in X-Band Radar Sea Surface Images." *IEEE Transactions on Geoscience and Remote Sensing* 52 (6): 3373–3381. <https://doi.org/10.1109/tgrs.2013.2272701>.
- "Guide to Meteorological Instruments and Methods of Observation. WMO-No. 8." 2008. www.wmo.int.
- Haralick, R M, and K Shanmugam. 1973. "Textural Features for Image Classification." *IEEE Transactions on Systems, Man, and Cybernetics* 3 (6): 610–621.
- Hasselmann, D E, M Dunckel, and J A Ewing. 1980. "Directional Wave Spectra Observed during JONSWAP 1973." *Journal of Physical Oceanography* 10 (8): 1264–1280.
- Hasselmann, K, T P Barnett, E Bouws, H Carlson, D E Cartwright, K Enke, and J A Ewing. 1973. *Measurements of Wind-Wave Growth and Swell Decay during the Joint North Sea Wave Project (JONSWAP)*.
- Hasselmann, K, and S Hasselmann. 1991. "On the Nonlinear Mapping of an Ocean Wave Spectrum into a Synthetic Aperture Radar Image Spectrum and Its Inversion." *Journal of Geophysical Research: Oceans* 96 (C6): 10713–10729.
- Hasselmann, K, R K Raney, W J Plant, W Alpers, R A Shuchman, D R Lyzenga, C L Rufenach, and M J Tucker. 1985. "Theory of Synthetic Aperture Radar Ocean Imaging: A MARSEN View." *Journal of Geophysical Research: Oceans* 90 (C3): 4659–4686.
- Hasselmann, S, C Brüning, K Hasselmann, and P Heimbach. 1996. "An Improved Algorithm for the Retrieval of Ocean Wave Spectra from Synthetic Aperture Radar Image Spectra." *Journal of Geophysical Research: Oceans* 101 (C7): 16615–16629.
- Hatten, Helge, F Ziemer, J Seemann, and J Nieto-Borge. 1998. "Correlation between the Spectral Background Noise of a Nautical Radar and the Wind Vector." In *Proc. 17th Int. Conf. Offshore Mechanics and Arctic Engineering (OMAE)*.
- Hersbach, Hans, Ad Stoffelen, and Sybren de Haan. 2007. "An Improved C-band Scatterometer Ocean Geophysical Model Function: CMOD5." *Journal of Geophysical Research: Oceans* 112 (C3).
- Holthuijsen, Leo H. 2010. *Waves in Oceanic and Coastal Waters*. Cambridge university press.
- Høyer, Jacob L, and J W Nielsen. 2006. "Satellite Significant Wave Height Observations in Coastal and Shelf Seas." In *Proceedings of the Symposium on 15 Years of Progress in Radar Altimetry, 13–18 March 2006, Venice, Italy*. ESA Special Publication, SP-614, Paper.

- Huang, Weimin, Ruben Carrasco, Chengxi Shen, Eric W Gill, and Jochen Horstmann. 2016. "Surface Current Measurements Using X-Band Marine Radar with Vertical Polarization." *IEEE Transactions on Geoscience and Remote Sensing* 54 (5): 2988–2997.
- Hydrometeorological State of the Marine Shelf Zone in the USSR*. 1983. Vol. 1. Leningrad: Hydrometeoizdat.
- Isaaks, E H, and R M Srivastava. 1989. "An Introduction to Applied Geostatistics. Oxford Univ. Press, New York." *An Introduction to Applied Geostatistics*. Oxford Univ. Press, New York.
- Jaagus, J, and A Kull. 2011. "Changes in Surface Wind Directions in Estonia during 1966-2008 and Their Relationships with Large-Scale Atmospheric Circulation." *Estonian Journal of Earth Sciences* 60 (4): 220–231. <https://doi.org/10.3176/earth.2011.4.03>.
- Jackson, Christopher R, and John R Apel. 2004. *Synthetic Aperture Radar: Marine User's Manual*. US Department of Commerce, National Oceanic and Atmospheric Administration, National Environmental Satellite, Data, and Information Service, Office of Research and Applications.
- Karagali, I, A Peña, M Badger, and C B Hasager. 2012. "Wind Characteristics in the North and Baltic Seas from the QuikSCAT Satellite." *Wind Energy* 17 (1): 123–140.
- Kriaučiūnienė, J, B Gailiušis, and M Kovalenkoviėnė. 2006. "Peculiarities of Sea Wave Propagation in Klaipėda Strait, Lithuania." *Baltica* 19 (1): 20–29.
- Kudryavtseva, Nadezhda A, and Tarmo Soomere. 2016. "Validation of the Multi-Mission Altimeter Wave Height Data for the Baltic Sea Region." *ArXiv Preprint ArXiv:1603.08698*.
- Kudryavtseva, Nadezhda, and Tarmo Soomere. 2017. "Satellite Altimetry Reveals Spatial Patterns of Variations in the Baltic Sea Wave Climate." *Earth System Dynamics* 8 (3): 697–706. <https://doi.org/10.5194/esd-8-697-2017>.
- Launiainen, Jouko, and Tuomas Laurila. 1984. "Marine Wind Characteristics in the Northern Baltic Sea." *Finnish Marine Research* 250: 52–86.
- Lee, P H Y, J D Barter, K L Beach, C L Hindman, B M Lake, H Rungaldier, J C Shelton, A B Williams, R Yee, and H C Yuen. 1995. "X Band Microwave Backscattering from Ocean Waves." *Journal of Geophysical Research: Oceans* 100 (C2): 2591–2611.
- Lehmann, A, K Getzlaff, and J Harlaß. 2011. "Detailed Assessment of Climate Variability in the Baltic Sea Area for the Period 1958 to 2009." *Climate Research* 46 (2): 185–196. <https://doi.org/10.3354/cr00876>.
- Lehner, S, A Pleskachevsky, D Velotto, and S Jacobsen. 2013. "Meteo-Marine Parameters and Their Variability Observed by High Resolution Satellite Radar Images." *Oceanography* 26 (2): 80–91.
- Lehner, S, J Schulz-Stellenfleth, S Brusch, and X M Li. 2008. "Use of TerraSAR-X Data for Oceanography." In *Synthetic Aperture Radar (EUSAR), 2008 7th European Conference On*, 1–4. VDE.
- Leppäranta, Matti., and Kai. Myrberg. 2009. *Physical Oceanography of the Baltic Sea*. Springer/Praxis Pub.
- Li, X M, and S Lehner. 2014. "Algorithm for Sea Surface Wind Retrieval from TerraSAR-X and TanDEM-X Data." *IEEE Transactions on Geoscience and Remote Sensing* 52 (5): 2928–2939.
- Li, X M, S Lehner, and T Bruns. 2011. "Ocean Wave Integral Parameter Measurements Using ENVISAT ASAR Wave Mode Data." *IEEE Transactions on Geoscience and Remote Sensing* 49 (1): 155–174.

- Li, X M, S Lehner, and M X He. 2008. "Ocean Wave Measurements Based on Satellite Synthetic Aperture Radar (SAR) and Numerical Wave Model (WAM) Data—extreme Sea State and Cross Sea Analysis." *International Journal of Remote Sensing* 29 (21): 6403–6416.
- Li, Xiaoming, Susanne Lehner, and Wolfgang Rosenthal. 2010. "Investigation of Ocean Surface Wave Refraction Using TerraSAR-X Data." *IEEE Transactions on Geoscience and Remote Sensing* 48 (2): 830–840.
- Liu, Xinlong, Weimin Huang, and Eric W Gill. 2016. "Wave Height Estimation from Shipborne X-Band Nautical Radar Images." *Journal of Sensors* 2016: 1–7. <https://doi.org/10.1155/2016/1078053>.
- Lyzenga, D R. 2002. "Unconstrained Inversion of Waveheight Spectra from SAR Images." *IEEE Transactions on Geoscience and Remote Sensing* 40 (2): 261–270.
- Lyzenga, D R, R A Shuchman, J D Lyden, and C L Rufenach. 1985. "SAR Imaging of Waves in Water and Ice: Evidence for Velocity Bunching." *Journal of Geophysical Research: Oceans* 90 (C1): 1031–1036.
- Lyzenga, D R, A L Maffett, and R A Shuchman. 1983. "The Contribution of Wedge Scattering to the Radar Cross Section of the Ocean Surface." *IEEE Transactions on Geoscience and Remote Sensing*, no. 4: 502–505.
- Madsen, Kristine Skovgaard, J L Høyer, and Carl Christian Tscherning. 2007. "Near-coastal Satellite Altimetry: Sea Surface Height Variability in the North Sea–Baltic Sea Area." *Geophysical Research Letters* 34 (14).
- Masuko, H, K I Okamoto, M Shimada, and S Niwa. 1986. "Measurement of Microwave Backscattering Signatures of the Ocean Surface Using X Band and Ka Band Airborne Scatterometers." *Journal of Geophysical Research: Oceans* 91 (C11): 13065–13083.
- Milman, Andrew S, Albert O Scheffler, and John R Bennett. 1993. "A Theory of the Synthetic Aperture Radar Images of Time-dependent Scenes." *Journal of Geophysical Research: Oceans* 98 (C1): 911–925.
- Monaldo, Frank. 1988. "Expected Differences between Buoy and Radar Altimeter Estimates of Wind Speed and Significant Wave Height and Their Implications on Buoy-Altitude Comparisons." *Journal of Geophysical Research* 93 (C3): 2285. <https://doi.org/10.1029/JC093iC03p02285>.
- Monaldo, Frank, Christopher Jackson, Xiaofeng Li, and William G Pichel. 2016. "Preliminary Evaluation of Sentinel-1A Wind Speed Retrievals." *IEEE Journal of Selected Topics in Applied Earth Observations and Remote Sensing* 9 (6): 2638–2642.
- Nieto Borge, Jose Carlos, Konstanze Reichert, and Jürgen Dittmer. 1999. "Use of Nautical Radar as a Wave Monitoring Instrument." *Coastal Engineering* 37 (3–4): 331–342.
- Nieto Borge, JoséCarlos, Germán Rodríguez Rodríguez, Katrin Hessner, and Paloma Izquierdo González. 2004. "Inversion of Marine Radar Images for Surface Wave Analysis." *Journal of Atmospheric and Oceanic Technology* 21 (8): 1291–1300.
- Niros, A, T Vihma, and J Launiainen. 2002. "Marine Meteorological Conditions and Air-Sea Exchange Processes over the Northern Baltic Sea in 1990s." *Geophysica* 38 (1–2): 59–87.
- Pascual, Ananda, Yannice Faugère, Gilles Larnicol, and Pierre-Yves Le Traon. 2006. "Improved Description of the Ocean Mesoscale Variability by Combining Four Satellite Altimeters." *Geophysical Research Letters* 33 (2).
- Passaro, Marcello, Luciana Fenoglio-Marc, and Paolo Cipollini. 2015. "Validation of Significant Wave Height From Improved Satellite Altimetry in the German Bight." *IEEE Transactions on Geoscience and Remote Sensing* 53 (4): 2146–2156. <https://doi.org/10.1109/TGRS.2014.2356331>.

- Plant, William J. 1990. "Bragg Scattering of Electromagnetic Waves from the Air/Sea Interface." In *Surface Waves and Fluxes*, 41–108. Springer.
- Plant, William J, and Gordon Farquharson. 2012. "Wave Shadowing and Modulation of Microwave Backscatter from the Ocean." *Journal of Geophysical Research: Oceans* 117 (C8).
- Plant, William J, and William C Keller. 1990. "Evidence of Bragg Scattering in Microwave Doppler Spectra of Sea Return." *Journal of Geophysical Research: Oceans* 95 (C9): 16299–16310.
- Pleskachevsky, A, S Jacobsen, B Tings, and E Schwarz. 2019. "Estimation of Sea State from Sentinel-1 Synthetic Aperture Radar Imagery for Maritime Situation Awareness." *International Journal of Remote Sensing*: 1–39. <https://doi.org/10.1080/01431161.2018.1558377>.
- Pleskachevsky, A L, S Lehner, and W Rosenthal. 2012. "Storm Observations by Remote Sensing and Influences of Gustiness on Ocean Waves and on Generation of Rogue Waves." *Ocean Dynamics* 62 (9): 1335–1351.
- Pleskachevsky, A L, W Rosenthal, and S Lehner. 2016. "Meteo-Marine Parameters for Highly Variable Environment in Coastal Regions from Satellite Radar Images." *ISPRS Journal of Photogrammetry and Remote Sensing* 119: 464–484.
- Pujol, Marie-Isabelle, Yannice Faugère, Guillaume Taburet, Stéphanie Dupuy, Camille Pelloquin, Michael Ablain, and Nicolas Picot. 2016. "DUACS DT2014: The New Multi-Mission Altimeter Data Set Reprocessed over 20 Years." *Ocean Science* 12 (5).
- Raudsepp, U, J Laanemets, G Haran, V Alari, J Pavelson, and T Kõuts. 2011. "Flow, Waves and Water Exchange in the Suur Strait, Gulf of Riga, in 2008." *Oceanologia* 53 (1): 35–56.
- Ray, Richard D, and B D Beckley. 2003. "Simultaneous Ocean Wave Measurements by the Jason and Topex Satellites, with Buoy and Model Comparisons Special Issue: Jason-1 Calibration/Validation." *Marine Geodesy* 26 (3–4): 367–382.
- Reichert, K. 1994. "Untersuchung Zur Azimuthalen Abhängigkeit Der Abbildung von Seegang Mit Dem Achiffsradar." University of Hamburg.
- Ren, Yongzheng, Susanne Lehner, Stephan Bruschi, Xiaoming Li, and Mingxia He. 2012. "An Algorithm for the Retrieval of Sea Surface Wind Fields Using X-Band TerraSAR-X Data." *International Journal of Remote Sensing* 33 (23): 7310–7336.
- Ressel, R, S Singha, S Lehner, A Rösel, and G Spreen. 2016. "Investigation into Different Polarimetric Features for Sea Ice Classification Using X-Band Synthetic Aperture Radar." *IEEE Journal of Selected Topics in Applied Earth Observations and Remote Sensing* 9 (7): 3131–3143.
- Ressel, Rudolf, Anja Frost, and Susanne Lehner. 2015. "A Neural Network-Based Classification for Sea Ice Types on X-Band SAR Images." *IEEE Journal of Selected Topics in Applied Earth Observations and Remote Sensing* 8 (7): 3672–3680.
- Schulz-Stellenfleth, J, T König, and S Lehner. 2007. "An Empirical Approach for the Retrieval of Integral Ocean Wave Parameters from Synthetic Aperture Radar Data." *Journal of Geophysical Research: Oceans* 112 (C3): C03019.
- Schulz-Stellenfleth, J, S Lehner, and D Hoja. 2005. "A Parametric Scheme for the Retrieval of Two-Dimensional Ocean Wave Spectra from Synthetic Aperture Radar Look Cross Spectra." *Journal of Geophysical Research: Oceans* 110 (C5): C05004.
- Schulz-Stellenfleth, Johannes. 2004. "Ocean Wave Measurements Using Complex Synthetic Aperture Radar Data." University of Hamburg.

- Schwarz, Egbert, Detmar Krause, Matthias Berg, Holger Daedelow, and Holger Maass. 2015. "Near Real Time Applications for Maritime Situational Awareness." *The International Archives of Photogrammetry, Remote Sensing and Spatial Information Sciences* 40 (7): 999–1003.
- Senet, Christian M, Joerg Seemann, Stylianos Flampouris, and Friedwart Ziemer. 2008. "Determination of Bathymetric and Current Maps by the Method DiSC Based on the Analysis of Nautical X-Band Radar Image Sequences of the Sea Surface (November 2007)." *IEEE Transactions on Geoscience and Remote Sensing* 46 (8): 2267–2279.
- Senet, Christian M, Jörg Seemann, and Friedwart Ziemer. 2001. "The Near-Surface Current Velocity Determined from Image Sequences of the Sea Surface." *IEEE Transactions on Geoscience and Remote Sensing* 39 (3): 492–505.
- Sepulveda, Hector Hito, Pierre Queffeuilou, and Fabrice Ardhuin. 2015. "Assessment of SARAL/AltiKa Wave Height Measurements Relative to Buoy, Jason-2, and Cryosat-2 Data." *Marine Geodesy* 38 (sup1): 449–465. <https://doi.org/10.1080/01490419.2014.1000470>.
- Singha, Suman, Domenico Velotto, and Susanne Lehner. 2015. "Dual-Polarimetric Feature Extraction and Evaluation for Oil Spill Detection: A near Real Time Perspective." In *Geoscience and Remote Sensing Symposium (IGARSS), 2015 IEEE International*, 3235–3238. IEEE.
- Singha, Suman, Michele Vespe, and Olaf Trieschmann. 2013. "Automatic Synthetic Aperture Radar Based Oil Spill Detection and Performance Estimation via a Semi-Automatic Operational Service Benchmark." *Marine Pollution Bulletin* 73 (1): 199–209.
- Soomere, T, and A Räämet. 2011. "Spatial Patterns of the Wave Climate in the Baltic Proper and the Gulf of Finland." *Oceanologia* 53 (null): 335–371.
- Soomere, Tarmo. 2005. "Wind Wave Statistics in Tallinn Bay." *Boreal Env. Res* 10 (2): 103–118.
- Stoffelen, Ad, and David Anderson. 1997. "Scatterometer Data Interpretation: Estimation and Validation of the Transfer Function CMOD4." *Journal of Geophysical Research: Oceans* 102 (C3): 5767–5780.
- Suursaar, Ü, J Jaagus, and T Kullas. 2006. "Past and Future Changes in Sea Level near the Estonian Coast in Relation to Changes in Wind Climate." *Boreal Environment Research* 11 (2): 123–142.
- Suursaar, U, Tiit Kullas, Mikk Otsmann, I Saaremaa, Juta Kuik, and Merike Merilain. 2006. "Cyclone Gudrun in January 2005 and Modelling Its Hydrodynamic Consequences in the Estonian Coastal Waters." *Boreal Environment Research* 11 (2): 143.
- The WAMDI Group. 1988. "The WAM Model—A Third Generation Ocean Wave Prediction Model." *Journal of Physical Oceanography* 18 (12): 1775–1810.
- Torres, Ramon, Paul Snoeij, Dirk Geudtner, David Bibby, Malcolm Davidson, Evert Attema, Pierre Potin, et al. 2012. "GMES Sentinel-1 Mission." *Remote Sensing of Environment* 120: 9–24. <https://doi.org/10.1016/j.rse.2011.05.028>.
- Tuomi, Laura, Kimmo K Kahma, and Heidi Pettersson. 2011. "Wave Hindcast Statistics in the Seasonally Ice-Covered Baltic Sea." *Boreal Environment Research* 16 (6): 451–472.
- Tuomi, Laura, Olga Vähä-Piikkiö, and Victor Alari. 2017. "Baltic Sea Wave Analysis and Forecasting Product BALTICSEA_ANALYSIS_FORECAST_WAV_003_010: Issue 1.0." <http://marine.copernicus.eu/documents/QUID/CMEMS-BAL-QUID-003-010.pdf>.

- Vachon, Paris W, Harald E Krogstad, and J Scott Paterson. 1994. "Airborne and Spaceborne Synthetic Aperture Radar Observations of Ocean Waves." *Atmosphere-Ocean* 32 (1): 83–112.
- Velotto, D, C Bentes, B Tings, and S Lehner. 2016. "First Comparison of Sentinel-1 and TerraSAR-X Data in the Framework of Maritime Targets Detection: South Italy Case." *IEEE Journal of Oceanic Engineering* 41 (4): 993–1006.
- Vicen-Bueno, Raul, Jochen Horstmann, Eric Terril, Tony de Paolo, and Jens Dannenberg. 2013. "Real-Time Ocean Wind Vector Retrieval from Marine Radar Image Sequences Acquired at Grazing Angle." *Journal of Atmospheric and Oceanic Technology* 30 (1): 127–139. <https://journals.ametsoc.org/doi/pdf/10.1175/JTECH-D-12-00027.1>.
- Vicen-Bueno, Raúl, Cristina Lido-Muela, and José Carlos Nieto-Borge. 2012. "Estimate of Significant Wave Height from Non-Coherent Marine Radar Images by Multilayer Perceptrons." *EURASIP Journal on Advances in Signal Processing* 2012 (1): 84. <https://doi.org/10.1186/1687-6180-2012-84>.
- Vignudelli, S, P Cipollini, Laurent Roblou, Florent Lyard, G P Gasparini, G Manzella, and M Astraldi. 2005. "Improved Satellite Altimetry in Coastal Systems: Case Study of the Corsica Channel (Mediterranean Sea)." *Geophysical Research Letters* 32 (7).
- "WaMoS II: Wave and Surface Current Monitoring System Operating Manual Version 4.0." 2012. OceanWaves GmbH: Luneburg, Germany. 2012. <http://oceanwaves.org>.
- Wei, Yanbo, Zhizhong Lu, Gen Pian, and Hong Liu. 2017. "Wave Height Estimation from Shadowing Based on the Acquired X-Band Marine Radar Images in Coastal Area." *Remote Sensing* 9 (8): 859.
- Wetzel, L B. 1990. "Sea Clutter." In *Radar Handbook 2nd Ed.*, edited by M Skolnik. New York: McGraw-Hill.

Acknowledgements

First and foremost, I would like to thank my supervisor Rivo Uiboupin for guiding and supporting me throughout my master's and PhD studies. I am grateful towards all my colleagues in the Department of Marine Systems at TUT, especially Tarmo Kõuts, Urmas Lips, Kaimo Vahter and Siim Pärt for their cooperation in providing *in situ* measurements. Special thanks go to Victor Alari for providing wave model products and highly adequate information concerning sea state modelling.

My biggest gratitude goes towards Andrey Pleskachevsky for being a mentor and co-supervisor for me in the subject of deriving meteo-marine parameters from radar imagery. I would also like to thank the rest of the DLR's SAR Oceanography group in Bremen, Germany for their warm welcome and the highly qualified knowledge shared by them in various SAR-related subjects. Special thanks to the DLR ground station Neustrelitz team for continuous cooperation and organization of the NRT services.

I am thankful to Aarne Männik, Madis-Jaak Lilover, Jaan Laanemets and Victor Alari for reviewing the thesis and providing helpful comments.

I am also thankful to Age, Polina and Silvie, as well as Mari-Liis, Mariliis, Kristel, Kati, Ilja, Kai, Oliver, Stella, Irina from our "coffee club" for...the love of Life! Thank you Laura for inviting me here in the first place.

Lastly, I cannot forget to express my deepest gratitude to my friends and family who have tolerated my egoism in pursuing the PhD degree.

I also thank the ESA for making Sentinel constellation data freely available. Special thanks to the Finnish Meteorological Institute, Swedish Meteorological and Hydrological Institute, Estonian Environmental Agency, and Latvian Environment, Geology and Meteorology Centre that have open data policy for wind and wave measurement data.

The thesis was supported by the European Regional Development Fund which financed the stay in DLR's SAR Oceanography group. The thesis was also supported by institutional research funding IUT (19-6), by Personal Research Funding PUT1378 of the Estonian Ministry of Education and Research, by the European Regional Development Fund and through CMEMS Copernicus grant WAVE2NEMO. Furthermore, the thesis was supported by the Estonian Science Foundation grant no. ETF8968 and by EUROSTARS program no. F12002. Lastly, coastal radar data was made available with the help of BONUS INNO project call2012inno-24 HARDCORE: "Harnessing coastal radars for environmental monitoring purposes".

Abstract

Radar Remote Sensing of Meteo-Marine Parameters in the Baltic Sea

Radar remote sensing data, which is independent of daylight and weather conditions, can provide valuable information on ocean wind and wave conditions. The moving targets, such as waves, can be defocused and shifted in radar images. This causes difficulties for accurate estimation of the total significant wave height in case of short windsea waves with strong local orbital velocities and wave breaking.

In the current study, data from different radar systems were used to adjust, validate and develop the algorithms for estimating wave parameters in the Baltic Sea where short and steep wind waves dominate. The developed wave height retrieval algorithms were implemented on the data originating from X- and C- band Synthetic Aperture Radar - SAR (TerraSAR-X/TanDEM-X and Sentinel-1 A/B), as well as from coastal marine radar. The total significant wave height was retrieved with empirical algorithms XWACE_C and CWAVE_S1-IW from TerraSAR-X/TanDEM-X and Sentinel-1 SAR data, correspondingly. The used methods are based on the spectral analysis of radar subscenes, Grey Level Co-occurrence Matrix (GLCM) image statistics, as well as on local wind information.

An additional term was incorporated into the XWAVE_C model function to improve the minimal windsea significant wave height retrieval by applying JONSWAP wave spectra. A second term to compensate spectral distortions triggered by windsea waves moving in SAR flight direction was also introduced in the algorithm. Compared to the original XWAVE_C, the improvements increased the accuracy of the algorithm by 5% in terms of correlation coefficient r while root mean square error (RMSE) was reduced by 20% between SAR-derived and measured wave heights. The JONSWAP parametrization was also implemented into German Aerospace Center's (DLR) near-real time operational SAR data processing service running in Neusterlitz ground station.

Different SAR-based wave height products were compared with collocated *in situ* data from available sea state measurements stations. The comparison showed good agreement with the correlation coefficient of 0.88 and RMSE less than 0.4 m. The spatial variability of wave heights on SAR-derived fields was compared with WAM and SWAN wave model results. The spatial comparison relying on Sentinel-1A/B scenes in varying sea state conditions resulted in r of 0.86 and RMSE of 0.33 m. The wind speed estimated from SAR images also showed good agreement with *in situ* data (r over 0.90 and RMSE less than 2.1 m s^{-1}).

A new empirical wave retrieval algorithm for X-band marine radar data was developed for the short steep windsea dominating in the Tallinn Bay. The method is based on the image spectrum parameters and GLCM statistics of the radar signal intensity. The validation results showed that wave height retrievals of the proposed algorithm for marine radar have similar accuracy in space and time ($r=0.86$; RMSE = 0.25 m) as the SAR counterparts. The significant wave height field over Tallinn bay area derived from marine radar data also showed a similar spatial pattern as previous modelling studies in comparable storm conditions.

The thesis also demonstrates that the sea state retrievals from radar data provide valuable information for operational and statistical monitoring of wave conditions in the Baltic Sea. The radar-derived sea state results provide additional information on spatial variability of the wave field in the coastal zone compared to *in situ* measurements, altimetry wave products and model forecast.

Lühikokkuvõte

Laine- ja tuuleväljade määramine Läänemeres radarkaugseire andmetest

Ilmastikutingimustest ja päevavalgusest sõltumatud radarkaugseire andmed võivad anda väärtuslikku teavet lainetuse ja meretuule olude kohta. Samas võivad liikuvad sihtmärgid, nagu näiteks lained, jääda radari pildile defokusseeritult või olla nihkunud oma reaalsest asukohast. See põhjustab raskusi kogu olulise lainekõrguse (tuulelaine ja ummiklaine) hindamisel, eriti kui on tegemist lühikese ja järsu tuulelainega, millel on suur lokaalne orbitaalkiirus ja esineb laine murdumine.

Doktoritöö käigus kasutati erinevate radarsüsteemide andmeid selleks, et edasi arendada ja valideerida empiirilisi algoritme laineparameetrite hindamiseks Läänemeres, kus domineerib lühike ja järsk tuulelainetus. Väljatöötatud lainekõrguse arvutamise meetodeid rakendati X- ja C-laineala tehisava radari (SAR) andmetele (vastavalt satelliitidel TerraSAR-X/TanDEM-X ja Sentinel-1 A/B), aga ka kaldaradari andmetele. Kogu oluline lainekõrgus leiti empiiriliste algoritmidega XWAVE_C ja CWAVE_S1-IW vastavalt TerraSAR-X/TanDEM-X ja Sentinel-1 A/B SAR andmetest. Kasutatud meetodid põhinevad radari alampildi spektraalanalüüsil, hall-tasemete esinemise maatriksi (GLCM) statistikal ning alampildilt arvatud tuule kiiruse tulemustel.

Doktoritöö käigus arendati edasi empiirilist algoritmi XWAVE_C. Algoritmi lisati täiendav liige tuulelaine minimaalse lainekõrguse täpsemaks hindamiseks kasutades JONSWAP eksperimendist määratud küllastunud laine spektrit. Samuti lisati algoritmi tingimus, mis kompenseerib spektraalseid moonutusi juhtudel, kui laine levimise suund ühtib satelliidi lennusuunaga. Võrreldes algse XWAVE_C algoritmiga paranes lainekõrguse hindamise täpsus: mõõdetud ja arvatud lainekõrguse korrelatsioon paranes 5% ja ruutkeskmise vea (RMSE) väärtus vähenes 20%. Töö praktilise väljundina rakendati JONSWAP lainespektril tuginev edasiarendus ka Saksamaa kosmosekeskuse (Neustrelitzi maajaama) SAR andmetel põhinevasse operatiivsesse lainetuse seire teenusesse.

SAR andmetest arvatud olulisi lainekõrgusi võrreldi olemasolevate *in situ* mõõtmistega. Võrdlus näitas head kokkulangevust – korrelatsioonikordaja $r = 0.88$ ja RMSE oli väiksem kui 0.4 m nii satelliidi TerraSAR-X/TanDEM-X, kui ka Sentinel-1 A/B jaoks. Laineparameetrite ruumiline võrdlus viidi läbi WAM ja SWAN lainemudeli tulemuste põhjal. Näiteks, olulise lainekõrguse võrdlus WAM mudeli ja Sentinel-1 A/B SAR andmete vahel erinevates lainetuse tingimustes andis r väärtuseks 0.86 ning RMSE väärtuseks 0.33 m. SAR piltide põhjal arvatud tuule kiirus oli samuti heas vastavuses *in situ* mõõdetud andmetega ($r > 0.9$, $RMSE < 2.1 \text{ m s}^{-1}$).

Tallinna lahte katva kaldaradari andmekogumi jaoks arendati uus empiiriline algoritm, mis põhinedes samuti alampildi spektraalanalüüsil ja GLCM statistikal hindab kogu olulist lainekõrgust nii ruumis kui ajas. Saadud empiirilise algoritmi valideerimine *in situ* mõõtmistega näitas head kokkulangevust ($r = 0.86$, $RMSE = 0.25 \text{ m}$), mis on võrreldav SAR andmetöötluse algoritmide täpsusega. Kaldaradari andmetest saadud lainekõrguse väli näitas varasemate uuringutega lähedasi ruumilisi mustreid sarnastes tormitingimustes.

Doktoritöö tulemused näitasid, et laine- ja tuuleväljade arvutamine radariandmetest kasutades empiirilisi meetodeid, võimaldab Läänemere lainetuse ja meretuule operatiivset jälgimist ja ajalise muutlikkuse statistilist analüüsi. Radari andmetest arvatud lainekõrguse ja tuulekiiruse väljad annavad täiendavat informatsiooni mereseisundi ruumilise muutlikkuse kohta võrreldes *in situ* punktmõõtmiste, satelliitaltimeetri andmete või lainemudeli prognoosiga.

Appendix

Publication I

Rikka, S., Pleskachevsky, A., Uiboupin, R. and Jacobsen, S. (2018). Sea state in the Baltic Sea from space-borne high-resolution synthetic aperture radar imagery. *International Journal of Remote Sensing*, 39(4), pp. 1256–1284.



Sea state in the Baltic Sea from space-borne high-resolution synthetic aperture radar imagery

Sander Rikka^a, Andrey Pleskachevsky^b, Rivo Uiboupin^a and Sven Jacobsen^b

^aDepartment of Marine Systems, Tallinn University of Technology, Tallinn, Estonia; ^bRemote Sensing Technology Institute, German Aerospace Center (DLR), Bremen, Germany

ABSTRACT

In this work, remote sensing synthetic aperture radar (SAR) data from X-band TerraSAR-X and TanDEM-X (TS-X and TD-X) satellites have been used to adapt the algorithms for estimating sea state parameters in the specific condition of the Baltic Sea with archipelago islands and where short steep sea state dominates. Since the moving targets can be defocused and shifted in SAR images, sea state consisting of short windsea waves with strong local orbital velocities and wave breaking needs additional effort for accurate estimation of the total significant wave height that consists of swell and windsea parts. The XWAVE_C algorithm, developed for the North Sea, where the long swell waves coming from the Atlantic Ocean are present during storms, was further enhanced for the short steep windsea which dominates under ordinary storm conditions in the Baltics. For the empirical XWAVE_C model function, based on the spectral analysis of subscenes as well as on local wind information, an additional term was incorporated for assessment the minimal windsea significant wave height by applying JONSWAP wave spectra. A term to compensate spectral distortions triggered by windsea waves moving in SAR flight direction has also been introduced. In total, 95 TS-X/TD-X StripMap scenes between 2012 and 2017 were acquired in Eastern Baltic Sea, processed and analysed. The wave height results from SAR images were compared with collocated *in situ* data from 11 available buoys. The analysed data include both high and low windsea conditions. The comparison of SAR-derived wave heights with measured wave heights shows high agreement with a correlation coefficient r of 0.88. The wind speed, estimated from SAR images, was compared to measurements from 14 collocated *in situ* stations, yielding a high agreement with an r value of 0.90. This article is focused on the algorithm developments; however, it is also the first study of sea state retrieval in the Baltic Sea using high-resolution satellite-based techniques. The results show the local variability in the wave fields connected to atmospheric features. The observed local wave height can increase by 1–2 m in kilometre-size cells that are accompanied by wind gusts. The developed algorithms are installed in the German Aerospace Center's (DLR) ground station Neustrelitz and can also be used in near-real-time.

ARTICLE HISTORY

Received 13 April 2017
Accepted 23 October 2017

1. Introduction

In the article at hand, a new methodology for spatial observation of meteo-marine parameters in the Baltic Sea is presented based on the newest remote sensing techniques which are realized in near-real-time (NRT) services for oceanographic applications. In the first place, the article deals with synthetic aperture radar (SAR) algorithm improvements and is addressed to potential users of remote sensing data such as meteorological service organizations.

The specific sea state conditions in the Baltic Sea and its SAR imaging were investigated, and existing algorithms were enhanced by validation with *in situ* measurements and wave model results. Sea state and wind fields are simultaneously derived from high-resolution satellite radar images acquired by TerraSAR-X (TS-X) and TanDEM-X (TD-X) satellites (Figure 1).

1.1. Overview

SAR is an active remote sensing instrument providing two-dimensional (2D) information of the normalized radar cross section (NRCS) σ_0 that represents the property of a surface to reflect the radar signal. The backscatter is governed by the surface roughness on the scale of the radar wavelength. In the case of a sea surface with long sloping swell waves, the radar return echo is dominated by the so-called Bragg scattering of short ripple capillary waves in the dimension of centimetres which are produced by wind stress to the sea surface under low and moderate wind conditions (e.g. Schulz-Stellenfleth 2004).

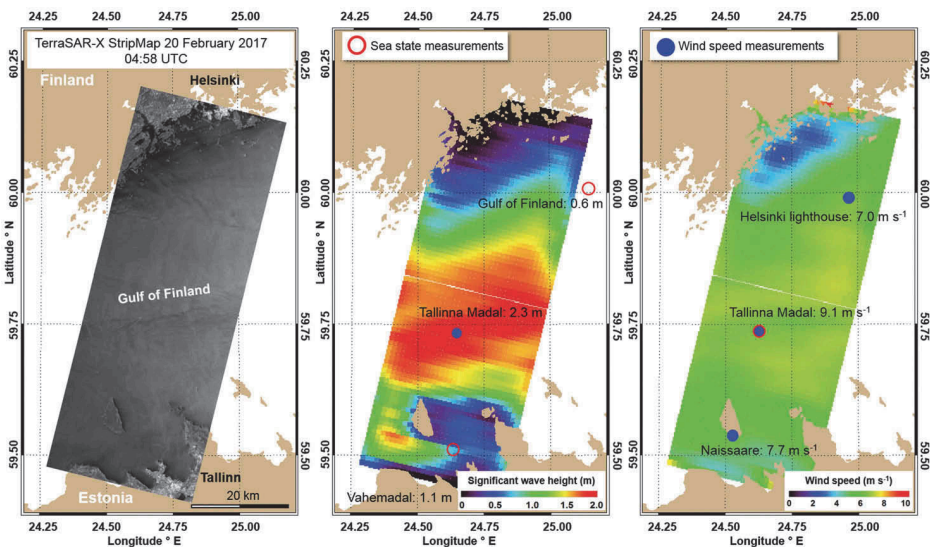


Figure 1. Meteo-marine parameters (total significant wave height H_5 and surface wind speed U_{10}) processed with $1\text{ km} \times 1\text{ km}$ posting using sea state processor (SSP) with the empirical XWAVE_C algorithm from satellite TS-X StripMap scene acquired over the Gulf of Finland of the Baltic Sea on 20 February 2017 at 04:58 UTC. Local wind speed is estimated for the same subscenes analysed. SSP is implemented into near-real-time processing chain at the German Aerospace Center (DLR) ground station Neustrelitz.

Under strong wind conditions, a series of additional backscattering takes place, e.g. wave breaking, or the individual wind waves are steep enough to produce direct reflections.

Because of the independence of daylight and weather, and with global high-resolution coverage, remote sensing data acquired by SAR are a unique source of 2D information on ocean surface for the open sea and coastal applications (Lehner et al. 2008; Li, Lehner, and Rosenthal 2010). Due to the rapid development of the satellite technology, processing methods, software realization and infrastructures in recent years, a variety of oceanographic and other maritime information is available in NRT (Schwarz et al. 2015). The NRT processed data can be transferred to organizations such as weather services, e.g. for validation of forecast models, only a few minutes after data acquisition. The various kinds of parallel processed data, for instance, significant wave height, surface wind speed, ice coverage, oil spills, etc., can be combined to increase the level of maritime situation awareness and serve coastal protection or deeper interdisciplinary geophysical investigations.

Since the launch of L-band SAR on-board Seasat in 1978, the mechanisms of SAR ocean surface imaging, and the extraction of wave and wind parameters have been investigated (Beal, Tilley, and Monaldo 1983; Masuko et al. 1986). The short operation period of Seasat SAR of 106 days was later followed by other well-known missions: European Radar Satellites ERS-1 and ERS-2, Envisat Advanced SAR (ASAR), up to recent high-resolution SAR satellites, e.g. TS-X and TD-X, COSMO-SkyMed, and Sentinel-1A/B. Parallel to satellite technology innovations, different inversion algorithms have been developed to estimate the oceanographic parameters and ocean wave spectra from SAR imagery (Beal, Tilley, and Monaldo 1983; Hasselmann and Hasselmann 1991; Hasselmann et al. 1996; Schulz-Stellenfleth, Lehner, and Hoja 2005).

The first generation original inversion method of Hasselmann and Hasselmann (1991) was based on a maximum likelihood matching of the first guess (prior) information available from a wave model and the data provided by the SAR wave image spectrum. From the first guess wave spectrum, the forward transform is applied to compute the associated SAR wave image spectrum. It is undisputed that second-generation retrievals, which use the complex information of the image cross spectra to remove the directional propagation ambiguity, are inherently superior to first generation retrievals using only SAR image variance spectra (Li, Lehner, and Rosenthal 2010). Empirical algorithms were considered to retrieve integral wave parameters for C-band SAR data (Schulz-Stellenfleth, König, and Lehner 2007) which were used for the ERS missions. This approach was further extended for using SAR data acquired by the Envisat without using *a priori* information (Li, Lehner, and He 2008).

Traditionally, for the estimation of sea state parameters from SAR images, the approach of fast Fourier transformation (FFT) is used, converting a subscene into an image spectrum. The following operations can be divided into two groups:

- Functions for transformation of the image spectra into wave spectra with a subsequent estimation of the integrated wave parameters (e.g. Alpers, Ross, and Rufenach 1981; Hasselmann and Hasselmann 1991; Hasselmann et al. 1996; Lyzenga 2002).
- Direct estimation of the parameters from the image spectrum without transformation with empirical functions deduced from large sets of representative data (e.g.

Schulz-Stellenfleth, König, and Lehner 2007; Li, Lehner, and Bruns 2011; Bruck 2015; Pleskachevsky, Rosenthal, and Lehner 2016).

The first type of methods is suitable for estimations of long swell wave's spectra, and its output can be assimilated into spectral wave models. The understanding of the non-linear SAR imaging of the moving sea surface waves plays a key role there and is incorporated in 'transfer functions' (Alpers, Ross, and Rufenach 1981). Moreover, this approach requires acquisitions with clearly visible wave-looking patterns without artefacts which are found by applying the homogeneity test. Furthermore, the azimuth travelling (in SAR flight direction) ocean waves should be longer than the so-called cut-off length (about 80 m for TS-X). Otherwise, the waves are substantially distorted and are not visible in the SAR images and thus are not represented in the image spectra. For example, the short windsea waves are typically imaged in TS-X as image noise with hardly recognizable wave pattern which cannot be transferred into wave spectra. Practically, especially in coastal areas where several natural effects, man-made objects and structures such as sand banks, wave breaking zones, ships and current boundaries are present in SAR images, only about 30% of the acquired images can be used for spectral transformation (Pleskachevsky, Rosenthal, and Lehner 2016). Although combination of two different algorithms (e.g. Shao, Li, and Sun 2015) could be used to overcome limitations, 'pure' empirical functions are more suitable for the short windsea waves and noisy images. The direct and robust estimation of parameters from subscene spectra with this approach allows fast, straightforward and trustworthy NRT processing of satellite scene tiles for all images while excluding about 0.5% of the data. Outliers occur for subscenes with strong local non-sea-state signal 'seeping' through filtering and checking procedures. Such a signal can be produced, for example, by amplified radar return from multiple reflections of ships or offshore constructions or from many ships in roadstead that modify the local statistics distribution.

The algorithms and functions to estimate significant wave height from TS-X and TD-X imagery have undergone a significant evolution in recent years. The first versions of XWAVE methods were developed for open ocean applications (Bruck and Lehner 2010; Lehner, Pleskachevsky, and Bruck 2012; Bruck and Lehner 2013). The latest version, XWAVE_C (C = coastal), is tuned specifically for coastal applications and has an accuracy of decimetres for H_s . The algorithm can recognize and remove the influence of non-sea state induced signals such as dry sandbars as well as non-linear SAR image distortions produced by, e.g., short wind waves and breaking waves. XWAVE_C is implemented into the sea sate processor (SSP) for fully automatic processing for NRT services in the German Aerospace Center's (DLR) ground station network (Schwarz et al. 2015; Pleskachevsky, Rosenthal, and Lehner 2016). The wind field estimation algorithm XMOD-2 works in parallel in SSP. XMOD-2, developed for TS-X and TD-X high-resolution data, is a non-linear geophysical model function (GMF) and an enhancement of previous X-Bands GMFs, e.g. by distinguishing between upwind and downwind properties of the sea surface backscatter (Li and Lehner 2014). The XMOD-2 is also realized in part of NRT processing chain in ground station Neustrelitz.

Many studies in the Baltic Sea using SAR data have been carried out on ice detection and classification (Berg, Dammert, and Eriksson 2015; Karvonen 2015; Laanemäe,

Uiboupin, and Rikka 2016), wind field parameters (Hasager et al. 2011) or other ocean surface characteristics (Karimova and Gade 2016; Rikka, Uiboupin, and Alari 2017). The current work focuses on the wave height estimation from TS-X and TD-X imagery in the Eastern Baltic Sea which is a largely unresearched area using SAR methods.

Up to now, the sea state in this area has not been investigated by space-borne radar equipment. The present study is the first investigation of the sea state in the Baltic Sea using an adoption of the high-resolution satellite-based technique. On SAR imagery, the short windsea either produces image clutter or is barely visible while being affected by strong non-linear distortions due to the defocusing effects of SAR processing (Pleskachevsky, Rosenthal, and Lehner 2016).

1.2. Specific of the sea meteo-marine conditions in Baltic Sea and SAR

The Baltic Sea, disconnected from open ocean waves, lies in temperate latitudes and therefore is primarily affected by the westerly airflow. In consequence, the wind blows approximately 50% of the time from South, South-West or West at the coastal stations of Western Estonia (Jaagus and Kull 2011). The predominant wind direction at the Baltic Sea sub-basins, on the other hand, has a quite uniform spatial distribution (Karagali et al. 2014) since the scale of weather patterns is usually much larger compared to the dimensions of a sub-basin. In the Gulf of Finland, for example, the wind mainly blows from South-West (Launiainen and Laurila 1984), while the prevailing direction is South in the Gulf of Bothnia (Tuomi, Kahma, and Pettersson 2011). The wind direction under storm conditions (winds with sustained speed over 15 m s^{-1}) usually is between 180° and 360° due to the movement of cyclones (Jönsson, Broman, and Rahm 2003).

The Eastern Baltic Sea, a partially tideless and semi-enclosed sea with the absence of prominent long swell waves and with a short memory time of the wave field (Soomere and Räämet 2011), is a challenging location to validate methods to estimate sea state parameters. The present study is the first investigation of the sea state in the Baltic Sea using high-resolution satellite-based techniques. A complex coastline, shallow areas with mean water depth of about 50 m, Archipelago Sea with thousands of islands and the significant wave height remaining mostly in the domain of 0–2 m (and rarely exceeds 4 m), produce complex wave and wind field conditions (Leppäranta and Myrberg 2009; Raudsepp et al. 2011; Tuomi, Kahma, and Pettersson 2011).

Prominent swell waves longer than 200 m and distinct amplitude (wave height over 5 m) are rarely registered in the Baltic Sea. However, the numerous islands cause developed swell waves seen in wind shadowing areas with the wavelength in order up to 100 m. The refracted swell systems also produce cross seas behind the islands. Figure 2 shows an example for refraction and cross sea in Tallinn Bay for the TS-X acquisition presented in Figure 1. In comparison to the wind waves with stronger wave orbital motion, the swell waves with the same amplitude are characterized by weaker orbital motion. The non-linear distortions of such waves are smaller, their SAR imaging is more stable and the refraction of swell waves with the peak wavelength L_p around 80 m (where L denotes to wavelength and P to peak) can be well observed and measured, although the amplitude of these waves is only about 20–30 cm.

The main feature in the Gulf of Finland, in comparison to, e.g. the North Sea, is the general lack of the swell contribution into total wave height, which can be considered as

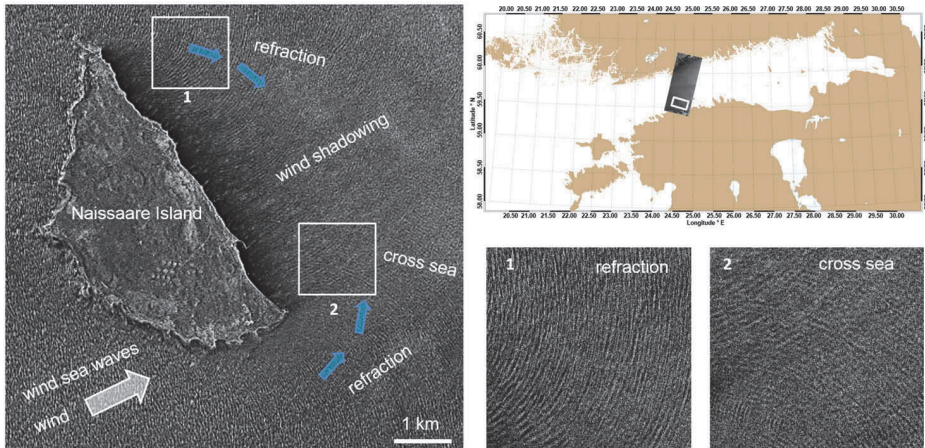


Figure 2. An example of wave refraction and cross sea near Naissaare Island in the Tallinn Bay acquired by TS-X on 20 February 2017 at 04:58 UTC (see Figure 1). The averaged wavelength of swell is about 80 m.

the square root of both squared windsea and swell amplitudes. Generally, in a case of n wave systems, total significant wave height can be defined as:

$$H_s = \sqrt{\sum_{i=1}^n H_{S,i}^2} \quad (1)$$

where the first system $n = 1$ can be assigned to swell with $H_{S,1}$ and second component $n = 2$ assigned to windsea wave height with $H_{S,2}$.

Another feature is the presence of numerous rocks, banks and islands influencing the local sea state via wave breaking, shadowing effects and the generation of cross-sea. All these contribute to complications in SAR imaging and its interpretation. The previous studies have shown that long swell waves with wavelengths > 100 m and with long wave crests are well imaged by TS-X, while the short wind waves are strongly smoothed, defocused and are hardly distinguishable in noisy SAR images (Pleskachevsky, Rosenthal, and Lehner 2016). Since swell waves result in a pronounced peak in the image spectrum, their contribution to total wave height amplitude can be accurately considered. Whereas the input of windsea is mostly based on noise analysis. Windsea wave crests are short and present a significant number of small, nonstable, fast and erratically moving targets for a SAR sensor. Such sea state is typically imaged as noise and is hardly recognized as a wave pattern. A strong windsea contribution to the total wave height is therefore equivalent to more substantial uncertainties by SAR imaging and needs additional effort. For example, the Doppler shift D_y (displacement in azimuth direction y) of a target moving with a radial velocity corresponding to a projected line-of-sight velocity of $\mathbf{u}_r = 1 \text{ m s}^{-1}$ towards the sensor flying with a platform velocity \mathbf{V}_{SAR} (7 km s^{-1} for TS-X) at distance R (514 km for TS-X), calculated as $D_y = (\mathbf{u}_r / \mathbf{V}_{\text{SAR}})R$ (Lyzenga et al. 1985), results in D_y of 88 m for an incidence angle of 35° .

The effect of the SAR imaging mechanisms of the moving sea surface, dependent on the local orbital wave velocities, is called ‘velocity bunching’ and is described in the literature, e.g., by Hasselmann et al. (1985). Consequently, the original wave pattern can hardly be seen on the resulting SAR image since moving wave-facets and crests are shifted to a non-real position. This means that the Doppler shift can differ strongly for the same total wave height and different sea state components. For example, for the total $H_S = 3$ m with, e.g., 25% contribution of the swell amplitude and 75% contribution of the windsea, the maximal possible orbital speed (according to linear wave theory, see Appendix 2) produced by both swell and windsea components is $u_{\max} \approx 1.90$ m s⁻¹ which results in maximal velocity bunching D_y of 180 m for an average incidence angle $\theta = 35^\circ$. The same total H_S consisting of only swell and not including windsea waves results in $u_{\max} \approx 0.70$ m s⁻¹ with maximal velocity bunching D_y of 60 m (Svendsen and Jonsson 1976; Appendix 2). The first case is most relevant for the Gulf of Finland, where the Doppler shift plays a primary role in storm conditions. This means stronger distortions in SAR images are found here in comparison to the sea state in the German Bight of the North Sea (the region for XWAVE_C tuning), where the swell component is stronger during the storms due to the open boundary with the North Atlantic. Therefore, to achieve a comparable accuracy of the SAR-based sea state information for the same total wave height value in the Gulf of Finland, a series of validations with the XWAVE_C algorithms have been carried out.

Figure 3 presents a series of typical SAR subscenes taken in the Gulf of Finland for different sea state conditions with wave heights of approximately 0.5, 1.5 and 3 m. For $H_S \approx 0.5$ m (no swell, windsea only), the waves are not imaged as structured brightness modulations but as image clutter. The strongest waves are imaged as

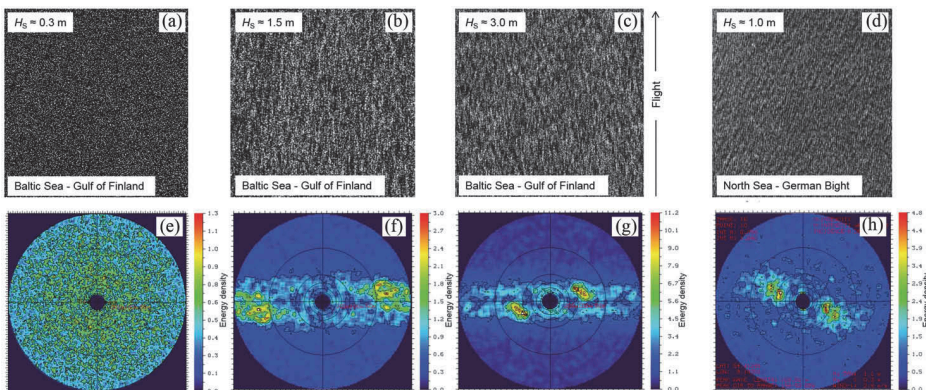


Figure 3. An example of the synthetic aperture radar (SAR) subscenes ((a), (b), (c)) and image spectrums ((e), (f), (g)) for different sea state conditions in the Gulf of Finland (three typical situations for approximately wave height of 0.5 m (a), 1.5 m (b) and 3 m (c)). Many short wave crests, which are fast and chaotically moving targets, are not imaged individually by SAR in original shape, but jointly produce a clutter in the SAR image and smoothed structures in sensor flight direction. For comparison, a typical acquisition in German Bight of the North Sea is given in (d). A stronger swell component is clearly visible in (h).

smoothed structures in sensor flight direction. For comparison, a typical subscene for the North Sea is given.

1.3. Objective

The current study focuses on the improvement of the wave height estimation from TS-X and TD-X imagery in the Eastern Baltic Sea, based on specifics in the Gulf of Finland, Gulf of Riga and Northern Baltic Proper, using the empirical algorithm XWAVE_C and SSP (Pleskachevsky, Rosenthal, and Lehner 2016). The processor includes the algorithm and series of operations such as data calibration and filtering artefacts, necessary for model function implementation and control of results. XWAVE approach was adopted and repeatedly validated for the short sea state dominant in the Gulf of Finland. Simulating WAVes Nearshore (SWAN) spectral wave model data were used for spatial collocations.

In a first step, the existing algorithm was applied to estimate the first guess wave height and to determine the sources of inaccuracies and outliers for collocated TS-X and measurement pairs. All available and acquired TS-X scenes were pre-processed; the spectral and GLCM parameters (Haralick and Shanmugam 1973) were collected and extracted for collocated points.

In the second step, the connections of errors were identified and explained. The correction was elaborated for selected parameters and tuned by RMSE minimizing (the pairwise differences between the two data sets were analysed: TS-X estimated data (1) and model/measurement data (2), related to location and time).

2. Satellite and data used

2.1. SAR data

For the presented study, German X-band SAR data from TS-X and TD-X satellites are used to estimate meteo-marine parameters. TS-X and TD-X are twin satellites operating from a 514 km height in a sun-synchronous orbit with a wavelength of 31 mm and a frequency of 9.6 GHz (Breit et al. 2010). The revisit cycle of the satellites is 11 days. However, the same region can be imaged more frequent at different incidence angles θ , which vary between 20° and 55°. The TS-X sensor has several imaging modes with different swath widths, scene lengths and resolutions (Eineder et al. 2008). For sea state analysis, the StripMap mode with 3 m resolution (1.25 m pixel) is most suitable as it provides a reasonable balance between spatial resolution and coverage.

For the current work, a total of 95 TS-X and TD-X Multi-Look Ground Range Detected (MGD) StripMap products were analysed. They were acquired in the Eastern Baltic Sea in 2013–2017 over buoy locations and coastal areas in both HH and VV polarizations. The data were provided by DLR via the EOWEB® interface. An individual StripMap image with the pixel spacing of 1.25 m covers approximately 30 km × 50 km; yet, the length of the covered area can be extended by ordering sequential images.

The calibrated NRCS σ_0 is first processed from the pixel digital number DN:

$$\sigma_0 = (\text{DN})^2 k_s \sin(\theta), \quad (2)$$

where k_s is the calibration factor given in the product and θ is local incidence angle of the radar signal. SAR image analysis is based on FFT of subscenes which result in image spectra. Before analysis, each pixel value $\sigma_0(x, y)$ of the subscene is normalized:

$$\sigma_0 = \frac{\sigma_0(x, y) - \sigma_0}{\sigma_0}, \quad (3)$$

where σ_0 is the mean value of σ_0 in the subscene. A standard FFT window of 1024×1024 pixels covers an area of $1280 \text{ m} \times 1280 \text{ m}$ for spatially enhanced TS-X StripMap images. In the study, both VV and HH polarization images are used, ordered especially for this study and acquired by other TS-X users in the Baltic Sea. The transition of HH images, mostly acquired for ship detection purposes, into VV is necessary for wind estimation (see Section 3.1.1).

A direct application of the empirical model function to a subscene often leads to inaccuracies in H_s with outliers in the range of metres (Pleskachevsky, Rosenthal, and Lehner 2016). The sources of these errors are in the first place many natural and man-made artefacts, for instance, ships, large wind farm constructions or natural effects such as current boundaries, wind streaks and atmospheric fronts. Even internal wave structures can impact the image spectra. Such spectral perturbations result in an integrated value which yields a contribution to the total energy not connected to the sea state. Filtering of such artefacts was implemented in SSP for TS-X imagery. After the statistics for a subscene are calculated, the subscene is additionally analysed with $100 \text{ m} \times 100 \text{ m}$ (optional) sliding window. The statistics of each window σ_0^{win} is compared with σ_0 of the subscene. In a case of $\sigma_0^{\text{win}} > q_{\text{ship}} \sigma_0$ with tuned q_{ship} value of 2.3 (for $100 \text{ m} \times 100 \text{ m}$ window), the outliers in the current window are replaced with the mean value of the subscene σ_0 .

2.2. In situ measurements

Figure 4 shows an overview of measurement station in Eastern Baltic Sea available and used in the current study. For sea state measurements, three different types of equipment were available:

- acoustic Doppler current profiler (ADCP) near the Hanko peninsula,
- wave rider buoys (four stations),
- pressure sensors (six stations).

In total, data from 11 measurement stations were collected which resulted in 117 collocation pairs between measured significant wave height and SAR-based wave height.

Wind measurements were obtained from 14 measurement stations which resulted in 102 collocation pairs. Wind measurement data are provided by the Finnish Meteorological Institute for four locations (Utö, Hanko, Helsinki lighthouse and Kalbådagrund). Data from Dirhami, Kihnu, Kunda, Naissaare, Osmussaare, Ristna, Sörve, Vaindloo and Vilsandi stations are provided by the Estonian Environmental Agency (KAUR), and data from Tallinna Madal (Tallinn Shallows) station are provided by the Department of Marine Systems at Tallinn University of Technology (MSI at TUT).

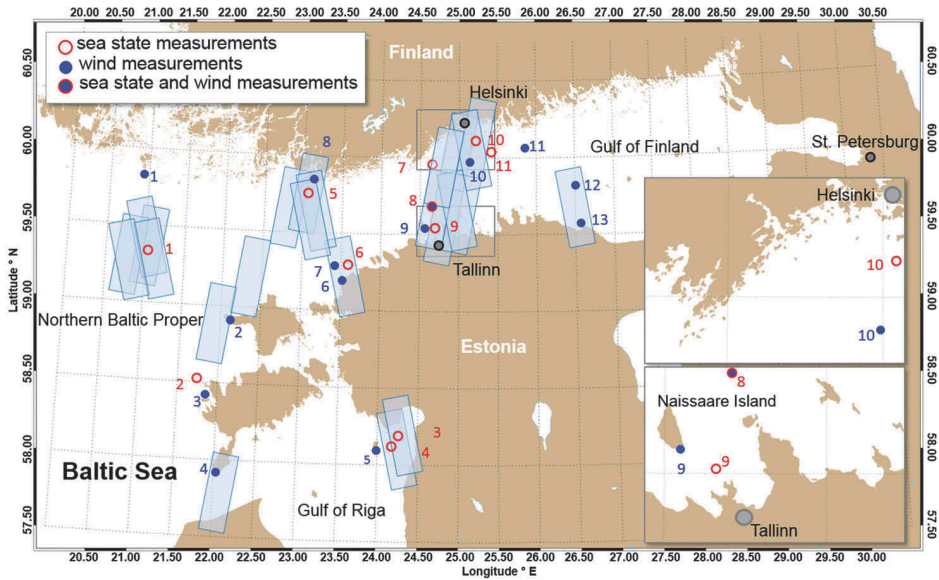


Figure 4. Eastern Baltic Sea, measurement stations and TS-X acquisitions. The zoom over Tallinn and Helsinki shows complications of coastal line. For the station's descriptions, see Table 1.

Table 1. Measurement stations.

No.	Station	Lon (° E)	Lat (° N)	Sensor type	Data collected
Wave measurements					
1	NBP	20.9960	59.2500	Waverider	$H_s/T_p/\gamma_p$
2	Vilsandi	21.6356	58.4886	Waverider	$H_s/T_p/\gamma_p$
3	Liivi Anderaa	24.1844	58.1065	Pressure	H_s/T_p
4	Liivi LM-2	24.1255	58.0860	Pressure	H_s/T_p
5	Hanko	23.1010	59.9650	Acoustic Doppler current profiler	$H_s/T_{mean}/\gamma_{mean}$
6	Neugrundi	23.5191	59.3451	Pressure	H_s/T_{mean}
7	Hästgrund	24.2085	59.9128	Pressure	H_s
8	Tallinna Madal-1	24.7320	59.7120	Pressure	$H_s/T_{mean}/\gamma_{mean}/W_s/W_{dir}/W_{gust}$
8	Tallinna Madal-2	24.7250	59.7028	Waverider	$H_s/T_p/\gamma_p$
9	Vahemadal	24.6662	59.5102	Pressure	$H_s/T_{mean}/\gamma_{mean}$
10	Länsi-tonnttu	25.1288	60.0817	Pressure	H_s
11	GoF	25.2350	59.9650	Waverider	$H_s/T_p/\gamma_p$
Wind measurements					
1	Utö	21.3731	59.7806	N/A	$W_s/W_{dir}/W_{gust}$
2	Ristna	22.0664	58.9208	WMT-52/WAV151	$W_s/W_{dir}/W_{gust}$
3	Vilsandi	21.8142	58.3828	WMT-52/WAV151	$W_s/W_{dir}/W_{gust}$
4	Sörve	22.0581	57.9136	WMT-52/WAV151	$W_s/W_{dir}/W_{gust}$
5	Kihnu	23.9703	58.0986	WMT-52/WAV151	$W_s/W_{dir}/W_{gust}$
6	Dirhami	23.5006	59.2114	WMT-52/WAV151	$W_s/W_{dir}/W_{gust}$
7	Osmussaare	23.3606	59.3039	WMT-52/WAV151	$W_s/W_{dir}/W_{gust}$
8	Hanko	22.9125	59.8086	N/A	$W_s/W_{dir}/W_{gust}$
9	Naissaare	24.5633	59.5408	WMT-52/WAV151	$W_s/W_{dir}/W_{gust}$
10	Helsinki lighthouse	24.9247	59.9494	N/A	$W_s/W_{dir}/W_{gust}$
11	Kalbädaggrund	25.6011	59.9908	N/A	$W_s/W_{dir}/W_{gust}$
12	Vaindloo	26.3611	59.8169	WMT-52/WAV151	$W_s/W_{dir}/W_{gust}$
13	Kunda	26.5414	59.5214	WMT-52/WAV151	$W_s/W_{dir}/W_{gust}$

H_s : Significant wave height; T_p : peak period; γ_p : peak propagation direction; T_{mean} : average period; γ_{mean} : average propagation direction; W_s : wind speed; W_{dir} : wind direction; W_{gust} : wind gusts speed.

3. Meteo-marine parameters from TerraSAR-X high-resolution data

This section deals with theoretical aspects and enhancements of the algorithm for sea state estimation in the Baltic Sea

3.1. Approach of meteo-marine estimation from TerraSAR-X imagery

3.1.1. Surface wind

Sea state is strongly dependent on local wind input which the TS-X can provide by analysing the same subscene used for wave height estimations by measuring the roughness of the sea surface (Li and Lehner 2014). The non-linear algorithm XMOD-2 has been developed for TS-X data that takes into account the full non-linear physical model function. The SAR wind field retrieval approach was first developed for C-band SAR provided by, for example, ERS-2 and Envisat ASAR. The empirically derived GMFs related the local wind conditions and sensor geometry to radar cross section values (e.g. CMOD4 or CMOD5). The relationship between X-band radar cross section, wind speed and direction, and incidence angle in XMOD-2 is given as:

$$\sigma_0(U, \theta, \phi) = B_0^p(U_{10}, \theta)(1 + B_1(U_{10}, \theta) \cos(\phi) + B_2(U_{10}, \theta) \cos(2\phi)), \quad (4)$$

where σ_0 is NRCS, U_{10} is the wind speed and ϕ is the relative wind direction. p is a constant with a value of 0.625. XMOD-2 is applicable for an incidence angle θ between 20° and 60° and wind speeds from 2 to 25 m s^{-1} . The parameter functions B_i , where $i = 0 \dots 2$, are tuned using the measurement data sets (Li and Lehner 2014). To determine wind direction, streak structures on the sea surface of the image are used. These are produced by turbulent airflow eddies at boundary layer (Etling and Brown 1993; Sikora and Ufermann 2004). Shadows behind the coast also give evidence of wind blowing from the coast.

Initially, the wave and wind algorithms were intended for VV polarization. However, for the NRT services, scenes in HH polarization are mostly acquired. Therefore, the conversion from NRCS acquired in HH σ_0^{HH} to σ_0^{VV} is necessary. The polarization ratio (PR), found to perform best for TS-X data, is based on an exponential PR function with coefficients of $X_0 = 0.61$ and $X_1 = 0.02$ (Masuko et al. 1986; Li and Lehner 2014; Shao et al. 2014):

$$\text{PR} = \frac{\sigma_0^{\text{VV}}}{\sigma_0^{\text{HH}}} = X_0 \exp(X_1 \theta), \quad (5)$$

where \exp denotes exponent. The difference in the imaging of sea state in HH and VV polarizations appears especially for the short and steep waves resulting in stronger non-linear effects. Defocusing streak structures appear with image spectra peaks at $k \approx 0.30$ (wavelength around 20 m). Another difference is the higher radar echo from ships in comparison to the wave signal (signal-to-noise ratio) in HH polarization, which 'jams' the wave signals in the image spectra. The ship pre-filtering procedure eliminates this error in most cases.

3.1.2. Sea state algorithm

An empirical function XWAVE_C uses the approach of a direct estimation of integrated sea state parameters from SAR image spectra without transformation into wave spectra.

This method was chosen because of the need for robust and rapid data processing which does not involve sophisticated and long mathematical iterations for the spectral transformation. Empirical algorithm XWAVE_C, developed for coastal areas, is based on the analysis of image spectra and was tuned according to collocated buoy data and coastal wave model results (Pleskachevsky, Rosenthal, and Lehner 2016).

To obtain integrated wave parameters, FFT operation is applied to the radiometrically calibrated subscene. Image power spectrum $IS(k_x, k_y)$ is calculated by integration over 2D wavenumber domain – k_x and k_y , where y marks satellite flight direction and $k^{\max} = \pi / \text{subscene_size}$:

$$E_{IS} = \int_{k_x^{\min}}^{k_x^{\max}} \int_{k_y^{\min}}^{k_y^{\max}} (IS)(k_x, k_y) dk_x dk_y = \int_{f_{\min}}^{f_{\max}} \int_0^{2\pi} (IS_{\theta})(f, \theta_{IS}) d\theta_{IS} df \quad (6)$$

The integration of $IS_{\theta}(f, \theta_{IS})$ is also parallel carried out, where $IS_{\theta}(f, \theta_{IS}) = IS(k_x, k_y) J$ indicates the transferring of image spectra IS from the 2D wavenumber domain k_x, k_y into the frequency-direction domain using the Jacobian term J . Differences between both calculations amount to about 1% of E_{IS} value due to numerical diffusion. The transfer was needed to compare the TS-X spectra with the measurements and to model wave spectra which are traditionally stored in the frequency-directional domain. The integration over wavenumber domain is limited by $k_{\max} = 0.02$ and $k_{\min} = 0.2$ which correspond to $L_{\max} = 600$ m and $L_{\min} = 30$ m, where wavenumber $k = \sqrt{k_x^2 + k_y^2}$.

The resulting XWAVE_C function for coastal application for the calculation of the total significant wave height can be presented by the equation:

$$H_S^{XWAVE_C} = a_1 \sqrt{B_1 E_{IS} \tan(\theta)} + a_2 B_2 + a_3 B_3 + a_4 B_4 + a_5 B_5, \quad (7)$$

where θ is local incidence angle of the radar beam, a_1 – a_5 are coefficients and B_1 – B_5 are functions of spectral parameters. The parameters $a_3 B_3, a_4 B_4, a_5 B_5$ are designed to remove the influence of non-sea state produced signals, such as dry sandbars as well as non-linear SAR image distortions produced by, e.g., short wind waves and breaking waves. B_1 represents noise scaling of the total energy E_{IS} (short wind waves and their breakings produce an additional noise that influences resulting energy, $B_1 = x_0 R^{\text{in/out}}$ with x_0 tuned using collocated buoy data). The ratio $R^{\text{in/out}} = N_{\text{in}}^S / N_{\text{out}}^S$ indicates the character of non-linearity of the imaging mechanism with spectrum noise N_{in}^S in domain inside of the so-called azimuthal cut-off wavenumber and spectrum noise N_{out}^S outside of the so-called azimuthal cut-off wavenumber (Appendix 1).

In the Baltic Sea, where the strong short windsea waves are dominating, their non-linear imaging and breaking produce prominent noise which makes B_1 more important. In the significant wave height estimation process, the term $a_2 B_2$ considers local wind speed from subscene. Full information about XWAVE_C algorithm can be seen in Pleskachevsky, Rosenthal, and Lehner (2016).

3.2. Improving the sea state algorithm for coastal areas: tuning and parameters used

The XWAVE_C algorithm was tuned and successfully applied in coastal waters of German Bight in the North Sea. When applied to short and steep sea state in the Eastern Baltic Sea, where the swell part of the total wave height is lower than that in German Bight, an additional effort was made to reach the initial accuracy and improve it. After closer inspection of all acquired data (collocated *in situ* point measurements and spatial wave model), the improvements were undertaken considering the non-linearity in SAR imaging of the windsea. A two source of underestimations was found and incorporated into the model function as additional corrections:

- underestimation of the windsea waves in areas with weak wind up to 8 m s^{-1} with noisy SAR images with hardly visible wave-like looking patterns (section 3.2.1.);
- strong wind $> 12 \text{ m s}^{-1}$ (transition into wave breaking regime) in SAR-flight direction undergo different imaging mechanism (section 3.2.2; Appendix 2).

3.2.1. Improvement by JONSWAP spectra

By comparison with *in situ* collocated data set, a series of underestimations of about 15% was found to be connected to the insufficiency in the sea state signal in the coastal areas with wind shadowing. However, the wind speed estimated in those coastal areas from the same TS-X scenes presents the values highly correlated to *in situ* measurements. The local wind speed estimated from subscenes was then used to calculate the JONSWAP spectra to adjust the local wave height. The minimum wave height was estimated and implemented as a filter into the model function.

The JONSWAP (JOint North Sea WAve observation Project) spectrum is the wave spectrum of a fully developed sea (Hasselmann et al. 1973; Hasselmann, Dunckel, and Ewing 1980). In the frequency domain, the distribution of wave energy among different wave frequencies $E_W(f)$ can be expressed as:

$$E_W(f) = \alpha g^2 (2\pi)^{-4} f^{-5} \exp\left(-\frac{5}{4} \left(\frac{f}{f_m}\right)^{-4}\right) \gamma^{\exp\left(-\frac{(f-f_m)^2}{2\sigma^2 f_m^2}\right)}, \quad (8)$$

where α is Phillips curve with fetch F (effective distance over which the wind blows with constant velocity):

$$\alpha = 0.76 \left(\frac{U_{10}^2}{Fg}\right)^{0.22}. \quad (9)$$

For the random cases, the averaged parameters can be applied with peak enhancement factor $\gamma = 3.3$ and the frequency at the maximum of the spectrum f_m .

$$f_m = 22 \left(\frac{g^2}{U_{10}F}\right)^{1/3}, \quad (10)$$

where $\sigma = 0.07$ for $f \leq f_m$, otherwise $\sigma = 0.09$. For calculation of the integrated wave energy $E_W = \int E_W(f) df$, the input of wind speed U_{10} and fetch F is required. The wind speed is

available from the analysed subscene (XMOD-2); for the fetch, a relatively low random value of 10 km was taken. The areas where XWAVE_C underestimates wave height (described above) are typically located in wind shadow areas ($0 \text{ m s}^{-1} < U_{10} < \approx 8 \text{ m s}^{-1}$). For the longer fetch, the sea state is already developed, and its SAR imaging allows correct estimates for the wave height; thus, those areas remain unaffected. This correction alters around 15% of the collocated points in the data set, but it affects many areas of the complicated topography of the Gulf of Finland. Using input from the XMOD-2 algorithm, JONSWAP spectrum is calculated to extract the minimum value for significant wave height which is applied to XWAVE_C estimated wave height: $H_s^{\min} = 4\sqrt{E_w}$.

3.2.2. Improvements for strong wind conditions

The comparison between measurement data and wave height estimated by original XWAVE_C (Pleskachevsky, Rosenthal, and Lehner 2016) shows H_s underestimation for waves in the range of about 1.5–5.0 m for the strong winds $U_{10} > \approx 12\text{--}14 \text{ m s}^{-1}$ with wind direction close to satellite flight direction. This can be explained by the interaction of two effects:

- the turbulent area in the front of the breaking wave crest produces an additional strong radar echo;
- the breaking waves have highly non-linear shape with the steep angle in the wave front, gentler slant in falling part and visibly lower angle in crest axes. It means the direct reflection takes place, and the non-linear smearing structures resulting from such waves to overlay the image of the real waves. Therefore, the peak maximum is smaller, the integrated energy is weaker and the underestimation occurs (Appendix 2).

For the cases where the difference between wind direction (windsea wave moving direction) and SAR platform ground track line is less than 20° , the correction was applied to XWAVE_C GMF function.

The correction was applied as an additional term for Eq. 7 by introducing the term $a_6 B_6$ for adjusting the wave amplitude lost by the impact of non-linear structures in the SAR image: $B_6 = E_{400}/E_{80}$ with a_6 tuned using local wave field variance. The corrections improve the results by about 6% for the collocated points but affect large areas in spatial consideration, for more information, see Sections 4.1 and 4.2.

3.2.3. Correction for wind speed

It was found that for series of collocation for the wind speed over 12 m s^{-1} derived with the XMOD-2 algorithm, an underestimation in the range $2\text{--}6 \text{ m s}^{-1}$ was also directly connected with the wind (and windsea waves) direction. This can be explained by differences in imaging of windsea waves travelling in the different directions (see explanation before). The XMOD-2 function, developed first for C-Band sensors such as Envisat-ASAR, does not resolve such fine-scale (in order of metre) effects. The wind speed is derived from mean NRCS value of the subscenes without the input of information on kind of sea state and its imaging. Therefore, the lost information can be returned from SAR-imaged sea state using local GLCM variance. This process has the same

background as underestimation of the wave height (see above), thus both corrections are applied for narrow wind-flight angles in domain $0\text{--}20^\circ$ and strong sea state with variance exceeding the mean variance of the data set. The applied correction can be represented by $\Delta U_{10} = \beta_{\text{wind}} R^{\text{in/out}}$ with constant β_{wind} with units of m s^{-1} . For the wind speed below 5 m s^{-1} , the sign of the correction can also be negative (overestimation) and is connected to the local variance of the subscene. The correction improves the results by about 12%, for more information, see [Sections 4.1 and 4.2](#).

4. Results and test cases

In this section, the statistical results of the collocated measurements are presented, and the improvements in spatial distributions of estimated sea state were considered. The test cases for different weather conditions are shown.

4.1. Statistics

The total significant wave height H_5 and wind speed U_{10} derived from SAR are used for comparisons with collocated *in situ* measured data (the description of the measurements, see [Table 1](#)). The TS-X/TD-X scenes were processed with $3 \text{ km} \times 3 \text{ km}$ posting with approximately 150 subscenes per StripMap image. The collocations were done with a time window of ± 20 min for comparison with wave model data and ± 20 min for buoys (the buoys recording time periods are inconsistent). For the spatial collocation, the closest SAR-subscenes are used with a mean value between subscene centre and measurement equipment location 0.7 km. In case the buoy is outside the image, the data up to 10 km were incorporated.

For the comparisons and tuning the root mean square error (RMSE), Pearson correlation coefficient r and Scatter Index (SI) are calculated for each data set. All collocated data are presented in scatterplots for wave height and wind speed.

[Figure 5](#) shows the sea state comparisons for all 117 collocated buoy measurements. The comparison between *in situ* buoy measurements with the mean value of 0.97 m and estimated wave height from TS-X sensor using the XWAVE_C method with all correction procedures discussed above is shown. The reached Pearson correlation coefficient $r = 0.88$, RMSE = 32 cm, SI = 0.33, with the regression slope $m = 0.83$. This is a significant improvement of the accuracy for sea state estimated using original XWAVE_C with $r = 0.85$, RMSE = 0.39 m and SI = 0.40. The advances are mostly visible in coastal areas for the weak wind conditions and over open sea for the strong wind under storm conditions.

[Figure 6](#) shows the collocated *in situ* data comparison with estimated wind speed results from the XMOD-2 algorithm with improvements described in [Section 3.2.3](#). The mean value over all 102 collocations amounts 8.51 m s^{-1} . The Pearson correlation coefficient r of 0.90 was improved against the initial value of 0.77. Other statistical parameters show improvement as well – for RMSE the original value was 2.98 m s^{-1} , whereas after the new developments the RMSE is 2.02 m s^{-1} . The SI value has also seen a significant drop from 0.35 down to 0.23. The slope of the regression line was improved from 0.68 to 0.86.

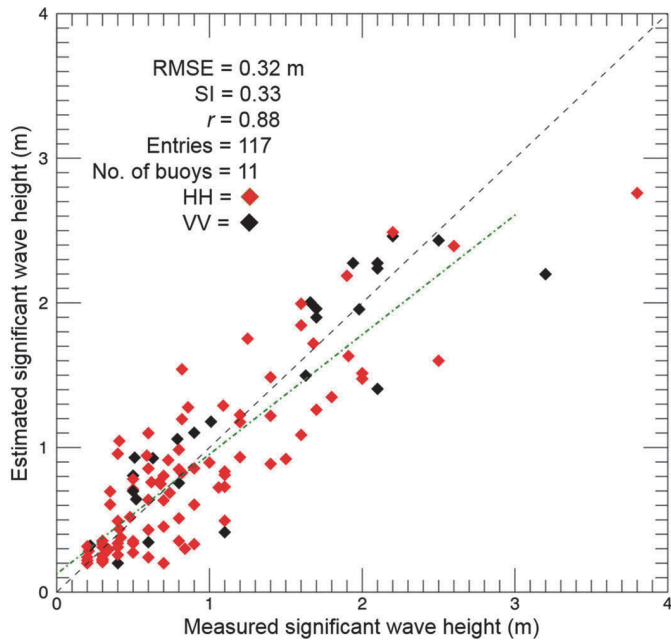


Figure 5. Scatterplot for sea state for available collocated data acquired over Eastern Baltic Sea 2013–2017 including 93 TS-X Scenes (overflights/events/days) with 95 individual StripMap images and 117 buoy collocations. Correlation coefficient for HH polarization is 0.87, RMSE is 0.32 and Scatter Index (SI) is 0.37; for VV polarization, the statistics are 0.90, 0.34 and 0.27 correspondingly.

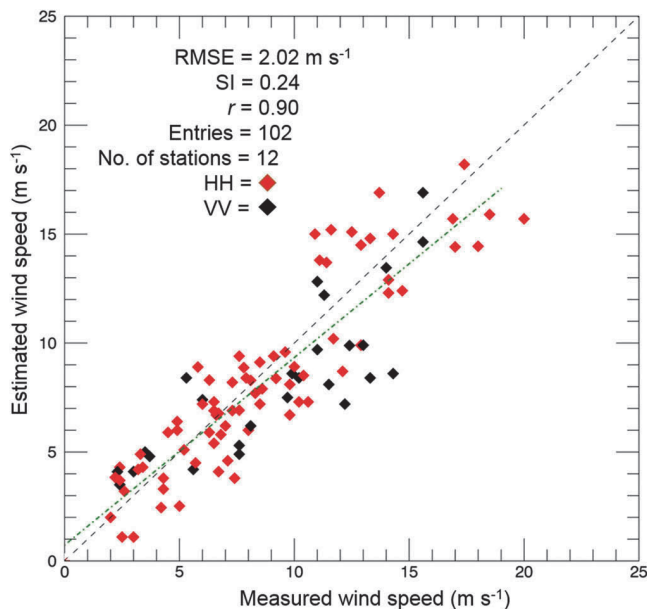


Figure 6. Scatterplot for surface wind speed for all available collocated data acquired over Eastern Baltic Sea 2013–2017 including 93 TS-X scenes (overflights/events/days) with 95 individual StripMap images and 102 collocations. Correlation coefficient for HH polarization is 0.93, RMSE is 1.92 and SI is 0.22; for VV polarization, the statistics are 0.82, 2.52 and 0.27 correspondingly.

4.2. Spatial distribution of meteo-marine parameters

In comparison to *in situ* buoy measurements at a single location, the satellite-borne SAR data allow to cover large areas and estimate the spatial distribution of investigated characteristics. The improvements in model function tuned using collocated point-measurements affect a large area in the space.

Figure 7 shows an example of spatial estimation of meteo-marine parameters from TS-X StripMap scene acquired over the Gulf of Finland on 7 January 2017 at 04:55 UTC under storm conditions. The improvements for significant wave height (first row) and surface wind speed (second row) are presented in the right column.

During the image acquisition time, strong southern wind over 15 m s^{-1} was present which falls right under the satellite ground track, and wind direction condition described previously. Several aspects can be observed by comparing the original XWAVE_C results with significant wave height estimated by including corrections explained in Section 3.

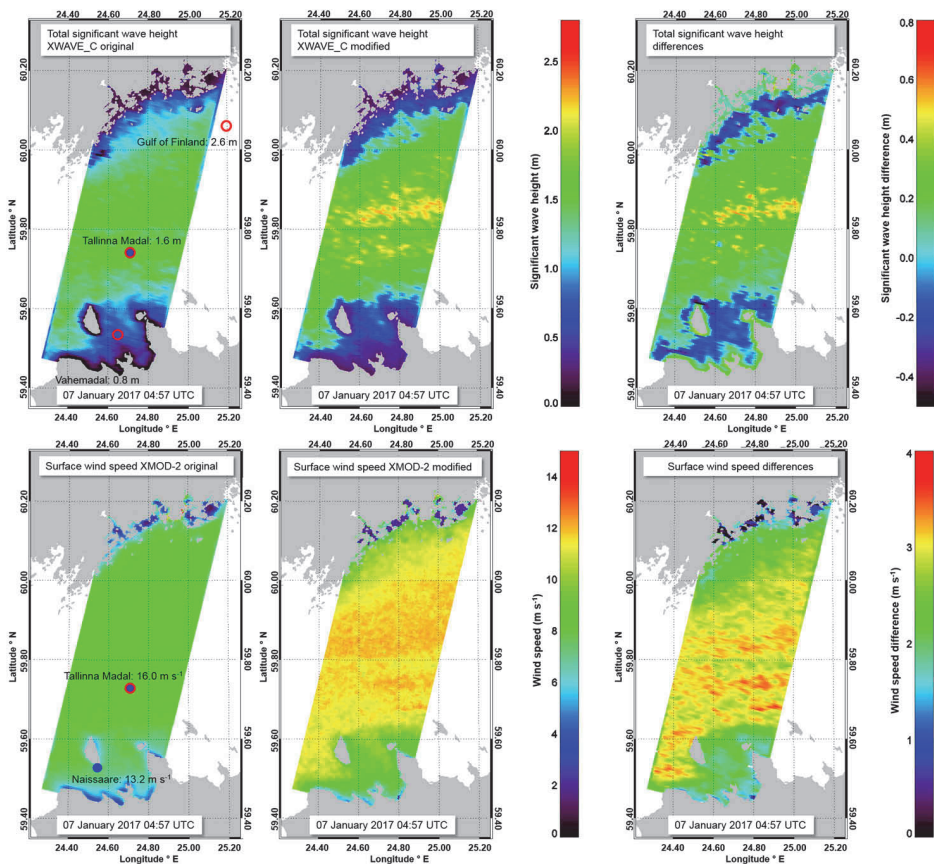


Figure 7. Example for spatial estimation of meteo-marine parameters from TS-X StripMap scene acquired over the Gulf of Finland on 7 January 2017 at 04:55 UTC under storm conditions. The significant wave height (first row) and surface wind speed (second row) estimated by original algorithms (left column), using corrections (middle column) and improvements (right column).

- the derived wave height is increased in the near-coast areas due to JONSWAP-based filter;
- in semi-enclosed areas between mainland and islands the wave height is reduced up to 40 cm;
- over the open part of the Gulf of Finland, where the wind has the strongest impact, and the fetch distance has increased, the wave height (previously underestimated) was elevated up to 1 m. The newly developed wave height correction is supported by the fact that the measured wave height in buoy station N-10 (Gulf of Finland) was 2.6 m, whereas original results were only 1.7 m.

The results also show that the function term a_5B_5 which was developed for the North Sea (switched on in the original version of XWAVE_C only in Wadden coastal areas of the North Sea) also need to be included for estimations in the Baltic Sea. The term a_5B_5 is a correction for overestimations produced by large structures such as sandbanks or ship wakes which have not been pre-filtered. In the case of the Baltic Sea, an abundance of small islands, shallow underwater areas and rocks influence the wave field (e.g. by considerable dissipation) and its SAR-imaging (e.g. wave breaking). These aspects prevent the development and propagation of swell towards the mainland, e.g. near Finnish coast.

From Figure 7 first row, it can be observed that the original estimation misses the impact of small islands near Finnish coast on sea state. After the a_5B_5 parameter was switched on for the Baltic Sea area, the significant wave height was reduced up to about 30 cm in areas corresponds to small island locations according to high-resolution land mask. It presents the dissipation and shadowing effects.

Figure 7 second row shows the wind conditions remain uniform and over the open part of the Gulf of Finland with the average value of about 8 m s^{-1} , whereas with correction, the wind field becomes more variable with easily recognizable gusts structures. The wind speed difference shows the local increase of up to 4 m s^{-1} in the open parts of the Gulf of Finland.

4.3. Test cases storm and examining with wave model results

To evaluate the spatial distribution of estimated characteristics, the SWAN wave model results (SWAN team 2014) are involved. SWAN numerical wave model is a third-generation wave model that uses a 2D equation to describe wave field (Booij, Ris, and Holthuijsen 1999; SWAN team 2014). It can be observed that the TS-X estimated data reproduced spatial patterns including wind dependent growth of the sea state (fetch dependence), shadowing effects by islands, etc. However, wind gusts/eddies and local variations of H_5 connected to local wind effects are not present in the model results. Two side-by-side comparisons are analysed for different situations: calm weather conditions on 3 November and storm on 29 October 2013.

For the current work, SWAN (40.85) was running in an operational mode for the Baltic Sea covering it with one nautical mile grid with the temporal resolution of 1 h. The wave spectrum consisted of 24 equally spaced directions and 32 frequencies distributed logarithmically in the range 0.05–1.00 Hz. ECMWF forcing which had a spatial resolution of $1/12^\circ$ and temporal resolution of 3 hours was used.

4.3.1. Storm weather case 29 October 2013

The storm on 29 October 2013 was developed under wind speeds reaching up to 21.6 m s^{-1} with the south-western direction (Viitak et al. 2016). For the case study, SWAN wave field from 29 October 2013 at 16:00 UTC was selected to set against with TS-X scene acquired at 15:45 UTC. SWAN results are overlaid with wave height field estimated from TS-X scene and are shown in Figure 8. The difference can be observed in the middle of Gulf of Finland, where SAR-derived wave height reflects the local wind effects and is more variable due to wind gusts. In general, wind gusts/eddies and local variations of H_5 are not present in the model results. In numerical wave modelling, the wind gustiness is hidden in the parameterizations of the wind input function, which is usually tuned to the mean value of U_{10} . Thus, the standard input for the wave modelling is a smoothed wind field where the spatial and temporal variability on meso- and local scales wind variability is routinely not included.

4.3.2. Calm weather case 3 November 2013

During calm weather on 3 November 2013, the moderate winds with the mean value of about 4.5 m s^{-1} with the south-western direction were dominating. For the case study, SWAN wave field from 3 November 2013 at 05:00 UTC was examined side by side with TS-X scene acquired at 05:06 UTC. The scene was acquired over Hanko and shows the low surface wind about 2.5 m s^{-1} with smaller areas where wind speed increased up to 7.0 m s^{-1} which causes visibly stronger wave height. Conversely, the model depicts more spatially homogeneous wind and sea state. SWAN results are overlaid with wave height field estimated from TS-X scene and are shown in Figure 9.

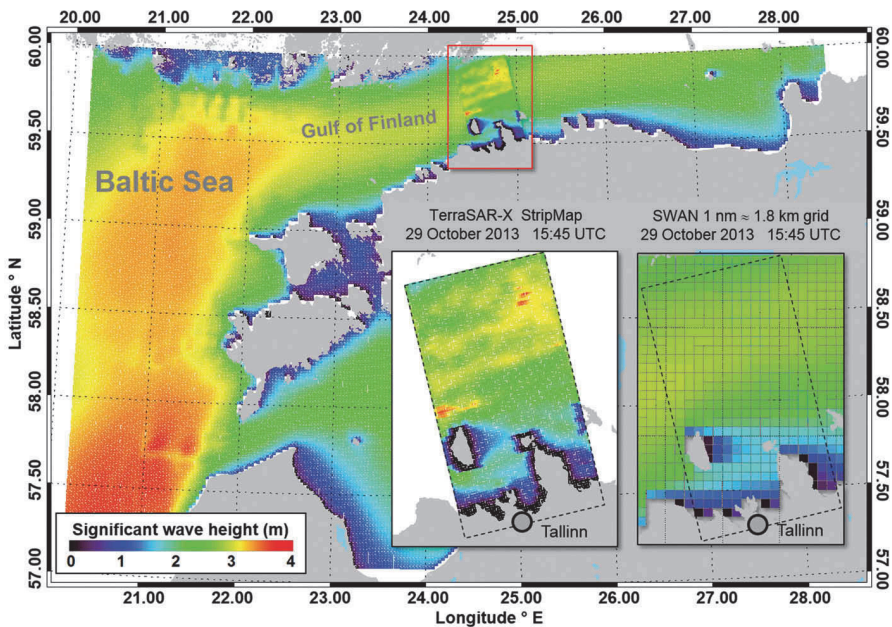


Figure 8. An example of the spatial overlaid of TS-X derived H_5 (1 km raster) over SWAN model results (1 nm \approx 1.8 km) for storm weather conditions. The scene acquired on 29 October 2013 at 15:45 depicts a more spatially unstable sea state than the model.

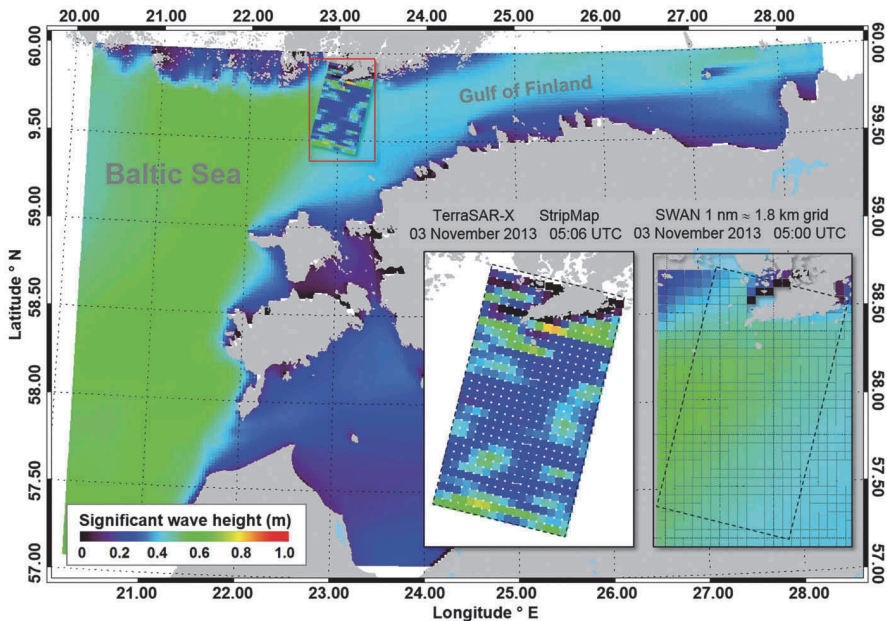


Figure 9. An example of the spatial overlaid of TS-X derived H_s (1 km raster) over SWAN model results (1 nm \approx 1.8 km) for calm weather conditions. The scene was acquired over Hanko on 3 November 2013 at 05:06 UTC. The low surface wind is about 2.5 m s^{-1} with increasing up to 7.0 m s^{-1} in areas with visible stronger wave height. The model results show more spatially uniform wind and sea state.

Table 2. Statistics comparison for sea state between TS-X and SWAN numerical model.

	Storm weather 29 October 2013		Calm weather 3 November 2013	
	TS-X	model	TS-X	model
H_s mean value, (m)	2.52	2.22	0.35	0.43
H_s maximal value, (m)	3.86	2.80	1.12	0.53
H_s SD, (m)	1.19	0.61	0.19	0.08

For both cases, the mean significant wave height shows similar values. However, the local variations in the SAR-derived values present nearly a third increase in local maximal wave height and double the value of the standard deviation (SD) (Table 2).

5. Discussion and conclusion

This section is related to algorithm developments in the first instance. A first assessment of the data gained during algorithm tuning and verification is given. Algorithm technical realization and possibilities are discussed.

5.1. Sea state function

The applicability of XWAVE_C algorithm to derive meteo-marine parameters from X-band high-resolution SAR data was improved by considering the data set of acquisitions over the Baltic Sea which is expressed by specific sea state conditions: generally short and steep windsea waves that play more role in total wave height than in open seas such as the North Sea where the long swell waves from Atlantic are often presented.

Usage of the measurements and wave model results allowed to achieve high accuracy of decimetres for wave height with RMSE = 0.32 m, although the wave structures are rarely visible in TS-X images. Due to the complications of short wave SAR imaging, the wave height is mostly estimated from noisy subscenes. To overcome the complications, a minimum wave height (for the waves completely not visible in the image) estimated from JONSWAP spectra based on local wind speed was introduced. Another important factor for the correction of underestimations of steep windsea breaking waves travelling in SAR flight direction was incorporated.

5.2. On comparisons with *in situ* and model data

In comparison to previous SAR missions, for instance, Envisat-ASAR, more variability of the sea state can be observed in TS-X images, including local wave refraction and dissipation. This abundance of information leads to complications and uncertainties by comparing the estimated parameters with *in situ* data. In fact, a buoy represents the statistics of a relatively small sector of sea state propagating towards the buoy, integrated over time (typically 20 min time series). In contrast, TS-X data represent H_s from subscene statistics of a wider 'frozen' area (snapshot) which include the spatial variability. Figure 10 presents an example for the case where the closest subscene to the

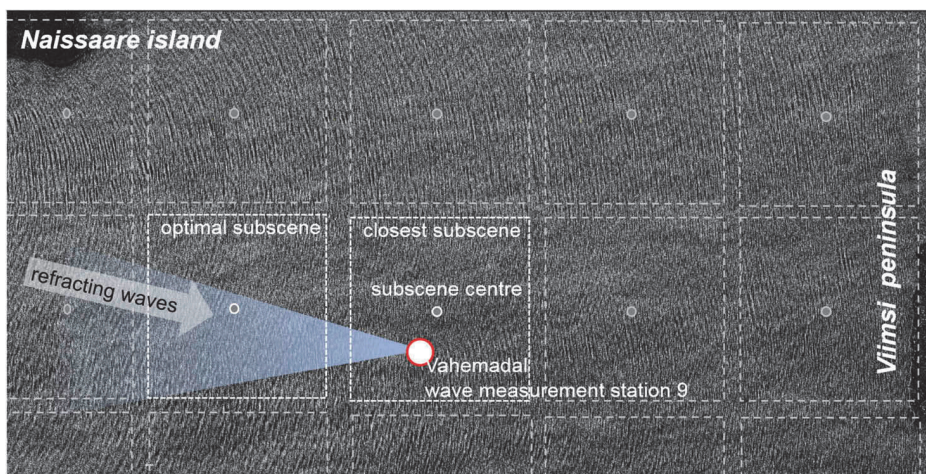


Figure 10. A zoom over measurement station Vahemadal of the TS-X StripMap image presented in Figure 1. The analysed subscenes (dashed lines) with centres (circles) processed with a 3 km step are shown. The sea state around measurement station is quite variable while the sensor measures sea state propagating to the equipment (blue marked area) integrated over time (typical 20 min time series). The subscene with the closest centre is not optimal for comparisons.

measurement equipment is not the optimal for comparisons. The scene (a cut from [Figure 1](#)) is processed in NRT mode with 3 km raster, and the comparisons were made automatically by finding the minimum distance between the subscene centres and the measurement equipment. According to the measured wave period of 5.6 s and measurement integration time, the waves propagating to the sensor are expected from the distance of about 5 km. Although described method could be included into automatic processing, it requires a priori information of both measured wave period and wave direction which are not available in NRT processing and can only be derived for each case individually.

The TS-X high-resolution effect also belongs to the *in situ* wind measurements. The atmospheric measuring stations are located on the shore where various land effects influence the wind. However, two stations – Tallinna Madal and Helsinki lighthouse, located in the open part of the Gulf of Finland – are usually within the TS-X scenes and improve the results significantly.

The comparisons of SAR-derived sea state with wave model also highlight the differences in parameter estimations: the model integrates the wave height over 15 min for a location and presents more spatial uniform sea state. The TS-X data, although presenting temporally ‘frozen’ waves, show more spatial variability as for calm and for storm wind conditions.

Furthermore, the wave models, for example, SWAN used in this study, use wind forcing which might include errors in case of fast moving cyclones and fronts. Moreover, forcing fields are usually given for every 3 hours with much larger spatial resolution compared to TS-X resolution. The large resolution also does not include local fine-scale wind field variations and gusts that are seen on TS-X imagery and which in turn influence wave height values. The example can be seen in [Figures 5 and 6](#) where SAR-derived wave field is much more variable than modelled wave field.

5.3. Local variability of sea state observed in Baltic Sea

The Baltic Sea, in conclusion, is a very complex region for wave height calculations using SAR methods. It is seen from previous studies that SAR methods work accurately on open ocean region where swell waves are the major contributor to the total wave field (Li, Lehner, and He 2008; Lehner et al. 2013; Bruck 2015; Pleskachevsky, Rosenthal, and Lehner 2016). In the Baltics, the wave field is mostly influenced by local wind field and is disturbed by numerous shallow areas, islands and rugged coastline, which allow estimating wave height mostly from noise information.

In total, 95 TS-X/TD-X images acquired over the Baltic Sea were collected and processed during algorithm validation and verification. The processed data are the first assessment of the spatial distribution of meteo-marine parameters and their relationships on a local scale in the Gulf of Finland. The data cover different weather conditions and sea state system combinations. The sea state and wind fields derived from TS-X imagery show strongest local inhomogeneities in wind fields (gusts) that are connected to higher local sea state. The local impact of these gusts on ocean waves can increase significantly if the speed of the gust propagation is close to the speed of the wave groups. Wind energy feeding the same wave group for a longer period causes the growth of individual waves and results in resonance. The earlier

studies using SAR data have already shown that wave groups with abnormal height in the North Sea are connected to atmospheric effects (Pleskachevsky, Lehner, and Rosenthal 2012). It turned out that they are caused by mesoscale wind gusts that are moving as an organized system across the sea and ‘drag’ the continuously growing waves. An identical effect, but on a smaller scale, where the local wave height increases by 1–2 m in kilometre-size clusters, accompanied by wind gusts, can now be observed and investigated in the Baltic Sea using new techniques based on satellite-borne SAR.

5.4. Algorithms and data for practical use and outlook

The developed model functions are included in NRT version of the SSP and can be used operationally at the German DLR ground station ‘Neustrelitz’ (Schwarz et al. 2015; Pleskachevsky, Rosenthal, and Lehner 2016). The processed data can be provided for the validation of forecast wave models during about 20 minutes. For the common users, a file with the data (lon, lat, H_s), the Google Earth file (.kmz) to preview the image file (.jpg) with color-coded wave heights are provided. For the Baltic Sea, the typical TS-X descending overfly is approximately 05:00 UTC and the ascending overfly around 16:00 UTC.

The collected databank of the TS-X scenes acquired over Eastern Baltic Sea consists of about 100 images and can continuously be extended. The reprocessing of the images can be made for estimation of other maritime parameters such as ice coverage classification (Ressel et al. 2016), oil pollution detection (Singha, Velotto, and Lehner 2015), ship detection and classification (Velotto et al. 2016) for a comprehensive interdisciplinary study of interconnection of the processes.

The algorithms are already extended and adopted for Sentinel C-Band IW (Interferometric Wide Swath mode with 10 m pixel resolution) SAR data with an accuracy of RMSE = 80 cm for total significant wave height. The comparison of events imaged by the different sensor at the same time and location become next goals of the investigations.

Acknowledgements

The authors express the gratitude to colleagues T. Kõuts, U. Lips and K. Vahter at Department of Marine Systems at TUT, Estonian Environmental Agency, as well as Finnish Meteorological Institute and Luode Consulting Oy for providing wave and wind measurement data. Special thanks go to V. Alari for providing wave model products and highly adequate information concerning sea state modelling. The authors are grateful to the DLR ground station “Neustrelitz” team for continuous cooperation and organization of the NRT services for the users.

The corresponding author gratefully acknowledges the European Regional Development Fund for financial support for the stay in DLR’s SAR Oceanography group. The author would also like to thank for the warm welcome by the SAR Oceanography group and the exceedingly qualified knowledge shared by them in various SAR-related subjects. Special thanks go to Stefan Wiehle for overlooking the article.

Disclosure statement

No potential conflict of interest was reported by the authors.

Funding

This study was supported by the Estonian Science Foundation grant no. ETF8968 and by EUROSTARS program no. F12002. The study was also supported by institutional research funding IUT (19-6) and PUT1378 of the Estonian Ministry of Education and Research and by the European Regional Development Fund.

References

- Alpers, W., and C. L. Rufenach. 1979. "The Effect of Orbital Motions on Synthetic Aperture Radar Imagery of Ocean Waves." *IEEE Transactions on Antennas and Propagation* 27 (5): 685–690.
- Alpers, W. R., D. B. Ross, and C. L. Rufenach. 1981. "On the Detectability of Ocean Surface Waves by Real and Synthetic Aperture Radar." *Journal of Geophysical Research: Oceans* 86 (C7): 6481–6498.
- Beal, R. C., D. G. Tilley, and F. M. Monaldo. 1983. "Large-And Small-Scale Spatial Evolution of Digitally Processed Ocean Wave Spectra from SEASAT Synthetic Aperture Radar." *Journal of Geophysical Research: Oceans* 88 (C3): 1761–1778.
- Berg, A., P. Dammert, and L. E. Eriksson. 2015. "X-Band Interferometric SAR Observations of Baltic Fast Ice." *IEEE Transactions on Geoscience and Remote Sensing* 53 (3): 1248–1256.
- Booij, N., R. C. Ris, and L. H. Holthuijsen. 1999. "A Third-Generation Wave Model for Coastal Regions: 1. Model Description and Validation." *Journal of Geophysical Research: Oceans* 104 (C4): 7649–7666.
- Breit, H., T. Fritz, U. Bals, M. Lachaise, A. Niedermeier, and M. Vonavka. 2010. "TerraSAR-X SAR Processing and Products." *IEEE Transactions on Geoscience and Remote Sensing* 48 (2): 727–740.
- Bruck, M., 2015. "Sea State measurements using TerraSAR-X/TanDEM-X data". PhD diss., Christian-Albrechts Universität, Kiel.
- Bruck, M., and S. Lehner. 2010. "Extraction of Wave Field from TerraSAR-X Data." *In ESA Special Publication* 679: 5.
- Bruck, M., and S. Lehner. 2013. "Coastal Wave Field Extraction Using TerraSAR-X Data." *Journal of Applied Remote Sensing* 7 (1): 073694–073694.
- Eineder, M., T. Fritz, J. Mittermayer, A. Roth, E. Boerner, and H. Breit, 2008. *TerraSAR-X Ground Segment, Basic Product Specification Document* (No. TX-GS-DD-3302). CLUSTER APPLIED REMOTE SENSING (CAF) OBERPFAFFENHOFEN (GERMANY).
- Etling, D., and R. A. Brown. 1993. "Roll Vortices in the Planetary Boundary Layer: A Review." *Boundary-Layer Meteorology* 65 (3): 215–248.
- Haralick, R. M., and K. Shanmugam. 1973. "Textural Features for Image Classification." *IEEE Transactions on Systems, Man, and Cybernetics* 3 (6): 610–621.
- Hasager, C. B., M. Badger, A. Peña, X. G. Larsén, and F. Bingöl. 2011. "SAR-based Wind Resource Statistics in the Baltic Sea." *Remote Sensing* 3 (1): 117–144.
- Hasselmann, D. E., M. Dunckel, and J. A. Ewing. 1980. "Directional Wave Spectra Observed during JONSWAP 1973." *Journal of Physical Oceanography* 10 (8): 1264–1280.
- Hasselmann, K., T. P. Barnett, E. Bouws, H. Carlson, D. E. Cartwright, K. Enke, J. A. Ewing, H. Gienapp, D. E. Hasselmann, P. Kruseman, A. Meerburg, P. Müller, D. J. Olbers, K. Richter, W. Sell, and H. Walden. 1973. *Measurements of Wind-Wave Growth and Swell Decay during the Joint North Sea Wave Project (JONSWAP)*. Hamburg, Germany: ANE German Bight, Deutsches Hydrographisches Institut.
- Hasselmann, K., and S. Hasselmann. 1991. "On the Nonlinear Mapping of an Ocean Wave Spectrum into a Synthetic Aperture Radar Image Spectrum and Its Inversion." *Journal of Geophysical Research: Oceans* 96 (C6): 10713–10729.
- Hasselmann, K., R. K. Raney, W. J. Plant, W. Alpers, R. A. Shuchman, D. R. Lyzenga, C. L. Rufenach, and M. J. Tucker. 1985. "Theory of Synthetic Aperture Radar Ocean Imaging: A MARSEN View." *Journal of Geophysical Research: Oceans* 90 (C3): 4659–4686.

- Hasselmann, S., C. Brüning, K. Hasselmann, and P. Heimbach. 1996. "An Improved Algorithm for the Retrieval of Ocean Wave Spectra from Synthetic Aperture Radar Image Spectra." *Journal of Geophysical Research: Oceans* 101 (C7): 16615–16629.
- Jaagus, J., and A. Kull. 2011. "Changes in Surface Wind Directions in Estonia during 1966–2008 and Their Relationships with Large-Scale Atmospheric Circulation." *Estonian Journal of Earth Sciences* 60 (4): 220.
- Jönsson, A., B. Broman, and L. Rahm. 2003. "Variations in the Baltic Sea Wave Fields." *Ocean Engineering* 30 (1): 107–126.
- Karagali, I., A. Peña, M. Badger, and C. B. Hasager. 2014. "Wind Characteristics in the North and Baltic Seas from the QuikSCAT Satellite." *Wind Energy* 17 (1): 123–140.
- Karimova, S., and M. Gade. 2016. "Improved Statistics of Sub-Mesoscale Eddies in the Baltic Sea Retrieved from SAR Imagery." *International Journal of Remote Sensing* 37 (10): 2394–2414.
- Karvonen, J. 2015. "Evaluation of the Operational SAR Based Baltic Sea Ice Concentration Products." *Advances in Space Research* 56 (1): 119–132.
- Laanemäe, K., R. Uiboupin, and S. Rikka, 2016. Sea Ice Type Classification in the Baltic Sea from TanDEM-X Imagery. In *EUSAR 2016: 11th European Conference on Synthetic Aperture Radar, Proceedings of* (pp. 1–4). VDE.
- Launiainen, J., and T. Laurila. 1984. "Marine Wind Characteristics in the Northern Baltic Sea." *Finnish Marine Research* 250: 52–86.
- Lehner, S., A. Pleskachevsky, and M. Bruck. 2012. "High-Resolution Satellite Measurements of Coastal Wind Field and Sea State." *International Journal of Remote Sensing* 33 (23): 7337–7360.
- Lehner, S., A. Pleskachevsky, D. Velotto, and S. Jacobsen. 2013. "Meteo-Marine Parameters and Their Variability Observed by High Resolution Satellite Radar Images." *Oceanography* 26 (2): 80–91.
- Lehner, S., J. Schulz-Stellenfleth, S. Bruschi, and X. M. Li, 2008, June. Use of TerraSAR-X Data for Oceanography. In *Synthetic Aperture Radar (EUSAR), 2008 7th European Conference on* (pp. 1–4). VDE.
- Leppäranta, M., and K. Myrberg. 2009. *Physical Oceanography of the Baltic Sea*. Berlin Heidelberg: Springer Science & Business Media/Praxis Publishing Ltd.
- Li, X., S. Lehner, and W. Rosenthal. 2010. "Investigation of Ocean Surface Wave Refraction Using TerraSAR-X Data." *IEEE Transactions on Geoscience and Remote Sensing* 48 (2): 830–840.
- Li, X. M., and S. Lehner. 2014. "Algorithm for Sea Surface Wind Retrieval from TerraSAR-X and TanDEM-X Data." *IEEE Transactions on Geoscience and Remote Sensing* 52 (5): 2928–2939.
- Li, X. M., S. Lehner, and T. Bruns. 2011. "Ocean Wave Integral Parameter Measurements Using ENVISAT ASAR Wave Mode Data." *IEEE Transactions on Geoscience and Remote Sensing* 49 (1): 155–174.
- Li, X. M., S. Lehner, and M. X. He. 2008. "Ocean Wave Measurements Based on Satellite Synthetic Aperture Radar (SAR) and Numerical Wave Model (WAM) Data—Extreme Sea State and Cross Sea Analysis." *International Journal of Remote Sensing* 29 (21): 6403–6416.
- Lyzenga, D. R. 2002. "Unconstrained Inversion of Waveheight Spectra from SAR Images." *IEEE Transactions on Geoscience and Remote Sensing* 40 (2): 261–270.
- Lyzenga, D. R., R. A. Shuchman, J. D. Lyden, and C. L. Rufenach. 1985. "SAR Imaging of Waves in Water and Ice: Evidence for Velocity Bunching." *Journal of Geophysical Research: Oceans* 90 (C1): 1031–1036.
- Masuko, H., K. I. Okamoto, M. Shimada, and S. Niwa. 1986. "Measurement of Microwave Backscattering Signatures of the Ocean Surface Using X Band and Ka Band Airborne Scatterometers." *Journal of Geophysical Research: Oceans* 91 (C11): 13065–13083.
- Pleskachevsky, A. L., S. Lehner, and W. Rosenthal. 2012. "Storm Observations by Remote Sensing and Influences of Gustiness on Ocean Waves and on Generation of Rogue Waves." *Ocean Dynamics* 62 (9): 1335–1351.
- Pleskachevsky, A. L., W. Rosenthal, and S. Lehner. 2016. "Meteo-Marine Parameters for Highly Variable Environment in Coastal Regions from Satellite Radar Images." *ISPRS Journal of Photogrammetry and Remote Sensing* 119: 464–484.

- Raudsepp, U., J. Laanemets, G. Haran, V. Alari, J. Pavelson, and T. Köuts. 2011. "Flow, Waves and Water Exchange in the Suur Strait, Gulf of Riga, in 2008." *Oceanologia* 53 (1): 35–56.
- Ressel, R., S. Singha, S. Lehner, A. Rösel, and G. Spreen. 2016. "Near Real Time Automated Sea Ice Classification Using Polarimetric TerraSAR-X Images." *IEEE Journal of Selected Topics in Applied Earth Observations and Remote Sensing* 9 (7): 2016.
- Rikka, S., R. Uiboupin, and V. Alari. 2017. "Applicability of SAR-based Wave Retrieval for Wind–Wave Interaction Analysis in the Fetch-Limited Baltic." *International Journal of Remote Sensing* 38 (3): 906–922.
- Schulz-Stellenfleth, J., 2004. "Ocean wave measurements using complex synthetic aperture radar data". PhD diss., University of Hamburg.
- Schulz-Stellenfleth, J., T. König, and S. Lehner. 2007. "An Empirical Approach for the Retrieval of Integral Ocean Wave Parameters from Synthetic Aperture Radar Data. Journal of Geophysical Research." *Oceans* 112 (C3): C03019.
- Schulz-Stellenfleth, J., S. Lehner, and D. Hoja. 2005. "A Parametric Scheme for the Retrieval of Two-Dimensional Ocean Wave Spectra from Synthetic Aperture Radar Look Cross Spectra." *Journal of Geophysical Research: Oceans* 110 (C5): C05004.
- Schwarz, E., D. Krause, M. Berg, H. Daedelow, and H. Maass. 2015. "Near Real Time Applications for Maritime Situational Awareness." *The International Archives of Photogrammetry, Remote Sensing and Spatial Information Sciences* 40 (7): 999.
- Shao, W., X. Li, and J. Sun. 2015. "Ocean Wave Parameters Retrieval from TerraSAR-X Images Validated against Buoy Measurements and Model Results." *Remote Sensing* 7 (10): 12815–12828.
- Shao, W., X. M. Li, S. Lehner, and C. Guan. 2014. "Development of Polarization Ratio Model for Sea Surface Wind Field Retrieval from TerraSAR-X HH Polarization Data." *International Journal of Remote Sensing* 35 (11–12): 4046–4063.
- Sikora, T. D., and S. Ufermann. 2004. Marine Atmospheric Boundary Layer Cellular Convection and Longitudinal Roll Vortices. *Synthetic aperture radar marine user's manual*. NOAA, Washington, DC, pp.321–330.
- Singha, S., D. Velotto, and S. Lehner, 2015, July. Dual-Polarimetric Feature Extraction and Evaluation for Oil Spill Detection: A near Real Time Perspective. In *Geoscience and Remote Sensing Symposium (IGARSS), 2015 IEEE International* (pp. 3235–3238). IEEE.
- Soomere, T., and A. Räämet. 2011. "Spatial Patterns of the Wave Climate in the Baltic Proper and the Gulf of Finland." *Oceanologia* 53: 335–371.
- Svendsen, I. A., and I. G. Jonsson. 1976. *Hydrodynamics of Coastal Regions*. Lyngby, Denmark: Den Private ingeniørfond, Technical University of Denmark.
- SWAN team. 2014. (Accessed April 2015). <http://swanmodel.sourceforge.net/>
- Tuomi, L., K. K. Kahma, and H. Pettersson. 2011. "Wave Hindcast Statistics in the Seasonally Ice-Covered Baltic Sea." *Boreal Environment Research* 16 (6): 451–472.
- Velotto, D., C. Bentes, B. Tings, and S. Lehner. 2016. "First Comparison of Sentinel-1 and TerraSAR-X Data in the Framework of Maritime Targets Detection: South Italy Case." *IEEE Journal of Oceanic Engineering* 41 (4): 993–1006.
- Viitak, M., I. Maljutenko, V. Alari, Ü. Suursaar, S. Rikka, and P. Lagemaa. 2016. "The Impact of Surface Currents and Sea Level on the Wave Field Evolution during St. Jude Storm in the Eastern Baltic Sea." *Oceanologia* 58 (3): 176–186.

Appendix 1. Spectral parameters and parameters of GLCM

The XWAVE approach has repeatedly been validated and adopted for the Baltic Sea conditions. To do this, all TS-X scenes were pre-processed, and the primary parameters estimated by scene analysis were collected (Table A1). A series of secondary parameters derived from the primary parameters such as rates between various kinds of energy E and noise in different spectra domains were additionally estimated (Pleskachevsky, Rosenthal, and Lehner 2016).

Table A1. Basic parameters of subscenes analysed.

N	Parameter	Description	Comment
1	$H_S^{XWAVE_C}$	Wave height estimated by XWAVE_C	First guess wave height
2	M_I	Mean intensity of subscene scaled	Used also for XMOD-2 wind speed estimation
3	M_I^{dB}	Mean intensity in decibel	Used also for XMOD-1 wind speed estimation
4	θ	Local incidence angle	Used for wind and wave
5	E_{IS}	Integrated energy (k -domain 0.01–0.21 corresponds to wavelength 30–600 m)	Basic energy for H_S estimation
6	E_{SF}	Integrated energy scaled and filtered by considering integration angle θ_{IS}	Was found to be dependent on ratio of parameters: 14/15
7	E_{NN}	Energy integrated with noise deduction (no noise)	Since the noise comes also from the waves, used for considering of one-dimensional spectra only
8	E_{MAX}	Energy max in the spectrum	Signal-to-noise ratio estimation
9	E_K	Energy integrated with dividing each spectral k -bin by k^2	Amplifying high frequency spectrum signals, e.g. ships
10	E_{30}	Integrated energy of a spectrum annulus corresponds to wavelength 30–80 m	Short waves and non-linear streak structures by breaking and defocusing
11	E_{400}	Integrated energy of a spectrum annulus corresponds to wavelength 80–400 m	Longer waves, working straightforward for swell
12	E_{600}	Integrated energy of a spectrum annulus corresponds to wavelength 300–600 m	Very long waves, wind streaks and sandbar edges impact
13	N^S	Spectrum noise	Signal-to-noise ratio estimation
14	N_{in}^S	Spectrum noise inside of the so-called cut-off domain of the spectrum	In case of linear imaging mechanism, this noise has the same level as outside of the cut-off domain N_{out}^S , Figure A1
15	N_{out}^S	Spectrum noise outside of the so-called cut-off domain of the spectrum	Together with N_{in}^S for assessment of imaging non-linearity, Figure A1

Additionally, the GLCM (Grey Level Co-occurrence Matrix) parameters for each subscene were estimated and analysed to correlate the wave height, spectral parameters and GLCM parameters. The idea of using GLCM image analysis for oceanography applications is not new and is mostly applied for ice coverage classification and oil detection. For this study, the eight GLCM parameters are stored and used for tuning: GLCM-mean, variance, correlation, entropy, homogeneity, energy, contrast and dissimilarity (Haralick and Shanmugam 1973).

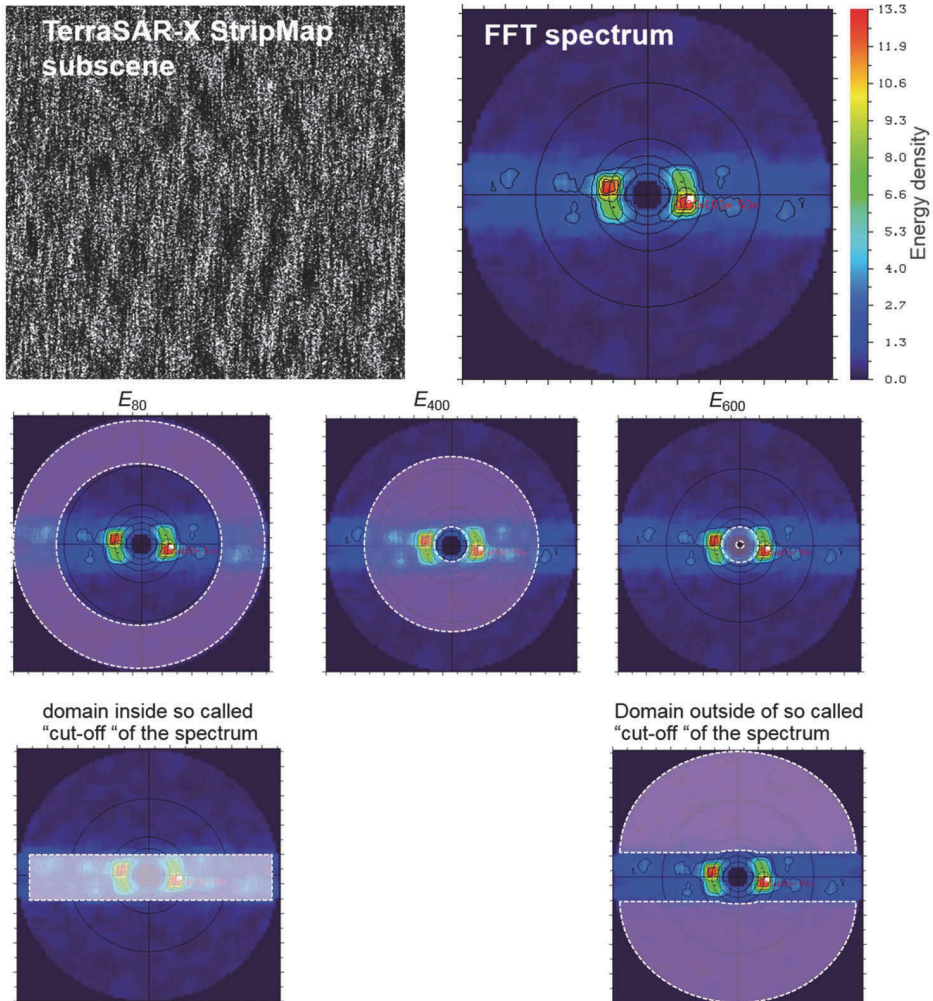


Figure A1. An explanation for Table A1. A TS-X StripMap subscene with FFT spectrum (first line). The same spectrums with circles indicate different integration domains: E_{80} , E_{400} , E_{600} (middle line), and the spectrum domain inside of the so-called cut-off and outside of cut-off for noise level estimations.

Appendix 2. Orbital wave velocity and maximal Doppler shift

For the large swell waves, a linear wave theory can be applied to estimate the surface motion (Alpers and Rufenach 1979). However, non-linearly shaped wind waves are hardly described using 1, 2 or even 10 Fourier components. Nonetheless, to get the notion of the expected order of surface velocities, the linear orbital motion for both systems is applied.

The linear or non-linear (but also non-viscid) wave theories are employed where velocities u and w are obtained by solving the equations for the velocity potential. As an analytical result, the 2D derived vortices-free wave orbital components \mathbf{u}_{orb} for horizontal x -direction and \mathbf{w}_{orb} for vertical z -direction, assuming the \sin -shaped surface, are the functions of wave height H , period T and wavenumber k (e.g. Svendsen and Jonsson 1976):

$$\mathbf{u}_{\text{orb}} = \frac{\pi H \cosh(k(z+d))}{T \sinh(kd)} \cos(kx - \omega t)$$

$$\mathbf{w}_{\text{orb}} = \frac{\pi H \sinh(k(z+d))}{T \sinh(kd)} \sin(kx - \omega t), \quad (\text{A1})$$

where d is water depth, $\omega = 2\pi/T$ is radian frequency. Both components are in antiphase and it means for the maximum of the one component if the second component is zero. For the estimation of the maximal orbital velocity at the surface ($z = 0$) a simplified formula can be used (time $t = 0$, $x = 0$, $\omega = 0$):

$$\mathbf{u}_{\text{orb}}^{\text{max}} = \frac{\pi H \cosh(kd)}{T \sinh(kd)}. \quad (\text{A2})$$

According to Eq. A2, for the waves with the same amplitude but with shorter wavelength, the orbital motion increases significantly (factor about two). For example, for the $H = 1.5$ m, $\mathbf{u}_{\text{orb}}^{\text{max}} = 0.42$ m s⁻¹ for averaged swell properties ($L = 350$ m, $T = 12$ s), and $\mathbf{u}_{\text{orb}}^{\text{max}} = 0.94$ m s⁻¹ for averaged windsea properties ($L = 50$ m, $T = 5$ s).

For the different waves (swell and windsea), the shape, geometry and local movements of the waves crest are completely different (Figure A2).

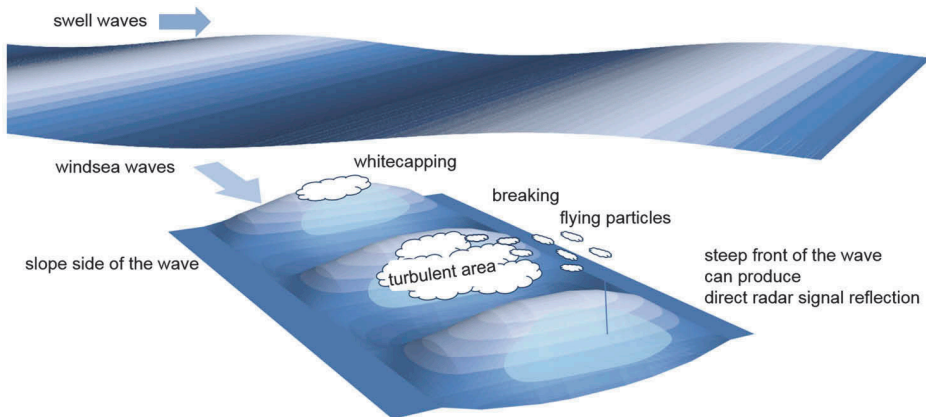


Figure A2. Idealized representation of the swell and windsea waves. While the swell wave can be imaged only under surface roughness at centimetre scale – Bragg scattering and its modulations – the windsea has a series of additional effect such as a direct reflection of waves travelling to satellite and breaking

Publication II

Rikka, S., Pleskachevsky, A., Jacobsen, S., Alari, V. and Uiboupin, R. (2018). Meteo-marine parameters from Sentinel-1 SAR imagery: towards near real-time services for the Baltic Sea. *Remote Sensing*, 10(5), pp. 757.



Article

Meteo-Marine Parameters from Sentinel-1 SAR Imagery: Towards Near Real-Time Services for the Baltic Sea

Sander Rikka^{1,*}, Andrey Pleskachevsky², Sven Jacobsen², Victor Alari¹ and Rivo Uiboupin¹

¹ Department of Marine Systems at Tallinn University of Technology, Tallinn 12618, Estonia; victor.alari@ttu.ee (V.A.); rivo.uiboupin@ttu.ee (R.U.)

² German Aerospace Center (DLR), Remote Sensing Technology Institute, Bremen 28199, Germany; andrey.pleskachevsky@dlr.de (A.P.); sven.jacobsen@dlr.de (S.J.)

* Correspondence: sander.rikka@ttu.ee; Tel.: +372-5342-8135

Received: 18 April 2018; Accepted: 9 May 2018; Published: 15 May 2018



Abstract: A method for estimating meteo-marine parameters from satellite Synthetic Aperture Radar (SAR) data, intended for near-real-time (NRT) service over the Baltic Sea, is presented and validated. Total significant wave height data are retrieved with an empirical function CWAVE_S1-IW, which combines spectral analysis of Sentinel-1A/B Interferometric Wide swath (IW) subscenes with wind data derived with common C-Band Geophysical Model Functions (GMFs). In total, 15 Sentinel-1A/B scenes (116 acquisitions) over the Baltic Sea were processed for comparison with off-shore sea state measurements (52 collocations) and coastal wind measurements (357 collocations). Sentinel-1 wave height was spatially compared with WAM wave model results (Copernicus Marine Environment Monitoring Service (CMEMS)). The comparison of SAR-derived wave heights shows good agreement with measured wave heights correlation r of 0.88 and with WAM model ($r = 0.85$). The wind speed estimated from SAR images yields good agreement with in situ data ($r = 0.91$). The study demonstrates that the wave retrievals from Sentinel-1 IW data provide valuable information for operational and statistical monitoring of wave conditions in the Baltic Sea. The data is valuable for model validation and interpretation in regions where, and during periods when, in situ measurements are missing. The Sentinel-1 A/B wave retrievals provide more detailed information about spatial variability of the wave field in the coastal zone compared to in situ measurements, altimetry wave products and model forecast. Thus, SAR data enables estimation of storm locations and areal coverage. Methods shown in the study are implemented in NRT service in German Aerospace Center's (DLR) ground station Neustrelitz.

Keywords: SAR; Sentinel-1; wave height; wind speed; Copernicus; CMEMS; Baltic Sea

1. Introduction

1.1. Meteo-Marine Parameters in the Baltic Sea in Relation to Synthetic Aperture Radar

Space-borne Synthetic Aperture Radar (SAR), known for its independence of daylight and weather, can provide two-dimensional (2D) information about the ocean surface with global coverage [1,2]. It is due to the Bragg scattering of the short capillary waves in the dimension of centimeters, produced by wind stress, which allows extraction of wave and wind parameters from radar imagery [3–5].

The investigation of SAR ocean surface imaging mechanisms and the extraction of wave and wind parameters started with the launch of L-band SAR onboard SEASAT in 1978 [3,4]. Since then, numerous different algorithms have been developed over time to estimate oceanographic parameters and ocean wave spectra from SAR imagery [6–8].

The methods for sea state estimation are largely divided into two main groups; first one being functions where image spectra are transferred into wave spectra using transfer functions (e.g., [6,7,9,10]). These methods are suitable for estimations of swell's spectra, and its output can be assimilated into spectral wave models. The key to success is to understand the nonlinear SAR imaging of the moving sea surface waves that can be incorporated in "transfer functions" [9]. This approach requires SAR acquisitions with clearly visible wave patterns (e.g., Sentinel-1 Wave Mode (WM) data, high resolution Stripmap Mode TerraSAR-X data). Otherwise, the waves are substantially distorted and are not visible in the SAR images and thus are not represented in the image spectra.

The second group of sea state estimation algorithms use a direct estimation of the wave parameters from the image spectrum with empirical functions (e.g., [11–14]). Although empirical methods for C-band SAR exist, e.g., CWAVE_ERS and CWAVE_ENVI [12,14], they are only applicable to ERS-2 and Envisat-ASAR WM data. The most recent method for Sentinel-1 WM data by Stopa et al. [15] uses neural network techniques to retrieve wave parameters. However, since Sentinel-1A/B WM data is not available over the coastal areas of world ocean (including the Baltic Sea), moderate resolution Interferometric Wide (IW) swath mode images are used for sea state parameter retrieval. Short windsea waves produce unclear wave pattern in Sentinel-1 IW mode and are hardly distinguishable from ocean clutter. The SAR images are being affected by strong non-linear distortions due to the defocusing effects. Empirical functions, deduced from large sets of representative data, are proven to be more suitable for the short windsea waves and noisy images. The direct estimation of wave parameters from subscene spectra allows fast, straightforward, and reliable near-real-time (NRT) processing of satellite scene while excluding only a fragment of the data [13,16].

For the semi-enclosed micro-tidal Baltic Sea with the absence of long swell waves and short wave "memory" [17], and the significant wave heights remaining mostly between 0 and 2 m (rarely exceeds 4 m [18,19]), the second type of mentioned methods is recommended [13,20,21]. Windsea waves are short-crested and represent a considerable number of small, nonstable, fast, and erratically moving targets for a SAR sensor. Such sea state is typically imaged similar to noise with radar echoes of every scatterer blurred in azimuth and shifted randomly in range direction due to the individual Doppler contribution. The resulting pattern is hardly recognized as a wave pattern. A strong windsea contribution to the total wave height is therefore equivalent to more substantial uncertainties in SAR imaging.

With the launch of C-band Sentinel-1A/B constellation, different methods to estimate meteo-marine parameters, software realizations, and infrastructure open possibilities for NRT services for oceanographic applications [16]. As shortly as 10 min after image downlink, information about wave height, wind speed, as well as ice coverage, oil spills, and ship detection can be transferred to interested institutions or weather services [13,20,22–24].

Sentinel-1A/B data is already used worldwide for different applications. For example, estimating wave-induced orbital velocities from which elevation spectra is derived over ice-covered regions [25], calculating significant wave height and mean wave period from Sentinel-1A/B StripMap images using semi-empirical methods [26], or using neural network techniques on Sentinel-1 data to retrieve wave height [15].

SAR-based wave products have also proven to be valuable in the open ocean applications for swell tracking (e.g., [27,28]). In operational wave monitoring and forecasting, several organizations provide relevant information on wave conditions in the Baltic Sea: Baltic Operational Oceanographic System (BOOS), Copernicus Marine Environment Monitoring Service (CMEMS). However, the inclusion of Sentinel-1 wave products over the Baltic Sea into the CMEMS product portfolio would improve the service quality which currently provides only model wave forecast, altimetry wave products, and in situ data [29–31].

1.2. Sentinel-1A/B Data over the Baltic Sea

The Baltic Sea is situated in temperate latitudes between 53°N to 66°N and from 9°E to 30°E which makes it one of the most frequently imaged locations by the Sentinel-1 satellites. Various parts of the Baltic Sea are imaged by Sentinel-1A/B daily and often even twice a day by ascending and descending orbits in the morning and in the evening correspondingly. The most suitable Sentinel-1A/B relative orbit numbers are 22 paired with 29, 51 with 58, and 124 with 131 (Figure 1).

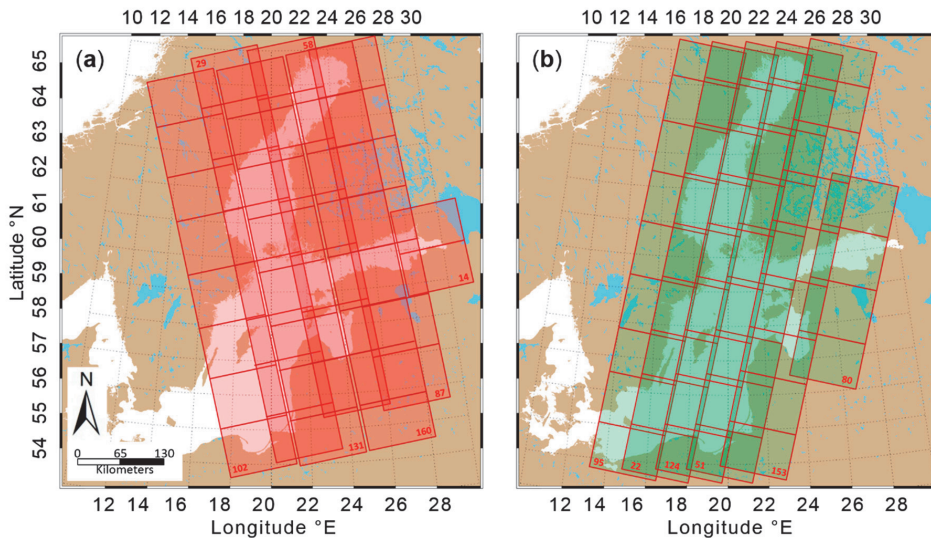


Figure 1. Sentinel-1A/B IW relative orbit overlays and corresponding orbit numbers over the Baltic Sea. (a) ascending/morning orbits and (b) descending orbits in the evenings.

Similar usability of satellite SAR data in the Baltic Sea was available when Envisat/ASAR (Advanced Synthetic Aperture Radar) was operational. With the launch of Sentinel-1A/B constellation and the freely available data on the Copernicus Open Access Hub, all the services can be continued. Different methods can be applied on the images to estimate meteo-marine parameters in the Baltic Sea for operational maritime awareness applications. The Sentinel-1 IW level-1 products have 250 km wide swath with 10 m pixel resolution to cover the length of the Baltic Sea with sequential SAR acquisitions.

1.3. Aim of the Study

The main purpose of this study is to assess current state-of-the-art method in estimating meteo-marine parameters, such as wind speed or total significant wave height, in the Baltic Sea from medium resolution Sentinel-1A/B IW swath mode satellite radar imagery. The main advantages of the method as well as challenges are also brought out. The study focuses on the possibilities of making the method available as a near-real-time service over the Baltic Sea using three examples of different sea state in comparison to spectral wave model and available in situ measurements.

The specific objectives of the study are: (i) to validate CWAVE_S1-IW wave retrievals in the Baltic Sea; (ii) to validate CMOD wind speed retrievals in the coastal zone of the Baltic Sea; (iii) to demonstrate potential of Sentinel-1A/B SAR wave retrievals with CWAVE_S1-IW algorithm for operational monitoring in coastal area.

2. Data

2.1. In Situ Data

Wind measurement data from 39 coastal stations (357 collocations with SAR data) around the Baltic Sea were used for statistical validation of Sentinel-1 wind retrievals (Figure 2). Sentinel-1 SAR sea state retrievals were validated with in situ wave measurements from 5 offshore stations (52 collocations with SAR data) (Table 1 and Figure 2).

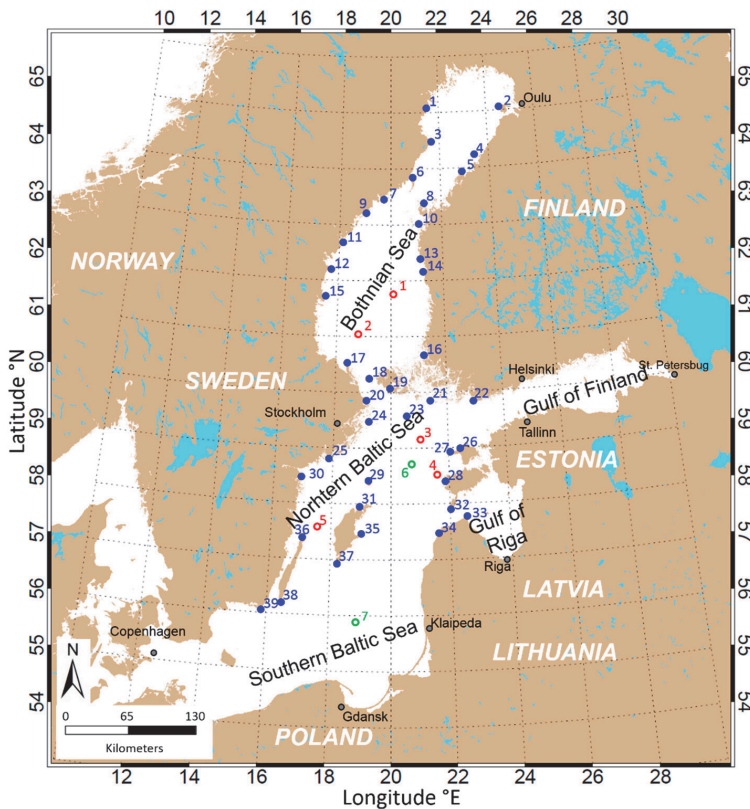


Figure 2. The map of the Baltic Sea and locations of measurement stations used in the study. The location of wave measurements—significant wave height, wave propagation direction, wave period (red), and coastal wind measurements—speed, gusts, direction (blue) are indicated on the map; green marks extra stations (virtual buoys).

Table 1. Overview of wave measurements used in the study. H_S represents total significant wave height.

No. (Origin)	Station	Lat (°N)	Lon (°E)	Sensor	Data Used
1 (FIN)	Selkämeri	61.8001	20.2327	Waverider	H_S
2 (SWE)	Finngrundet	61.0000	18.6667	Waverider	H_S
3 (FIN)	NBP	59.2500	20.9968	Waverider	H_S
4 (EST)	Vilsandi	58.4889	21.6333	Waverider	H_S
5 (SWE)	Knolls grund	57.5167	17.6167	Waverider	H_S
6	NBP Extra	58.7500	20.8271	Virtual buoy	H_S
7	Södra Östersjön	55.9167	18.7833	Virtual buoy	H_S

2.2. Sentinel-1A/B Data

The C-band SAR data from Sentinel-1A/B, namely IW mode data, are used for estimation of meteo-marine parameters in this study. The IW mode allows combining large swath width of 250 km in range direction with moderate geometric (5×20 m) resolution. Sentinel-1A/B products are available in single (HH or VV) or dual polarizations (HH+HV, VV+VH). For the meteo-marine parameter estimation, either one of the single polarization data is used. The Normalized Radar Cross Section (NRCS) σ_0 is firstly processed from image pixel digital number (DN):

$$\sigma_0 = \frac{DN^2}{k_s^2} \quad (1)$$

where k_s is the calibration factor given in the products metadata. The process of estimating sea state parameters is based on FFT (Fast Fourier Transform) of the subscene. Before the analysis, each pixel value $\sigma_0(x, y)$ of the subscene is normalized resulting in a value $\sigma_n(x, y)$:

$$\sigma_n = \frac{\sigma_0(x, y) - \sigma_0}{\sigma_0} \quad (2)$$

where σ_0 is the mean value of σ_0 in the subscene.

Images were processed with a 3 nautical mile grid with the FFT window of 1024×1024 pixels with four-factor resampling and Gaussian smoothing. The processing was implemented for latitudes up to 65°N .

Although all the Sentinel-1A/B IW scenes (460 scenes) over the Baltic Sea from the beginning of 2015 until the end of 2016 were processed, only 15 overpasses (number of acquisitions per satellite overpass ranged from 5 to 9) were selected for validation of the meteo-marine parameter retrieval method as well as for analysis and comparison. All the selected data in Table 2 were acquired in VV polarization. The SAR data for validation were selected to have equal representation of different meteo-marine conditions (i.e., high and low sea states) (Table 2).

Table 2. Sentinel-1A/B acquisitions used for the study. Relative orbit numbers with acquisitions per scene are listed. Mean and maximum significant wave height and wind speed calculated with the methods described in Section 3 are shown with the number of collocations per overpasses.

Sentinel-1 UTC	Relative Orbit no.	Images in Scene	Mean/Max H_s per Scene	Mean/Max U_{10} per Scene	Collocations (Wave/Wind)
11 January 2015 16:19	29	6	2.4/7.5	9.0/18.7	3/11
22 April 2015 16:28	102	6	0.3/1.7	2.6/11.8	2/3
04 June 2015 05:04	22	9	0.9/2.8	5.3/14.0	4/32
11 June 2015 04:56	124	9	0.6/2.1	4.1/11.5	5/28
25 June 2015 04:56	124	8	0.8/1.8	5.1/13.8	5/27
28 June 2015 05:04	22	9	0.6/2.2	3.4/8.7	4/25
05 July 2015 04:56	124	9	0.7/2.5	4.7/12.4	4/22
28 July 2015 04:56	124	9	0.9/2.4	6.6/14.4	5/25
08 August 2015 05:04	22	9	1.7/2.9	10.8/16.0	4/31
08 September 2015 16:19	29	6	1.3/2.7	8.5/17.3	3/19
02 October 2015 05:04	22	9	1.8/3.6	11.6/19.1	4/32
02 October 2015 16:19	29	5	2.5/4.8	13.2/18.2	1/16
02 November 2015 04:56	124	9	1.6/2.4	10.7/17.1	5/32
09 August 2016 16:19	29	6	1.9/3.7	9.7/13.8	1/28
14 December 2016 04:56	124	7	1.4/2.6	8.6/13.9	2/26
15		116			52/357

2.3. Spectral Wave Model

The wave model WAM [32] is a third-generation wave model which solves the action balance equation without any a priori restriction to the evolution of spectrum. The action density spectrum N is considered instead of the energy density spectrum E because in the presence of ambient currents,

action density is conserved, but energy density is not. Action density is related to energy density through the relative frequency [33]:

$$N(\sigma, \theta) = \frac{E(\sigma, \theta)}{\sigma} \quad (3)$$

The variable σ is the relative frequency (as observed in a frame of reference moving with the current velocity) and θ is the wave direction (the direction normal to the wave crest of each spectral component). The action balance equation in Cartesian coordinates reads:

$$\frac{\partial N}{\partial t} + \left(\vec{c}_g + \vec{U} \right) \nabla_{x,y} N + \frac{\partial c_\sigma N}{\partial \sigma} + \frac{\partial c_\theta N}{\partial \theta} = \frac{S_{wind} + S_{nl4} + S_{wc} + S_{bot}}{\sigma} \quad (4)$$

On the left-hand side of Equation (4) the first term represents the local rate of change of action density in time; the second term denotes the propagation of wave energy in two-dimensional geographical space, where \vec{c}_g is the group velocity and \vec{U} is the ambient current. The third term represents shifting of the relative frequency due to variations in depths and currents (with propagation velocity c_σ in σ space). The fourth term represents depth-induced and current-induced refraction (with propagation velocity c_θ in θ space). At the right-hand side of the action balance equation is the source term that represents physical processes which generate, redistribute, or dissipate wave energy in the WAM model. These terms denote, respectively, wave growth by the wind S_{wind} , non-linear transfer of wave energy through four-wave interactions S_{nl4} and wave dissipation due to whitecapping S_{wc} and bottom friction S_{bot} .

A pre-operational version of the WAM model which is since April 2017 used for the production of CMEMS wave forecast over the Baltic Sea was used [29]. The model domain covers the Baltic Sea with a grid resolution of one nautical mile, yielding 800×775 model grid points. The model was forced with High Resolution Limited Area Model (HIRLAM) winds with a spatial resolution of 11 km and temporal resolution of one hour. In winter, ice concentration data from the Finnish Meteorological Institute's Ice Service was used. Model grid points in which the ice concentration exceeds 30% are excluded from the calculation. Data assimilation was not used in the wave model.

3. Methods

3.1. Wind

Sea state is strongly dependent on local wind characteristics which SAR data can provide. By analyzing the roughness of the sea, wind speed is received using Geophysical Model Functions (GMF) which relate the local wind conditions and sensor geometry to radar cross section values.

For Sentinel-1 IW data, separate GMFs are used for HH or VV polarizations. For HH, CMOD4 function, developed by Stoffelen et al. [34] is used, and for VV polarization CMOD5.N algorithms shows the best results [35]. The selection of the respective GMF is based on an extensive comparison of GMF performance in comparison with an advanced scatterometer (ASCAT), METOP-A, and METOP-B satellite data performed by [36]. As stated in [36], Thompson polarization ratio [37] with $\alpha = 1$ is applied to HH polarized data. Also following the authors' suggestion, a bias of 0.004 is subtracted from VV polarized data, to achieve an overall better agreement with scatterometer data. In total, an accuracy of approximately 1.5 m s^{-1} has been found in the comparison with the ASCAT data within the validity range of 2–25 m s^{-1} of the two GMFs [36]. In the current processing procedure, no information from the cross-polar channel is exploited, although a future application of a respective GMF as e.g., proposed by [38] is foreseen to improve wind data reliability in storm situations. The data analyzed in this paper is entirely in the validity range of the applied GMFs for co-polar channels.

In the common procedure, GMFs in general and thus also the CMOD algorithms are inversion methods and require the local wind direction to reduce the number of free parameters in the forward calculation. For the work presented in this paper, wind direction from Weather Research and Forecasting Model (WRF) is used [39]. The model is run for the given area and time of the data

acquisition. Initial and boundary conditions are adopted from the corresponding National Oceanic and Atmospheric Administration Global Forecast System (NOAA GFS) analysis model values. For NRT applications, NOAA GFS Forecast values are used instead and the model is run shortly prior to satellite data downlink with a configuration based on the scene parameters (region and time) available in the data processing system schedule. Finally, WRF model values for the wind direction are interpolated to the sea state calculation grid and wind speeds are calculated directly within the sea state algorithm procedure for a given subcell.

3.2. Sea State

An empirical algorithm CWAVE_S1-IW, developed by Pleskachevsky et al. [20], is used to estimate integrated sea state parameters straight from SAR image spectra without transformation into wave spectra. The method is chosen since traditional functions (image spectrum transfer to wave spectrum) are not able to calculate total significant wave height from Sentinel-1 IW mode imagery in the Baltic Sea. The main reasons are the relatively coarse resolution of Sentinel-1A/B and generally lower sea state without long swell compared to the open ocean.

In comparison to e.g., TerraSAR-X/TanDEM-X StripMap scenes with about 3 m resolution, the Sentinel-1A/B IW mode resolution is by an order of magnitude larger. In case of such Sentinel-1 SAR imaging setting the wave structures, if visible, are disturbed by the vast amount of noise. In addition, a standard FFT window of 1024×1024 pixels covers a relatively large area of 10240×10240 m. To overcome the limitation, four-factor resampling and Gaussian smoothing were applied to selected subscenes. The modified resolution becomes to 2.5 m with areal coverage of 2560×2560 m [20].

An important part of sea state estimation is pre-filtering of any natural or man-made objects from subscene which yields to inaccuracies in wave height estimation. Such spectral perturbations result in an integrated value which leads to the total image energy not connected to the sea state. The radar signal disturbances can be divided into two main groups:

- radar signal much stronger than background backscatter from sea state produced mainly by ships or offshore constructions. In these cases, the subscene is additionally analyzed with 100×100 m sliding window. The statistics of each window σ_0^{win} is compared with σ_0 of the subscene. In a case of $\sigma_0^{win} > q_{ship}\sigma_0$ with tuned q_{ship} value of 2.3 (for 100×100 m window), the outliers in the current window are replaced with the mean value of the subscene σ_0 [20];
- radar signal much weaker than background backscatter from sea state produced, for example, by oil spills, or commonly occurring algae blooms in the Baltic Sea [20]. In those cases, the filtering algorithm was extended by employing $\sigma_0^{win} > q_{spills}\sigma_0$ with tuned threshold coefficient q_{spills} .

To obtain integrated wave parameters, FFT operation is applied to the radiometrically calibrated subscene. Image power Spectrum $IS(k_x, k_y)$ is calculated by integration over 2D wavenumber domain:

$$E_{IS} = \int_{k_x^{min}}^{k_x^{max}} \int_{k_y^{min}}^{k_y^{max}} IS(k_x, k_y) dk_x dk_y \quad (5)$$

The integration over wavenumber domain is limited by $k_{max} = 0.003$ and $k_{min} = 0.201$ which correspond to wavelength of 2000 to 30 m, where wavenumber $k = \sqrt{k_x^2 + k_y^2}$. In the Sentinel-1A/B image spectra the wavenumber domain $\sim 0.201 < k < 0.060$ represents the clutter produced by waves shorter than about 100 m. The domain $\sim 0.060 < k < 0.010$ represents long waves with wavelength of $\sim 100 < L_p < 600$ m, and the domain $\sim 0.010 < k < 0.003$ represents the longest structures such as wind streaks [20].

During the algorithm's development, it became clear that estimating sea state parameters based only on image spectral properties is not accurate enough. Additional information about each subscene is therefore acquired by using Grey Level Co-occurrence Matrix (GLCM) [40]. By using image texture analysis, accuracy in low and high sea state was improved [20].

The resulting function CWAVE_S1-IW for Sentinel-1A/B imagery to calculate total significant wave height is expressed as:

$$H_S^{XWAVE-C} = a_0 \sqrt{B_0 E_{IS} \tan(\theta)} + \sum_{i=1}^n a_i B_i \quad (6)$$

where θ is local incidence angle, a_i are coefficients, and B_i are functions of spectral parameters, wind and GLCM results.

The first term in Equation (6) connects the sea state and image spectra energy which contributes the most in the case of long prominent waves with over 100 m wavelengths. The non-linearity of the imaging mechanism is represented by the B_0 , which represents noise scaling of total image spectrum energy E_{IS} . The relation $B_0 = KE_{IS}^{100}/E_{IS}^{600}$, where K serves as a constant found by collocating buoy data, connects the spectrum energy between the wavelength domain of 30–100 m (noisy part of the image spectrum) with the wavelength domain of 100–600 m (the area where wave-looking patterns can be observed). The rest of the terms in Equation (6) represent a series of corrections and filtering of different origins. For example, to consider the wind speed, the term $a_1 B_1$, where $B_1 = U_{10}$, is used. Full information about the function development, tuning and results can be found in [20].

3.3. Comparison Methods

The total significant wave height H_S and wind speed U_{10} derived from SAR are used for comparisons with collocated in situ measurements. The Sentinel-1A/B scenes were processed with 3×3 nautical miles posting with $\sim 30 \times 45 = \sim 1350$ subscenes per IW image. The collocations were done for five Sentinel-1A/B scenes with a time window of ± 20 min and almost 30 min for one case. For the rest of the nine cases, the time difference between the measurements or WAM model data and SAR-derived values is less than 5 min (Table 2). For the spatial collocation, the closest SAR-subscenes are used with a mean value between subscene centre and measurement equipment location or WAM wave model grid point being 4.1 km and 0.7 km, correspondingly. In case the buoy location remains outside the image, the results from the closest subscene to the SAR acquisition edge in the range of up to 10 km was incorporated.

In the case of the wind speed comparison, the average distance between in situ measurement location and the closest subscene centre is 7.7 km. The reason is that the majority of the stations are at the coast (Figure 2) and the SAR subscenes which are close to the shore (contaminated by land backscatter) are filtered out. The time difference remains the same as for wave height comparison, mostly below 5 min.

The Root Mean Square Error (RMSE), Pearson correlation coefficient r , and Scatter Index (SI) (where $SI = RMSE / (\text{average of observations})$) are calculated for each collocated dataset for the statistical comparisons. Standard deviation (STD) is used to measure variabilities of datasets. All collocated data are presented in scatterplots for wave height and wind speed.

4. Results

4.1. Validation

The inter-comparison and the scatter plots in Figure 3 show a good general agreement of SAR wave retrievals and WAM model fields with in situ wave measurements. The corresponding correlation coefficients are 0.88 to 0.89 (Table 3). Also, the RMSE of SAR-derived wave heights and WAM model wave heights are very similar, 0.40 m and 0.39 m correspondingly (Table 3). Slightly poorer statistics ($r = 0.81$ and $RMSE = 0.47$ m) are observed when the SAR wave is compared with WAM model data (based on 52 collocated observations), which indicates that SAR and model data resolve distinct aspects of the observed wave parameters. Therefore, SAR and model data could both provide complementary information for accurate description of the wave field. The benefits of multiple data sources for

understanding wave field variations are discussed in Sections 4.2 and 5.1 based on characteristic examples of wave conditions.

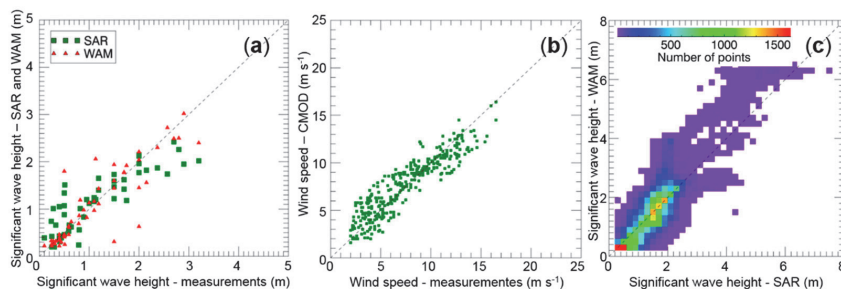


Figure 3. (a) Scatterplot for sea state for available collocated data acquired over the Baltic Sea including 15 Sentinel-1A/B scenes (overflights/events/days) with 116 individual Sentinel-1 IW mode images and 52 buoy collocations. The correlation coefficient between SAR and in situ measurements is 0.88, RMSE is 0.40 m, and Scatter Index is 0.37. (b) Scatterplot for surface wind speed for all available collocated data acquired over the Baltic Sea. The correlation coefficient r is 0.91, RMSE is 1.43 m s^{-1} , and SI is 0.19. (c) Histogram plot for all the collocated SAR versus WAM results. The bin size for histogram calculations is 0.2 m. The statistics between the datasets are as follows: $r = 0.86$, RMSE = 0.47 m, and SI = 0.33.

Table 3. Overview of inter-comparison of significant wave height and wind speed: correlation coefficient (r), root mean square error (RMSE), scatter index (SI), and number of collocations (n). The values in brackets in the 3rd column represent the statistics when all collocated data of Synthetic Aperture Radar (SAR) and wave model (WAM) wave fields were used (49,315 collocations).

Parameter	SAR vs. In Situ Wave Height	SAR vs. WAM Wave Height	SAR vs. In Situ Wind Speed	WAM vs. In Situ Wave Height
r	0.88	0.81 (0.86)	0.91	0.89
RMSE	0.40	0.47 (0.47)	1.43	0.39
SI	0.37	0.42 (0.33)	0.19	0.36
n	52	52 (49314)	357	52

Scatter plot on Figure 3b shows the collocated in situ data comparison with estimated wind speed results from the corresponding CMOD algorithm. The wind speed varied from 2 m s^{-1} to 17 m s^{-1} with the mean wind speed value of all 357 collocations being 7.53 m s^{-1} . The correlation coefficient between SAR wind retrievals and coastal wind speed measurements was 0.91 (Table 3).

Figure 3c shows the wave height histogram plot of all 49314 SAR-derived values and the corresponding WAM results. Figure 3c clearly indicates that most values are around 1 m. The statistics between the two methods in the case of a larger dataset (49,314 collocations) is slightly better compared to the dataset that was collocated with 52 observations— $r = 0.86$ and RMSE = 0.47 m (Table 3).

4.2. Case Studies: High, Medium, and Low Sea State

A high sea state example from 11 January 2015 (16:19 UTC) is presented in Figure 4a–c. Considering the general Baltic Sea wave conditions, high significant wave height values (up to 7.5 m) were observed along the Polish and Lithuanian coasts. Both the SAR-derived results and WAM model field show good general agreement in the wave height values and location of maximum ($r = 0.91$). The area of the storm on the SAR image is smaller and does not spread as much to the north as in the WAM results. The maximum significant wave height from SAR is about 0.5 m higher

(Figure 4b, Table 4). Another region with some differences between the wave fields retrieved with the two different methods is seen in the Bothnia Sea area, where SAR-derived wave height along the Swedish coast is about two meters lower compared to the model data.

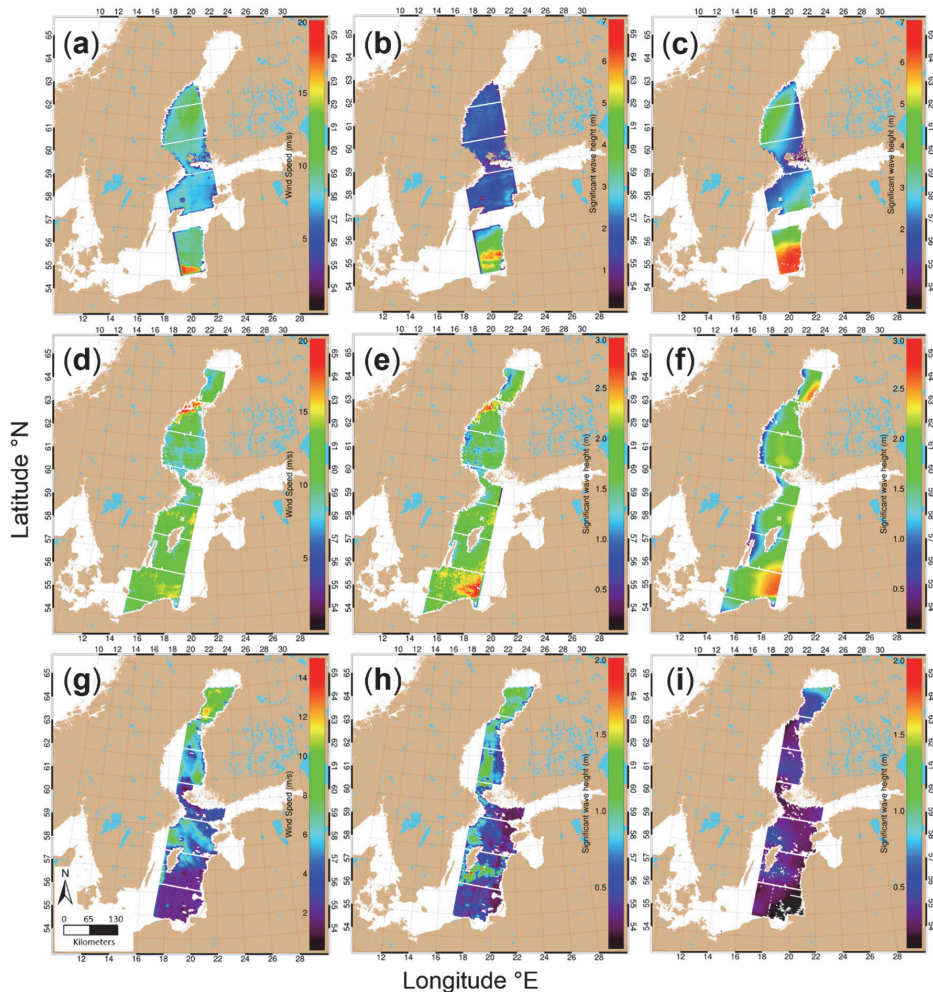


Figure 4. Examples of spatially collocated SAR wind (a,d,g) fields, SAR wave fields (b,e,h) and WAM wave fields (c,f,i) during three characteristic situations over the Baltic Sea: high sea state on 11 January 2015 at 16:19 (a–c), medium sea state on 2 October 2015 at 04:56 (d–f) and low sea state on 5 July 2015 at 04:56 (g–i).

The second example depicts medium sea state conditions in the Baltic Proper and the Gulf of Bothnia on 2 October 2015 (Figure 4d–f). Again, a good general match between wave fields (considering the wave height and spatial pattern) estimated from SAR data and the WAM model outcome can be observed. SAR-derived wave height field is more variable (STD from 1.14 m to 1.51 m) than the model field (STD from 0.17 m to 1.48 m), which is the case for all examples (Table 4). Also, there are some differences in the wave field pattern along the Swedish coast where the wave height is underestimated by WAM model data compared to SAR-derived fields.

Table 4. Statistics between Sentinel-1 H_S retrievals and WAM numerical model outputs.

Time UTC	Variable	Sentinel-1	WAM
11 January 2015 16:19:22 High sea state	Mean (m)	2.41	3.02
	Maximum (m)	7.47	6.97
	STD (m)	1.51	1.48
	r		0.91
	RMSE (m)		1.02
02 October 2015 05:04:47 Medium sea state	Mean (m)	1.82	1.68
	Maximum (m)	3.62	2.65
	STD (m)	1.32	0.57
	r		0.51
	RMSE (m)		0.39
05 May 2015 04:56:28 Low sea state	Mean (m)	0.57	0.33
	Maximum (m)	1.84	1.02
	STD (m)	1.14	0.17
	r		0.51
	RMSE (m)		0.41

Most commonly occurring, the low sea state [19] example on 5 July 2015 over the Baltic Sea (H_S is around 1 m) is presented in Figure 4g–i. Although WAM wave model results are smoother and lower than SAR-derived values, they represent a very similar large-scale pattern. One can notice the increased wave height values to the north and to the south of Gotland Island. A similar pattern from both datasets is also observed in Bothnia Sea region. The low sea state conditions might not be the most relevant from a safe navigation point of view and operational monitoring/forecasting of the wave conditions is not as critical as during storm conditions. Nevertheless, it is still relevant for routine environmental monitoring and therefore noteworthy that during the low sea state, most of the wave field variability is lost in the model outcome compared to SAR-derived values. A similar example from TerraSAR-X satellite data is presented in Rikka et al. [21], where during low sea state conditions the local wave height increases by 0.5–1 m in kilometre-size “islands” (small local area with elevated wave height values). In Sentinel-1A/B (Figure 4g–i), the size of the observed “island” is larger due to larger SAR resolution and processing grid step which does not allow retrieving such fine scale variations as in the case of TerraSAR-X data. Similarly, Romeiser et al. [41] showed that in hurricane situations, the wavelength is analogously retrieved in island-like fashion from C-band satellite radar.

The case studies showed good general agreement between the SAR-derived and WAM model wave fields. However, there are some differences between the results obtained with the two methods: (i) the area and the location of the storm might be different; (ii) the wave height variability of WAM model fields is lower compared to the SAR-derived fields. The variation in WAM model fields is lost mostly due to wind forcing fields (HIRLAM) used in the wave modelling which have 1 h temporal resolution and 11 km spatial resolution. Therefore, the forcing fields do not include local fine-scale wind field variations and gusts that influence the radar backscatter and related wave field pattern on SAR imagery.

5. Discussion

The current study, as well as previous studies [13,15,21–25] demonstrate the advantages of SAR data in general and Sentinel-1 A/B IW data in particular for the operational sea state monitoring (downstream) services. The meteo-marine parameters derived from Sentinel-1 A/B IW data provide added value to operational monitoring/forecasting services (NRT open source data with high spatial resolution and large spatial coverage; frequency of acquisitions) and statistical analysis (large dataset with sufficient spatial coverage in the coastal zone). Together with the unrestricted access to operational in situ data collected by various Baltic Sea countries and model forecast (e.g., CMEMS, BOOS), the SAR-derived meteo-marine parameters form a basis for improving maritime situation

awareness. Furthermore, other applications in the Baltic Sea region, e.g., oil spill detection (impact of wave-wind conditions on detection accuracy), sea ice monitoring (waves under ice), wave-circulation coupling [42], etc. will benefit from incorporation of the Sentinel-1 A/B sea state products in these service chains [29,43].

5.1. Benefits of Sentinel-1A/B IW Wave Field Data for Operational Services

An independent time series from 1 August 2016 until the end of 2016 from four separate locations demonstrate the benefits of using SAR-derived significant wave height retrievals (Figure 5).

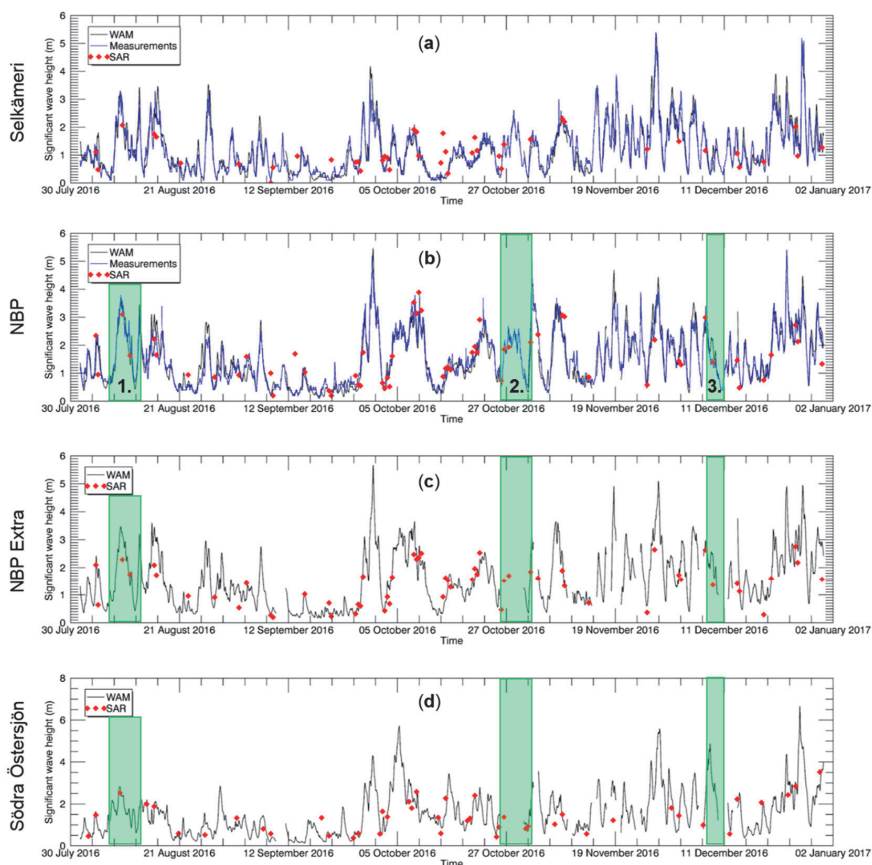


Figure 5. A timeseries from 1 August 2016 until the end of 2016 from four stations. Two stations—Selkämeri and NBP (Figure 2, Table 1)—include all the data: measurement, WAM, and SAR-derived results; other two stations—NBP Extra (58.7500°N, 20.8271°E; no. 6 in Figure 2) and Södra Östersjön (55.9167°N, 18.7833°E; no. 7 in Figure 2) include WAM result and SAR-derived significant wave height. Highlighted areas indicate some benefits of using SAR data over the Baltic Sea: “case 1” and “case 3” bring out the variability aspect of SAR-derived values whereas “case 2” shows missing measurements that can be replaced with SAR data.

In areas where average significant wave height is very low, for example, Selkämeri station in Figure 5a, the SAR-derived results ($r = 0.79$) are not as accurate as the results over the open part of the

Baltic Sea in the NBP station ($r = 0.92$) on Figure 5b. It is known from previous studies that dominant wave height in the Baltic Sea is around 1 m [19] and relatively low spatial resolution of Sentinel-1 IW mode data might complicate the accurate wave height estimation.

In Figure 5b,c three cases highlighted in green are brought out to explain the benefits of using SAR data. In “case 1” of Figure 5b, one can observe that both WAM wave model results and SAR-derived results match closely with the in situ measurements of the NBP station. However, in Figure 5c which represents a location 60 km away from NBP, a mismatch between SAR and WAM results can be seen in the “case 1” region. The reason could be that since SAR represents better detailed spatial variability/pattern, the actual significant wave height was lower than WAM had predicted at the specific time and location. “Case 3” in Figure 5b,c shows good general match between in situ measurements, SAR-derived wave height, and WAM output in separate places, suggesting that the wave field was spatially more uniform. In general, SAR-derived results could be used as validation data for wave models.

Since the Baltic Sea is seasonally ice-covered, in situ measurement devices are removed for the winter period. Similarly, when the buoys have technical problems (e.g., no data connection) or during their maintenance, highly valuable information is lost. Moreover, wave models may also have short periods with technical problems when no wave forecast is provided. These situations can be observed in “case 2” in Figure 5c, where SAR-derived results become the only source of wave information.

Figure 5d demonstrates the added benefit of using SAR data to retrieve wave information over the poorly sampled area. Although Södra Östersjön station (55.9167°N, 18.7833°E) is included into BOOS measurement stations, the last unrestricted access measurement data was received in 2011. However, Southern Baltic Sea is a location where the highest waves occur [18,19]. As no in situ measurements are carried out in the region, the SAR-derived results would be highly valuable for model validation and/or assimilation into the wave model.

5.2. Statistical Mapping of Coastal/Regional Wave Field: Comparison with Altimetry

Although Sentinel-1A/B are not able to cover the extent of the Baltic Sea (or any sea in that matter) as frequently as wave models can, the SAR data can be as valuable as any other satellite-based wave product (e.g., altimetry products). Altimetry products validations have shown reliable performance (RMSE less than 0.5 m) in the open ocean [44–47] and in the coastal sea (RMSE up to 0.37 m) [48–52]. However, the spatial coverage of altimetry products is limited and restricted to offshore areas (30–70 km from coast) [53]. The low-resolution altimetry wave products/algorithms and open ocean SAR wave mode products (not available for the coastal areas, including Baltic Sea) are not sufficient for local and regional applications in the complex coastal environment, such as Baltic Sea. The sea state products derived from Sentinel-1 SAR IW data provide information over a large area, including the coastal zone with similar product accuracy ($r = 0.88$, RMSE = 0.40 m, Table 3) to the altimetry products. Thus, the high-resolution SAR wave data would provide added value for user communities dealing with coastal processes. Moreover, SAR wave products enable to resolve detailed spatial variability while in situ data describes detailed temporal variability in a limited number of locations (Figures 4 and 5).

Besides NRT, an example of SAR data benefits is the statistical analysis of wave conditions (e.g., wave climate). Figure 6 represents the average wind speed and significant wave height values from Sentinel-1A/B IW data over the 2015 and 2016 interpolated onto WAM wave model grid. The average significant wave height values over the two-year period (Figure 6c) generally represent similar values to previous studies that used either model data reanalysis or altimetry products over a longer period (up to 23 years) (e.g., Figure 6 in Tuomi et al. [19]; Figure 2 in Kudryavtseva et al. [54]). There are clearly higher average wave height values in the open parts of the Baltic Sea (around 1.8 m) and lower values in the Gulf of Riga (up to 1.0 m in the open part; below 0.8 m in the coastal areas) or the Bothnian Sea (from 0.7 m to 1.2 m). However, from Figure 6a we can conclude that more than 100 points would be necessary for calculating average values since a limited number of samples may cause artificial features and improbable wind speed/wave height fields (e.g., in Southern Baltic Sea

(Figure 6b). Considering the long-term objectives of the Copernicus program and the revisit cycle of the Sentinel-1 mission, the statistical bases for wave mapping will improve over time.

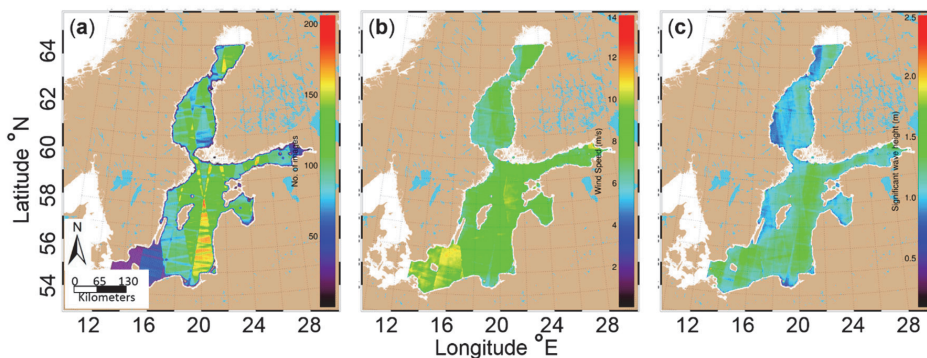


Figure 6. (a) Number of SAR points; (b) average wind speed; and (c) average significant wave height over 2015–2016 interpolated to WAM model grid.

Compared to altimetry, SAR data have a benefit of much higher resolution and larger coverage. For example, Kudryavtseva et al. [54] calculated average significant wave height maps for the Baltic Sea over the period of 23 years using approximately 660,000 data points with the end-resolution of $0.2 \times 0.1^\circ$. To retrieve the analogous map from SAR data, over 3 billion data points can be obtained from a two year period (using the 3 nm processing step). Furthermore, SAR data provides much greater detail, especially in the coastal zones where the vicinity of the coastline influences the altimetry signal and the related wave height retrievals.

6. Conclusions

A method for sea state parameter and marine wind estimation from Sentinel-1 IW SAR imagery in the Baltic Sea (proposed by Pleskachevsky et al. [20]) was validated. The sea state parameters were retrieved from image spectrum using an empirical algorithm CWAVE_S1-IW to estimate integrated sea state parameters directly from SAR image spectra without transformation into wave spectra. The study shows that wave field retrievals from Sentinel-1 IW SAR data correlate with in situ data ($r = 0.88$, RMSE = 0.40) as well as with WAM wave model ($r = 0.86$, RMSE = 0.47). Furthermore, the wind speed retrievals that were derived with the CMOD algorithm correlated with the values recorded at the coastal meteorological stations ($r = 0.91$, RMSE = 1.43).

The advantages of Sentinel-1 SAR IW mode wave products in Baltic Sea were demonstrated. The free/open data, high spatial resolution, large spatial coverage, and frequent acquisitions of Sentinel-1 A/B IW images leads to the following improvements that Sentinel-1 can offer to operational wave field monitoring and forecasting: (i) improved description of spatial variability of significant wave height; (ii) improved estimation of the area and the location of the storms during high sea state.

Considering the advantages, the operational wave product retrieved from Sentinel-1 A/B IW mode data by a dedicated algorithm for the coastal ocean (including Baltic Sea) would be valuable for many communities dealing with wave modelling, operational monitoring, and forecasting, etc. The SAR wave field retrievals would improve the downstream of monitoring services by improving the forecast accuracy, thus enabling a better understanding of coastal processes.

This work contributes to the uptake of Sentinel-1 A/B IW data in the fully automated operational service for meteo-marine parameter retrieval in the Baltic Sea. Implementation of Sentinel-1 sea state products for assimilation into an operational wave model and usage for model forecast quality checking

would improve general marine awareness. All the SAR processing methods presented in the study are running as NRT services in the German Aerospace Center's (DLR) ground station, Neustrelitz.

Author Contributions: S.R. was responsible for designing the study, processing and analysis of SAR data, interpretation of the results and writing the manuscript; A.P. was responsible for CWAVE_S1-IW method development and contributed in data analysis; S.J. was responsible for method development and contributed in writing the manuscript; V.A. performed wave model experiments and contributed in writing the paper; R.U. contributed in interpretation of results and writing the paper.

Acknowledgments: The authors express the gratitude towards ESA for making Sentinel constellation data freely available. Special thanks to Finnish Meteorological Institute (FMI), Swedish Meteorological and Hydrological Institute (SMHI), Estonian Environmental Agency (KAUR), and Latvian Environment, Geology and Meteorology Centre that have open data policy for wind and wave measurement data. We would also like to thank colleagues T. Kõuts, U. Lips, and K. Vahter at Department of Marine Systems at TUT for providing wave and wind measurement data. The authors are grateful for the DLR ground station Neustrelitz team for continuous cooperation and organization of the NRT services for the users. The corresponding author gratefully acknowledges the European Regional Development Fund for financial support for the stay in DLR's SAR Oceanography group. The author would also like to thank for the warm welcome by the SAR Oceanography group and the exceedingly qualified knowledge shared by them in various SAR-related subjects. The study was supported by institutional research funding IUT (19-6), by Personal Research Funding PUT1378 of the Estonian Ministry of Education and Research, by the European Regional Development Fund and through CMEMS Copernicus grant WAVE2NEMO.

Conflicts of Interest: The authors declare no conflict of interest.

References

1. Lehner, S.; Schulz-Stellenfleth, J.; Brusch, S.; Li, X.M. Use of TerraSAR-X data for oceanography. In Proceedings of the 2008 7th European Conference on Synthetic Aperture Radar (EUSAR), Rome, Italy, 26–30 May 2008; pp. 1–4.
2. Li, X.; Lehner, S.; Rosenthal, W. Investigation of ocean surface wave refraction using TerraSAR-X data. *IEEE Trans. Geosci. Remote Sens.* **2010**, *48*, 830–840.
3. Beal, R.C.; Tilley, D.G.; Monaldo, F.M. Large-And Small-Scale Spatial Evolution of Digitally Processed Ocean Wave Spectra from SEASAT Synthetic Aperture Radar. *J. Geophys. Res. Oceans* **1983**, *88*, 1761–1778. [[CrossRef](#)]
4. Masuko, H.; Okamoto, K.I.; Shimada, M.; Niwa, S. Measurement of Microwave Backscattering Signatures of the Ocean Surface Using X Band and Ka Band Airborne Scatterometers. *J. Geophys. Res. Oceans* **1986**, *91*, 13065–13083. [[CrossRef](#)]
5. Schulz-Stellenfleth, J. *Ocean Wave Measurements Using Complex Synthetic Aperture Radar Data*; University of Hamburg: Hamburg, Germany, 2004.
6. Hasselmann, K.; Hasselmann, S. On the Nonlinear Mapping of an Ocean Wave Spectrum into a Synthetic Aperture Radar Image Spectrum and Its Inversion. *J. Geophys. Res. Oceans* **1991**, *96*, 10713–10729. [[CrossRef](#)]
7. Hasselmann, S.; Brüning, C.; Hasselmann, K.; Heimbach, P. An Improved Algorithm for the Retrieval of Ocean Wave Spectra from Synthetic Aperture Radar Image Spectra. *J. Geophys. Res. Oceans* **1996**, *101*, 16615–16629. [[CrossRef](#)]
8. Schulz-Stellenfleth, J.; Lehner, S.; Hoja, D. A Parametric Scheme for the Retrieval of Two-Dimensional Ocean Wave Spectra from Synthetic Aperture Radar Look Cross Spectra. *J. Geophys. Res. Oceans* **2005**, *110*, C05004. [[CrossRef](#)]
9. Alpers, W.R.; Ross, D.B.; Rufenach, C.L. On the Detectability of Ocean Surface Waves by Real and Synthetic Aperture Radar. *J. Geophys. Res. Oceans* **1981**, *86*, 6481–6498. [[CrossRef](#)]
10. Lyzenga, D.R. Unconstrained Inversion of Waveheight Spectra from SAR Images. *IEEE Trans. Geosci. Remote Sens.* **2002**, *40*, 261–270. [[CrossRef](#)]
11. Bruck, M. *Sea State Measurements Using TerraSAR-X/TanDEM-X Data*; Christian-Albrechts-Universität zu Kiel: Kiel, Germany, 2015.
12. Li, X.M.; Lehner, S.; Bruns, T. Ocean Wave Integral Parameter Measurements Using ENVISAT ASAR Wave Mode Data. *IEEE Trans. Geosci. Remote Sens.* **2011**, *49*, 155–174. [[CrossRef](#)]
13. Pleskachevsky, A.L.; Rosenthal, W.; Lehner, S. Meteo-Marine Parameters for Highly Variable Environment in Coastal Regions from Satellite Radar Images. *ISPRS J. Photogr. Remote Sens.* **2016**, *119*, 464–484. [[CrossRef](#)]
14. Schulz-Stellenfleth, J.; König, T.; Lehner, S. An Empirical Approach for the Retrieval of Integral Ocean Wave Parameters from Synthetic Aperture Radar Data. *J. Geophys. Res. Oceans* **2007**, *112*, C03019. [[CrossRef](#)]

15. Stopa, J.E.; Mouche, A. Significant wave heights from Sentinel-1 SAR: Validation and applications. *J. Geophys. Res. Oceans* **2017**, *122*, 1827–1848. [[CrossRef](#)]
16. Schwarz, E.; Krause, D.; Berg, M.; Daelow, H.; Maass, H. Near Real Time Applications for Maritime Situational Awareness. *Int. Arch. Photogr. Remote Sens. Spat. Inf. Sci.* **2015**, *40*, 999–1003. [[CrossRef](#)]
17. Soomere, T.; Räämet, A. Spatial Patterns of the Wave Climate in the Baltic Proper and the Gulf of Finland. *Oceanologia* **2011**, *53*, 335–371. [[CrossRef](#)]
18. Björkqvist, J.-V.; Lukas, I.; Alari, V.; van Vledder, G.P.; Hulst, S.; Pettersson, H.; Behrens, A.; Männik, A. Comparing a 41-year model hindcast with decades of wave measurements from the Baltic Sea. *Ocean Eng.* **2018**, *152*, 57–71. [[CrossRef](#)]
19. Tuomi, L.; Kahma, K.K.; Pettersson, H. Wave hindcast statistics in the seasonally ice-covered Baltic sea. *Boreal Environ. Res.* **2011**, *16*, 451–472.
20. Pleskachevsky, A.; Jacobsen, S.; Tings, B.; Schwarz, E. Sea State from Sentinel-1 Synthetic Aperture Radar Imagery for Maritime Situation Awareness. *Int. J. Remote Sens.* submitted.
21. Rikka, S.; Pleskachevsky, A.; Uiboupin, R.; Jacobsen, S. Sea state in the Baltic Sea from space-borne high-resolution synthetic aperture radar imagery. *Int. J. Remote Sens.* **2018**, *39*, 1256–1284. [[CrossRef](#)]
22. Ressel, R.; Singha, S.; Lehner, S.; Rösel, A.; Spreen, G. Investigation into Different Polarimetric Features for Sea Ice Classification Using X-Band Synthetic Aperture Radar. *IEEE J. Sel. Top. Appl. Earth Obs. Remote Sens.* **2016**, *9*, 3131–3143. [[CrossRef](#)]
23. Singha, S.; Velotto, D.; Lehner, S. Dual-polarimetric feature extraction and evaluation for oil spill detection: A near real time perspective. In Proceedings of the 2015 IEEE International on Geoscience and Remote Sensing Symposium (IGARSS), Milan, Italy, 26–31 July 2015; pp. 3235–3238.
24. Velotto, D.; Bentes, C.; Tings, B.; Lehner, S. First Comparison of Sentinel-1 and TerraSAR-X Data in the Framework of Maritime Targets Detection: South Italy Case. *IEEE J. Ocean. Eng.* **2016**, *41*, 993–1006. [[CrossRef](#)]
25. Ardhuin, F.; Stopa, J.; Chapron, B.; Collard, F.; Smith, M.; Thomson, J.; Doble, M.; Blomquist, B.; Persson, O.; Collins III, C.O. Measuring ocean waves in sea ice using SAR imagery: A quasi-deterministic approach evaluated with Sentinel-1 and in situ data. *Remote Sens. Environ.* **2017**, *189*, 211–222. [[CrossRef](#)]
26. Shao, W.; Zhang, Z.; Li, X.; Li, H. Ocean wave parameters retrieval from Sentinel-1 SAR imagery. *Remote Sens.* **2016**, *8*, 707. [[CrossRef](#)]
27. Ardhuin, F.; Chapron, B.; Collard, F. Observation of swell dissipation across oceans. *Geophys. Res. Lett.* **2009**, *36*. [[CrossRef](#)]
28. Collard, F.; Ardhuin, F.; Chapron, B. Monitoring and analysis of ocean swell fields from space: New methods for routine observations. *J. Geophys. Res. Oceans* **2009**, *114*. [[CrossRef](#)]
29. Tuomi, L.; Vähä-Piikkiö, O.; Alari, V. *Baltic Sea Wave Analysis and Forecasting Product BALTICSEA_ANALYSIS_FORECAST_WAV_003_010*; Issue 1.0, CMEMS, 2017.
30. Tuomi, L.; Vähä-Piikkiö, O.; Alari, V. CMEMS Baltic Monitoring and Forecasting Centre: High-resolution wave forecast in the seasonally ice-covered Baltic Sea. In Proceedings of the 8th International EuroGOOS Conference, Bergen, Norway, 3–5 October 2017.
31. Von Schuckmann, K.; Le Traon, P.-Y.; Alvarez-Fanjul, E.; Axell, L.; Balmaseda, M.; Breivik, L.-A.; Brewin, R.J.; Bricaud, C.; Drevillon, M.; Drillet, Y.; et al. The Copernicus marine environment monitoring service ocean state report. *J. Oper. Ocean.* **2016**, *9*, s235–s320. [[CrossRef](#)]
32. Group, T.W. The WAM model—A third generation ocean wave prediction model. *J. Phys. Ocean.* **1988**, *18*, 1775–1810. [[CrossRef](#)]
33. Whitham, G.B. *Linear and Nonlinear Waves*; John Wiley & Sons: New York, NY, USA, 1974.
34. Stoffelen, A.; Anderson, D. Scatterometer data interpretation: Estimation and validation of the transfer function CMOD4. *J. Geophys. Res. Oceans* **1997**, *102*, 5767–5780. [[CrossRef](#)]
35. Hersbach, H.; Stoffelen, A.; de Haan, S. An improved C-band scatterometer ocean geophysical model function: CMOD5. *J. Geophys. Res. Oceans* **2007**, *112*. [[CrossRef](#)]
36. Monaldo, F.; Jackson, C.; Li, X.; Pichel, W.G. Preliminary evaluation of Sentinel-1A wind speed retrievals. *IEEE J. Sel. Top. Appl. Earth Obs. Remote Sens.* **2016**, *9*, 2638–2642. [[CrossRef](#)]
37. Thompson, D.R.; Elfouhaily, T.M.; Chapron, B. Polarization ratio for microwave backscattering from the ocean surface at low to moderate incidence angles. In Proceedings of the 1998 IEEE International on Geoscience and Remote Sensing Symposium (IGARSS'98), Seattle, WA, USA, 6–10 July 1998; pp. 1671–1673.

38. Horstmann, J.; Falchetti, S.; Wackerman, C.; Maresca, S.; Caruso, M.J.; Graber, H.C. Tropical cyclone winds retrieved from C-band cross-polarized synthetic aperture radar. *IEEE Trans. Geosci. Remote Sens.* **2015**, *53*, 2887–2898. [[CrossRef](#)]
39. Skamarock, W.C.; Klemp, J.B.; Dudhia, J.; Gill, D.O.; Barker, D.M.; Wang, W.; Powers, J.G. *A Description of the Advanced Research WRF Version 2 (No. NCAR/TN-468+ STR)*; National Center For Atmospheric Research Boulder Co Mesoscale and Microscale Meteorology Div: Boulder, CO, USA, 2005.
40. Haralick, R.M.; Shanmugam, K. Textural Features for Image Classification. *IEEE Trans. Syst. Man Cyber.* **1973**, *3*, 610–621. [[CrossRef](#)]
41. Romeiser, R.; Graber, H.C.; Caruso, M.J.; Jensen, R.E.; Walker, D.T.; Cox, A.T. A new approach to ocean wave parameter estimates from C-band ScanSAR images. *IEEE Trans. Geosci. Remote Sens.* **2015**, *53*, 1320–1345. [[CrossRef](#)]
42. Alari, V.; Staneva, J.; Breivik, Ø.; Bidlot, J.-R.; Mogensen, K.; Janssen, P. Response of water temperature to surface wave effects in the Baltic Sea: Simulations with the coupled NEMO-WAM model. In Proceedings of the EGU General Assembly Conference Abstracts, Vienna Austria, 17–22 April 2016; p. 4363.
43. European Maritime Safety Agency. *EMSA CleanSeaNet First Generation Report*; EMSA: Lisboa, Portugal, 2011.
44. Ducet, N.; Le Traon, P.-Y.; Reverdin, G. Global high-resolution mapping of ocean circulation from TOPEX/Poseidon and ERS-1 and-2. *J. Geophys. Res. Oceans* **2000**, *105*, 19477–19498. [[CrossRef](#)]
45. Pascual, A.; Faugère, Y.; Larnicol, G.; Le Traon, P.Y. Improved description of the ocean mesoscale variability by combining four satellite altimeters. *Geophys. Res. Lett.* **2006**, *33*. [[CrossRef](#)]
46. Pujol, M.-I.; Faugère, Y.; Taburet, G.; Dupuy, S.; Pelloquin, C.; Ablain, M.; Picot, N. DUACS DT2014: The new multi-mission altimeter data set reprocessed over 20 years. *Ocean Sci.* **2016**, *12*, 1067–1090. [[CrossRef](#)]
47. Ray, R.D.; Beckley, B. Simultaneous ocean wave measurements by the Jason and Topex satellites, with buoy and model comparisons special issue: Jason-1 calibration/Validation. *Mar. Geod.* **2003**, *26*, 367–382. [[CrossRef](#)]
48. Bouffard, J.; Vignudelli, S.; Cipollini, P.; Menard, Y. Exploiting the potential of an improved multimission altimetric data set over the coastal ocean. *Geophys. Res. Lett.* **2008**, *35*. [[CrossRef](#)]
49. Cazenave, A.; Bonnefond, P.; Mercier, F.; Dominh, K.; Toumazou, V. Sea level variations in the Mediterranean Sea and Black Sea from satellite altimetry and tide gauges. *Glob. Plan. Chang.* **2002**, *34*, 59–86. [[CrossRef](#)]
50. Kudryavtseva, N.A.; Soomere, T. Validation of the multi-mission altimeter wave height data for the Baltic Sea region. *arXiv*, 2016; arXiv:1603.08698.
51. Madsen, K.S.; Høyer, J.; Tscherning, C.C. Near-coastal satellite altimetry: Sea surface height variability in the North Sea–Baltic Sea area. *Geophys. Res. Lett.* **2007**, *34*. [[CrossRef](#)]
52. Vignudelli, S.; Cipollini, P.; Roblou, L.; Lyard, F.; Gasparini, G.; Manzella, G.; Astraldi, M. Improved satellite altimetry in coastal systems: Case study of the Corsica Channel (Mediterranean Sea). *Geophys. Res. Lett.* **2005**, *32*. [[CrossRef](#)]
53. Høyer, J.L.; Nielsen, J. Satellite significant wave height observations in coastal and shelf seas. In Proceedings of the Symposium on 15 Years of Progress in Radar Altimetry, Venice, Italy, 13–18 March 2006.
54. Kudryavtseva, N.; Soomere, T. Satellite altimetry reveals spatial patterns of variations in the Baltic Sea wave climate. *arXiv*, **2017**, arXiv:1705.01307.



Publication III

Rikka, S., Uiboupin, R., Kõuts, T., Vahter, K. and Pärt, S. A Method for Significant Wave Height from Circularly Polarized X-band Marine Radar Images. *IEEE Geoscience and Remote Sensing Letters*

A Method for Significant Wave Height Estimation From Circularly Polarized X-Band Coastal Marine Radar Images

S. Rikka¹, R. Uiboupin, T. Kõuts, K. Vahter, and S. Pärt

Abstract—Circularly polarized X-band coastal marine radar data have been used to develop the algorithm for estimating significant wave height (H_S) in the Tallinn Bay in the Gulf of Finland directly from radar images. Since sea state in the Tallinn Bay is mainly dominated by slight (WMO-3) windsea, the traditional methods where backscatter intensity variance spectrum is transferred to wave spectrum do not resolve wave height retrievals with sufficient accuracy. In contrast, an empirical method which uses only image spectrum and its parameters has proven to be applicable under these conditions. A wave height retrieval algorithm was developed for the short steep wind sea using image spectrum parameters in addition to Grey level co-occurrence matrix (GLCM) statistics of the radar signal intensity. In total, 1678 collocation pairs from October 18, 2016 to November 14, 2016 were used in the algorithm tuning process. The H_S results from radar images were collocated with *in situ* data from three buoys representing variable meteo-marine conditions. The comparison of radar-derived H_S with measured H_S shows high agreement with a correlation coefficient r of 0.78 (RMSE—0.23 m) for tuning data set. The method validation with independent data sets from January and June showed high correlation values of 0.82 (RMSE—0.26 m) and 0.89 (RMSE—0.25 m) correspondingly. In case of $H_S > 0.5$ m, the validation resulted in higher correlation (over 0.93) and lower RMSE (from 0.15 to 0.21 m). The spatial variability of wave height from radar imagery is demonstrated based on the commonly occurring north-western storm.

Index Terms—Baltic sea, GLCM, radar remote sensing, sea surface, wave height.

I. INTRODUCTION

THE sea-state parameters, such as significant wave height (H_S) or wind speed, are among the key parameters monitored for coastal protection, navigation, as well as offshore industry operations purposes. Therefore, most commonly wave gauges from fixed platforms or moored buoys are being used. To measure waves from greater distances, e.g., coastal stations or offshore platforms, marine X-band radars, among others, provide images of ocean surface due to the dependence of the backscattered signal on winds, ocean surface heights, currents, and long ocean waves [1]–[3].

Manuscript received March 27, 2018; revised August 30, 2018; accepted December 5, 2018. This work was supported in part by BONUS INNO under Project call2012Inno-24 Harnessing Coastal Radars for Environmental Monitoring Purposes, in part by Institutional Research Funding under Grant IUT (19-6), and in part by Personal Research Funding of the Estonian Ministry of Education under Grant PUT1378. (Corresponding author: Sander Rikka.)

The authors are with the Department of Marine Systems, Tallinn University of Technology, 12618 Tallinn, Estonia (e-mail: sander.rikka@tu.ee).

Color versions of one or more of the figures in this letter are available online at <http://ieeexplore.ieee.org>.

Digital Object Identifier 10.1109/LGRS.2018.2886631

It is well known that sea surface signatures are visible to X-band marine radar in HH or VV polarizations known as sea clutter [4]. The backscattering occurs because long surface waves modulate small-scale surface roughness which in turn modulates the radar backscatter. The modulation is a nonlinear process affected by three main effects: hydrodynamic and tilt modulation as well as shadowing [2], [3], [5]. Additional scattering mechanisms, e.g., wedge scattering [6] and scattering from microbreakers [4], contribute more towards the high incidence angles above 85°. At grazing incidence, shadowing modulation which is caused by the very low radar backscatter coming from diffraction in the geometrically shadowed areas of the waves have a major importance [2], [7].

Sequential radar images, with their high spatio-temporal resolution, offer an opportunity to derive and study wave field parameters in space and time. This has been used in a variety of applications, e.g., measuring spectral wave parameters [8], wave groups [9], or individual waves [10], [11]. Other related measurements include near-surface currents [12], [13] and bathymetry [14], [15] as well as surface winds [16]–[18]. To retrieve significant wave heights, one may transfer the radar image spectrum to a real wave amplitude spectrum using a modulation transfer function [8]. A major disadvantage of this method is the need for a calibration of each single radar installation site using *in situ* wave-measuring sensors [19], [20]. An alternative method is to evaluate shadowing in the X-band marine radar to estimate H_S without external reference for calibration [21]–[23].

In the paper at hand, an idea of using empirical methods to retrieve H_S from sequential radar image spectrums, without any modulation transfer function, is explored. The idea originates from synthetic aperture radar (SAR) data processing where image characteristics are used to measure sea state parameters in near-real-time applications [24], [25]. To apply the similar method on the marine radar images, incoherent non-Dopplerized circularly polarized radar data in the Paljassaare peninsula in the Tallinn Bay is used.

Tallinn Bay, situated in the Gulf of Finland in the Baltic Sea (Fig. 1), has previously been under the investigation relating to ship wakes and erosion caused by them [26]–[29]. Natural sea state in Tallinn Bay is inhomogeneous and generally small (WMO-1–WMO-3) influenced by local wind speed and direction; though, waves with the period of up to 8 s (WMO-6) have been recorded. High sea state is mostly generated by western winds which yield to waves propagating into the bay from between the mainland and Naissaare island [29]–[31].

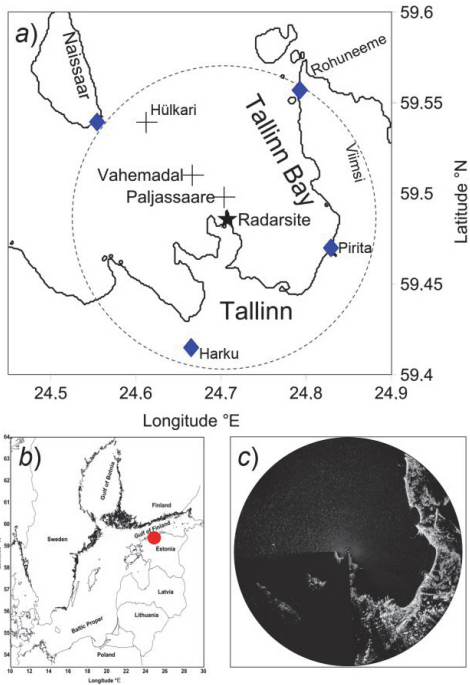


Fig. 1. Map of the Baltic Sea with zoomed-in view over Tallinn Bay area showing the radarsite in the middle (star) and buoy measurement location (crosses: Paljassaare, Vahemadal, Hülkari) for validation. Blue diamonds represent atmospheric measurement stations. On the below right, an example of a radar image over Tallinn Bay.

Extreme waves with the H_S up to 4.5 m entering the Tallinn Bay have been recorded [30].

In this letter, a new method for sea-state estimation is presented where the total significant wave height is obtained straight from the rasterized marine radar images using the empirical method. This letter is organized as follows. In Section II, the data description and the background of the method is overviewed and in Section III, the resulting method is presented and validated with the case studies and examples over the Tallinn Bay. In Section IV, the discussion and conclusion are given.

II. DATA

A. Paljassaare Radar Data

Shore-based marine radar data over the Tallinn Bay area was acquired for the current work (Fig. 1). The radar is located on the Paljassaare peninsula (24.70753° E, 59.48558° N) with the tower high of 26 m (27 m from sea level). The radar antenna is working in X-band, 9374 ± 30 MHz frequency, and the signal is circularly polarized.

The radar images are rasterized to rectangular 5 by 5 m pixel resolution with the dimensions of 4096 by 4096 pixels with the range of about 10 km from radar tower. 64 consecutive images are transferred at the beginning of every full hour. The time resolution of the consecutive images is 3 s.

TABLE I
OVERVIEW OF MEASUREMENT STATIONS

Buoy station	Paljassaare	Vahemadal	Hülkari
Longitude °E	24.7033	24.6662	24.6116
Latitude °N	59.4982	59.5102	59.5394
Distance (km)	1.42	3.60	8.07
Collocations	551	575	552

B. Buoy Measurements

Tallinn Bay has a stationary measurement station at Vahemadal lighthouse equipped with SeaGuard SW (Andersaa data instruments) measuring currents, water temperature, and salinity as well as basic wave parameters with a pressure sensor (Fig. 1, Table I). Sea-state parameters such as H_S and current speeds are measured all year around. The Vahemadal data allows extended validation of radar-derived sea state.

During the period from October 18, 2016 to November 14, 2016, two temporary mooring stations with pressure-based wave sensors were deployed within the radar range to have data for parametrization of H_S estimation algorithm. The mooring stations were at different distances from the radar tower to estimate incidence angle and shadowing effects on the radar data (Fig. 1, Table I).

Wave measurements at Hülkari and Paljassaare stations were carried out with piezoelectric pressure recorder LM2 by PTR Group OÜ, Tallinn, Estonia, pressure sensor from Keller Ltd (Switzerland). Instrument recorded pressure values at a given rate of 4 Hz. To measure the height of the water column above the sensor as precise as possible with wave periods less than 4 s, the instruments were installed approximately 2 m below surface. Measured pressure data were used for calculation of wave parameters [32], [33].

III. H_S ESTIMATION ALGORITHM

A. Image Preprocessing

Radar is an active remote sensor providing 2-D information of the normalized radar cross section (NRCS) σ_0 . The NRCS represents the surface reflectance of the radar signal and is defined as the normalized energy flux scattered by a unit area of the surface into a given direction. The backscatter is governed by the surface roughness on the scale of the radar wavelength. If the roughness of the imaged surface approximately satisfies the Bragg condition, constructive interference of the reflected radar signal in the direction of the sensor occurs.

The used σ_0 is first retrieved from pixel digital number DN

$$\sigma_0 = \text{DN}^2 \sin(\theta) \quad (1)$$

where θ is the local incidence angle of the signal. The value of each pixel $\sigma_0(x, y)$ of the subscene (x and y represent pixel coordinates) is then normalized resulting in $\sigma_n(x, y)$ used for sea state estimations

$$\sigma_n(x, y) = \frac{\sigma_0(x, y) - \langle \sigma_0 \rangle}{\langle \sigma_0 \rangle} \quad (2)$$

where $\langle \sigma_0 \rangle$ is the mean value of σ_0 in the subscene. Radar image analysis is based on a 2-D fast Fourier transform (FFT)

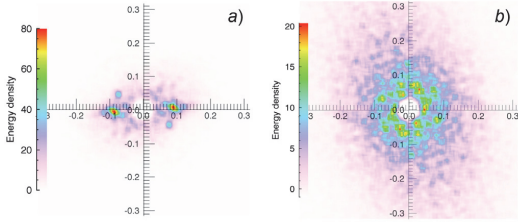


Fig. 2. (a) Image spectrum for January 4, 2017 at 10:00 UTC. (b) Image spectrum for June 5, 2017 at 10:00 UTC at the Vahemadal station.

of subscene which results in image spectra. The FFT window of 512×512 pixels covering the area of 2560×2560 m is used in the study with the overlap of 256 pixels for the calculations. FFT analysis is applicable for subscenes with sea state signal only, e.g., ships and other artifacts must be removed beforehand (done manually for the current study). To obtain the integrated value of the directional wave number E_{IS} , image power spectrum $IS(k_x, k_y)$ is integrated over k_x and k_y wavenumber in the 2-D domain

$$E_{IS} = \int_{k_x^{\min}}^{k_x^{\max}} \int_{k_y^{\min}}^{k_y^{\max}} IS(k_x, k_y) dk_x dk_y. \quad (3)$$

The integration is limited by $k_{\min} = 0.02$ and $k_{\max} = 0.36$ where $k = \sqrt{k_x^2 + k_y^2}$. All the image parameters, as well as the 2-D FFT spectrum is calculated for eight sequential images separately, and then averaged together. Thereafter, spectrum parameters, e.g., total integrated image spectrum energy or integrations in different wavenumber domains, are calculated for the averaged spectrum which is smoothed with boxcar average with a width of 7 pixels.

Fig. 2 presents examples smoothed image spectra for different sea-state conditions with radar-derived H_S of 2.5 and 0.5 m correspondingly. The method allows estimating H_S even in the case when imaged waves are not presented as wave-like looking structures.

B. Parametrization of H_S Estimation Algorithm

The H_S retrieval method was tuned using the collocated *in situ* data from three buoys deployed in the Tallinn Bay. In addition to traditional image parameters, e.g., image spectrum energy in different wavelength domains, and image spectrum noise statistics Grey level co-occurrence matrix (GLCM) statistics of the input radar signal were also calculated. The input signal for GLCM calculations are divided into 15 levels and frequency pairs are counted in the horizontal and vertical direction with one-pixel distance. The average value of both directions is then considered. The most well-known GLCM parameters such as entropy, homogeneity, contrast, variance, and mean as well as image spectrum parameters were used for sensitivity analysis [34].

The calculated parameters were tested against measured *in situ* values and best-fit trendline technique together with the Pearson correlation coefficient was used to choose image parameters that contain valuable information for H_S estimation. On Fig. 3(a), image spectrum energy E_{IS} is compared

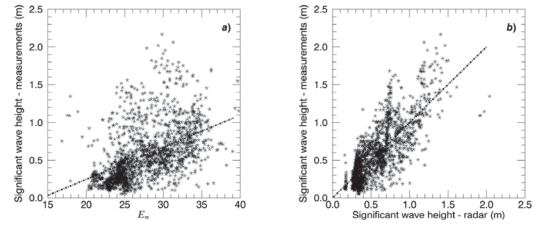


Fig. 3. (a) Measured H_S against E_{IS} . (b) Measured H_S against radar-derived H_S .

with measured H_S which is the starting point of algorithm parametrization ($r = 0.49$).

An empirical algorithm function uses the approach of a direct estimation of integrated sea-state parameters from radar image spectra without transformation into wave spectra. The algorithm is based on image spectra analysis and can be expressed for H_S estimation as follows:

$$H_S = a_0 \sqrt{B_0 E_{IS} \tan(\theta)} + \sum_{i=1, n}^n a_i B_i \quad (4)$$

where θ is local incidence angle, a_i are coefficients tuned during the validation. The functions B_i are designed to consider the effects caused by the distance between the subscene and radar tower, and shallow incidence angles that influence the imaging mechanisms

$$B_0 = f(d, \theta) = \frac{\theta}{d^4} \quad (5)$$

$$B_1 = f(d, \theta, \mu) = \mu((1 - \tan(\theta)) + \tan(d)) \quad (6)$$

$$B_2 = f(d, \theta, \sigma^2) = \sigma^2(\tan(\theta) + \tan(d)) \quad (7)$$

where the $\mu = (\mu_x + \mu_y)/2$ and $\sigma^2 = (\sigma_x^2 + \sigma_y^2)/2$ are mean and variance values, respectively,

$$\mu_x = \sum_{i=0}^{G-1} i P_x(i); \quad \mu_y = \sum_{j=0}^{G-1} j P_y(j) \quad (8)$$

$$\sigma_x^2 = \sum_{i=0}^{G-1} (P_x(i) - \mu_x(i))^2; \quad \sigma_y^2 = \sum_{j=0}^{G-1} (P_y(j) - \mu_y(j))^2 \quad (9)$$

where μ_x , μ_y , σ_x , and σ_y are the means and variances of P_x and P_y . $P_x(i)$ is the i th entry in the marginal-probability matrix obtained by summing the rows of $P(i, j)$ [analogous for $P_y(j)$ for columns of $P(i, j)$]. G denotes to a number of GLCM levels used.

After using all the beneficial parameters, the H_S is derived from radar data [Fig. 3(b)]. The results show higher agreement between collocated *in situ* measurements and calculated values from radar images with RMSE of 0.23 m, Pearson correlation coefficient of 0.78 and Scatter index of 0.41.

C. Validation of the Algorithm

To validate the proposed method, H_S was also calculated for two independent data sets. January 2017 [Fig. 4(a)] and June 2017 [Fig. 4(b)] radar data are compared with measurements from the Vahemadal station. The radar-derived H_S

TABLE II
STATISTICAL PARAMETERS FOR VALIDATION DATA SETS.

	January (January $H_S > 0.5$ m)	June (June $H_S > 0.5$ m)
r	0.82 (0.93)	0.89 (0.96)
RMSE (m)	0.26 (0.21)	0.25 (0.15)
SI	0.40 (0.23)	0.55 (0.17)
No. of col.	744 (454)	720 (255)

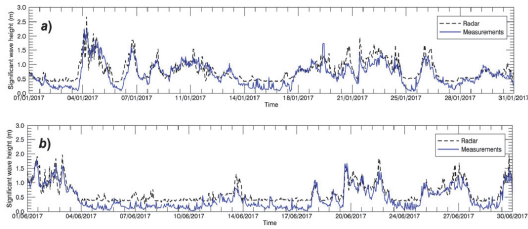


Fig. 4. Measured H_S (blue) and radar-derived H_S values (black) for (a) January 2017 and (b) June 2017 in the Vahemadal station.

values represent similar values to measured significant wave height with r of 0.82 for January and r of 0.89 for June data set (Fig. 4, Table II).

However, it is clearly seen in Fig. 4 that in low sea-state conditions, the radar-derived H_S values are overestimated. The reason might be that the radar signal loses its sensitivity at low sea state conditions with the limit being around 0.5 m which is a well-known limitation of marine radar data [10], [17], [35]–[38]. To demonstrate the difference, the statistics are also calculated for the H_S values over 0.5 m which show significant improvement (Table II).

D. Case Study During NW Storm

In comparison to *in situ* buoy measurements at a specific location, the radar data allow to cover larger areas and estimate the spatial distribution of investigated characteristics. Fig. 5(a) shows an example of spatial estimation of average H_S from marine radar images acquired between March 26, 2017 and March 28, 2017 when north-western winds were blowing with the average wind speed of 6.3 m/s (gusts up to 21.9 m/s).

The results in Fig. 5(a) are retrieved by interpolation from 29 by 29 pixels to 60 by 60 pixels using the Kriging method [39]. Although the interpolation has some negative effects on the edges of the data, the general H_S results show similar outcome as previous studies in [30], [40].

It is well seen from Fig. 5(a) how high waves propagate into Tallinn Bay between the mainland and Naissaare island having the local maximum around the tip of Paljassaare peninsula where the depth of the sea is up to 40 m. As the depth decreases, the wave height also decreases while propagating towards the coast.

The time series of *in situ* measurements and radar estimates of H_S also show good agreement during the storm event [Fig. 5(b)] with the correlation of 0.93 (RMSE=0.15).

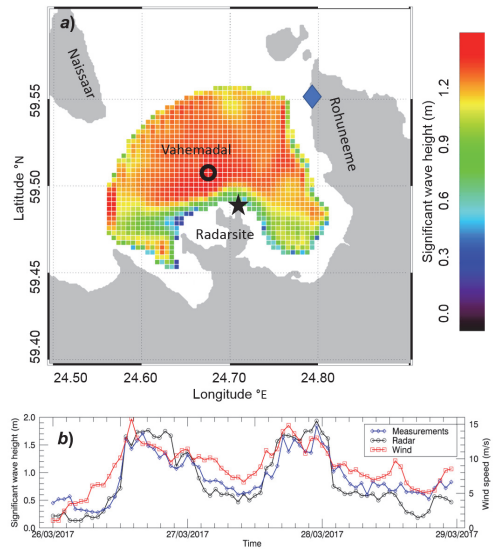


Fig. 5. (a) Average H_S for the north-west storm over the Tallinn Bay area. (b) Measured H_S (blue with diamonds), radar-derived H_S (black with rings) and wind speed at the Rohuneeme station (red with circles) for the storm period.

Moreover, the effect of wind variations in Rohuneeme station on local wave conditions can be observed.

IV. CONCLUSION

An empirical algorithm to derive significant wave height from high-resolution X-band marine radar data was developed for the low sea state conditions using Tallinn bay data set. The method relies purely on image spectra analysis together with GLCM statistics to overcome the limitations of transferring image spectra into wave spectra. Empirical methods on SAR data have proven to be accurate in the variety of sea-state conditions including specific low sea state conditions of the Baltic Sea [24], [41]–[44].

The study shows that wave field retrievals from marine radar data using developed algorithm correlate well with *in situ* measurements (r over 0.80, RMSE less than 0.30 m). The method was validated with January and June data set to test the algorithm in different of conditions. Validation of the method shows better correlation between measured H_S and radar-derived H_S values – $r = 0.82$ (RMSE=0.26 m and SI=0.40) and $r = 0.89$ (RMSE 0.25 and SI=0.55) correspondingly. In case of $H_S > 0.5$ m the validation resulted in higher correlation (over 0.93) and lower RMSE (below 0.21 m).

The developed method has a major advantage over previous studies (see [8], [19], [20], [23]) by utilizing all the rasterized data up to about 10 km from radar tower. This is achieved by using only image spectrum parameters and GLCM statistics of the sea surface imaged by radar.

ACKNOWLEDGMENT

The authors would like to thank Cybernetica AS for their collaboration in setting up radar data transferring and rasterizing images.

REFERENCES

- [1] P. H. Y. Lee *et al.*, "X band microwave backscattering from ocean waves," *J. Geophys. Res.*, vol. 100, no. C2, pp. 2591–2611, 1996.
- [2] W. J. Plant and G. Farquharson, "Wave shadowing and modulation of microwave backscatter from the ocean," *J. Geophys. Res., Oceans*, vol. 117, no. C8, pp. 1–14, 2012.
- [3] I. R. Young, W. Rosenthal, and F. Ziemer, "A three-dimensional analysis of marine radar images for the determination of ocean wave directionality and surface currents," *J. Geophys. Res., Oceans*, vol. 90, no. C1, pp. 1049–1059, 1985.
- [4] L. B. Wetzel, *Sea Clutter in Radar Handbook*, 2nd ed., M. Skolnik, Ed. New York, NY, USA: McGraw-Hill, 1990.
- [5] W. J. Plant and W. C. Keller, "Evidence of Bragg scattering in microwave Doppler spectra of sea return," *J. Geophys. Res., Oceans*, vol. 95, no. C9, pp. 16299–16310, 1990.
- [6] D. R. Lyzenga, A. L. Maffett, and R. A. Shuchman, "The contribution of wedge scattering to the radar cross section of the ocean surface," *IEEE Trans. Geosci. Remote Sens.*, vol. GRS-21, no. 4, pp. 502–505, Oct. 1983.
- [7] D. E. Barrick, "Near-grazing illumination and shadowing of rough surfaces," *Radio Sci.*, vol. 30, no. 3, pp. 563–580, 1995.
- [8] J. C. Nieto-Borge, K. Reichert, and J. Dittmer, "Use of nautical radar as a wave monitoring instrument," *Coastal Eng.*, vol. 37, nos. 3–4, pp. 331–342, Aug. 1999.
- [9] H. Dankert, J. Horstmann, S. Lehner, and W. Rosenthal, "Detection of wave groups in SAR images and radar image sequences," *IEEE Trans. Geosci. Remote Sens.*, vol. 41, no. 6, pp. 1437–1446, Jun. 2003.
- [10] H. Dankert and W. Rosenthal, "Ocean surface determination from X-band radar-image sequences," *J. Geophys. Res., Oceans*, vol. 109, no. C4, pp. 1–11, 2004.
- [11] J. C. Nieto-Borge, G. R. Rodríguez, K. Hessner, and P. I. González, "Inversion of marine radar images for surface wave analysis," *J. Atmos. Ocean. Technol.*, vol. 21, pp. 1291–1300, Aug. 2004.
- [12] W. Huang, R. Carrasco, C. Shen, E. W. Gill, and J. Horstmann, "Surface current measurements using X-band marine radar with vertical polarization," *IEEE Trans. Geosci. Remote Sens.*, vol. 54, no. 5, pp. 2988–2997, May 2016.
- [13] C. M. Senet, J. Seemann, and F. Ziemer, "The near-surface current velocity determined from image sequences of the sea surface," *IEEE Trans. Geosci. Remote Sens.*, vol. 39, no. 3, pp. 492–505, Mar. 2001.
- [14] P. S. Bell and J. C. Osler, "Mapping bathymetry using X-band marine radar data recorded from a moving vessel," *Ocean Dyn.*, vol. 61, no. 12, pp. 2141–2156, 2011.
- [15] C. M. Senet, J. Seemann, S. Flampouris, and F. Ziemer, "Determination of bathymetric and current maps by the method DiSC based on the analysis of nautical X-band radar image sequences of the sea surface (November 2007)," *IEEE Trans. Geosci. Remote Sens.*, vol. 46, no. 8, pp. 2267–2279, Aug. 2008.
- [16] H. Dankert and J. Horstmann, "A marine radar wind sensor," *J. Atmos. Ocean. Technol.*, vol. 24, pp. 1629–1642, Sep. 2007.
- [17] H. Dankert, J. Horstmann, and W. Rosenthal, "Ocean surface winds retrieved from marine radar-image sequences," in *Proc. IEEE Int. Geosci. Remote Sens. Symp. (IGARSS)*, Sep. 2004, pp. 1903–1906.
- [18] R. Vicen-Bueno, "Real-time ocean wind vector retrieval from marine radar image sequences acquired at grazing angle," *J. Atmos. Ocean. Technol.*, vol. 30, no. 1, pp. 127–139, 2013.
- [19] R. Carrasco, M. Strefler, and J. Horstmann, "A simple method for retrieving significant wave height from Dopplerized X-band radar," *Ocean Sci.*, vol. 13, no. 1, pp. 95–103, 2017.
- [20] R. Vicen-Bueno, C. Lido-Muela, and J. C. Nieto-Borge, "Estimate of significant wave height from non-coherent marine radar images by multilayer perceptrons," *EURASIP J. Adv. Signal Process.*, vol. 2012, p. 84, Dec. 2012.
- [21] R. Gangeskar, "An algorithm for estimation of wave height from shadowing in X-band radar sea surface images," *IEEE Trans. Geosci. Remote Sens.*, vol. 52, no. 6, pp. 3373–3381, Jun. 2014.
- [22] X. Liu, W. Huang, and E. W. Gill, "Wave height estimation from shipborne X-band nautical radar images," *J. Sensors*, vol. 2016, Jul. 2016, Art. no. 1078053.
- [23] Y. Wei, Z. Lu, G. Pian, and H. Liu, "Wave height estimation from shadowing based on the acquired X-band marine radar images in coastal area," *Remote Sens.*, vol. 9, no. 8, p. 859, 2017.
- [24] A. L. Pleskachevsky, W. Rosenthal, and S. Lehner, "Meteo-marine parameters for highly variable environment in coastal regions from satellite radar images," *ISPRS J. Photogramm. Remote Sens.*, vol. 119, pp. 464–484, Sep. 2016.
- [25] E. Schwarz, D. Krause, M. Berg, H. Daelow, and H. Maass, "Near real time applications for maritime situational awareness," *Int. Arch. Photogram., Remote Sens. Spatial Inf. Sci.*, vol. XL-7/W3, no. 7, pp. 999–1003, 2015.
- [26] A. Erm and T. Soomere, "The impact of fast ferry traffic on underwater optics and sediment resuspension," *Oceanologia*, vol. 48, pp. 283–301, 2006.
- [27] J. Kask, A. Talpas, A. Kask, and K. Schwarzer, "Geological setting of areas endangered by waves generated by fast ferries in Tallinn Bay," *Proc. Estonian Acad. Sci., Eng.*, vol. 9, no. 3, pp. 185–208, 2003.
- [28] T. Soomere, K. E. Parnell, and I. Didenkulova, "Water transport in wake waves from high-speed vessels," *J. Marine Syst.*, vol. 88, no. 1, pp. 74–81, 2011.
- [29] T. Soomere and K. Rannat, "An experimental study of wind waves and ship wakes in Tallinn Bay," *Proc. Estonian Acad. Sci., Eng.*, vol. 9, no. 3, pp. 157–185, 2003.
- [30] T. Soomere, "Wind wave statistics in Tallinn Bay," *Boreal Environ. Res.*, vol. 10, no. 2, pp. 103–118, 2005.
- [31] L. Tuomi and K. K. H. Kahma Pettersson, "Wave hindcast statistics in the seasonally ice-covered Baltic sea," *Boreal Environment Res.*, vol. 16, no. 6, pp. 451–472, 2011.
- [32] V. Alari, U. Raudsepp, and A. Erm, "Comparison of ADV measured near-bed orbital speed and latter derived from wave gauge measurements at intermediate water depths," in *Proc. IEEE/OES Baltic Int. Symp. (BALTIC)*, Aug. 2010, pp. 1–7.
- [33] V. Alari, U. Raudsepp, and T. Kõuts, "Wind wave measurements and modelling in Küdema Bay, Estonian Archipelago Sea," *J. Marine Syst.*, vol. 74, pp. S30–S40, Dec. 2008.
- [34] R. M. Haralick, K. Shanmugam, and I. Dinstein, "Textural features for image classification," *IEEE Trans. Syst., Man, Cybern.*, vol. SMC-3, no. 6, pp. 610–621, Nov. 1973.
- [35] *Wave and Surface Current Monitoring System Operating Manual Version 4.0*. OceanWaves GmbH, Luneburg, Germany, 2012.
- [36] D. V. Ivonin, V. A. Telegin, P. V. Chernyshov, S. A. Myslenkov, and S. B. Kuklev, "Possibilities of X-band nautical radars for monitoring of wind waves near the coast," *Oceanology*, vol. 56, no. 4, pp. 591–600, 2016.
- [37] Y. Liu, W. Huang, E. W. Gill, D. K. Peters, and R. Vicen-Bueno, "Comparison of algorithms for wind parameters extraction from shipborne X-band marine radar images," *IEEE J. Sel. Topics Appl. Earth Observ. Remote Sens.*, vol. 8, no. 2, pp. 896–906, Feb. 2015.
- [38] L. Wang, X. Wu, X. Yue, K. Ma, and Y. Tian, "A novel algorithm in estimating signal-to-noise ratio for ocean wave height inversion from X-band radar images," *IEEE Geosci. Remote Sens. Lett.*, vol. 13, no. 3, pp. 344–348, Mar. 2016.
- [39] E. H. Isaaks and R. M. Srivastava, *An Introduction to Applied Geostatistics*. New York, NY, USA: Oxford Univ. Press, 1989.
- [40] V. Alari and U. Raudsepp, "Depth induced breaking of wind generated surface gravity waves in Estonian coastal waters," *Boreal Environ. Res.*, vol. 15, no. 3, pp. 295–300, 2010.
- [41] A. Pleskachevsky, S. Jacobsen, B. Tings, and E. Schwarz, "Estimation of sea state from sentinel-1 synthetic aperture radar imagery for maritime situation awareness," *Int. J. Remote Sens.*, to be published, doi: 10.1080/01431161.2018.1558377.
- [42] A. Pleskachevsky, S. Jacobsen, B. Tings, E. Schwarz, and D. Krause, "Sea state retrieval from Sentinel-1 SAR imagery: Towards near maritime situation awareness," in *Proc. 12th Eur. Conf. Synth. Aperture Radar (EUSAR)*, Aachen, Germany, Jun. 2018, pp. 1–6.
- [43] S. Rikka, A. Pleskachevsky, S. Jacobsen, V. Alari, and R. Uiboupin, "Meteo-marine parameters from Sentinel-1 SAR imagery: Towards near real-time services for the Baltic Sea," *Remote Sens.*, vol. 10, no. 5, p. 757, 2018.
- [44] S. Rikka, A. Pleskachevsky, R. Uiboupin, and S. Jacobsen, "Sea state in the Baltic Sea from space-borne high-resolution synthetic aperture radar imagery," *Int. J. Remote Sens.*, vol. 39, no. 4, pp. 1256–1284, 2018.

Publication IV

Rikka, S., Uiboupin, R., & Alari, V. (2017). Applicability of SAR-based wave retrieval for wind-wave interaction analysis in the fetch-limited Baltic. *International journal of remote sensing*, 38(3), 906–922.

Applicability of SAR-based wave retrieval for wind–wave interaction analysis in the fetch-limited Baltic

Sander Rikka^a, Rivo Uiboupin^a and Victor Alari^{b*}

^aModelling and Remote Sensing, Marine Systems Institute at Tallinn University of Technology, Tallinn, Estonia; ^bInstitute of Coastal Research, Helmholtz-Zentrum Geesthacht, Geesthacht, Germany

ABSTRACT

In this article, a method for the detection of wave field parameters from synthetic aperture radar (SAR) imagery in the fetch-limited Baltic Sea is presented. Over the Baltic Sea region, common south-west (SW) and west (W) winds induce steep waves with shorter wavelengths compared with ocean waves. Thus, with the use of previous SAR sensors (e.g. ENVISAT/ASAR), it was not possible to detect individual waves and retrieve image wave number spectra. Since the year 2007, when TerraSAR-X (TS-X) reached its orbit, high spatial resolution data is available for measuring the sea-state parameters: the individual waves up to 30 m wavelength and their refraction can be distinguished. The main objective of this work was to demonstrate the capability of detecting wave field parameter from (TS-X) imagery in the Baltic Sea. The wave field parameters obtained from the SAR imagery were compared with *in situ* measurements and the Simulating WAVes Nearshore (SWAN) wave model. The comparison of SAR-based wave field information with buoy measurements showed high agreement in case of wave propagation direction ($r = 0.95$) and wavelength ($r = 0.83$). A significant correlation is also seen between SWAN- and SAR-derived wave propagation direction ($r = 0.87$) and wavelengths ($r = 0.91$). With the case studies, it is shown that SAR data enables one to detect land shadow effects and small-scale wave field variations in the coastal zone. It was shown that SAR data is also valuable for improving and interpreting the wave model results. In consequence of common slanting fetch cases over the Baltic Sea region, it was demonstrated that the peak wave directions differ from the mean wind directions up to 43°.

ARTICLE HISTORY

Received 25 April 2016
Accepted 30 November 2016

1. Introduction

The Baltic Sea is a large inland sea with seasonal ice-coverage located between 53° N to 66° N and from 9° E to 30° E. The total area of the Baltic Sea with its several topographically and geographically separated sub-basins is 392,978 km². The mean water depth is 54 m, whereas the deepest part, Landsort Deep, reaches 459 m (Leppäranta and Myrberg 2009).

CONTACT Sander Rikka  sander.rikka@msi.ttu.ee  Department of Modelling and Remote Sensing, Marine Systems Institute at Tallinn University of Technology, Akadeemia Rd 15a, Tallinn, Estonia

*Present affiliation: Marine Systems Institute at Tallinn University of Technology

Complex wave conditions are produced in the Baltic Sea due to the complexity of the sea: mainly shallow areas, narrow bays, thousands of islands, etc. In addition, heavy ice conditions during winter complicate the instrumental measurements of wave parameters. Systematical wave measurements began in the early 1970s by the Helsinki University of Technology and the Finnish Institute of Marine Research (FIMR). Periodical measurements started in the Bothnian Sea from 1972 (Kahma 1976, 1981). Currently, numerous studies have been carried out using wave model estimations (Jönsson, Broman, and Rahm 2003; Cieřlikiewicz and Paplińska-Swempel 2008; Soomere et al. 2008; Räämet 2010; Tuomi, Kahma, and Pettersson 2011; Alari 2013; Suursaar 2013; Siewert, Schlamkow, and Saatho 2015).

Typical wave field parameters can differ significantly, depending on the sub-basin of the Baltic Sea. Wave periods remain short, usually not exceeding 7–8 s, which means that long-period swell is almost absent (Leppäranta and Myrberg 2009; Raudsepp et al. 2011). The dominant wavelengths are between 20 and 70 m. However, wavelengths can grow up to 130 m in case of favourable conditions: wind speed, duration, direction stability, and water depth (Hydrometeorological...1983; Kriauciūnienė, Gailiūšis, and Kovalenkoviėnė 2006). The longest possible fetch in the Baltic Sea is 700 km in the Baltic Proper. Along the major axis of the Gulf of Finland (GoF), the longest fetch is 500 km. In the Baltic Sea, the waves are propagating typically in the direction of the wind. Dominant wind direction and thus main forcing for wave field generation in the Baltic Sea region is from sector 180–270° (Jaagus and Kull 2011). However, together with the geometry of the Baltic Sea, slanting fetch cases are often observed where the wind direction and peak wave direction differ from each other up to 50° in deep water (Pettersson, Kimmo, and Tuomi 2010). Wind speed in the Baltic Sea region has a clear annual cycle, with monthly mean wind speeds above the yearly average in autumn-winter and below that in spring-summer (Niros, Vihma, and Launiainen 2002). Over the Baltic Sea, the yearly average wind speeds are 6–8 m s⁻¹ and the monthly values deviate about it up to 1.5 m s⁻¹ (Niros, Vihma, and Launiainen 2002; Suursaar, Jaagus, and Kullas 2006).

Since 2007, when TerraSAR-X (TS-X) reached its orbit, new opportunities have been made available for the retrieval of information on surface wind waves in the Baltic Sea. Its high-resolution data enables one to detect two-dimensional (2D) wave spectra even in the Baltic Sea, where the wavelength is significantly smaller compared with the ocean waves. The adeptness of the TS-X sensor for the open ocean regions has been demonstrated in previous studies (Ming Li, Lehner, and Wolfgang 2010; Diaz Méndez et al. 2010; Lehner, Pleskachevsky, and Bruck 2012; Bruck and Lehner 2013). The TS-X sensor is capable of measuring wavelengths as short as 30 m (Lehner, Pleskachevsky, and Bruck 2012), which gives the reason to explore its advantages for wave field observations and analysis over the Baltic Sea regions as well.

The current work focuses on the wave propagation direction and the peak wavelength in different locations of the Baltic Sea. Wave measurements data and wave model estimations (Simulating WAVes Nearshore – SWAN) are used for the validation of synthetic aperture radar (SAR)-based wave retrievals. The wind propagation direction is analysed together with the wave propagation direction to (i) demonstrate the slanting fetch phenomenon, which is common in the Baltic Sea, using multi-source wave information and (ii) wave field variability when waves travel through straits and across sills.

2. Estimation of wave parameters

2.1. Data

For the current work, the TS-X multilook ground range detect (MGD) Stripmap products were used. The data was provided by German Aerospace Center (DLR) via the EOWEB® interface. Images were acquired with both HH and VV polarizations. Single image usually covers the area of about 30×50 km with a pixel spacing of 1.25 m. The azimuth resolution of the image is 3.3 m, and the range resolution – depending on the incidence angle of the acquisition – varies between 1.7 and 3.5 m. The products were gridded to 1.25 m resolution by a DLR prior to further processing and wave parameter retrieval.

A total of 43 TS-X images were acquired between 2012 and 2013 (Figure 1), of which 35 were matched with either buoy location or SWAN results. Since some images covered several buoy locations, there are 44 matchups with buoy data and 55 matchup pairs with SWAN data (Table 1). There were four major characteristic regions of interests – a) open sea

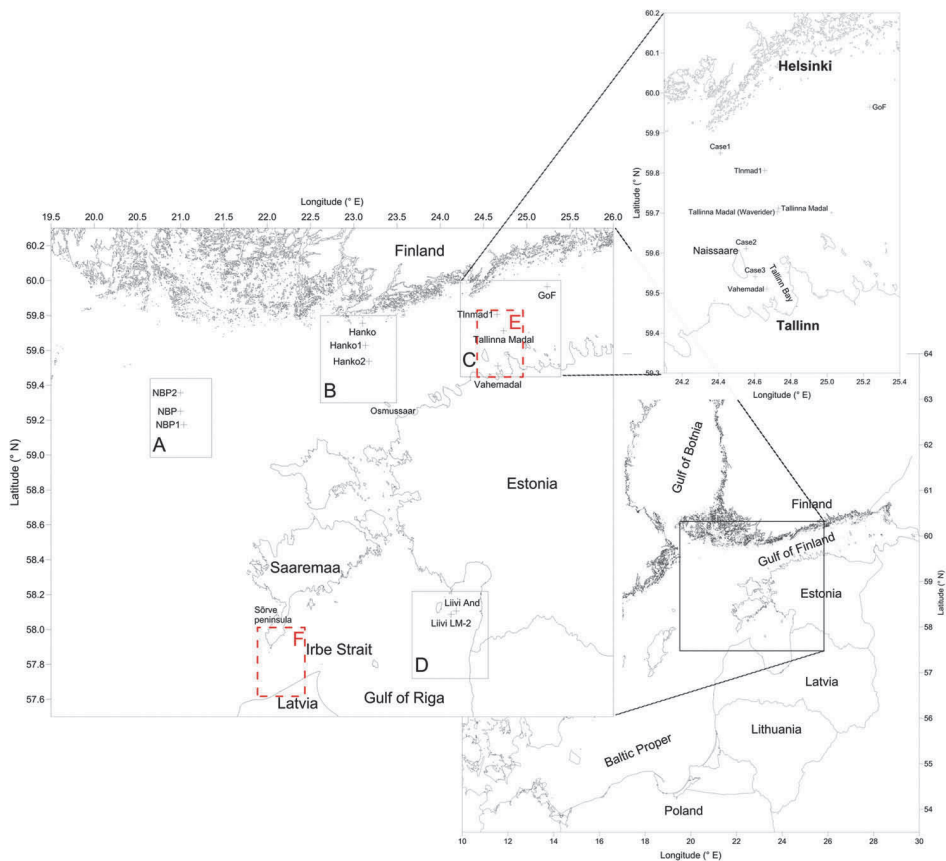


Figure 1. Map of the Baltic Sea; Northern Baltic Proper with four major study regions and matching buoy locations where images were acquired; detailed view over the Tallinn Bay area in Gulf of Finland. Four study regions – A) Northern Baltic Proper, B) region near the Hanko peninsula, C) region over Tallinna Madal and Helsinki, and D) Gulf of Riga. Red dashed lines show the regions of two case studies presented in Figure 4 (Tallinna Madal case – E) and Figure 9 (Irbe Strait case – F).

Table 1. Overview of data used in the study. Region (A, B, C, D) refers to boxes on Figure 1.

	Region							
	A		B		C		D	
No. of images	6		11		15		3	
Polarization	HH	VV	HH	VV	H	VV	HH	VV
No. of images	3	3	5	6	8	7	3	0
Matching buoys	NBP		Hanko		Tallinna Madal Temp. Buoy Vahemadal GoF		Liivi And Liivi LM-2	
No. of matches	6		7		25		6	
Matching SWAN locations	NBP NBP1 NBP2		Hanko Hanko1 Hanko2		Tallinna Madal Tallinna madal1 Vahemadal		Liivi And Liivi LM-2	
No. of matches	12		21		16		6	

conditions are represented by Northern Baltic Proper (with buoy station named NBP); b) entrance of the GoF is represented by measurements near the Hanko peninsula (Hanko buoy station); c) central part of the GoF is represented by a number of stations between Tallinn and Helsinki (stationary buoy stations Tallinna Madal, Vahemadal, GoF and temporary buoy station nearby to Tallinna Madal); and d) the Gulf of Riga (GoR) area is represented by measurements at the entrance of the Pärnu bay (buoy stations Liivi And and Liivi LM-2). Images were acquired during stormy conditions (wind speed $>9 \text{ m s}^{-1}$) to capture well-developed wave field conditions on the SAR image.

Extracted wave field parameters from the SAR data were compared with *in situ* buoy measurements. Three different buoy types were used: Acoustic Doppler Current Profiler (ADCP), Waveriders, and pressure sensors. In total, eight buoy stations and five additional grid points for SWAN comparisons (numbered items on Figure 1 and in Table 1) covering different timeframes were used. Data from Baltic Sea Bathymetry Database (Baltic Sea Hydrographic Commission 2013) was used for the topography settings in wave characteristics retrieval from different buoy measurements. Detailed information about the timeframes, locations, and buoy types is shown in Table 2.

The SAR-based wave field parameters were compared with the SWAN numerical wave model data. SWAN is a third-generation wave model (Booij, Ris, and Holthuijsen 1999; SWAN team 2014) that uses 2D equation to describe wave action:

$$\frac{\partial N}{\partial t} + (\mathbf{c}_g + \mathbf{U}) \nabla_{x,y} N + \frac{\partial c_\sigma N}{\partial \sigma} + \frac{\partial c_\theta N}{\partial \theta} = \frac{S_{\text{tot}}}{\sigma}. \quad (1)$$

The first term represents the local rate of change of action density; the second term denotes the propagation of wave energy in 2D geographical space, with \mathbf{c}_g being the group velocity and \mathbf{U} the ambient current. The third term represents the effect of shifting of the radian frequency due to variations in depth and mean currents. The fourth term represents the depth-induced and current-induced refraction. The quantities c_σ and c_θ are the propagation velocities in spectral space (σ, θ) , with σ and θ representing the radian frequency and propagation direction, respectively. The right-hand side contains the source term S_{tot} that represents all physical processes known that generate, dissipate, or redistribute wave energy in SWAN.

Table 2. Information about the different timeframes, buoy locations, and types.

Station	Timeframe	Longitude (° E)	Latitude (° N)	Buoy type	Data collected
NBP	2012–2013	20.9960	59.2500	Waverider	$H_s/T_p/\gamma_p$
Hanko	8 September 2013– 26 November 2013	23.1010	59.9650	ADCP	$H_s/T_{avg}/\gamma_{avg}$
Tallinna Madal	2012–2013	24.7320	59.7120	Pressure	H_s/T_{avg}
Tallinna Madal	11 October 2013– 17 November 2013	24.7250	59.7028	Waverider	$H_s/T_p/\gamma_p$
Vahemadal	2012–2013	24.6662	59.5102	Pressure	H_s/T_{avg}
GoF	2012–2013	25.2350	59.9650	Waverider	$H_s/T_p/\gamma_p$
Liivi And	25 August 2012– 21 September 2012	24.1844	58.1065	Pressure	H_s/T_p
Liivi LM-2	25 August 2012– 17 September 2012	24.1255	58.0860	Pressure	H_s/T_p
NBP1	2012–2013	21.0345	59.1741	SWAN	$H_s/T_p/\gamma_p$
NBP2	2012–2013	20.9960	59.3566	SWAN	$H_s/T_p/\gamma_p$
Hanko1	2012–2013	23.1367	59.6289	SWAN	$H_s/T_p/\gamma_p$
Hanko2	2012–2013	23.1752	59.5371	SWAN	$H_s/T_p/\gamma_p$
Tlnmad1	2012–2013	24.6551	59.5102	SWAN	$H_s/T_p/\gamma_p$

H_s : significant wave height; T_p : peak period; γ_p : peak propagation direction; T_{avg} : average period; γ_{avg} : average propagation direction.

The extracted parameters from the SWAN wave model were significant wave height, peak wave direction, and peak wavelength. The output data of SWAN had a temporal resolution of 1 h. SWAN (version 40.85) was running in operational mode for the Baltic Sea covering it with one nautical mile grid. The wave spectrum in SWAN consisted of 24 equally spaced directions and 32 frequencies distributed logarithmically in the frequency range 0.05–1.00 Hz. The integration time step of 15 min was used. The model was forced with winds from ECMWF, which had a spatial resolution of 1/12 of a degree and a temporal resolution of 3 h. Digital topography covering the entire Baltic Sea with a resolution of 1 nautical mile (Seifert, Tauber, and Kayser 2001) was used. Current and spatial varying water levels were not considered in this study.

The SWAN model has been validated for coastal waters in the Baltic Sea (Alari, Raudsepp, and Kõuts 2008; Raudsepp et al. 2011; Viitak et al. 2016) as well as for offshore areas (Björkqvist et al., forthcoming). For the Baltic Proper area, the overall bias between the measurements and the model was –3 cm (model underestimated) and for GoF it was –1 cm (Björkqvist et al. 2016). The model also performs extremely well in the coastal areas and during extreme storms (Viitak et al. 2016). Therefore, this model is suitable for Baltic Sea conditions and provides a fair estimate of the wave parameters.

Wind measurements at Ristna station are provided by Estonian Environmental Agency (KAUR) and at Tallinna Madal station by Marine Systems Institute at Tallinn University of Technology. Utö, Hanko, and Kalbodagrund wind measurements are provided by the Finnish Meteorological Institute (FMI).

Matchup data pairs between SAR and *in situ* data as well as between SAR and SWAN were formed using the following criteria: (1) time difference between SAR acquisition and *in situ* measurements is less than 5 min in case of pressure sensor data (Tlnmad, Vahemad, Liivi LM-2, Liivi And), 30 min in case of Hanko station, and 1 h in case of Waverider data (at locations NBP, GoF, and SWAN model data); (2) the centre of the SAR sub-image (512 × 512 pixels) was located at the geographical location of measurement buoy or at the centre of the SWAN model grid point.

2.2. Method

The SAR sensor measures the backscatter, which is a measure of the roughness of the surface. Over the water surface, short surface waves, whose wavelength is similar to the ones of the radar signal, are the cause of surface roughness. Constructive interference in the direction of sensor occurs, when these small capillary waves (Bragg condition) with wavelength λ_B are related to radar wave frequency or wavelength λ_r at the incidence angle θ by the following equation:

$$\lambda_B = \lambda_r / 2 \sin \theta. \quad (2)$$

For moderate incidence angles (20° – 60°), Bragg scattering is the dominant scattering mechanism (Lehner et al. 1998), which is nearly always satisfied because of the uniform distribution of the small-scale waves (Jackson and Koch 2005).

By applying the fast Fourier transform (FFT) for the SAR sub-image, a 2D image spectrum is retrieved. The maximum values on the spectrum indicate the peak wavenumber and peak propagation direction of all visible waves on the sub-image. Refracting waves around island for instance produce spectra with multiple peaks. Since peak wavenumber is obtained from the spectrum, wavelength is easily calculated by taking a reciprocal value:

$$\lambda = \frac{2\pi}{\sqrt{k_x^2 + k_y^2}}, \quad (3)$$

and the peak wave propagation direction is calculated by

$$\gamma = \arctan\left(\frac{k_y}{k_x}\right), \quad (4)$$

where λ is the peak wavelength and γ is the peak direction with respect to the image spectrum. Peak coordinates in the wave number space are given by k_x and k_y , where y denotes azimuth (satellite flight direction) and x denotes range direction. Owing to the static nature of the SAR image, the retrieved peak direction has an ambiguity of 180° , which has to be eliminated with the information about wave direction from the cross spectrum or other sources. For our case, either information from measurements or SWAN data was used.

Surface waves are described by the dispersion relationship, which relates angular frequency ω to wavenumber k and water depth h :

$$\omega = \sqrt{gk \tanh(kh)}, \quad (5)$$

where g is acceleration of gravity and \tanh denotes a hyperbolic tangent. In deep water, where $kh \rightarrow \infty$, the $\tanh(kh) \approx 1$ and equation (5) reduces to $\omega = \sqrt{gk}$. Simple translation of angular frequency $\omega = 2\pi/T$, where T is referred to as the wave period.

Retrieval of the image spectrum and the related wave field parameters consists of several sub-activities. First, the FFT operator is used to calculate the image wavenumber spectrum. Spectrum calculations also include speckle filtering. Here we have used Hanning filtering in Fourier analysis (α factor of 0.5) and boxcar average for smoothing. The dominant wavelength, represented as the maximum value on the spectrum image,

and the wave propagation direction can be read from the 2D spectrum using equations 3 and 4, respectively.

Integrated spectral energy E is calculated from the SAR image wavenumber spectrum using the following equation:

$$E = \int_{k_{\max}}^{k_{\min}} \int_{2\pi}^0 S(k, \varphi) dk d\varphi, \quad (6)$$

where $S(k, \varphi)$ is the image spectrum obtained through FFT. Wavenumber limits are set as follows: $k_{\max} = 0.04 \text{ rad m}^{-1}$ and $k_{\min} = 0.41 \text{ rad m}^{-1}$, which correspond to wavelengths $\lambda_{\max} = 150 \text{ m}$ and $\lambda_{\min} = 15 \text{ m}$, respectively. The spectrum energy calculated is used in the XWAVE (Ming Li, Lehner, and Wolfgang 2010; Bruck et al. 2011; Lehner, Pleskachevsky, and Bruck 2012) algorithm to which the method generally agrees.

The sub-image size for the spectrum analysis was 512×512 pixels ($640 \times 640 \text{ m}$) for all the comparisons and case study images in order to study the coastal zone where a smaller box size allows one to measure closer to the shore. Also considering that the wavelengths in the Baltic Sea often remain between 20 and 80 m, there would be 8–30 single waves on one sub-image for the spectrum analysis. Wavenumber resolution in this case is 0.002 m.

The results of wave field parameters derived from the satellite imagery were compared with *in situ* measurements and wave model outputs. Wave propagation direction and peak periods from SAR calculations were collocated with wave model and *in situ* measurement values and presented on scatter plots with Pearson correlation coefficient r and p -value. The root mean square deviation (RMSD) and bias were also calculated between SAR, *in situ* measurements, and wave model values (SAR minus buoy or wave model values).

3. Results and case studies

Figures 2 and 3 show the comparison of the derived TS-X integrated sea-state parameters collocated with *in situ* buoy measurements and SWAN wave model results. Comparison demonstrates that the TS-X sensor is suitable for the estimation of wave

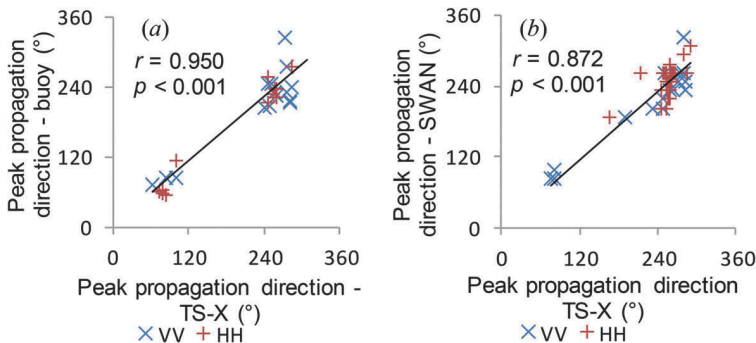


Figure 2. (a) Wave propagation direction derived from TS-X compared to *in situ* measurements, (b) wave propagation direction derived from TS-X compared to SWAN wave model results.

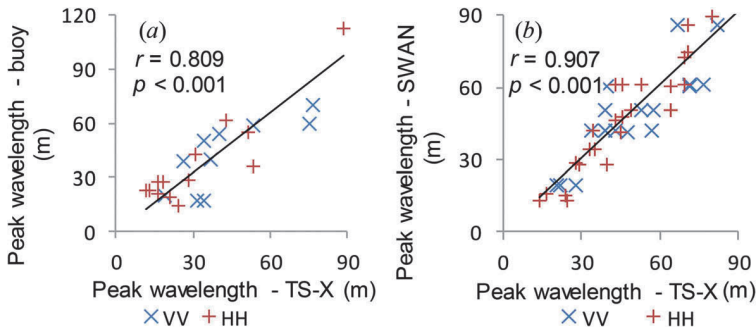


Figure 3. (a) Peak wavelength calculated from the TS-X spectrum data compared to wavelengths from buoy measurements, (b) peak wavelength retrieved from the TS-X spectrum compared to peak wavelengths from the SWAN wave model.

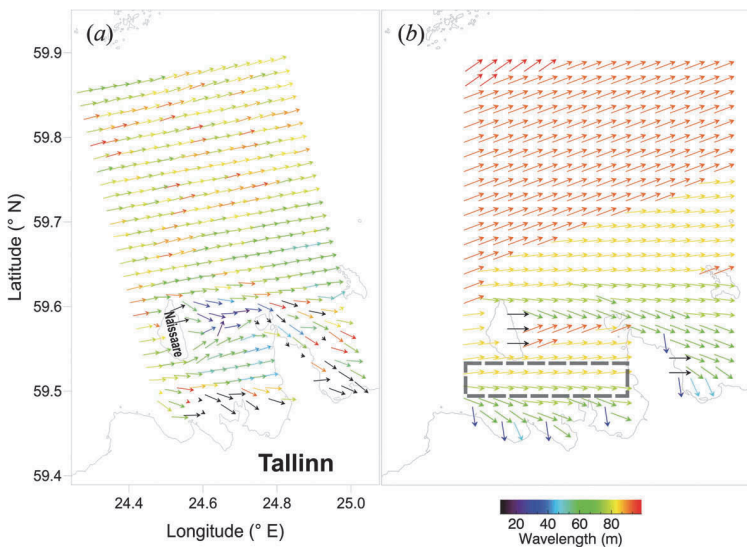


Figure 4. (a) Wavelength field derived from the TS-X Stripmap image, VV polarized acquired 29 October 2013 15:45 UTC. (b) SWAN wavelength field from 29 October 2013 16:00 UTC. Colour scheme indicates the wavelength and the arrow direction represents the wave propagation direction. The grey rectangle represents the wavelength decrease transect (Figure 8) for SAR data.

parameters in the Baltic Sea, where the magnitude of wave characteristics (wavelength, period, wave height, etc.) is significantly lower than in the open ocean.

High correlation is seen in case of all of the compared parameters. The results showed a correlation coefficient (r) of 0.95 between the peak direction values obtained from buoy and SAR data ($p < 0.001$; RMSD = 30.00°; bias = 0.40°; Figure 2(a)) and the corresponding value in case of the wave model and SAR data was 0.87 ($p < 0.001$; RMSD = 25°; bias = 0.16°; Figure 2(b)). Peak wavelength from SAR data correlated well with buoy measurements and model results, with the corresponding r values of 0.81 ($p < 0.001$; RMSD = 13.20 m; bias = -0.18 m; Figure 3(a)) and 0.91 ($p < 0.001$; RMSD = 9.40 m; bias = -0.006 m; Figure 3(b)).

The SAR data was collected using different polarizations in order to assess the SAR wave retrieval algorithm dependence on polarization (Figures 2 and 3). It was demonstrated that imaging the waves of the Baltic Sea is independent of polarization; thus, it is universally applicable for the retrieval of wave field parameters (wavelength and wave direction).

It is due to the location of the Baltic Sea in temperate latitudes that the wave propagation directions are not spread evenly across the propagation direction spectrum (Figures 2(a) and (b)). Climatologically, dominant wind direction is from sector 180–270° (S, SW, and W) in the Baltic Sea (Jaagus and Kull 2011) and during most of the test cases presented here, southwesterly and westerly winds were dominating. In the context of SAR geometry, this means that on most of the images the range travelling waves were observed. In Figures 2(a) and (b) it is seen that the majority of the measurements fall close to 240°. Moreover, waves in the GoF tend to propagate along the longer axis of the Gulf either from the west or from the east, which is seen in Figures 2(a) and (b) (measurements below 100°). GoF itself has a heading similar to the dominant wind direction, which furthermore explains the similarity.

Kriauciūnienė, Gailiūsis, and Kovalenkoviėnė (2006) referred to Hydrometeorological...1983 that dominant wavelengths mainly remain between 20 and 70 m and can reach up to 130 m. Our results remain mostly between the same values – from 20 to 80 m (Figures 3(a) and (b)). The longer wavelengths (over 100 m) were observed on the SAR imagery; however, buoy data was not available from these areas for validation (Figure 4). In general, the results from the study agree greatly with previous articles, which once again proves the adeptness of the TS-X sensor over the coastal regions.

Our results show that the TS-X sensor is capable of detecting even shorter waves than earlier suggested – 30 m (Lehner, Pleskachevsky, and Bruck 2012). In Figures 3(a) and (b), the lower limit of the wavelength is around 20 m.

3.1. Case study: waves

We present a case showing a TS-X data comparison with an *in situ* measured wave spectrum. TS-X Stripmap image with VV polarization was acquired over the Tallinn Bay area in the GoF on 29 October 2013 15:45 UTC (Figure 4). In Figure 4, the arrows indicate the wave propagation direction; colour coding represents wavelength.

In this case, a small campaign was also carried out from 11 October to 17 November 2013 when a Waverider type of buoy was measuring information nearby the Tallinna Madal buoy station (Figure 1). The temporary Waverider buoy provided the wave frequency–direction spectrum. Sub-image sample size was 512 × 512 pixels. The 1D spectrum derived from TS-X and the one given by buoy show good agreement, as can be seen in Figure 5(c). The corresponding sub-scene and 2D spectrum calculated from SAR data are given in Figures 5(a) and (b), respectively. There is a slight shift in the peaks on the 1D spectrum; however, qualitatively the two spectra follow the same pattern.

Sea-state characteristics in coastal areas change rapidly in the spatial domain (Ming Li, Lehner, and Wolfgang 2010; Bruschi et al. 2011; Lehner, Pleskachevsky, and Bruck 2012) and the SAR imagery provides an opportunity to indirectly measure the wave field parameters with a high spatial resolution. It must be emphasized that in the Baltic

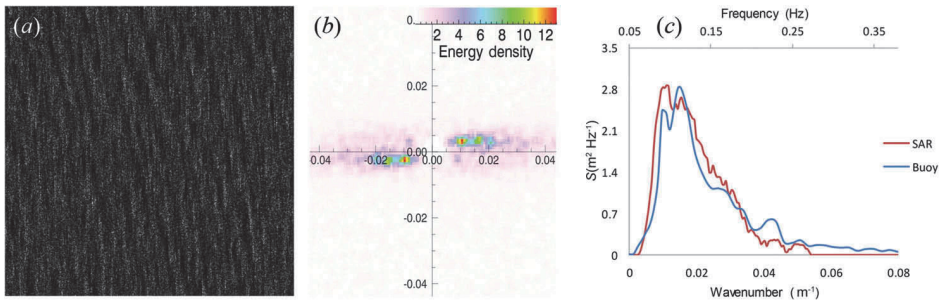


Figure 5. (a) TS-X 512 × 512 pixels VV polarized sub-scene taken over buoy station presented in Figure 1 (Tallinna Madal Waverider), (b) 2D SAR wavenumber spectrum (m^{-1}), c) 1D spectrum.

Sea, well-developed and structural sea state (steady unidirectional wind with the magnitude of 9 m s^{-1} for about 10 h prior to the SAR image acquisition) is suggested to retrieve the proper spectrum and correct wave properties from the SAR image.

In the following example, we examined the wave field parameters in three different locations indicated as Case1, Case2, and Case3 in Figure 1. In the middle of the GoF (Case1 in Figures 1, 6, and 7), the waves propagate in the direction of the wind from the W–SW and the corresponding wave propagation direction derived from the SAR 2D wavenumber spectrum is 86° and the wavelength is 82 m, which is near the upper limit of the cases shown in Figure 3(a). The long wavelengths are because the SAR image represents one of the severest storms in 2013, with wind speeds reaching 22 m s^{-1} . The sub-images near the island of Naissaare (Case2 and Case3, Figure 1) demonstrate land shadow effect. As the waves are propagating from the W–SW, it is evident that the waves are refracted by shallow water surrounding the island. Case2 in Figures 6 and 7 represents the sub-scene northwest from the island of Naissaare where the wave propagation direction is 120° and the wavelength is 80 m, whereas on the sub-scene extracted from the southern part of the Naissaare coast (Case3 in Figures 6 and 7) the peak wave propagation direction is 60° and the wavelength is 84 m. The wavelengths of refracted waves are similar (Figure 7); however, the refracted wave fields (Case2 and

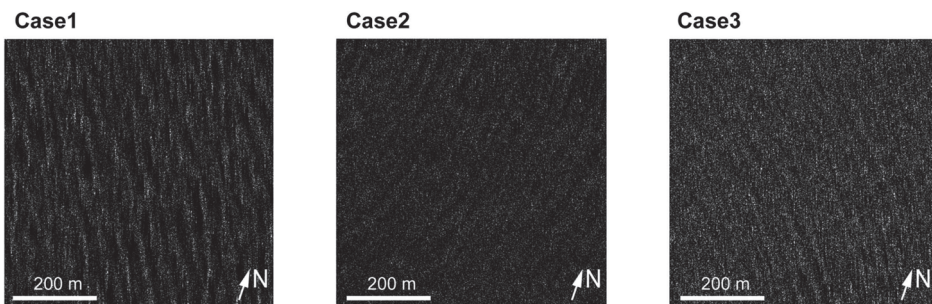


Figure 6. TS-X 512 × 512 pixel sub-scenes from TS-X VV polarized image acquired on 29 November 2013 15:45 UTC (Case1, Case2, and Case3 on Figure 1); Case1 represents the northernmost location on the TS-X wave field (Figure 1), Case2 and Case3 represent locations near the island of Naissaare (Figure 1).

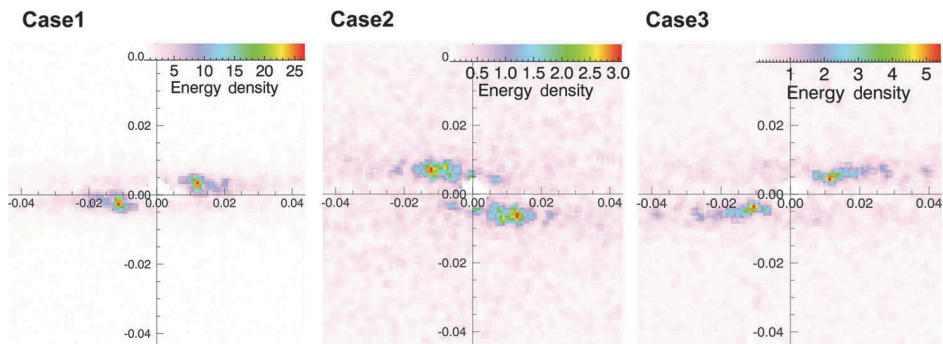


Figure 7. 2D wavenumber spectrum derived from the TS-X sub-scenes presented on Figure 6. On Case1 the wave propagation direction is 86° , on Case2 it is 120° , and on Case3 the direction is 60° . The wavelengths are 82 m, 80 m, and 84 m, respectively.

Case3 in Figure 7) are more disturbed by nonlinear effects – the spectrum is strongly perturbed by nonlinear artefacts and defocusing due to sea state moving in the range direction.

We can observe that the wavelength (Figure 8(a)) decreases near the coastal areas. This phenomenon can be noticed on waves that are propagating into Tallinn Bay in the region between the mainland and the Naissaare Island. The shortening of wavelengths near the coast can be observed in Figure 4. The wavelengths of 70 m, which can be seen 15 km offshore along the wave propagation axis, decrease to below 40 m near the coast (Figure 8(a)). It is interesting to notice that the wavelength decrease is not observable from the SWAN wave model results. This might be the result of too large spatial scale and imprecision in bathymetry data.

The SAR imagery has high spatial resolution, which gives reason to compare the wave parameters from SAR (640 m resolution) against SWAN wave model outputs (1.0 nm or 0.5 nm resolution). In this case, wave propagation results from the SAR imagery (Figure 4) are interpolated into the SWAN wave model grid, and the standard deviation from all the values is calculated in order to measure the variability. The variability is analysed based on the two case studies showed in Figure 4 (29 October 2013 15:45 UTC) and the second image not presented here, taken on 16 September 2012 16:02 UTC. Both cases show that SAR data is more variable than the wave model. For the first case, standard deviation of the wave propagation direction is 21.90° for SWAN and 26.80° for SAR and for the wavelengths 8.40 m and 9.60 m, respectively. The second case shows a similar outcome, with even larger variability differences. The standard deviation of the wave propagation direction for SWAN was 12.70° and for the SAR data the corresponding value was 23.40° . The same is seen in the wavelength values, for SWAN 9.30 m and SAR 20.70 m.

The variability of the wavelengths can be observed in Figure 4. When compared with the SWAN outputs, the greatest difference is seen in the wavelength values. In general, the wave propagation directions are similar. However, the wave propagation and wavelength values from the SWAN image (Figure 4(b)) are very homogeneous and the changes are strictly straight lines, whereas from the SAR image (Figure 4(a)) the values change on a much smaller scale. The greatest difference is seen in the central part of the

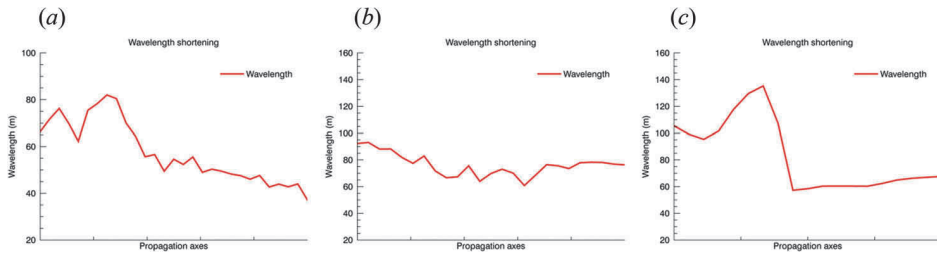


Figure 8. Averaged wavelengths transect. (a) Transect from Figure 4(a), (b) transect from Figure 9(a), and (c) transect from Figure 9(b).

GoF. The wavelength values from the SAR imagery vary from 60 m to 90 m, whereas from the SWAN results the values remain all over 80 m. The wavelength values near the Naissaare Island also differ between the SAR and SWAN results. Very sudden changes in the wave propagation direction and wavelength can be observed from the SWAN image, whereas changes in the SAR imagery are much smoother.

For the next example, we consider the wavelength field (Figure 9) over Irbe Strait between the Sõrve peninsula at the south of Saaremaa and the Kolka peninsula in Latvia. It was the highpoint of the storm named St. Jude (Viitak et al. 2016). During the storm, wind speeds reached up to 21.60 m s^{-1} and wind was blowing from the direction S–SW.

Irbe Strait is a particularly interesting location because of the bathymetry. To the west of the Irbe Strait is the open part of the Baltic Sea with great depths (100 m and more). To the east of the strait is GoR, with depths of up to 67 m (Baltic Sea Hydrographic Commission 2013). The relatively shallow Irbe Strait, with an average depth of approximately 10 m and a maximum depth of a 23 m, separates these two regions. Thus, the region of Irbe Strait where the shallow 10 m sill causes wave breaking provides an opportunity to investigate wave field variations caused by shallow regions.

Unfortunately, *in situ* wave data was not available from the Irbe strait. However, it is interesting to observe the differences between the SAR and SWAN results. The SWAN model shows that when longer waves (100–140 m) from the open part of the Baltic Sea propagate over the sill of Irbe Strait, the wave transformation is estimated to be extremely strong, resulting in a sudden decrease of wavelength to half of the original wavelength (60–70 m) (Figure 8(c)). However, wavelengths obtained from the SAR imagery show a much smoother change of waves traveling over the sill (Figure 8(b)). In some regions (south from the tip of Sõrve peninsula), one can observe nearly the same magnitude of wavelength decrease as from SWAN calculations (from 100 to 60 m). However, these similar patterns between SAR and SWAN are not consistent in the southern part of the Strait. Similar to Figure 4, the spatial variations of wavelengths between SAR and SWAN data can be seen in Figure 9. On the SWAN image, the wavelength changes are again sudden and mostly dependent on bathymetry. Yet, on the SAR imagery, smaller variations in wavelengths are seen throughout the image.

The two case studies demonstrate that the observed wave fields (SAR) are more complex than is often pictured with the wave model forecasts. This is especially well seen around islands where waves are refracted. Small variations in the wave fields can

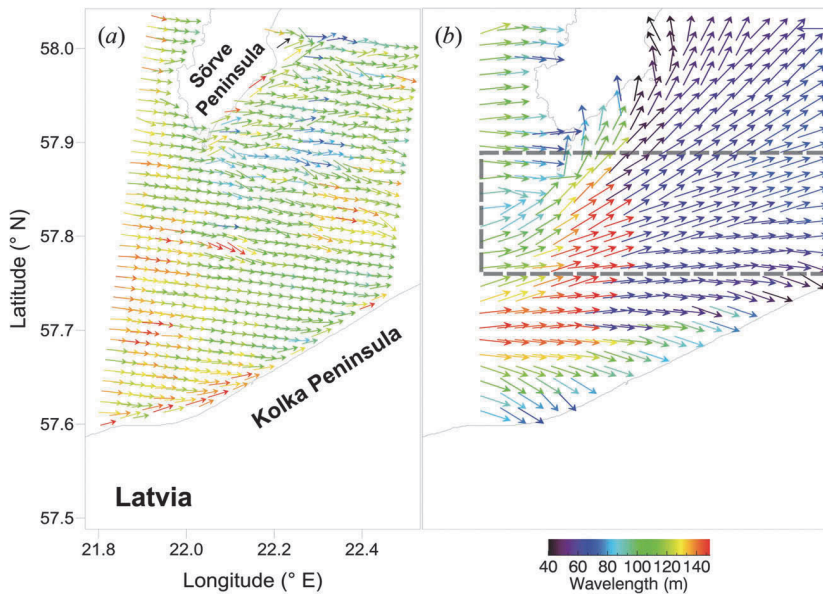


Figure 9. (a) Wavelength field derived from the TS-X Stripmap image, VV polarized image acquired on 29 October 2013 04:58 UTC. (b) SWAN wavelength field from 29 October 2013 05:00 UTC.

be observed in both images – Figures 4 and 9. Thus, information retrieved from the SAR imagery can strongly improve the wave model outcomes in a small scale and in complex situations.

3.2. Case study: wind

High correlation coefficients were seen between the wave propagation direction results from the SAR imagery and buoy measurements (Figure 2). Therefore, we replaced the wave propagation direction measurement (as no wave buoy data was available at Osmussaare station at that time) with the SAR imagery from 16 October 2012, 16:00 UTC to investigate the wave and wind field interactions on a larger scale (Figure 10). The slanting fetch effect in the GoF is observed using multisource data during a storm event on 16 October 2012 by comparing the wave propagation and wind directions in different locations along the axis of GoF.

Over the open part of the Baltic Sea (NBP), the wave propagation direction (217° for SWAN and 225° for measurements) closely follows the wind direction (229° ; comparing the values from Utö and NBP) (Figure 10). In the Ristna meteorological station, the wind direction is more to the east (236°). This causes a slight difference between the wind and wave directions. In the NBP, the measured wave propagation direction agrees well with the SWAN calculations.

However, in the GoF (Hanko and Osmussaare locations), we see that as the wind direction in Hanko has changed nearly 10° , the wave propagation direction has changed significantly more, 35° for SWAN and 23° for measurements. This phenomenon

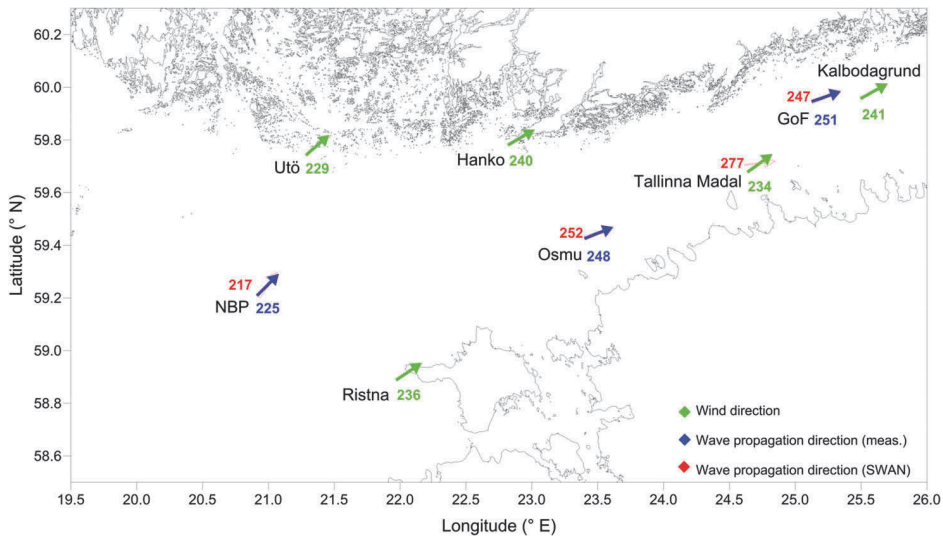


Figure 10. Wave and wind direction measurements and SWAN wave model results from 16 October 2012 16:00 UTC. The wave propagation direction measurement that is replaced with SAR data is at Osmu location.

continues, if we look further to the east at GoF and Kalbodagrund stations. The wind direction in Kalbodagrund (241°) has remained nearly the same as in Hanko (240°), whereas the wave propagation direction has turned even more towards the east (247° for SWAN and 251° for the measurements). In this case, the wave propagation differs from the wind direction by about 10°.

These slanting fetch cases are common in the Baltic Sea region as described in Pettersson, Kimmo, and Tuomi (2010). In the current example, we could show difference between the wave and wind directions of up to 43° (at Tallinna Madal, where SWAN calculations show 277° and wind measurements show 234°), which is close to the difference shown by Pettersson, Kimmo, and Tuomi (2010). Although the SAR measurements were not as frequent as the buoy measurements to present more noticeable examples, they were significant enough to demonstrate that SAR data provide valuable spatial information, which can be used for wave field analysis in case of lack of *in situ* data.

4. Conclusion

X-band SAR sensor has proved its usability over the Baltic Sea region. It is shown that significantly lower wave field parameters compared with the open ocean are detectable by the sensor.

An FFT-based method was proposed for the detection of wave field parameters (direction, wavelength) from the SAR imagery in the Baltic Sea. It was found that the TS-X sensor is capable of detecting lower wavelength values of 20 m. On the other hand, well-developed wave fields are required to retrieve the proper spectrum and hence correct wave field parameters from the SAR imagery. Therefore, the TS-X images that are

acquired during the time of rather strong winds (9 m s^{-1}) could be used for wave field analysis.

Comparison of SAR data with buoy measurements and SWAN wave model outputs showed good correlation between all of the compared parameters. Significant correlation is seen between the SAR-derived and buoy-measured wave propagation direction ($r = 0.95$, $p < 0.001$, $\text{RMSD} = 30.00^\circ$, $\text{bias} = 0.40^\circ$) and wavelengths ($r = 0.81$, $p < 0.001$, $\text{RMSD} = 13.20 \text{ m}$, $\text{bias} = -0.18 \text{ m}$). Comparison of SAR-based wave field information with SWAN wave model outputs also showed good agreement in case of wave propagation direction ($r = 0.87$, $p < 0.001$, $\text{RMSD} = 25.00^\circ$, $\text{bias} = 0.16^\circ$) and wavelengths ($r = 0.91$, $p < 0.001$, $\text{RMSD} = 9.40 \text{ m}$, $\text{bias} = -0.006 \text{ m}$).

The results of wave field parameters received with the algorithm did not depend on the geographical location or the imaging mode or the SAR image polarization. Therefore, it can be concluded that the algorithm is applicable to other smaller-scale waterbodies.

It was demonstrated that SAR images enable the evaluation of small-scale wave field variations in the coastal zones where sea-state characteristics change rapidly in the spatial domain. The case study showed that the SAR sensor enables one to track the refracted waves around shallow areas with islands and peninsulas, despite the strong nonlinear effects from the range travelling waves.

High-resolution satellite images with detailed wave information provide a good opportunity for integrating the wave model and remote-sensing data. Analysis showed that information from the SAR imagery is more variable than wave model outputs. For the image taken on 29 October 2013, the standard deviation of the wave propagation direction was 21.90° for SWAN and 26.80° for SAR and for the wavelengths 8.40 m and 9.60 m , respectively. For the second case, the standard deviation of the wave propagation direction for SWAN was 12.70° and for the SAR data the corresponding value was 23.40° . The same was seen in wavelength values – 9.30 m for SWAN and 20.70 m for SAR. These results could improve the wave model outputs significantly.

Similar to that in the validation phase, the SAR products proved their usability (high correlation coefficients and high values for other statistical parameters): they can be used in place of the buoy measurements in places where there is a lack of buoy measurements. In our case, we calculated the wave propagation direction from the SAR imagery and replaced it with measurements to analyse the wave and wind field interactions (slanting fetch effect in GoF) on a larger scale. It was demonstrated that slanting fetch cases are regular in the Baltic Sea and the wave propagation direction can differ from the wind direction up to 43° in deep water.

Acknowledgements

We express our gratitude to our colleagues T. Kõuts, U. Lips, and K. Vahter at Marine Systems Institute as well as to Finnish Meteorological Institute and Loude Consulting Oy for providing wave measurements data. This study was financially supported by the Estonian Science Foundation through grant no. ETF8968 and by EUROSTARS program no. F12002. This work was supported by institutional research funding IUT (19-6) of the Estonian Ministry of Education and Research.

Disclosure statement

No potential conflict of interest was reported by the authors.

Funding

This study was financially supported by the Estonian Science Foundation through grant no. ETF8968 and by EUROSTARS program no. F12002 and this work was supported by institutional research funding IUT (19-6) of the Estonian Ministry of Education and Research.

References

- Alari, V. 2013. "Multi-Scale Wind Wave Modeling in the Baltic Sea". PhD diss., Tallinn University of Technology.
- Alari, V., U. Raudsepp, and T. Kõuts. 2008. Wind Wave Measurements and Modelling in Küdema Bay, Estonian Archipelago Sea. *Journal of Marine Systems* S30–S40. 10.1016/j.jmarsys.2007.11.014.
- Baltic Sea Hydrographic Commission. 2013. "Baltic Sea Bathymetry Database". (Accessed March 25 2016). <http://data.bshc.pro>
- Björkqvist, J. V., I. Lukas, V. Alari, G. P. Van Vledder, S. Hulst, H. Pettersson, and A. Behrens. Forthcoming. Comparing a 41 Year Model Hindcast with Decades of Wave Measurements from the Baltic Sea. *Ocean Engineering*
- Booij, N., R. C. Ris, and L. H. Holthuijsen. 1999. A Third-Generation Wave Model for Coastal Regions: 1. Model Description and Validation. *Journal of Geophysical Research: Oceans* 104:(C4) 7649–7666. 10.1029/98JC02622.
- Bruck, M., and S. Lehner. 2013. Coastal Wave Field Extraction Using Terrasar-X Data. *Journal of Applied Remote Sensing* 7:(1) 10.1117/1.JRS.7.073694.
- Bruck, M., M. T. Pontes, E. Azevedo, and S. Lehner. 2011. "Study of Sea-State Variability and Wave Groupiness Using Terrasar-X Synthetic Aperture Radar Data". Proceedings of the 9th EWTEC 5–9.
- Brusch, S., P. Held, S. Lehner, W. Rosenthal, and A. Pleskachevsky. 2011. Underwater Bottom Topography in the Coastal Areas from Terrasar-X Data. *International Journal of Remote Sensing* 32:(16) 4527–4543. 10.1080/01431161.2010.489063.
- Cieślakiewicz, W., and B. Papińska-Swerpel. 2008. A 44-Year Hindcast of Wind Wave Fields over the Baltic Sea. *Coastal Engineering* 55:(11) 894–905. 10.1016/j.coastaleng.2008.02.017.
- Diaz Méndez, G. M., S. Lehner, F. J. Ocampo-Torres, X. Ming Li, and S. Brusch. 2010. Wind and Wave Observations off the South Pacific Coast of Mexico Using Terrasar-X Imagery. *International Journal of Remote Sensing* 31:(17–18) 4933–4955. 10.1080/01431161.2010.485217.
- Hydrometeorological State of the Marine Shelf Zone in the USSR*. 1983. Vol. 1, No. 1. Leningrad. Hydrometeoizdat. 175. In Russian
- Jaagus, J., and A. Kull. 2011. Changes in Surface Wind Direction in Estonia during 1966–2008 and Their Relationships with Large-Scale Atmospheric Circulation. *Estonian Journal of Earth Sciences* 60:(4) 220–231. 10.3176/earth.2011.4.03.
- Jackson, C. H., and W. Koch. 2005. synthetic aperture radar marine user's manual. (Accessed march 11 2016). www.sarusermanual.com
- Jönsson, A., B. Broman, and L. Rahm. 2003. Variations in the Baltic Sea Wave Fields. *Ocean Engineering* 30:(1) 107–126. 10.1016/S0029-8018(01)00103-2.
- Kahma, K. K. 1976. "Preliminary Results of Wind Wave Measurements in the Southern Part of the Bothnian Sea". Proceedings of the 10th conference of the Baltic Oceanographers, Part 1, Göteborg, Sweden.
- Kahma, K. K. 1981. A Study of the Growth of the Wave Spectrum with Fetch. *Journal of Physical Oceanography* 11:(11) 1503–1515. 10.1175/1520-0485(1981)011<1503:ASOTGO>2.0.CO;2.

- Kriauciūnienė, J., B. Gailiūšis, and M. Kovalenkoviėnė. 2006. Peculiarities of Sea Wave Propagation in Klaipėda Strait, Lithuania. *Baltica* 19:(1) 20–29.
- Lehner, S., J. Horstmann, J. Koch, and W. Rosenthal. 1998. Mesoscale Wind Measurements Using Recalibrated ERS SAR Images. *Journal of Geophysical Research: Oceans* 103:(C4) 7847–7856. [10.1029/97JC02726](https://doi.org/10.1029/97JC02726).
- Lehner, S., A. Pleskachevsky, and M. Bruck. 2012. High-Resolution Satellite Measurements of Coastal Wind Field and Sea State. *International Journal of Remote Sensing* 33:(23) 7337–7360. [10.1080/01431161.2012.685975](https://doi.org/10.1080/01431161.2012.685975).
- Leppäranta, M., and K. Myrberg. *Physical Oceanography of the Baltic Sea*. Praxis: Springer; 2009.
- Ming Li, X., S. Lehner, and R. Wolfgang. 2010. “Investigation of Ocean Surface Wave Refraction Using Terrasar-X Data”. *IEEE Transactions on Geoscience and Remote Sensing* 48:(2) 830–840. [10.1109/TGRS.2009.2033177](https://doi.org/10.1109/TGRS.2009.2033177).
- Niros, A., T. Vihma, and J. Launiainen. 2002. Marine Meteorological Conditions and Air-Sea Exchange Processes over the Northern Baltic Sea in 1990s. *Geophysica* 38:(1–2) 59–87.
- Pettersson, H., K. K. Kimmo, and L. Tuomi. 2010. Wave Directions in a Narrow Bay. *Journal of Physical Oceanography* 40:(1) 155–169. [10.1175/2009JPO4220.1](https://doi.org/10.1175/2009JPO4220.1).
- Räämet, A. 2010. “Spatio-Temporal Variability of the Baltic Sea Wave Fields”. PhD diss., Tallinn University of Technology.
- Raudsepp, U., J. Laanemets, G. Haran, V. Alari, J. Pavelson, and T. Kõuts. 2011. Flow, Waves, and Water Exchange in the Suur Strait, Gulf of Riga, in 2008. *Oceanologia* 53:(1) 35–56. [10.5697/oc.53-1.035](https://doi.org/10.5697/oc.53-1.035).
- Seifert, F., B. Tauber, and B. Kayser 2001. “A High Resolution Spherical Grid Topography of the Baltic Sea 2nd Edition. Baltic Sea Science Congress Stockholm 25-29. November Poster 147”, www.io-warnemuende.de/iowtopo.
- Siewert, M., C. Schlankow, and F. Saatho .2015. Spatial Analyses of 52 Years of Modelled Sea State Data for the Western Baltic Sea and Their Potential Applicability for Offshore and Nearshore Construction Purposes. *Ocean Engineering* 96:284–294. [10.1016/j.oceaneng.2014.12.029](https://doi.org/10.1016/j.oceaneng.2014.12.029).
- Soomere, T., A. Behrens, L. Tuomi, and J. W. Nielsen. 2008. Wave Conditions in the Baltic Proper and in the Gulf of Finland during Windstorm Gudrun. *Natural Hazards and Earth System Sciences* 8 (1):37–46. DOI:[10.5194/nhess-8-37-2008](https://doi.org/10.5194/nhess-8-37-2008).
- Suursaar, Ü. 2013. Locally Calibrated Wave Hindcasts in the Estonian Coastal Sea in 1966–2011. *Estonian Journal of Earth Sciences* 62:(1) 42–56. [10.3176/earth.2013.05](https://doi.org/10.3176/earth.2013.05).
- Suursaar, Ü., J. Jaagus, and T. Kullas. 2006. Past and Future Changes in Sea Level near the Estonian Coast in Relation to Changes in Wind Climate. *Boreal Environment Research* 11:(2) 123–142.
- SWAN team. 2014. (Accessed april 15 2015).<http://swanmodel.sourceforge.net/>
- Tuomi, L., K. K. Kahma, and H. Pettersson. 2011. Wave Hindcast Statistics in the Seasonally Ice-Covered Baltic Sea. *Boreal Environment Research* 16:(6) 451–472.
- Viitak, M., I. Maljutenko, V. Alari, Ü. Suursaar, S. Rikka, and P. Lagemaa. 2016. The Impact of Surface Currents and Sea Level on the Wave Field Evolution during St. Jude Storm in the Eastern Baltic Sea. *Oceanologia* in Press. [10.1016/j.oceano.2016.01.004](https://doi.org/10.1016/j.oceano.2016.01.004).

Publication V

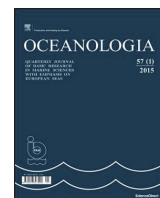
Viitak, M., Maljutenko, I., Alari, V., Suursaar, Ü., Rikka, S., & Lagemaa, P. (2016). The impact of surface currents and sea level on the wave field evolution during St. Jude storm in the eastern Baltic Sea. *Oceanologia*, 58(3), 176–186.



Available online at www.sciencedirect.com

ScienceDirect

journal homepage: www.elsevier.com/locate/oceano



ORIGINAL RESEARCH ARTICLE

The impact of surface currents and sea level on the wave field evolution during St. Jude storm in the eastern Baltic Sea[☆]

Marili Viitak^{a,*}, Ilja Maljutenko^a, Victor Alari^{b,1}, Ülo Suursaar^c, Sander Rikka^a, Priidik Lagemaa^{a,d}

^aTallinn University of Technology, Marine Systems Institute, Tallinn, Estonia

^bHelmholtz-Zentrum Geesthacht, Centre for Material and Coastal Research, Geesthacht, Germany

^cUniversity of Tartu, Estonian Marine Institute, Estonia

^dEstonian Environment Agency, Estonian Weather Service, Estonia

Received 5 October 2015; accepted 29 January 2016

Available online 16 February 2016

KEYWORDS

SWAN;
Wave–current–surge
interaction;
Extreme storm;
Hindcast;
SAR

Summary A third generation numerical wave model SWAN (Simulating WAVes Nearshore) was applied to study the spatio-temporal effect of surface currents and sea level height on significant wave height; and to describe the mechanisms responsible for wave–current interaction in the eastern Baltic Sea. Simulation results were validated by comparison with in situ wave measurements in deep and shallow water, carried out using the directional wave buoy and RDCP respectively, and with TerraSAR-X imagery. A hindcast period from 23 to 31 October 2013 included both a period of calm to moderate weather conditions and a severe North-European windstorm called St. Jude. The prevailing wind directions were southerly to westerly. Four simulations with SWAN were made: a control run with dynamical forcing by wind only; and simulations with additional inputs of surface currents and sea level, both separately and combined. A clear effect of surface currents and sea level on the wave field evolution was found. It manifested itself as an increase or decrease of significant wave height of up to 20%. The strength of the interaction was

[☆] This study was financially supported by the Estonian Science Foundation Grant 9278, by institutional research funding IUT19-6 of the Estonian Ministry of Education and Research and by the Estonian Research Council grant PUT595.

* Corresponding author at: Tallinn University of Technology, Marine Systems Institute, Akadeemia tee 15a, 12618 Tallinn, Estonia. Tel.: +372 53803824.

E-mail address: viitak.marili@gmail.com (M. Viitak).

¹ Current address: Marine Systems Institute at Tallinn University of Technology, Estonia.

Peer review under the responsibility of Institute of Oceanology of the Polish Academy of Sciences.



Production and hosting by Elsevier

<http://dx.doi.org/10.1016/j.oceano.2016.01.004>

0078-3234/© 2016 Institute of Oceanology of the Polish Academy of Sciences. Production and hosting by Elsevier B.V. This is an open access article under the CC BY-NC-ND license (<http://creativecommons.org/licenses/by-nc-nd/4.0/>).

influenced by the propagation directions of waves and surface currents and the severity of weather conditions. An increase in the wave height was mostly seen in shallower waters and in areas where waves and surface currents were propagating in opposite directions. In deeper parts of the eastern Baltic Sea and in case of waves and surface currents propagating in the same direction a decrease occurred.

© 2016 Institute of Oceanology of the Polish Academy of Sciences. Production and hosting by Elsevier B.V. This is an open access article under the CC BY-NC-ND license (<http://creativecommons.org/licenses/by-nc-nd/4.0/>).

1. Introduction

In the event of a storm at sea, rough wave and severe surge conditions may lead to significant coastal and property damage or even to loss of life (e.g. Feser et al., 2015). Correct quantification of met-ocean parameters of a storm using numerical models and forecasting systems helps to reduce the storm related risks and mitigate consequences. Because in nature there is a feedback system between processes, detailed information about different interactions would provide us with a better understanding and improved predictability of hydrodynamic conditions at sea. For instance, an important feedback occurs between slowly-varying currents and highly varying waves. So far, the issue is little studied in the Baltic Sea.

The groundbreaking work of wave–current interaction was done by Longuet-Higgins and Stewart in a series of papers (1960, 1961, 1964). They described the interaction using radiation stress and demonstrated the energy transfer between waves and currents. Bretherton and Garrett (1968) introduced the idea of action conservation. Since then numerous papers have been published on the application of the theory including those by Wolf and Prandle (1999), Guedes Soares and de Pablo (2006) and Van der Westhuysen (2012). Alari (2013) studied the local storm surge effect on wave field in Pärnu Bay, Baltic Sea. He showed that sea level has a significant effect on wave field during extreme weather conditions. However, the effect of surface currents on wave field in the eastern Baltic Sea has had little attention.

The objectives of the present study were firstly, to assess the one-way interaction between waves, surface currents and sea level in almost tideless (up to 10 cm (Feistel et al., 2008)) coastal areas. We tried to find out the mechanisms by which surface currents and sea level rise influence the evolution of significant wave height under stormy conditions. This could help to improve modelling systems and see if it is worth further investigating the coupling of wave and hydrodynamic models in the Baltic Sea. Secondly, we studied the effect of spatial variability of surface currents and sea level on wave field. This would also indicate in which sea areas these interactions might be important during severe storms.

The paper is structured as follows: In Section 2 data and methods are presented including the description of measured and remotely sensed data and the description of numerical models and their set-ups. Section 3 presents the calculation results and discussion. The main conclusions and recommendations for further studies are summed up in Section 4.

2. Data and methods

2.1. Investigation area and measurements

The area of investigation is the eastern Baltic Sea, which is shown in Fig. 1. It includes two large gulfs – the Gulf of Finland and the Gulf of Riga. Water depth varies between 0 and 170 m. The Eastern section of the Baltic Sea, including the Gulf of Finland and Gulf of Riga, are extremely prone to storm surge (e.g. Wolski et al., 2014). The Gulf of Finland is connected with Baltic Proper with no barrier to the propagation of the waves, which allows, under certain meteorological conditions, long and high waves to enter the region (Leppäranta and Myrberg, 2009). According to Kahma and Petterson (1993) the mean significant wave height in spring is 0.5 m with peak period of 3.8 s and in winter 1.3 m with period of 5.3 s. Higher waves are produced in storm conditions (Soomere et al., 2008). In the Gulf of Riga wave propagation and growth are limited by shallow and narrow straits. Annual average wave height is between 0.25 and 0.5 m (Suursaar et al., 2012). According to Raudsepp et al. (2011) the peak period ranges between 2.3 and 8 s.

In Fig. 1 red and black squares show the stations where the measurements were taken for comparison with the simulations. Measurements in the Gulf of Finland (Fig. 1, station A) were conducted by the Finnish Meteorological Institute (FMI) at a site where water depth is 43 m. The device used was the

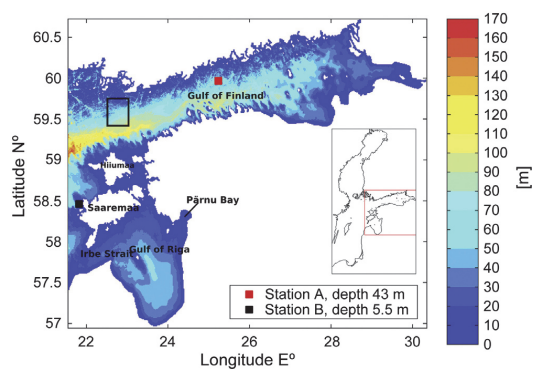


Figure 1 Eastern Baltic Sea bathymetry with grid resolution of 0.5 nautical miles. This area also represents the nested grid area. The black rectangle is the area of SAR measurements.

WAVERIDER MKIII directional wave buoy, which measures surface acceleration. Waves with period of 1.6 s and higher were registered. Measurements close to Saaremaa Island (Fig. 1, Station B) were conducted by the Estonian Marine Institute (Suursaar, 2013). The water depth at the measurement site was 5.5 m. The measurements were taken with a bottom mounted RDCP-600 (Recording Doppler Current Profiler), which measured the instantaneous dynamic pressure above its sensor. The pressure was further converted to surface elevation spectra with linear wave theory. Due to the attenuation of the pressure signal, there was a high-frequency cut-off and only waves with period of 2.6 s and bigger were measurable. As a result the realistic significant wave height can be higher than measured.

For remotely sensed data, a TerraSAR-X multi-look ground range detect (MGD) Stripmap product was used. The image was acquired with VV polarization and the pixel size was 1.25 m. Here the image acquired for the morning of 29 October 2013 (at 04:57 UTC) was used, which coincided with the storm maximum. The area of the image is shown on Fig. 1 as a black rectangle.

2.2. Numerical model

The SWAN model used in this study is a third-generation numerical wave model developed at the Delft University of Technology, in The Netherlands (Booij et al., 1999). Waves are described with the two-dimensional wave action density spectrum. The action density spectrum N is considered instead of the energy density spectrum E because in the presence of ambient currents, action density is conserved, but energy density is not. Action density is related to energy density through the relative frequency σ (Whitham, 1974):

$$N(\sigma, \theta) = \frac{E(\sigma, \theta)}{\sigma}. \quad (1)$$

Relative frequency is observed in a frame of reference moving with the current velocity, and θ is the wave propagation direction (the direction normal to the wave crest of each spectral component). SWAN solves the spectral action balance equation without any *a priori* restrictions on the spectrum for the evolution of wave growth (Booij et al., 1999). The action balance equation in Cartesian coordinates reads:

$$\frac{\partial N}{\partial t} + (\mathbf{c}_g \rightarrow + \mathbf{u} \rightarrow) \nabla_{x,y} N + \frac{\partial c_\sigma N}{\partial \sigma} + \frac{\partial c_\theta N}{\partial \theta} = \frac{S_{wind} + S_{nl3} + S_{nl4} + S_{wc} + S_{bot} + S_{db}}{\sigma}. \quad (2)$$

On the left-hand side of Eq. (2) the first term represents the local rate of change of action density in time; the second term denotes the propagation of wave energy in two dimensional geographical space, where $\mathbf{c}_g \rightarrow$ is the group velocity and \mathbf{u} is the ambient current. The third term represents the shifting of the relative frequency due to variations in depths and currents (with propagation velocity c_σ in σ space). The fourth term represents depth induced and current-induced refraction (with propagation velocity c_θ in θ space). On the right-hand side of the action balance equation is the source term that represents all physical processes which generate, redistribute or dissipate wave energy. These terms denote, respectively, wave growth by the wind S_{wind} , non-linear

transfer of wave energy through three-wave S_{nl3} and four-wave interactions S_{nl4} and wave dissipation due to white-capping S_{wc} , bottom friction S_{bot} and depth-induced wave breaking S_{db} (The SWAN team, 2013a).

2.3. Accounting for currents and sea level in SWAN

The SWAN is not capable of calculating surface currents and sea levels. In order to take them into account they have to be presented as input. If there is no current or sea level input data, they are assumed to be zero (The SWAN team, 2013b).

2.3.1. Wind

Two mechanisms are used to describe the transfer of wind energy to waves – a resonance mechanism and a feed-back mechanism. For a more precise description see Phillips (1957) and Miles (1957). Wave growth is the sum of linear (A) and exponential (B) growth:

$$S_{wind}(\sigma, \theta) = A + BE(\sigma, \theta), \quad (3)$$

in which A and B depend on wave frequency and direction, and wind speed and direction. Linear wave growth contributes to the initial stages of wave growth. As the waves grow they start to affect the wind induced pressure field, which results in a larger energy transfer from the wind as the waves grow.

To account for the currents the apparent local wind speed and directions are used (The SWAN team, 2013a). In the presence of surface currents travelling opposite to the wave direction the transfer of wind energy to the waves is stronger and vice versa.

2.3.2. Kinematic effects

In Eq. (2) the kinematic effects are presented with left-side terms, except the time derivative term. As stated by Whitham (1974), wave energy propagation velocities in spatial and spectral space can be described by the kinematics of a wave train. In spatial space it reads:

$$\frac{d\vec{x}}{dt} = \mathbf{c}_g \rightarrow + \vec{u} = \frac{1}{2} \left(1 + \frac{2|\vec{k}|d}{\sinh(2|\vec{k}|d)} \right) \frac{\sigma \vec{k}}{|\vec{k}|^2} + \vec{u}, \quad (4)$$

where \mathbf{k} is wave number vector and d is the total water depth. In spectral space:

$$\mathbf{c}_\sigma = \frac{\partial \sigma}{\partial d} \left(\frac{\partial d}{\partial t} + \vec{u} \nabla_{x,y} d \right) - \mathbf{c}_g \vec{k} \frac{\partial \vec{u}}{\partial s}, \quad (5)$$

$$\mathbf{c}_\theta = \frac{-1}{k} \left(\frac{\partial \sigma}{\partial d} \frac{\partial d}{\partial m} + \vec{k} \frac{\partial \vec{u}}{\partial m} \right), \quad (6)$$

where s is the space coordinate in the wave propagation direction of θ and m is a coordinate perpendicular to s (The SWAN team, 2013a).

From kinematics in spatial space and spectral space (Eqs. (4)–(6)) it is observed that, when waves and currents are propagating in opposite directions, the second left-side term will be smaller in value in Eq. (2). This will result in an increase in the wave energy and therefore also in the wave

height. With waves and currents propagating in the same direction the effect is reversed.

As the sea level changes the total water depth influences the height of the waves. In nearshore regions, the group velocity decreases with decreasing water depth. To maintain a constant flux of energy transport an increase in the energy density occurs. This results in an increase of the wave height. With varying surface current and sea level refraction occurs (Eq. (6)).

2.3.3. Depth-induced wave breaking

Sea level will determine the maximum height of the waves beyond which the waves will start to break. Energy dissipation due to depth-induced wave breaking follows the analogy of breaking of a bore applied to random waves (Battjes and Janssen, 1978):

$$S_{db}(\sigma, \theta) = \frac{D_{tot}}{E_{tot}} E(\sigma, \theta), \quad (7)$$

where $D_{tot} = -\alpha_{BJ} Q_b \bar{\sigma} H_{max}^2 (8\pi)^{-1}$ is the mean rate of energy dissipation per unit horizontal area due to wave breaking, $\alpha_{BJ} = 1$, $\bar{\sigma}$ is the mean frequency, Q_b is the fraction of breaking waves and $H_{max}^2 = \gamma d$ is the maximum wave height that can exist at the given depth d where γ is the breaker parameter (set to 0.73). E_{tot} is the total wave energy integrated over all directions and frequencies (The SWAN team, 2013a).

During a surge the water depth deepens and the fraction of breaking waves reduces. This has the effect of moving the breaking zone towards the coast and increasing wave heights in coastal areas.

2.3.4. Whitemapping

Whitemapping is represented by the pulse-based model of Hasselmann (1974):

$$S_{wc}(\sigma, \theta) = -\Gamma \bar{\sigma} \frac{k}{\bar{k}} E(\sigma, \theta), \quad (8)$$

where \bar{k} is the mean wave number. The coefficient Γ depends on the overall wave steepness (The SWAN team, 2013a). In the presence of opposing currents waves experience enhanced whitemapping, because with opposing current wave number and wave steepness increases.

2.3.5. Bottom friction

The empirical model of JONSWAP (Hasselmann et al., 1973) is used to express bottom friction

$$S_{bot} = -C_b \frac{\sigma^2}{g^2 \sinh^2(kd)} E(\sigma, \theta), \quad (9)$$

where $C_b = 0.038 \text{ m}^2 \text{ s}^{-3}$ is the bottom friction coefficient (The SWAN team, 2013a).

As the surface currents affect the spectral wave energy, the bottom friction will also experience change. Bottom friction will increase with increasing wave energy e.g. in the case of an opposite current.

2.4. Model set-up and dynamical forcing

A nine-day period was chosen for the simulations, from 23.10.2013 to 31.10.2013. This includes calm to moderate weather conditions and a storm. In order to achieve realistic

Table 1 Description of SWAN simulations.

r1 – simulation 1	(Reference simulation) wind
r2 – simulation 2	Wind and surface currents
r3 – simulation 3	Wind and sea level
r4 – simulation 4	Wind, surface currents and sea level

results in coastal areas, a nesting approach was used. The whole Baltic Sea region was simulated with a resolution of 1 nautical mile (nm). From there boundary conditions were obtained for the eastern Baltic Sea area, which had a resolution of 0.5 nm. The area of the 0.5 nm grid is shown in Fig. 1.

SWAN was forced with a 10 m wind field from the atmospheric model HIRLAM (Unden et al., 2002) interpolated on a model grid. HIRLAM wind fields had a spatial resolution of 11 km and a temporal resolution of 1 h. Additionally, input of surface currents and sea level were taken from the HIROMB model (Funkquist and Kleine, 2007; Lagema, 2012). Current values for the 1 nm grid were taken at a depth of 2 m. For the 0.5 nm grid the depth was 1.5 m. The SWAN computational grid and HIROMB horizontal grid were defined to be identical in order to avoid interpolation errors.

For bathymetry the Baltic Sea Bathymetry Database data was used (Baltic Sea Hydrographic Commission, 2013). Bathymetry was interpolated to the SWAN computational grid which was identical to HIROMB horizontal grid.

The integration time step for SWAN simulations was 10 min with directional bin width of 10° . Input fields of wind, currents and sea level to the wave model had a time step of 1 h. Output of SWAN was also requested once per hour.

Four simulations with SWAN were made using different dynamical forcings. Wind, surface currents and sea level were considered. In Table 1 there is a description of all the simulations. First a reference simulation with SWAN where there was only forcing by wind. On the second simulation, in addition to the wind, surface currents were included. With the third simulation, wind and sea level impact were taken into account. Finally, in the fourth simulation, all the dynamical forcings were present.

In this study it is assumed that the current and sea level are not affected by the wave field.

2.5. Wave parameters and statistics

The main focus of this study is to investigate the effects of hydrodynamics on significant wave height (Hs), which is defined as the mean height of the highest third of waves. In SWAN it is expressed as $H_s = 4 \sqrt{\int \int E(\omega, \theta) d\omega d\theta}$, where ω is the radian frequency.

To evaluate the performance of the model, four statistical parameters were calculated for simulations and measurements: the root mean square error (RMSE), the scatter index (SI), the mean deviation (BIAS) and the correlation coefficient:

$$RMSE = \sqrt{\frac{1}{N} \sum_{i=1}^N (a_i - b_i)^2}, \quad (10)$$

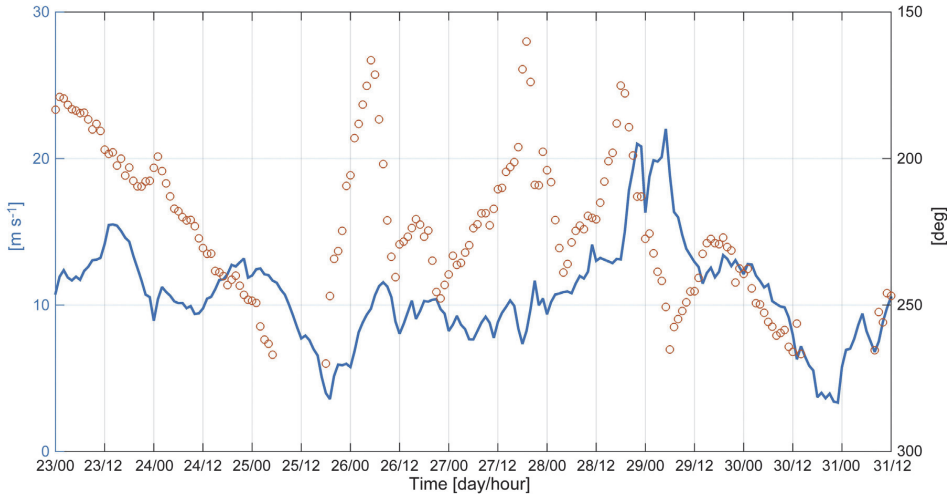


Figure 2 A time series of HIRLAM mean wind speed (blue line) and direction (red circles) near station B from modelling period 23.10.2013 to 31.10.2013. (For interpretation of the references to colour in this figure legend, the reader is referred to the web version of this article.)

$$SI = \frac{RMSE}{\frac{1}{N} \sum_{i=1}^N b_i} \times 100\%, \quad (11)$$

$$BIAS = \frac{\sum_{i=1}^N (a_i - b_i)}{N}, \quad (12)$$

where a is the model data, b is the measurement and N is the number of elements.

In order to see the effects of different dynamical forcings, the significant wave height changes were studied by comparing the significant wave height of each model simulation ($n = 2, 3, 4$) with the reference simulation $n = 1$ at every time moment t :

$$\Delta Hs^n(t) = Hs^n(t) - Hs^1(t). \quad (13)$$

To see the maximum range of possible change in significant wave height, the maximum difference over the time period of the storm day (whole day 29.10.2013) was calculated. The maximum difference ΔmHs^n for each grid point (lon, lat) was found as:

$$\Delta mHs^n = \Delta Hs^n(t_{max}^n), \quad (14)$$

where t_{max}^n (Eq. (15)) is the time when the difference of significant wave height (Eq. (13)) is maximum:

$$t_{max}^n = \text{argmax}(|\Delta Hs^n(t)|). \quad (15)$$

The maximum relative change was also calculated:

$$\Delta rHs^n = \frac{\Delta mHs^n}{Hs^1} \times 100\%, \quad (16)$$

where

$$Hs^1 = Hs^1(t_{max}^n), \quad (17)$$

and significant wave height of reference run r1 Hs^1 was found at time moment t_{max}^n .

3. Results and discussion

3.1. Weather and sea state

A time series of HIRLAM 10 m mean wind speed and direction near the west coast of Saaremaa near measurement station B (see Fig. 1) is shown in Fig. 2.

From 23.10.2013 to 28.10.2013 mean wind speed ranges between 4 and 15 m s⁻¹ which is considered to be calm to moderate weather. The storm, named St. Jude, lasted three days. It arrived in Estonia in the evening of 28.10.2013 and reached its highpoint in the early morning of the 29th. The weather started to calm down at the beginning of the next day.

At the peak of the storm, on 29.10.2013 at 04.00 mean wind speed, current velocity, sea level and significant wave height are shown in Fig. 3. During the storm the mean wind speed reaches 22 m s⁻¹ (Fig. 3a). Wind was blowing from the sector S–SW, which is one of the most frequent wind directions in the Baltic Sea (Jaagus and Kull, 2011).

In Fig. 3b the simulated surface current velocities and propagation directions (every 10th vector is displayed) at the highpoint of the storm are displayed. Current speed reaches up to 195 cm s⁻¹ in the Irbe strait. In the Gulf of Finland, in Pärnu bay and around Hiiumaa and Saaremaa the highest currents are up to 90 cm s⁻¹. The simulated surge reached up to 200 cm, compared to the model zero level (Fig. 3c). To the south east of Hiiumaa and Saaremaa, on the Finnish coast and in the Irbe strait the surge was up to 80 cm. In the deeper parts of the eastern Baltic it ranged from 80 to 100 cm. Simulated significant wave height (Fig. 3d) reached 6.5 m in the eastern Baltic Sea. Entering the Gulf of Finland and Gulf of Riga the wave height starts to decrease. Near the shore significant wave height is up to 2.5 m.

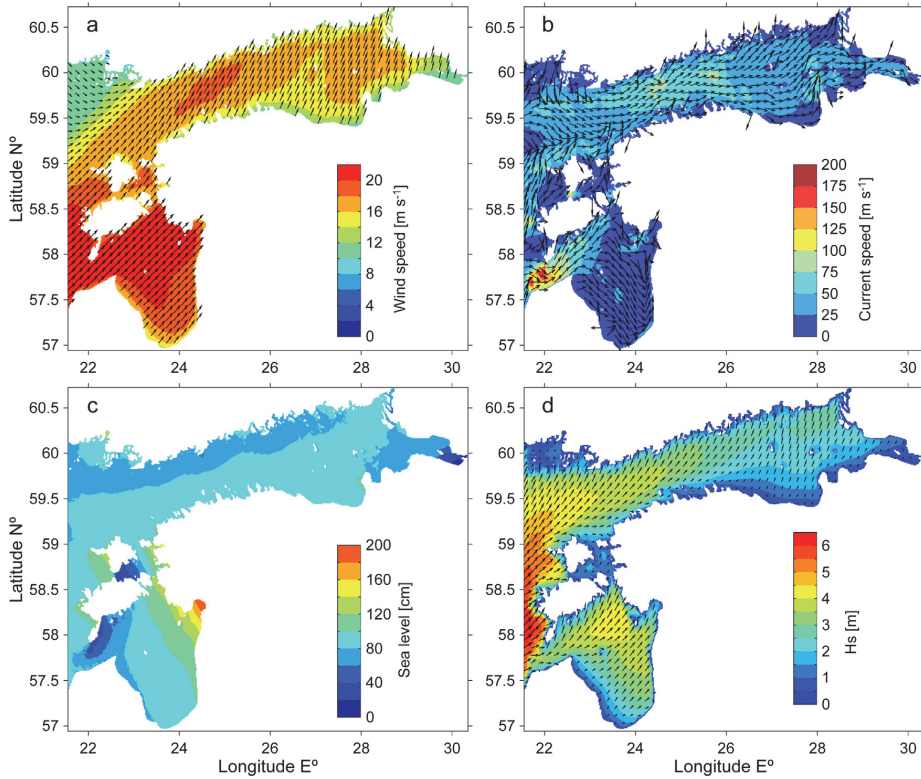


Figure 3 On 29.10.2013 at 04:00: (a) mean wind speed and direction (from HIRLAM model); (b) current velocity and direction (from HIROMB model); (c) the increase in the sea level (from HIROMB model); and (d) significant wave height (from SWAN model).

3.2. Comparison to measurements

Significant wave height is compared with measurements taken in deep water (depth 43 m) and close to the shore

(measurement station A and B on Fig. 1, respectively). Wave direction is compared to SAR data. The model point chosen for comparison with station A is ca 200 m away with a water depth of 42.85 m.

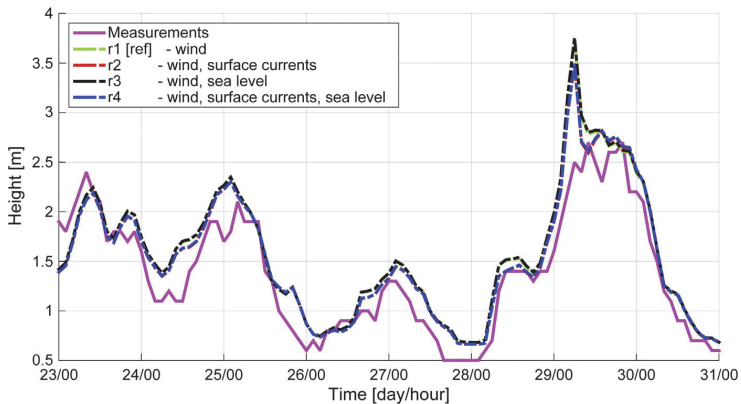


Figure 4 Comparison of measurements of significant wave height taken in Gulf of Finland in station A and SWAN simulations r1 to r4.

Table 2 RMSE, scatter index, BIAS and correlation coefficient are calculated from comparison of measurements in Gulf of Finland (measurement station A, Fig. 1) and model results. (a) In the time period from 23.10.2013 00.00 to 31.10.2013 23.00 – the whole modelling period. (b) Time period during the storm, 28.10.2013 00.00 to 30.10.2013 12.00.

	RMSE [cm]	Scatter index [%]	BIAS [cm]	Correlation coefficient
(a) 23.10.2013 00.00 to 31.10.2013 23.00				
Simulation 1	28	22	19	0.95
Simulation 2	25	19	15	0.95
Simulation 3	29	22	19	0.95
Simulation 4	25	19	16	0.95
(b) 28.10.2013 00.00 to 30.10.2013 12.00				
Simulation 1	36	21	26	0.95
Simulation 2	29	17	21	0.96
Simulation 3	37	22	27	0.95
Simulation 4	30	18	21	0.96

In Fig. 4, significant wave height from all four simulations (r1–r4) is compared. The time period for the validation in deep water covers the whole simulation period from 23.10.2013 to 31.10.2013. Simulated significant wave height follows the variability of the measurements well. In general the wave height is overestimated by the model in all runs. On 29.10.13 there is an unexpected overshoot in all the simulations. It is not caused by meteorological forcing time steps, as the wind is interpolated linearly over time for the model input. Simulations r2 and r4 show a slight improvement in the model results compared to r1 and r3.

Next the statistical parameters for significant wave height are calculated using Eqs. (10)–(12). Calculated over the period of 23.10.2013 00.00 to 31.10.2013 23.00 (Table 2a), the best results are produced with simulations r2 and r4, where surface currents are accounted for. RMSE for the reference simulation r1 is 28 cm, SI 22% and BIAS 19 cm. Taking into account currents (r2) RMSE decreases 3 cm, scatter index 3% and BIAS 4 cm. Considering only sea level

in the simulations has a negative impact on the results. This may be due to the fact that the measurement point is situated in deep water. The study of Alari (2013) shows that sea level plays a more significant role in shallower waters. Correlation between measurements and the model is reasonably good, 0.95 for all the simulations.

Now looking separately at the statistics for the storm period 28.10.2013 00.00 to 30.10.2013 12.00 (Table 2b), it is apparent that accounting for surface currents improves the comparison significantly. As the RMSE of reference simulation r1 in storm conditions is 36 cm, it decreases when taking account of currents by 7 cm. The scatter index and BIAS also show improvement. Correlation goes from 0.95 (r1 and r3) to 0.96 (r2 and r4).

The *ad hoc* measurements at station B near Saaremaa Island lasted from 26.10.2013 to 31.10.2013. Measurements were taken at a location where there were large gradients in water depth. In the model bathymetry the closest point to the measurement station had a depth of 21.10 m. Therefore another point in shallower water, with depth of 7.83 m, was chosen as a comparison point. The latter point is ca 1 km away from station B.

In Fig. 5 it can be seen that, as with the deeper water, the model again overestimates measurements. Reference simulation r1 is closest to the measured results. Taking currents into account (r2), the significant wave height is overestimated even more. Considering sea level and also surface currents, both increase the wave height compared to simulations r1 and r2. In the case of current being accounted for, the increase of significant wave height can be explained by the changes in the group velocity of waves. With a decrease in the group velocity in the case of opposing current, in order to maintain energy flux, the wave energy density has to increase.

Model deviations from measurements increase when more dynamical forcings are added to the simulations (Table 3). This can be caused by several factors. In shallow water bottom effects occur, making the balance between wind, surface currents and sea level quite complicated. For example, unknown local bathymetrical features not resolved by the model may be the cause of increasing errors (Tuomi et al., 2014). While the water depth at station B was 5.5 m only,

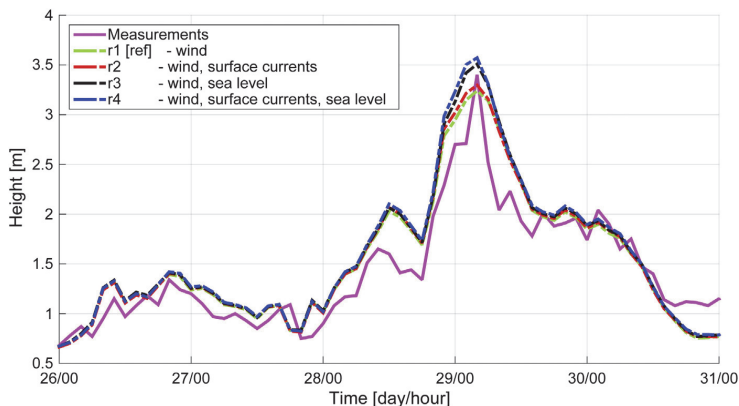


Figure 5 Comparison of measurements of significant wave height taken close to Saaremaa at station B and SWAN simulations r1 to r4.

Table 3 RMSE, scatter index, BIAS and correlation coefficient between measurements taken close to Saaremaa (measurement station B, Fig. 1) and model simulations.

Simulation	RMSE [cm]	Scatter index [%]	BIAS [cm]	Correlation coefficient
1	26	18	9	0.93
2	27	19	10	0.93
3	29	21	12	0.93
4	30	22	13	0.94

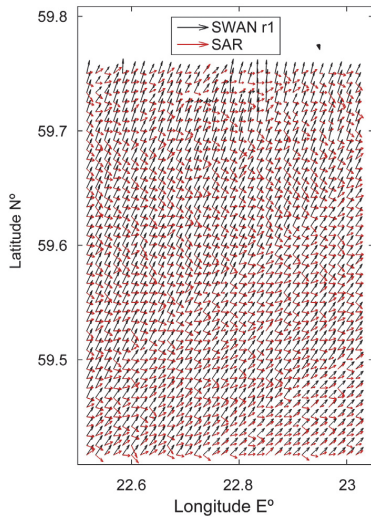


Figure 6 SWAN peak direction in simulation 1 (black arrows) are compared with SAR image (red arrows) on 29.10.2013 at 05.00. (For interpretation of the references to colour in this figure legend, the reader is referred to the web version of this article.)

Table 4 RMSE between SWAN and SAR peak directions.

	Simulation			
	1	2	3	4
RMSE [°]	47.10	49.01	47.08	48.94

water depth at the model point was 7.83 m. This calls for higher-resolution simulations, which are outside the scope of the present study.

Peak wave peak directions calculated with SWAN were compared to results from SAR images. The area of validation is shown in Fig. 1. In Fig. 6 SWAN reference simulation peak directions (red arrows) and directions provided by SAR (black arrows) are displayed. A moderate difference between the directions can be seen. In Table 4 RMSE of direction for all four simulations is presented. It varies between 47.08 and 49.01°. Simulation 3, where water level was included in the simulation, produces the best result, with RMSE of 47.08°.

3.3. Spatio-temporal impact of currents and sea-level

In order to quantify the impact of different dynamical forcings, the maximum difference of significant wave height ΔmHs^n and relative change ΔrHs^n were found with Eqs. (13)–(17). It was seen from the validations that current and sea-level effects are most noticeable during the St. Jude storm. For this reason the day of 29.10.2013 was chosen to evaluate the spatial variability of the wave field.

In Fig. 7 the probability density functions of spatial ΔmHs^n distribution are presented on a logarithmic scale. It shows the distribution of maximum difference of significant wave height. With simulation r2 (red line), where wind and surface currents were taken into account, there is a decrease in the wave height of up to 50 cm and an increase as big as 40 cm compared to r1. When taking account of wind and sea level (r3, black line) the difference ranges from –10 to 100 cm. With varying sea level the increase in the wave height is more evident. This should be the case, since with increased water

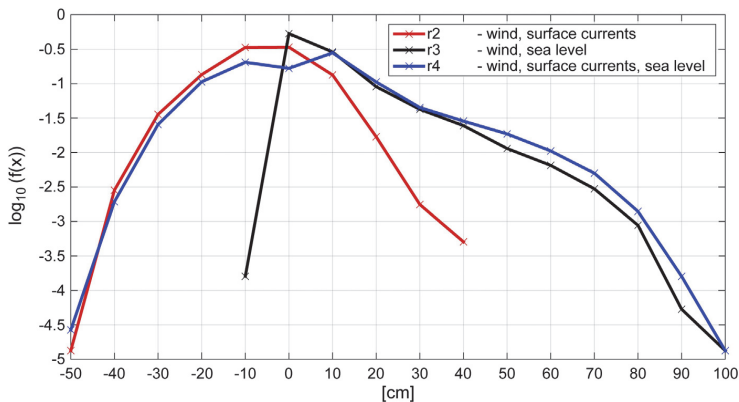


Figure 7 Significant wave height maximum differences ΔmHs^n logarithmical probability distribution for simulations r2, r3 and r4 on 29.10.2013.

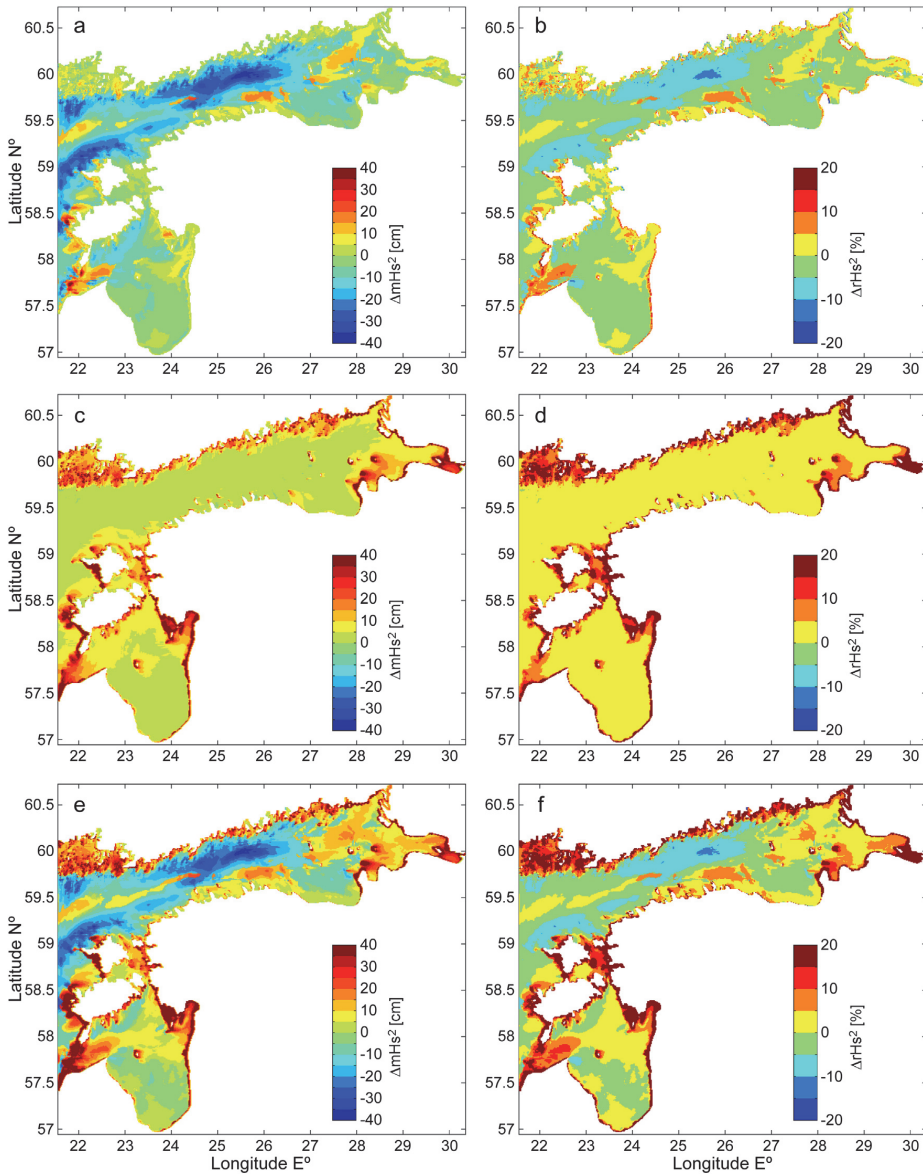


Figure 8 Time maximum absolute difference ΔmHs^n and relative difference ΔrHs^n in the significant wave height. (a and b) for r2; (c and d) for r3; (e and f) for r4. Values in a range -40 to 40 cm and -20 to 20% are shown in the figure.

level the dissipation is less. Accounting for all the dynamical forcings, the difference of ΔmHs^4 ranges from -50 to 100 cm.

Next the spatial variability of maximum difference of significant wave height ΔmHs^n is shown in Fig. 8 on the left side and relative change ΔrHs^n on the right side. The colour bar ranges from -40 cm to 40 cm in the case of absolute differences and from -20% to 20% for the relative changes.

In Fig. 8a and b the maximum absolute difference and relative change in the significant wave height when taking

account of surface currents (r2) is shown. Increase in the wave height is most evident near coasts and in narrow straits. In the southern part of the Gulf of Finland near the coast there is an increase of up to 10 cm (5%). In the north-east of the Gulf of Riga there is an increase of up to 20 cm (10 – 15%). Near the west coast of Hiiumaa wave height difference is about 10 – 20 cm (up to 20%). In Saaremaa and in the Irbes strait the difference can reach as much as 40 cm (up to 20%).

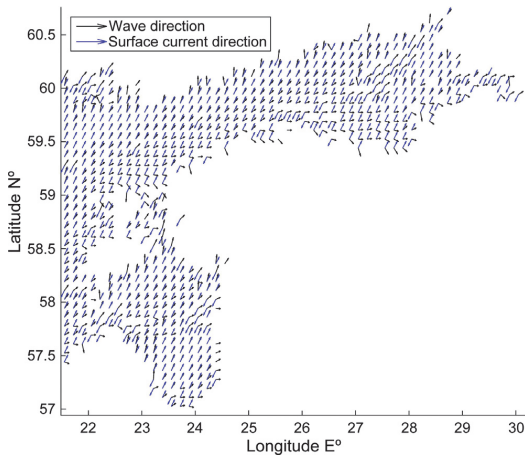


Figure 9 Propagation directions for waves in run r2 and surface currents on the time moments of maximum differences on 29.10.2013. Every 10th vector is displayed.

In Fig. 9 every 10th vector of wave and current propagation direction at time moment t_{\max} (of simulation r2) are displayed. Wave directions are shown with black arrows and surface currents with blue arrows. As waves and surface currents approach opposite directions, currents have the effect of elevating wave height. For example in Fig. 9 in Pärnu bay, the Irbe strait and on the west coast of the islands Hiiumaa and Saaremaa the waves and surface currents are propagating in opposite directions (or the current direction is deflected right of the wave directions). This results in a greater wave height increase, seen also in Fig. 8a.

In the case of currents being accounted for, a decrease of the significant wave height occurs in deeper parts of the eastern Baltic Sea. In the Gulf of Riga and Gulf of Finland there is a decrease of up to 15 cm (5%). In the Gulf of Finland between 25–26°E and 58.8–60°N wave height decreases up to 40 cm (20%) (Fig. 8a and b). In Fig. 9 it is seen that in these areas waves and surface currents are propagating more or less in the same direction and this results in a decrease of significant wave height, which is also consistent with the theory.

It is likely that the maximum differences in significant wave height occur in a specific phase of the surface currents inertial oscillation. The magnitude of the increase and decrease of significant wave height is influenced by current velocity. For example in the Irbe strait the current velocity reaches up to 195 cm s^{-1} (Fig. 3b) and from Fig. 8a and b it is seen that in this area the significant wave height is one of the things most strongly affected by the surface currents.

In Fig. 8c and d the maximum difference and relative change of significant wave height when considering wind and sea level in the run (r3) is shown. In deeper parts of the eastern Baltic Sea, where the waves are not affected by the sea bed, there is an increase in the significant wave height of about 5 cm with relative increase of 5%. Near the coast, where the bottom effects come into play, a bigger increase in

the wave height is noticeable. In coastal areas the maximum difference of significant wave height between reference run r1 and r3 is up to 40 cm (20%). Also in specific locations in the Gulf of Finland and in the Gulf of Riga there is a possible increase in wave height of 40%. It is seen that areas most significantly affected by sea-level are well exposed to the wind. This is also consistent with the work by Alari (2013).

In Fig. 8e and f it is shown the joint effect of surface currents and sea level on the wave field. On areas open to the wind the total impact of surface currents and sea level on wave height increases. For example in Pärnu bay when accounting for just currents the difference is up to 20 cm (10–15%), but the joint effect increases the wave height up to 40 cm (20%). The spatial variability patterns of surface current effects and sea level both remain. The decrease in the significant wave height remained more or less in the same areas where it was when there were just surface currents present.

4. Conclusions

Analysis of spatio-temporal patterns of wave–current–surge interaction in the eastern Baltic Sea and the corresponding mechanisms showed the impact of surface currents and sea level to the evolution of significant wave height. In deep (>20 m) water, surface currents improved the model-data comparison, especially in storm conditions. Variations in sea level had a negligible effect in deep waters, but in shallower water the effect of sea level was even larger than that of the surface currents. The extra increase in wave height was most noticeable in storm conditions and in wind exposed areas. During extreme storms, the joint effect of currents and sea level produced changes in the significant wave height from lowering it by as much as 50 cm (mostly offshore), compared to the control run, to increasing it up to 100 cm (nearshore). The relative differences of up to 20% being distributed non-symmetrically. Considering the effect of surface currents only, the range was between –50 and 40 cm whereas the sea level induced changes were between –10 and 100 cm, compared to the control run. The differences in significant wave heights were favoured under a specific phase of inertial oscillation of the surface currents.

As the wave growth effect is concentrated in the narrow coastal zone, even a 0.5 nautical mile model grid was not accurate enough to capture all the local topographical features. For further studies of this kind, higher resolution models should be used and appropriate (directional) measurements in shallow water are needed for model validation.

Acknowledgment

We are grateful to Benjamin Matterson for providing language help.

References

- Alari, V., 2013. *Multi-scale wind wave modeling in the Baltic Sea*. (PhD Dissertation). Tallinn Univ. Technol., 134 pp.
- Baltic Sea Hydrographic Commission, 2013. *Baltic Sea Bathymetry Database version 0.9.3*, (Downloaded from <http://data.bshc.pro/> on 21.03.2015).

- Battjes, J.A., Janssen, J.P.F.M., 1978. Energy loss and set-up due to breaking of random waves. In: Proc. of the 16th International Conference on Coastal Engineering, 569–587, <http://dx.doi.org/10.1061/9780872621909.034>.
- Booij, N., Ris, R.C., Holthuijsen, L.H., 1999. A third-generation wave model for coastal regions: 1. Model description and validation. *J. Geophys. Res.* 104 (C4), 7649–7666, <http://dx.doi.org/10.1029/98JC02622>.
- Bretherton, F.P., Garrett, C.J.R., 1968. Wavetrains in inhomogeneous moving media. *Proc. Roy. Soc. A: Math. Phys.* 302 (1471), 529–554, <http://dx.doi.org/10.1098/rspa.1968.0034>.
- Feistel, R., Nausch, G., Wasmund, N., 2008. *State and Evolution of the Baltic Sea, 1952–2005: A Detailed 50-year Survey of Meteorology and Climate, Physics, Chemistry, Biology and Marine Environment*. John Wiley & Sons, Hoboken, 712 pp.
- Feser, F., Barcikowska, M., Krueger, O., Schenk, F., Weisse, R., Xia, L., 2015. Storminess over the North Atlantic and northwestern Europe – a review. *Q. J. Roy. Meteor. Soc.* 141 (687), 350–382, <http://dx.doi.org/10.1002/qj.2364>.
- Funkquist, L., Kleine, E., 2007. An introduction to HIROMB, an operational baroclinic model for the Baltic Sea. SMHI Rep. *Oceanogr.* 37, 1–39.
- Guedes Soares, C., de Pablo, H., 2006. Experimental study of the transformation of wave spectra by a uniform current. *Ocean Eng.* 33 (3–4), 293–310, <http://dx.doi.org/10.1016/j.oceaneng.2005.05.005>.
- Hasselmann, K., 1974. On the spectral dissipation of ocean waves due to whitecapping. *Bound.-Lay. Meteorol.* 6 (1), 107–127, <http://dx.doi.org/10.1007/BF00232479>.
- Hasselmann, K., Barnett, T.P., Bouws, E., Carlson, H., Cartwright, D. E., Enke, K., Ewing, J.A., Gienapp, H., Hasselmann, D.E., Kruseman, P., Meerburg, A., 1973. *Measurements of Wind-Wave Growth and Swell Decay During the Joint North Sea Wave Project (JONSWAP)*. Deutsches Hydrogr. Inst.
- Jaagus, J., Kull, A., 2011. Changes in surface wind directions in Estonia during 1966–2008 and their relationships with large-scale atmospheric circulation. *Est. J. Earth Sci.* 60 (4), 220–231, <http://dx.doi.org/10.3176/earth.2011.4.03>.
- Kahma, K.K., Petterson, H., 1993. *Wave Statistics from the Gulf of Finland*. Finnish Inst. Marine Rep., Intern. Rep. 1.
- Lagemaa, P., 2012. *Operational forecasting in Estonian marine waters*. (Ph.D. diss.). Tallinn Univ. Tech., 130 pp.
- Leppäranta, M., Myrberg, K., 2009. *Physical Oceanography of the Baltic Sea*. Springer-Verlag, Berlin, Heidelberg, 378 pp., <http://dx.doi.org/10.1007/978-3-540-79703-6>.
- Longuet-Higgins, M.S., Stewart, R.W., 1960. Changes in the form of short gravity waves on long waves and tidal currents. *J. Fluid Mech.* 8 (4), 565–583, <http://dx.doi.org/10.1017/S0022112060000803>.
- Longuet-Higgins, M.S., Stewart, R.W., 1961. The changes in amplitude of short gravity waves on steady non-uniform currents. *J. Fluid Mech.* 10 (4), 529–549, <http://dx.doi.org/10.1017/S0022112061000342>.
- Longuet-Higgins, M.S., Stewart, R.W., 1964. Radiation stresses in water waves; a physical discussion, with applications. *Deep Sea Res. Oceanogr. Abstr.* 11 (4), 529–562, [http://dx.doi.org/10.1016/0011-7471\(64\)90001-4](http://dx.doi.org/10.1016/0011-7471(64)90001-4).
- Miles, J.W., 1957. On the generation of surface waves by shear flows. *J. Fluid Mech.* 3 (2), 185–204, <http://dx.doi.org/10.1017/S0022112057000567>.
- Phillips, O.M., 1957. On the generation of waves by turbulent wind. *J. Fluid Mech.* 2 (5), 417–445, <http://dx.doi.org/10.1017/S0022112057000233>.
- Raudsepp, U., Laanemets, J., Haran, G., Alari, V., Pavelson, J., Kõuts, T., 2011. Flow, waves, and water exchange in the Suur Strait, Gulf of Riga, in 2008. *Oceanologia* 53 (1), 35–56, <http://dx.doi.org/10.5697/oc.53-1.035>.
- Soomere, T., Behrens, A., Tuomi, L., Nielsen, J.W., 2008. Wave conditions in the Baltic Proper and in the Gulf of Finland during windstorm Gudrun. *Nat. Hazards Earth Syst.* 8 (1), 37–46, <http://dx.doi.org/10.1016/j.eccs.2014.08.001>.
- Suursaar, Ü., 2013. Locally calibrated wave hindcasts in the Estonian coastal sea in 1966–2011. *Est. J. Earth Sci.* 62 (1), 42–56, <http://dx.doi.org/10.5697/oc.54-3.421>.
- Suursaar, Ü., Kullas, T., Aps, R., 2012. Currents and waves in the northern Gulf of Riga: measurements and long-term hindcast. *Oceanologia* 54 (3), 421–447, <http://dx.doi.org/10.5697/oc.54-3.421>.
- The SWAN team, 2013a. *SWAN: Scientific and Technical Documentation. Cycle III version 40.91*. Delft University of Technology, Department of Civil Engineering, The Netherlands.
- The SWAN team, 2013b. *SWAN: User Manual. Cycle III version 40.91*. Delft University of Technology, Department of Civil Engineering, The Netherlands.
- Tuomi, L., Pettersson, H., Fortelius, C., Tikka, K., Björkqvist, J.V., Kahma, K.K., 2014. Wave modelling in archipelagos. *Coast. Eng.* 83, 205–220, <http://dx.doi.org/10.1016/j.coastaleng.2013.10.011>.
- Uden, P., Rontu, L., Jarvinen, H., Lynch, P., Calvo, J., Cats, G., Cuxart, J., Eerola, K., Fortelius, C., Garcia-Moya, J.A., Jones, C., Lenderlink, G., McDonald, A., McGrath, R., Navascues, B., Nielsen, N.W., Odegaard, V., Rodriguez, E., Rummukainen, M.A., 2002. *HIRLAM-5 Scientific Documentation*. Swedish Meteorol. Hydrol. Inst., Sweden.
- Van der Westhuysen, A.J., 2012. Spectral modeling of wave dissipation on negative current gradients. *Coast. Eng.* 68, 17–30, <http://dx.doi.org/10.1016/j.coastaleng.2012.05.001>.
- Whitham, G.B., 1974. *Linear and Nonlinear Waves*. John Wiley, New York, 55 pp.
- Wolf, J., Prandle, D., 1999. Some observations of wave–current interaction. *Coast. Eng.* 37 (3), 471–485, [http://dx.doi.org/10.1016/S0378-3839\(99\)00039-3](http://dx.doi.org/10.1016/S0378-3839(99)00039-3).
- Wolski, T., Wiśniewski, B., Giza, A., Kowalewska-Kalkowska, H., Boman, H., Grabbi-Kaiv, S., Hammarklint, T., Holfort, J., Lydeikaite, Ž., 2014. Extreme sea levels at selected stations on the Baltic Sea coast. *Oceanologia* 56 (2), 259–290, <http://dx.doi.org/10.5697/oc.56-2.259>.

Curriculum vitae

Personal data

Name: Sander Rikka
Date of birth: 22 July 1989
Place of birth: Estonia
Citizenship: Estonian

Contact data

E-mail: sander.rikka@taltech.ee

Education

2014–2019 Tallinn University of Technology—PhD
2012–2014 Tallinn University of Technology, Earth Sciences—MSC,
2008–2012 Tallinn University of Technology, Engineering Physics—BSC
2005–2008 High school

Language competence

Estonian – Native
English – Fluent
French – Basic skills
German – Basic skills

Professional employment

2014 – present Department of Marine Systems at TUT, Junior Researcher
2012 – 2014 Department of Marine Systems at TUT, Engineer

Scientific work

Publications according to ETIS

1.1.

Rikka, S.; Uiboupin, R.; Kõuts, T.; Vahter, K.; Pärt, S. (2019). A Method for Significant Wave Height Estimation from Circularly Polarized X-band Coastal Marine Radar Images. *IEEE Geoscience and Remote Sensing Letters*, 1–5.10.1109/LGRS.2018.2886631.

Rikka, S.; Pleskachevsky, A.; Jacobsen, S.; Alari, V.; Uiboupin, R. (2018). Meteo-Marine Parameters from Sentinel-1 SAR Imagery: Towards Near Real-Time Services for the Baltic Sea. *Remote Sensing*, 10 (5), 1–17.10.3390/rs10050757.

Rikka, S.; Pleskachevsky, A.; Uiboupin, R.; Jacobsen, S. (2018). Sea State in the Baltic Sea from Space-borne High Resolution Synthetic Aperture Radar Imagery. *International Journal of Remote Sensing*, 39 (4), 1256–1284.10.1080/01431161.2017.1399475.

Rikka, S.; Uiboupin, R.; Alari, V. (2017). Applicability of SAR based wave retrieval for wind-wave interaction analysis in the fetch-limited Baltic. *International Journal of Remote Sensing*, 38 (3), 906–922.10.1080/01431161.2016.1271472.

Viitak, M.; Maljutenko, I.; Alari, V.; Suursaar, Ü.; Rikka, S.; Lagemaa, P. (2016). The impact of surface currents and sea level on the wave field evolution during St. Jude storm in the eastern Baltic Sea. *Oceanologia*, 58 (3), 176–186.10.1016/j.oceano.2016.01.004.

3.1

Rikka, S.; Pleskachevsky, A.; Uiboupin, R.; Jacobsen, S. (2017). SEA STATE PARAMETERS IN HIGHLY VARIABLE ENVIRONMENT OF BALTIC SEA FROM SATELLITE RADAR IMAGES. *Geoscience and Remote Sensing Symposium (IGARSS), 2017 IEEE*

International Geoscience and Remote Sensing Symposium July 23–28, 2017 - Fort Worth, Texas, USA. IEEE, 10.1109/IGARSS.2017.8127621

- Laanemäe, K.; Uiboupin, R.; Rikka, S.; (2016). Sea Ice Type Classification in the Baltic Sea from TanDEM-X Imagery. *Proceedings of EUSAR 2016: 11th European Conference on Synthetic Aperture Radar: 11th European Conference on Synthetic Aperture Radar, Hamburg, Germany*, 6–9 June 2016. Berlin: Institute of Electrical and Electronics Engineers Inc, 657–660. (EUSAR Proceedings).
- Rikka, S.; Uiboupin, R.; Alari, V. (2014). Estimation of wave field parameters from TerraSAR-X imagery in the Baltic Sea. *IEEE Journal of Oceanic Engineering*, 1–6.

3.2

- Rikka, S.; Uiboupin, R.; Pleskachevsky, A.; Alari, V.; Jacobsen, S.; Kõuts, T. (2018). Radarkaugseire kasutamine Läänemere lainetuse ja tuuleväljade määramiseks. Peterson, U.; Lillemaa, T. (Toim.). *Kaugseire Eestis 2018: artiklikogumik* (32–40). Tartu Ülikooli Tartu Observatoorium.
- Rikka, Sander; Uiboupin, Rivo; Alari, Victor (2014). Laineparameetrite määramine Läänemeres radariandmete põhjal. Anne Aan, Kirke Narusk (Toim.). *Kaugseire Eestis 2014* (22–30). Keskkonnaagentuur.

3.4

- Kõuts, T.; Rikka, S.; Käärman, L.; Usk, A. (2018). Operational Wave Height Monitoring Using Navigation Buoys and Marine Radars in the Baltic Sea. In: E. Buch, V. Fernández, D. Eparkhina, P. Gorringer, G. Nolan (Ed.). *Operational Oceanography serving Sustainable Marine Development*. (157–163). The 8th International EuroGOOS Conference, Bergen, Norway, from 3 to 5 October 2017. EuroGOOS AISBL.

5.2

- Rikka, S.; Uiboupin, R.; Pleskachevsky, A.; Alari, V.; Jacobsen, S.; Kõuts, T. (2018). Radar remote sensing of the meteo-marine parameters in the Baltic Sea. *Proceedings: 2nd Baltic Earth Conference, The Baltic Sea in Transition, Helsingør, Denmark, 11 to 15 June 2018*. Ed. Köppen, S.; Reckermann, M. International Baltic Earth Secretariat Publications, 139–140.
- Rikka, S.; Uiboupin, R.; Alari, V.; Viitak, M. (2013). Läänemere lainevälja 2D spektri leidmine kasutades TerraSAR-X satelliidi infot. *Abstract book: 9th Baltic Sea Science Congress, 26–30 August, 2013, Klaipeda, Lithuania*. Coastal Research and Planning Institute of Klaipeda University (KU CORPI), 234.

Elulookirjeldus

Isikuandmed

Nimi: Sander Rikka
Sünniaeg: 22.07.1989
Sünnikoht: Eesti
Kodakondsus: Eesti

Kontaktandmed

E-post: sander.rikka@taltech.ee

Hariduskäik

2014 – 2018 Tallinna Tehnikaülikool, Maateadused—PhD
2012 – 2014 Tallinna Tehnikaülikool, Maateadused—MSC
2008 – 2012 Tallinna Tehnikaülikool, Tehniline füüsika—BSC
1996 – 2008 —Keskharidus

Keelteoskus

Eesti keel – Emakeel
Inglise keel – Kõrgtase
Prantsuse keel – Algtase
Saksa keel – Algtase

Teenistuskäik

2014 – tänaseni TTÜ Meresüsteemide Instituut, Nooremteadur
2012 – 2014 TTÜ Meresüsteemide Instituut, Insener

Teadustegevus

Publikatsioonid Eesti Teadusinfosüsteemi klassifikaatori järgi

1.1.

Rikka, S.; Uiboupin, R.; Kõuts, T.; Vahter, K.; Pärt, S. (2019). A Method for Significant Wave Height Estimation from Circularly Polarized X-band Coastal Marine Radar Images. *IEEE Geoscience and Remote Sensing Letters*, 1–5.10.1109/LGRS.2018.2886631.

Rikka, S.; Pleskachevsky, A.; Jacobsen, S.; Alari, V.; Uiboupin, R. (2018). Meteo-Marine Parameters from Sentinel-1 SAR Imagery: Towards Near Real-Time Services for the Baltic Sea. *Remote Sensing*, 10 (5), 1–17.10.3390/rs10050757.

Rikka, S.; Pleskachevsky, A.; Uiboupin, R.; Jacobsen, S. (2018). Sea State in the Baltic Sea from Space-borne High Resolution Synthetic Aperture Radar Imagery. *International Journal of Remote Sensing*, 39 (4), 1256–1284.10.1080/01431161.2017.1399475.

Rikka, S.; Uiboupin, R.; Alari, V. (2017). Applicability of SAR based wave retrieval for wind-wave interaction analysis in the fetch-limited Baltic. *International Journal of Remote Sensing*, 38 (3), 906–922.10.1080/01431161.2016.1271472.

Viitak, M.; Maljutenko, I.; Alari, V.; Suursaar, Ü.; Rikka, S.; Lagemaa, P. (2016). The impact of surface currents and sea level on the wave field evolution during St. Jude storm in the eastern Baltic Sea. *Oceanologia*, 58 (3), 176–186.10.1016/j.oceano.2016.01.004.

3.1

Rikka, S.; Pleskachevsky, A.; Uiboupin, R.; Jacobsen, S. (2017). SEA STATE PARAMETERS IN HIGHLY VARIABLE ENVIRONMENT OF BALTIC SEA FROM SATELLITE RADAR IMAGES. *Geoscience and Remote Sensing Symposium (IGARSS), 2017 IEEE*

International Geoscience and Remote Sensing Symposium July 23–28, 2017 - Fort Worth, Texas, USA. IEEE, 10.1109/IGARSS.2017.8127621

- Laanemäe, K.; Uiboupin, R.; Rikka, S.; (2016). Sea Ice Type Classification in the Baltic Sea from TanDEM-X Imagery. *Proceedings of EUSAR 2016: 11th European Conference on Synthetic Aperture Radar: 11th European Conference on Synthetic Aperture Radar, Hamburg, Germany, 6-9 June 2016*. Berlin: Institute of Electrical and Electronics Engineers Inc, 657–660. (EUSAR Proceedings).
- Rikka, S.; Uiboupin, R.; Alari, V. (2014). Estimation of wave field parameters from TerraSAR-X imagery in the Baltic Sea. *IEEE Journal of Oceanic Engineering*, 1–6.

3.2

- Rikka, S.; Uiboupin, R.; Pleskachevsky, A.; Alari, V.; Jacobsen, S.; Kõuts, T. (2018). Radarkaugseire kasutamine Läänemere lainetuse ja tuuleväljade määramiseks. Peterson, U.; Lillemaa, T. (Toim.). *Kaugseire Eestis 2018: artiklikogumik* (32–40). Tartu Ülikooli Tartu Observatoorium.
- Rikka, Sander; Uiboupin, Rivo; Alari, Victor (2014). Laineparameetrite määramine Läänemeres radariandmete põhjal. Anne Aan, Kirke Narusk (Toim.). *Kaugseire Eestis 2014* (22–30). Keskkonnaagentuur.

3.4

- Kõuts, T.; Rikka, S.; Käärman, L.; Usk, A. (2018). Operational Wave Height Monitoring Using Navigation Buoys and Marine Radars in the Baltic Sea. In: E. Buch, V. Fernández, D. Eparkhina, P. Gorringer, G. Nolan (Ed.). *Operational Oceanography serving Sustainable Marine Development*. (157–163). The 8th International EuroGOOS Conference, Bergen, Norway, from 3 to 5 October 2017. EuroGOOS AISBL.

5.2

- Rikka, S.; Uiboupin, R.; Pleskachevsky, A.; Alari, V.; Jacobsen, S.; Kõuts, T. (2018). Radar remote sensing of the meteo-marine parameters in the Baltic Sea. *Proceedings: 2nd Baltic Earth Conference, The Baltic Sea in Transition, Helsingør, Denmark, 11 to 15 June 2018*. Ed. Köppen, S.; Reckermann, M. International Baltic Earth Secretariat Publications, 139–140.
- Rikka, S.; Uiboupin, R.; Alari, V.; Viitak, M. (2013). Läänemere lainevälja 2D spektri leidmine kasutades TerraSAR-X satelliidi infot. *Abstract book: 9th Baltic Sea Science Congress, 26-30 August, 2013, Klaipeda, Lithuania*. Coastal Research and Planning Institute of Klaipeda University (KU CORPI), 234.

